Universität Rostock Traditio et Innovatio

Mechanistic Understanding and Improvement of Photochemical Proton Reduction Catalyzed by Iron Carbonyl Complexes for Sustainable Hydrogen Production

Kumulative Dissertation

zur Erlangung des akademischen Grades

doctor rerum naturalium (Dr. rer. nat.)

am Institut für Chemie

der Mathematisch-Naturwissenschaftlichen Fakultät

der Universität Rostock

vorgelegt von

Steffen Fischer

geb. am 18.06.1986

in Rostock

Rostock, April 2021

https://doi.org/10.18453/rosdok_id00003292

GutachterInnen:
Prof. Dr. Ralf Ludwig, Universität Rostock, Institut für Chemie
Prof. Dr. Angelika Brückner, Rostock, Leibniz-Institut für Katalyse e. V.

Jahr der Einreichung: 2021
Jahr der Verteidigung: 2021

ACKNOWLEDGEMENT

The author thanks in the first place Professor Ralf Ludwig for providing an exciting research topic of high contemporary relevance. The scientific, financial, and moral support, the honest feedback and the granted freedom were highly appreciated and very helpful.

Parts of this work were founded by the BMBF with the project Light2Hydrogen, by the ESF with the project PS4H and by the Ministry for Education, Science and Culture of Mecklenburg-Vorpommern.

Many thanks go out to Enrico Barsch for his support and supervision during the author's diploma phase and beyond. Enrico Barsch build the gateway to this work and taught the author on how to reasonably approach scientific questions. He considerably supported to establish the collaboration with the team at the LIKAT.

The author thanks Mathias Beller, Henrik Junge, Felix Gärtner, Michael Karnahl, Nils Rockstroh, Alastair Lennox, Dirk Hollmann, Anja Kammer and Petra Bartels for the nice and fruitful collaborative works at the Leibniz Institute for Catalysis (LIKAT Rostock). Acknowledgments are sent to Oliver Kühn, Olga S. Bokareva of the physics department for their contributions with Time-dependent DFT calculations. Also, many thanks to Matthias Bauer and Roland Schoch for the possibility to jointly conduct the XAS experiments.

The author appreciates the commitment of his master students Arend Rösel and Elisabeth Oberem as well as the work of Romina Eggers, who was supervised by the author during her Bachelor thesis. They contributed to this work with the synthesis of the preformed $[Net_4][Fe(CO)_6(\mu\text{-}CO)(\mu\text{-}PR_2)]$ complexes, with cyclo-voltammetry experiments, good company in the office and a helping hand for reloading the MCT detector with liquid nitrogen.

Furthermore, the author thanks Dr. Wolfgang Baumann for greatly mastering the NMR spectrometer and acquiring great spectra from samples that lack of the presence of deuterated solvents. Without the technical support by Peter Kumm, Martin Riedel, Roland Weihs and Patrick Quade this work would have hardly been possible. Also, many thanks to Sabine Haack, Anette Surkus and Robert Francke for their advices regarding electrochemistry experiments and exciting collaborative research.

Special thanks to the whole working group of Prof. Ludwig in the Physical and Theoretical Chemistry department at the University of Rostock, especially Anika Wilhelms, Anne-Katrin

Hallmann and Andreas Appelhagen for organizational support and entertainment. There was always a supportive and cordial spirit in the team.

Special thanks also to Claudia Cozma and her team from Centogene, for supporting and pushing.

The author declares heartfelt gratitude for Andreas Gottwald for giving him faithful company starting even before the beginning of the journey in the field of chemistry. Also, many thanks and warm regards to all other brothers, friends, and companions as well as former band members who supported the author and never gave up on him.

The author thanks sincerely his loving mother, father, sister, and the rest of the family for always being encouraging, inspiring and supporting. The author also thanks his beloved Josephin for the warm support and patience during the last sprints of this work.

ABSTRACT

This work addresses the investigation of the mechanism of three homogeneous, photocatalytic proton reduction systems that produce the energy carrier hydrogen. All three systems had been introduced by the Beller working group and make use of self-assembling, simple iron carbonyls to catalyze the hydrogen evolution reaction. Although a comparably high activity was found for these systems, they were far away from efficient application on a large scale.
For a better understanding of the mechanisms and to find starting points for an improvement of the systems, continuous flow IR spectroscopy coupled with gas volumetry (operando spectroscopy) was applied in this work. Besides this, other supporting or complementary methods were utilized like XAS and NMR spectroscopy as well as ESI-MS, cyclic voltammetry, and quantum chemical computation.

The first system consists of triethylamine as sacrificial reductant and electron donor, an iridium complex as photosensitizer, and $[Fe_3(CO)_{12}]$ as catalyst precursor. In this work, $[HFe_3(CO)_{11}]^-$ and $[HFe(CO)_4]^-$ were identified as active species and resting state or dormant species. Furthermore, the reaction conditions required for their formation were investigated. As concluded from kinetic experiments, electron transfer from triethylamine to the excited iridium complex constitutes the rate determining step of the system. Poisoning of the catalyst by bipyridine ligands dissociated from the photosensitizer was found as a deactivating process together with light induced CO dissociation from the catalyst.

In the second system, additionally phosphine is applied as co-catalyst. In this work, the formation of the [FeFe] – hydrogenase mimic $[Fe_2(CO)_6(\mu\text{-}CO)(\mu\text{-}P(R)_2)]^-$ was observed. This species is inert to poisoning by bipyridine, which improves the stability of the system. Furthermore, the requirements on the phosphine substituents and the reaction conditions necessary for the formation of a catalytically active diferrate species were investigated. Application of presynthesized $[NEt_4][Fe_2(CO)_6(\mu\text{-}CO)(\mu\text{-}P(C_6H_4\text{-}4\text{-}CF_3)_2)]$ was found to increase the initial H_2 production rate by 80% and the H_2 yield by 10% compared with the in-situ generated catalyst. The formation of less active $[Fe_2(CO)_5(P(R)_3)(\mu\text{-}CO)(\mu\text{-}P(R)_2)]^-$ in case of addition of excessive amounts of phosphine and the decomposition of the iridium photosensitizer throughout the reaction were identified as deactivation mechanisms with the latter being the weakest point of the system.

The third system makes use of a heteroleptic copper photosensitizer $[Cu(P\text{^}P)(N\text{^}N)]^+$ instead of the iridium complex. In this work, it was confirmed that the copper complex is in chemical equilibrium with its homoleptic form $[Cu(N\text{^}N)_2]^+$. As in the second system, the P-C cleavage at the phosphine ligand was observed. The resulting active proton reducing assembly was

found to be composed of the heteroleptic $[Cu(P^P)(N^N)]^+$ photosensitizer and the $[Fe_2(CO)_6(\mu\text{-}CO)(\mu\text{-}P(Ph)_2)]^-$ catalyst. Based on these findings, the Beller group developed a photocatalytic system, in which both, photosensitizer and catalyst are generated in-situ, thus avoiding time consuming synthesis.

The results presented in this work, prove that application of spectroscopic methods and mechanistic investigations contribute substantially to the improvement and understanding of catalytic systems.

TABLE OF CONTENTS

LIST OF FIGURES

LIST OF ABBREVIATIONS

adt^H	Azadithiolato ligand
bda	2,2'-bipyridine-6,6'-dicarboxylate
bdt	Benzene-1,2-dithiolate
B_{MD}	System B with pre-synthesized (molecular defined) diiron catalyst
bpy	Bipyridine
Bu	Butyl
Bz	Benzyl group
C_H	System C with homoleptic **Cu*PS*** and add. Xantphos ligand
C_{IS}	System C with in-situ generated **Cu*PS***
cot	Cyclooctatetraene
Cu*PS*	Copper photosensitizer [Cu(bathocuproine)(Xantphos)]PF_6
CV	Cyclic voltammetry
cy	Cyclohexane
DHLA	Dihydrolipoic acid
DPEPhos	Bis[(2-diphenylphosphino)phenyl] ether
dppv	Cis-1,2-bis(diphenylphosphino)ethylene
DSPEC	Dye-sensitized photoelectrochemical cell
EPR	Electron paramagnetic resonance spectroscopy
ESI-MS	Electrospray ionization mass spectrometry
$Fc^{+/0}$	Ferrocene redox couple
HEC	Hydrogen evolution catalyst
*i*Pr	Iso-propyl group
IR	Infrared Spectroscopy
Ir*PS*	Iridium photosensitizer [Ir(bpy)$(ppy)_2$]PF_6
ISC	Inter system crossing
MLCT	Metal-to-ligand charge-transfer
MPA	3-Mercaptopropionic acid
N^N	Chelating diimine ligand with two binding nitrogen atoms
NHE	Normal hydrogen electrode
NMR	Nuclear magnetic resonance spectroscopy
P^P	Chelating ligand with two binding phosphorous atoms
PEC	Photoelectrochemical cell
ppy	2-Phenylpyridine
PS	Photosensitizer
PS*	Photosensitizer in excited state

Pyr	N-pyrrolyl group
pyS	pyridyl thiolate ligand
QD	Quantum dot
QY	Quantum yield
RHE	Reversible hydrogen electrode
SC	Semi-conductor
SCE	Saturated calomel electrode
SR	Sacrificial Reductant / Sacrificial Reagent
STH	Solar-to-Hydrogen
TEA	Triethylamine
TEOA	Triethanolamine
THF	Tetrahydrofuran
TOF	Turn over frequency
TON	Turn over number
TPPTS	Sodium triphenylphosphine trisulfonate
UV	Ultraviolet light
Vis	Visible light
WOC	Water oxidation catalyst
WRC	Water reduction catalyst
XAS	X-Ray absorption spectroscopy

I. INTRODUCTION

The epoch of fossil energy carriers is fading since conventional sources are increasingly exhausted. The growing exploitation of unconventional sources (like shale oil and gas) is accompanied by higher risks for environmental pollution and a low energy return on investment. The latter has decreased by half in the last four decades. Furthermore, the emission of the greenhouse gas carbon dioxide is the driving force for climate change that raises deep environmental, public health and socioeconomic concerns.[1,2]

These drawbacks inevitably call for a transition towards renewable energy sources, which is one of the main challenges in the 21st century. Most renewable energy technologies rely on sunlight, which strikes the earth's surface with $90 \cdot 10^{15}$ W. This would cover the $18.5 \cdot 10^{12}$ W worldwide average rate of primary energy demand of 2019[3] by almost 5000 fold. Wind power-, photovoltaic- or hydropower plants etc. can transform this energy into electricity. However, these technologies are subject to intermittency and intensity fluctuations and require technical possibilities to distribute and store energy. The most common options of storing electricity are based on reversible conversion into chemical energy e.g. batteries or hydrogen.[1]

Batteries have the potential to power the vehicle transport sector by 70% in 2050 according to scenarios like the IRENA REmap Case[2]. Their heavy weight and the fact that they are constituted of limited materials like lithium are drawbacks of this technology.

Hydrogen is required as solar fuel and alternative energy carrier in sectors that are hard to electrify as well as feedstock in industry[2]. It has a light weight and can store energy for entire seasons[2]. The energy that is stored in hydrogen can either be released by combustion or be converted into electricity within fuel cells. As byproduct, both processes generate nothing but water (equation 1).

$$H_2 + \frac{1}{2} O_2 \underset{\text{Electrolysis / Water Splitting } (E^0 = 1.23\ V)}{\overset{\text{Combustion } (\Delta_R G^0 = -237\ kJ\ mol^{-1})}{\rightleftharpoons}} H_2O \qquad (1)$$

The deficiency of hydrogen is its low volumetric energy density (0.0025 $kWh*L^{-1}$). There are several approaches to address this challenge: by liquidation, the energy density of hydrogen can be increased up to 2.5 $kWh*L^{-1}$. However, this is still three times lower than the density of gasoline (8.07 $kWh*L^{-1}$). Furthermore, the liquidation process consumes 30 − 40% of the stored hydrogen's energy content[4]. There are alternative storage methods under research like the hydrogenation of small molecules like CO_2 [5] or storage in metal hydrides and highly porous materials like metal organic frameworks[6].

Today, hydrogen is majorly produced petrochemically in energy demanding processes like steam reforming of natural gas at 800 °C and 40 bar in the presence of nickel catalysts[7]. Only three percent of the hydrogen is produced via electrolysis.[8] Electrolysis can be a solution for

the challenges that come along with fossil energy but only if renewable sources are used as primary energy form. For example, with a combination of current photovoltaic silicon cells[1] (average efficiency η = 15%) and platinum-based electrolysis cells[2] (η = 70%), solar energy can be stored in hydrogen with a total efficiency of 10%[1].

An alternative[3] to this assembly constitutes the direct photoelectrochemical and photochemical water splitting (Artificial photosynthesis). In this approach, solar energy is absorbed by single materials or multiple components that use this energy to split water into hydrogen and oxygen. The efficiency of such systems is typically assessed with the quantum yield (QY) or solar-to-hydrogen yield (η_{STH}). That describes the ratio between the amount of evolved hydrogen molecules and the number of incident photons multiplied by the number of electrons involved in the reaction (equation 2).[1]

$$QY = \eta_{STH} = \frac{2 \cdot n_{H_2}}{n_{Photon}} \qquad (2)$$

Prototypes of photosynthetic reactions are found in nature[9]. While biological systems have an efficiency of no more than 1%, artificial photochemical water splitting can theoretically reach conversion efficiencies of 30-40% [1,5,10,11].

1.1 Water Splitting: Concept, Approaches and Materials

Water splitting happens in two half reactions: the water reduction and water oxidation (equations 3 and 4).

$$2\,H^+ + 2\,e^- \longrightarrow H_2 \qquad E = -0.41\ V \text{ vs. NHE at pH} = 7 \qquad (3)$$

$$2\,H_2O \longrightarrow O_2 + 4\,H^+ + 4\,e^- \qquad E = +0.81\ V \text{ vs. NHE at pH} = 7 \qquad (4)$$

First, sunlight is absorbed by a molecule or semiconductor material called the photosensitizer (PS). The latter uses the excitation energy for an electron-hole separation lifting the electron to a more reducing electrochemical level (Figure I.1). Before the electron and hole recombine, the electron is transferred to a proton reduction catalyst (commonly known as water reduction catalyst or hydrogen evolution catalyst, HEC) where it is used to reduce protons from water to form hydrogen (equation 3). The hole in the light absorbing unit is filled by another catalyst (water oxidation catalyst, WOC) that captures electrons from water. This process is accompanied by the release of oxygen (equation 4). In that way the light harvesting, charge generation, separation and accumulation, as well as catalytic water reduction and oxidation take place in one single device.[10,12]

[1] Alternatively, Dye Sensitized Solar Cells can be used (DSSC, efficiency in laboratory environment = 12.3%).[100]
[2] By use of alkaline water electrolyzers, noble metals are avoided at the expense of strong alkaline electrolytes.[22]
[3] Further alternatives: microbiological hydrogen generation and thermolysis of water by concentrated solar power

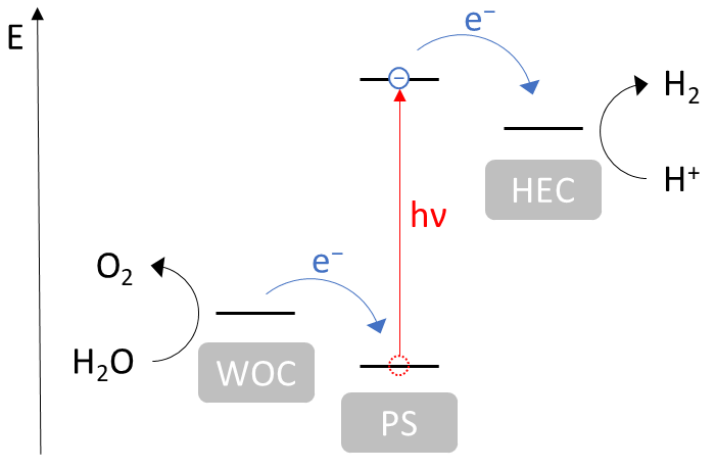

Figure I.1. Simplified scheme for photocatalytic water splitting. A photocatalytic water splitting device comprises a Photosensitizer (PS), a water oxidation catalyst (WOC) and a Hydrogen evolution catalyst (HEC).

1.2 Heterogeneous Solid-state Photoelectrochemical Cells

Water splitting devices based on solid-state semiconductor materials are called photoelectrochemical cells (PECs). They are the most promising approach for sustainably hydrogen production since they are anticipated to have a low environmental impact and might be most cost effective[1]. Development of heterogeneous water splitting devices is very challenging since there are many requirements on the semiconductor material: It must provide a band gap of smaller than 3 eV that is small enough to absorb a large portion of the solar spectrum (λ > 400nm).[13] At the same time this gap must be wide enough to correspond to the necessary overpotential for water splitting (> 1.23 V)[1,14]. Also, the absolute positions of the two band edges need to be lower than the redox level for water reduction (−0.41 V vs. NHE and −0.44 V vs. $Fc^{+/0}$ in acetonitrile at pH = 7)[15] and higher than that of water oxidation (0.81 vs. NHE at pH = 7). If the use of a HEC and WOC is omitted, the surface of the semiconductor material must be catalytically active for both half-reactions. Since these requirements are very demanding, it has not yet been possible for a single material to meet them. Hence, research has mostly been focused on multi component materials that follow an electrochemical Z-scheme.

An example of a solid-state water splitting PEC is the artificial leaf with NiMoZn as proton reduction catalyst together with a cobalt-based oxygen evolving complex on a triple junction amorphous Si (3jn-a-Si) solar cell[16,17]. It comprises only earth-abundant materials and operates under simple conditions at 100 mW cm^{-2} sun irradiation. However, a solar to hydrogen yield of only η_{STH} = 2.5% was achieved. A Comparable performance for water splitting was accomplished with a carbon nanodot - carbon nitride (C_3N_4) nanocomposite with a η_{STH} of 2%[18,19]. The most prominent example is a PEC based on $GaInP_2$/GaAs, which yielded hydrogen with an efficiency of η_{STH} = 12.4%[20] that could be further increased to n_{STH} = 16% if the photoelectrode was placed outside the electrolyte[21]. Given the fact that the latter system

is based on scarce elements and has yet only been measured in a laboratory environment, these numbers show that solid state semiconductor PEC currently cannot compete with PV-electrolyzer systems.

1.3 Homogeneous/ Molecular Water Splitting

In contrast to solid state semiconductors, molecular catalysts, such as organo-metal complexes and organic dyes allow for easy modifications of their structure through ligand design. Thereby, their energy levels, spectral responses and sterical configuration can be fine-tuned and energy-efficient mechanistic pathways can be promoted.[1,10,13,22] Another advantage over heterogeneous systems is the high metal-atom economy, meaning that up to 100% of the metal atoms can contribute to the catalytic reaction, which saves material costs[22]. Investigation of the reaction mechanism of molecular water splitting systems is possible with standard laboratory techniques, such as spectroelectrochemistry, stopped-flow UV-Vis spectroscopy, *in-situ* IR spectroscopy, *in-situ* NMR spectroscopy and mass spectrometry.[22]

The half reactions water reduction and water oxidation are commonly studied and optimized independently. This simplifies the multi-component systems and facilitates investigations of their reaction mechanisms.[12]. In doing so, one of the two half reactions is substituted by sacrificial reagents that either accept or donate electrons while being converted irreversibly into waste products. Both half reactions can later be recombined for an overall water splitting device or take place on a physically separated cathode and anode in a dye sensitized photo-electro-chemical cell (DSPEC, vide infra)[1,13]. This is analogous to the situation in nature where the two processes take place in two different redox cycles in photo system I (reduction) and II (oxidation, vide infra).[16]

1.4 Homogeneous Water Reduction - Components

In contrast to water splitting, in photocatalytic water reduction systems, the water oxidation cycle is replaced by a sacrificial reductant (or sacrificial electron donor reagent). This leaves the system with the sacrificial reductant (SR), the photosensitizer (PS) and the proton reduction catalyst (= water reduction catalyst or hydrogen evolution catalyst HEC) as major components. From the former to the latter, electrons are transferred upon excitation of the PS by light, resulting in the reduction of the catalyst. The electrons are then consumed in the water reduction reaction and hydrogen is produced (Figure I.2).

1.4.1 The Sacrificial Reductant

During the donation of an electron by the SR to the PS, the SR is sacrificed, meaning it is oxidized and irreversibly transformed into inert molecules. This is necessary in order to avoid

charge recombination that is the electron back transfer from the reduced PS to the oxidized SR. Another requirement on the SR is the thermodynamic adequacy with the PS: The electrochemical potential E(SR^+/SR) has to be lower than E(PS^*/PS^-) or E(PS^+/PS^*) depending on the quenching mechanism of the PS (oxidative or reductive quenching, vide infra, Figure I.2, right).[23]

Several small molecules have been vastly applied in photochemical proton reduction. Besides oxalates and thiols, mostly amines like triethylamine (TEA) and triethanolamine (TEOA) as well as ascorbic acid have been used. The amines show oxidation potentials around 0.7 V vs. SCE (≈ 0.3 V vs. $Fc^{+/0}$)[24], work under basic conditions and require an organic solvent. In contrast, mono-deprotonated ascorbic acid exhibits an oxidation potential around 0.5 V vs. SCE (≈ 0.1 V vs. $Fc^{+/0}$)[24] and can be applied in a neutral or acidic aqueous medium.[23]

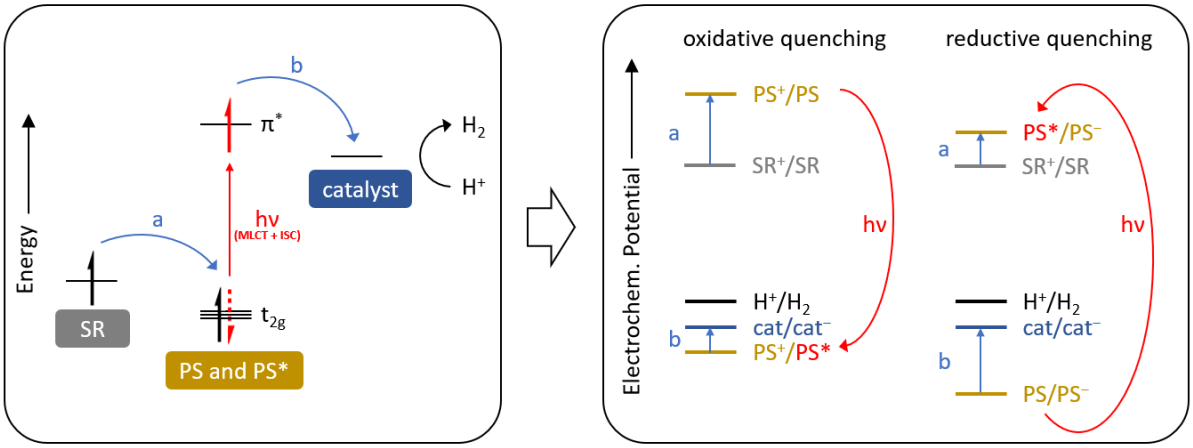

Figure I.2. Simplified description of electron transfer process in photocatalytic water reduction. Left: simplified molecular orbital depiction of an organometallic PS. The cycle begins with excitation of an electron of the PS by visible light irradiation. This triggers a metal to ligand charge transfer (MLCT) and a subsequent intersystem crossing (ISC). In the case of oxidative quenching, the excited electron is first transferred to the catalyst (process b), where it is used to reduce protons and generate hydrogen. After that, the electron hole in the t_{2g} orbital of the oxidated PS (PS^+) is filled by electron transfer from the SR (process a) and the PS is restored. In the case of reductive quenching the both processes occur in another order: after excitation of the PS, first the hole in the t_{2g} orbital is filled by an electron from the SR (process a). After that, the electron in the π* orbital of the reduced PS (PS^-).is transferred to the catalyst (process b) and the PS is restored. Right: Depiction of the electrochemical potential of each redox step for the oxidative quenching or the reductive quenching.

1.4.2 The Photosensitizer

The photosensitizer introduces the energy into the system by harvesting photons. An absorbed photon induces the promotion of an electron to an energetically higher, previously unoccupied orbital. In case of organometallic complexes as PS, this process occurs as metal-to-ligand charge transfer and is followed immediately by an intersystem crossing.[25] The result is the charge separated, exited triplet state of the PS (PS*). The latter can have both, enhanced oxidative and/or reductive power compared to the unexcited state[23]. therefore, compared to the PS, the PS* is more prone to receive an electron from the SR, which is referred to as reductive quenching. In parallel, the PS* is more inclined to donate an electron to the catalyst, a process called oxidative quenching (Figure I.2). In case of reductive quenching, the PS is

regenerated by transfer of the electron from PS^- to the catalyst, while in case of oxidative quenching, the PS is restored by electron transfer from the SR to the PS^+.[23] Which of the two mechanisms takes place depends on the nature of all components: the SR, PS, catalyst and solvent.

The PS has to meet several requirements. In order to harvest sunlight with high efficiency, it must absorb light in a broad range within the visible region. It also needs to have a long-lived excited-state lifetime, provide reversible redox processes, and show stability in the ground and excited states over a prolonged irradiation time. The potentials of the PS or PS* must comply with those of the sacrificial reagent and the catalyst. E.g. in case of reductive quenching, the potential $E(PS^*/PS^-)$ must be higher than the oxidation potential of the SR and the potential $E(PS/PS^-)$ must be lower than the reduction potential of the catalyst (see Figure I.2, right). For large-scale applications, the PS needs to be low prized. Thus, noble metals should be avoided[26]

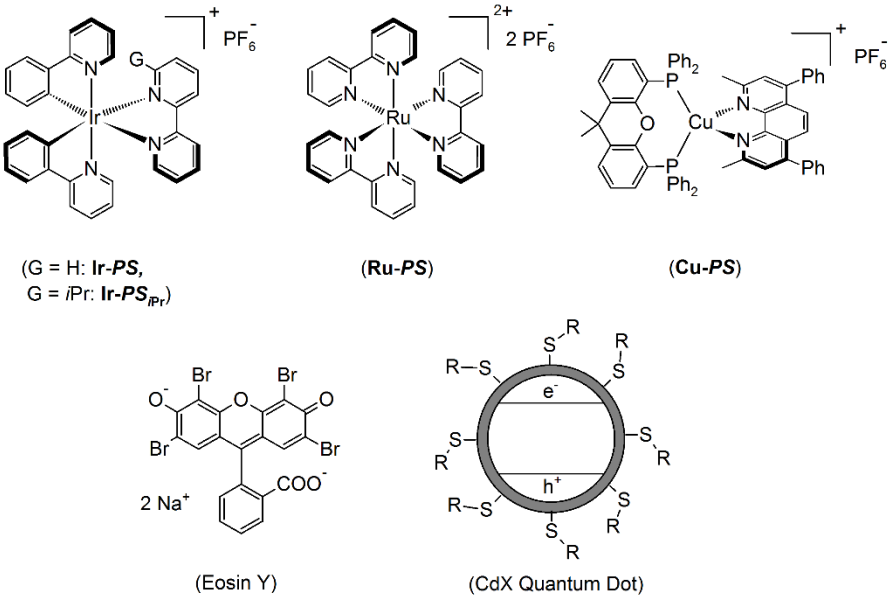

Figure I.3. Photosensitizers for the photocatalytic proton reduction.

There are several classes of molecular PS described in literature. One class is represented by organometallic coordination complexes[25,27]. The properties of these PS can be adjusted by the choice of the metal and the design of the ligands that are typically conjugated and feature low-lying unoccupied π* orbitals.[25] Some of the earliest and best described complexes comprise Ruthenium as central atom such as $[Ru(bpy)_3]^{2+}$ [28–30] (**Ru*PS***, bpy = bipyridine, Figure I.3,). A higher photostability and an 8-fold improved performance regarding water reduction was observed when using cyclometalated Iridium complexes as PS like $[Ir(bpy)(ppy)_2]^+$ (**Ir*PS***, ppy = phenylpyridine, Figure I.3).[31] Other complexes have been developed that incorporate platinum[32] or rhenium[33]. Furthermore, non-noble metal based photosensitizers have been

found that are composed of earth abundant elements only and are thus more likely to be suitable for large scale applications: e.g. iron[34,35], zinc[36,37], magnesium[36], or copper[38,39] complexes (**Cu*PS***, Figure I.3,). Especially the latter is worth mentioning since Cu shows a d^{10} configuration. This configuration rules out deactivating ligand-field excitation states that otherwise would compete with the metal-to-ligand charge transfer, as is the case for other first row transition metals. By this, there is no need for expensive support ligands like e.g. carbene-based ligands used in iron PS.[25]

Metal-free, pure organic dyes constitute another class of photosensitizers. E.g. xanthene derivates like Eosin Y[40] (Figure I.3) or Triphenylamines[41,42] have been successfully applied in molecular photocatalytic water reduction systems.

The third class of photosensitizers presented here, are the quantum dots (QD, Figure I.3). These are nano-crystals (also called molecular crystals[43,44]) of semi-conductor (SD) materials like CdSe or CdTe with a diameter of 2 – 10 nm surrounded by capping agents[45]. They claim a position in the transient area between the field of heterogeneous and homogeneous catalysis since they combine bulk-solid and molecular properties and form colloidal dispersions with water.[26,46] Compared with organic and organometallic PS, they show an increased durability, higher light absorption coefficients and can also allow for multiple exciton generation by a single photon.[45] The Fine-tuning of the light-absorptive and electrochemical properties is realized by modifying the size of the QD particles. Due to the effect of quantum size confinement, the energy gap between their valance- and the conduction band increases with decreasing particle size. This does not only affect the absorption range within the electromagnetic spectrum but also shifts the band gab edges to more reducing and oxidizing potentials.[47,48] To allow for a synthesis of small spherical, uniform and water-soluble nano-crystals, the use of capping agents like thiols is indispensable. After formation of the nano-crystals, the capping agents remain bound to the surface atoms of the QD forming micelle entities and acting as stabilizers against both, rapid oxidation and surface recombination in an aqueous environment.[26,46]

1.4.3 The Catalyst

Photocatalytic water reduction involves the transfer of two electrons and protons respectively and is a kinetically sluggish reaction. Because of that, the reaction requires a high overpotential. In order to lower this overpotential, overcome the high reaction barriers and accelerate the reaction rate, a catalyst needs to be introduced into the system.[22] For allowing a thermodynamically feasible electron transfer from the PS to the protons, the catalyst's reduction potential $E(cat/cat^-)$ has to be lower than the potential of the hydrogen evolution reaction $E(2H^+/H_2)$ (=−0.41 V vs. NHE and −0.44 V vs. $Fc^{+/0}$ in acetonitrile at PH = 7; Equation 3)[15] and higher than the reduction potential of the PS $E(PS/PS^-)$ (in case of reductive quenching of the PS, see Figure I.2, right). For large-scale applications, the catalyst should consist of sustainable,

low-cost, earth abundant as well as non-toxic ingredients[49,50] and should be easy to synthesize or better assemble itself in solution.[10] Another requirement on the catalyst is a long-term stability under reaction conditions, in the presence of water and under illumination, and high intrinsic catalytic activity.[22]

The productivity and stability of the catalyst are mostly assessed by the turnover number (TON) that is the number of Hydrogen molecules produced per molecule of the catalyst (Equation 5)

$$TON = \frac{n_{H_2}}{n_{catalyst}} \quad (5)$$

The catalytic activity is displayed by the turnover frequency (TOF), the number of Hydrogen molecules produced per catalyst molecule and time interval (Equation 6)

$$TOF = \frac{n_{H_2}}{n_{catalyst} \cdot t} \quad (6)$$

Over the course of the reaction, the catalyst is subject to several transformation processes resulting in various catalyst states. The most significant states and intermediates are described here: Before being added to the reaction solution, the catalyst is present in its precursor form, a preferably easy to handle and easy to synthesize complex. At the beginning of the reaction, the precursor is converted into the active species. This is the most important species since it is a highly reactive complex and mediates the catalytic process. During the course of the catalytic cycle, the active species reacts with water and receives electrons while being transformed into short-living intermediates. The slowest of these processes is the rate-determining step. Note that in multi-component systems, this overall rate-determining step may be located in any of the system's cycles.[51]

Due to its high reactivity, the active species is likely to be subject to side or back reactions. If in such a reaction, the active species is in chemical equilibrium with the produced complex, the latter is referred to as dormant or resting state, which is present in high concentrations. Both, the active species and the resting state can be directly applied to the reaction solution, e.g. with the help of stabilizing ions or ligands. This avoids preceding conversion processes and thus induction periods of low activity as is the case in application of the precursor form. Undesired irreversible side reactions cause the deactivation of the catalyst, which leads to decomposition products and the end of the hydrogen production.[51]

A mechanistic understanding of the described processes is indispensable for allowing for aimed manipulations in order to increase the activity and stability of the system or for scaling up the process from laboratory to industrial scale. There are a variety of tools that help to identify the catalyst's intermediates and to acquire concentration time data in kinetic experi-

ments. These tools imply methods like NMR-, EPR-, IR-, UV-Vis and X-ray absorption spectroscopy (XAS), as well as mass spectrometry, electrochemistry and computational chemistry.[22,51]

With the exception of EPR spectroscopy[4], all these techniques have been used in this work to elucidate the mechanism of photocatalytic water reduction systems that comprise the application of iron carbonyls as catalyst precursors. The investigated system and used methods are described below. Before that, the currently most prominent homogeneous systems for photocatalytic water reduction are summarized with the focus on earth abundant catalysts, especially those based on iron.

1.5 Homogeneous Water Reduction - Examples

One of the first successful water reduction systems consisted of a $[Ru(bpy)_3]^{2+}$ complex as PS, a $Rh(bpy)_2Cl_3$ as mediator (redox relay), Triethanolamine (TEOA) as sacrificial electron donor and K_2PtCl_6 as catalyst precursor.[29,52] Notably, it was found that the PS underlies an oxidative quenching mechanism and that the Pt complex is the source for Pt colloids, which serve as microelectrode for the proton reduction.[53,54]

Since it is a requirement on the catalyst to be low-prized, it was necessary to withdraw complexes of expensive noble metals and focus research on those that were made out of earth abundant elements. As a result, complexes of Co, Ni, Fe or Mo were found as functional catalysts.[49,50] The following exemplary systems are confined to these catalysts with a broader focus on iron based ones. Investigation results on the reaction mechanisms illustrate the challenges in the design of a functional and scalable photocatalytic reduction system.

1.5.1 Cobalt and Nickel Based Catalysts

One of the most prominent systems that involves cobalt makes use of the cobalt dithiolene complex $[Co(bdt)_2]^-$ (bdt = benzene-1,2-dithiolate). In 1:1 water-acetonitrile, with ascorbic acid as SR and the standard PS $[Ru(bpy)_3]^{2+}$, a TON of 2300 was achieved (Figure I.4).[55]

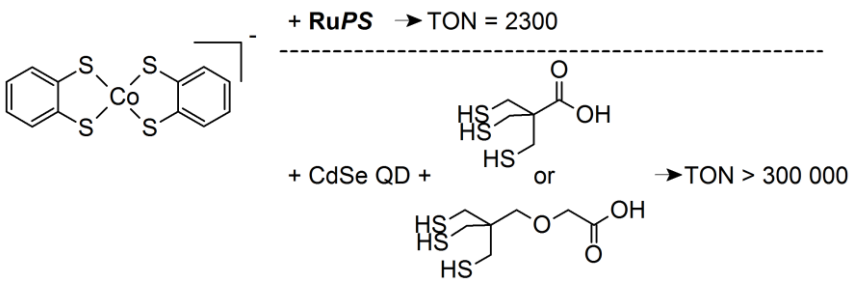

Figure I.4. Cobalt based catalyst $[Co(bdt)_2]^-$ used in photocatalytic proton reduction.

[4] However, EPR spectroscopy was used by collaborating colleagues. See section 1.5.3 to 1.5.5.

However, if CdSe quantumdots with tripodal S-donor capping agents were applied as PS in pure water, the TON was increased to over 300 000, the most active water reduction system with a well-defined molecular catalyst that has been reported up to this date.[56]

A successful nickel based water reduction catalyst was obtained by use of pyridyl thiolate ligands to form $[Ni(pyS)_3]^-$ (Figure I.5). Together with the noble metal free Eosin Y as PS and triethylamine (TEA) as sacrificial reagent in an ethanol water mixture at pH 12.2, a TON of 5500 was observed after 40 hours. Although the PS shows a higher quenching constant for oxidative quenching in comparison to reductive quenching, the latter was found to propel the hydrogen production under catalytic conditions due to the high concentration of TEA. In the late course of the reaction, buildup of unstable PS^- leads to a bleaching of the PS and the deactivation of the system. As the diironcomplex in nature (vide infra), the catalyst benefits from the pendant base effect provided by the coordinating nitrogen.[57]

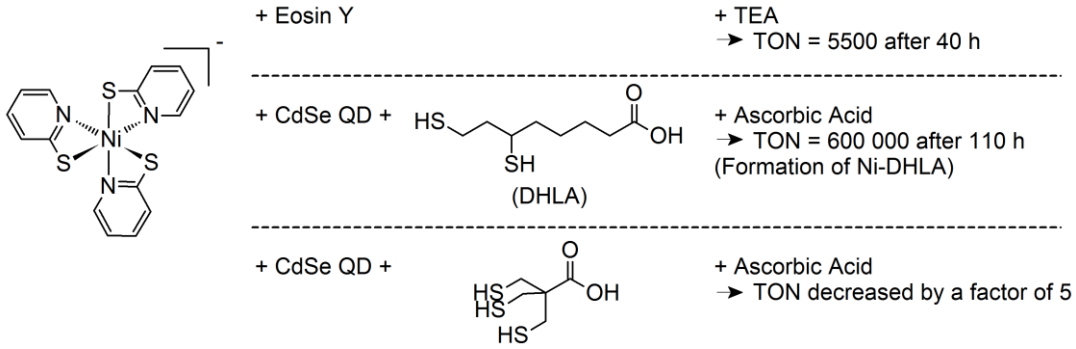

Figure I.5. Nickel based catalyst $[Ni(pyS)_3]^-$ used in photocatalytic proton reduction.

Application of quantumdots with dihydrolipoic acid (DHLA) as capping agents results in a TON of impressive 600 000 (enhancement by a factor of > 100). However, the high turnover numbers are mainly associated to dissociation of DHLA from the PS and the in situ formation of a Ni-DHLA complex as active species. This was confirmed by a control experiment that showed similar turnover numbers when $Ni(NO)_3$ was applied as catalyst precursor.[58] When using non-dissociating tripodal capping agents, the hydrogen yield was decreased by a factor of five compared to the DHLA containing system.[56]

Comparable high TONs were observed at similar conditions if the catalyst was replaced by nickel coordinated by two 2-Mercaptophenol ligands (Ni2b, Figure I.6). Together with Eosin Y as PS and TEA as sacrificial reagent in an ethanol water mixture, a TON of about 6000 was achieved. In contrast, the S,S derivate 2,2-Benzenedithiol (Ni2a, Figure I.6) did not show any hydrogen production.

By the example of this system, the correlation of the electrochemical potential with the catalytic activity of the catalyst can be demonstrated: In electrocatalysis, **Ni2b** reduces protons at −1.64

V vs. SCE while **Ni2a** has a reduction potential at −2.25 V vs. SCE. The first value is still more negative than Eosin Y can provide (−1.3 V vs. SCE) but is nevertheless closer to the reduction potential of the PS. A QD is likely much more reducing. That is why with CdSe, a tripodal capping agent and ascorbic acid (H_2A) as sacrificial reagent, both the **Ni2a** derivate (TON_{Ni} = 100 000) and the **Ni2b** derivate (TON_{Ni} = 300 000) show catalytic activity with the trend of thermodynamic favorability.[50,59]

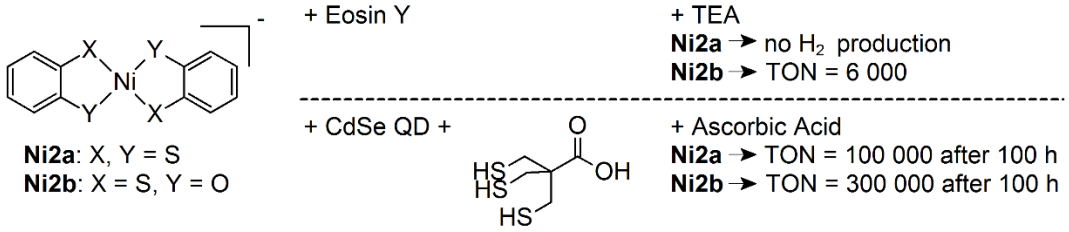

Figure I.6. Nickel based catalyst with 2-Mercaptophenol (Ni2b) or 2,2-Benzenedithiol ligands (Ni2a) used in photocatalytic proton reduction.

1.5.2 Iron Hydrogenase Active site and Mimics

In nature, proton reduction is catalyzed by hydrogenase that occurs in a number of bacteria, archaea and some eukarya. All known forms of this metalloenzyme incorporate iron in their respective active sites. Besides a mononuclear [Fe] complex, two binuclear [NiFe] and [FeFe] active sites were structurally and mechanistically elucidated and described in literature.[60,61] Of those three, the [FeFe] complex shows the highest catalytic performance. It features characteristic structure motives[62–66] (Figure I.7, top, left) and is the template for numerous synthetic proton reduction catalysts[22,50,60,61,67–71]. The two iron atoms are coordinated by a CO and CN^- ligand respectively, both of which are strong field ligands that lead to a low-spin configuration at the metal centers. Furthermore, a bridging CO ligand and an azadithiolato (adt^H) bridge coordinates to the iron atoms. The nitrogen bridgehead acts as pendant base and proton relay that plays an important role in the biological catalytic cycle. One of the iron atoms possesses an open coordination site that is able to bear a hydride ligand. The other iron atom is linked via a bridging cysteine sulfur atom to a cubane [4Fe-4S] cluster that mediates the electron transfer to the active side. The [FeFe] complex is bound to a highly optimized functional protein matrix that provides the pocket for the catalytic reaction interacting electrostatically or via hydrogen-bonds with the ligands. The matrix also comprises pathways for the electrons, protons and hydrogen molecules to and from the protein surface[60].

The simplified catalytic cycle of the [FeFe]-hydrogenase includes a respectively twofold protonation and reduction that leads to an intermediate with a protonated nitrogen bridgehead and a terminal hydride bound to the previously open coordination site at the iron. After combination of the proton at the ammonium bridge with the hydride, hydrogen is released. The existence

of the described intermediate highlights the importance of the adt^H ligand and the terminal hydride in the biological mechanism.[60,61] The catalytic cycle is rapidly repeated resulting in a TOF for the hydrogenase complex that can reach a number of up to 10^4 s^{-1}.[72]

[FeFe]-hydrogenase active site mimics have been successfully applied in electrocatalytic proton reduction.[61] The iron catalyst with the highest performance for this reaction is [dppv(CO)Fe(adt)Fe(CO)dppv] (dppv = 1,2-bis(diphenylphosphino)ethylene; Figure I.7, top, second from the left) . It catalyzes the hydrogen evolution reaction with strong acids like CF_3COOH at already −1.11 V vs. $Fc^{+/0}$ with a TOF of 58 000 s^{-1}. The dppv ligand ensures the same rigidity as In the [FeFe]-hydrogenase, which increases the lifetime of the terminal Fe-H bond that is present in the catalytic cycle of this reaction.[61]

Mimics of the [FeFe]-hydrogenase active site have also been successfully applied for the photoinduced proton reduction reaction: Wang, Sun and co-workers[73] introduced $[Fe(adt^{Bz})(CO)_5(P(Pyr)_3)]$ (Pyr = N-pyrrolyl, Bz = benzyl; Figure I.7, top, third from the left) as catalyst together with the iridium complex $[Ir(bpy)(ppy)_2]^+$ (**IrPS,** Figure I.3) as PS and triethylamine (TEA) as SR. The catalyst achieved a TON of 466 after 8 hours of light irradiation.

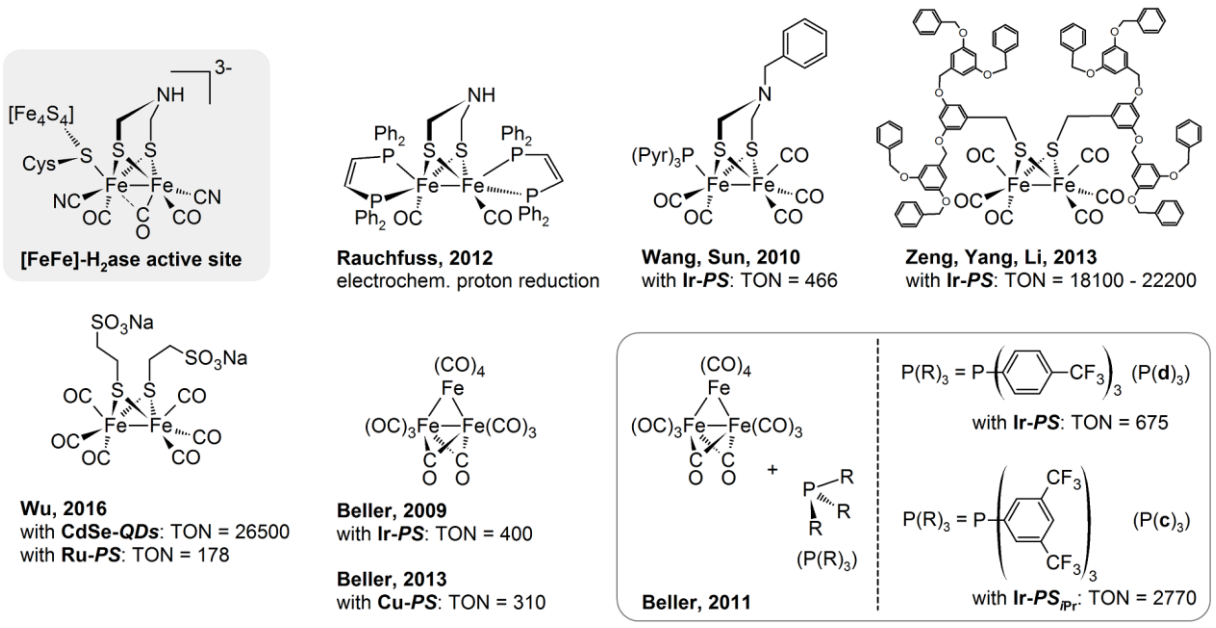

Figure I.7. [FeFe]-Hydrogenase active-site structure and its mimics applied as catalysts in electrochemical and photochemical proton reduction.

Using the same PS and SR, Zeng, Yang, Li and co-workers applied another binuclear iron complex with dendritic coordination spheres (Figure I.7, top, right).[74] The dendritic ligands encapsulated the iron complex while mimicking the protein matrix of the enzyme. This type of [FeFe] hydrogenase active site mimics accomplished TONs from 18 100 to up to 22 200. However, please note that the system was tested on a very small scale with catalyst concentrations

of only 10 nmol L^{-1}. Systems like these show that the photocatalytic proton reduction can occur via abiological reaction mechanisms without a nitrogen atom in the thiolate bridge.

Jian, Wu and co-workers demonstrated that application of quantum dots as PS like CdTe capped with 3-mercaptopropionic acid (MPA) (Figure I.3) could substantially increase the performance of the iron catalyzed photoinduced proton reduction achieving TONs of up to 52 800.[75] This high performance should mainly be attributed to the quantum dot PS. A similar system with $[Fe_2(\mu\text{-}S(CH_2)_2SO_3Na)_2(CO)_6]$ as catalyst (Figure I.7, bottom, left) and ascorbic acid as SR showed a TON of 26 500 if MPA capped CdSe quantum dots were employed, but only a TON of 178 if the organometallic complex $[Ru(bpy)_3][PF_6]_2$ (**Ru*PS***, Figure I.3) was added as PS.[76]

1.5.3 Simple Iron Carbonyls as Catalyst (System A)

The Beller group could demonstrate that the photocatalytic water reduction reaction can also be catalyzed by simple, commercially available iron(0) carbonyl complexes.[77,78] This finding showed that it was possible to save expenses on ligands like adt, which otherwise would require a three step synthesis[79]. In the system presented by the Beller group, the reaction was carried out in a mixture of THF/TEA/H_2O (volumetric ratio: 4/1/1) with TEA being the SR. Again, the complex $[Ir(bpy)(ppy)_2]PF_6$ (**Ir*PS***, Figure I.3) was used as PS. Various iron(0) carbonyls were respectively applied as catalysts each showing a similarly high activity: $[Fe(CO)_5]$, $[Fe_2(CO)_9]$, $[Fe_3(CO)_{12}]$ (Figure I.7, bottom, second from the left), $[HNEt_3][HFe_3(CO)_{11}]$ and $[Fe(CO)_3(cot)]$ (cot = cyclooctatetraene). A lower, but still significant activity was observed for the mononuclear catalysts $[NEt_4][HFe(CO)_4]$, $Na_2[Fe(CO)_4]$ (Collman's reagent), $[NEt_4][Fe(CO)_3(NO)]$ and $[Fe(CO)_3$(benzylideneacetone)$]$. At optimized **Ir*PS*** and catalyst concentrations, a TON of 400 was reported for $[Fe_3(CO)_{12}]$ after six hours of irradiation with a 300 W Xe-light source with 420 nm UV cut-off filter(concentrations: 7.5 µmol **Ir*PS***, 4.5 µmol $[Fe_3(CO)_{12}]$ in 10 mL THF/TEA/H_2O 4/1/1).

Control experiments revealed that all components (SR, PS, catalyst and light) are needed for hydrogen evolution. It was demonstrated that water is the only source of hydrogen, as proven by experiments with D_2O where exclusively D_2 was detected via gas chromatography.

In degradation experiments it was shown that both the **Ir*PS*** and the catalyst are decomposed during the reaction. **Ir*PS*** was deactivated by irradiation even in the absence of the catalyst, while the catalyst degraded only under turnover conditions.

Furthermore, spectroscopic methods were used to investigate the reaction mechanism. EPR studies carried out by D. Hollmann[80] on a light irradiated solution of the **Ir*PS*** in THF/TEA/H_2O (8/2/1) confirmed that the excited **Ir*PS**** can be reductively quenched in the presence of TEA resulting in the reduced **Ir*PS*$^-$**. The signal was found to rapidly decline with time, probably owing to a degradation of the **Ir*PS*$^-$**.

In a solution containing all components of the system, but in the absence of light irradiation, $[Fe_3(CO)_{12}]$ was found by EPR spectroscopy[80] to be reduced directly by TEA in a preliminary reaction to form the radical $[Fe_3(CO)_{12}]^{\bullet-}$, which decomposes via decarbonylation into $[Fe_3(CO)_{11}]^{\bullet-}$, $[Fe_2(CO)_8]^{\bullet-}$ and another unknown mononuclear diamagnetic species. All three radicals were measured with a ratio of 1:66:32. The detection of $[Fe_2(CO)_8]^{\bullet-}$ was further confirmed by Raman spectroscopy.

If the **Ir*PS*** was absent instead, solutions of either $[Fe(CO)_5]$, $[Fe_2(CO)_9]$ or $[Fe_3(CO)_{12}]$ in THF/TEA/H_2O (4/1/1) were found to show a purple color after 15 min of light irradiation. After removing the solvent of such solutions, a hydride signal at $\delta = -14.8$ ppm was found in the ^{1}H-NMR spectra in C_6D_6. The ^{1}H-NMR signal and the color of the solution indicated the formation of $[HFe_3(CO)_{11}]^-$ regardless of the applied iron carbonyl.

Operando IR investigations were carried out by E. Barsch on the complete system with 6.1 µmol $[Fe_3(CO)_{12}]$ and 10 µmol **Ir*PS*** in 20 mL THF/TEA/H_2O 16/4/1. The low water content had to be chosen because of total absorption by water in the spectral region for metal carbonyl complexes when using an IR cell with a optical path length of 0.48 mm. The EPR- and IR investigations showed that all the iron material is converted into $[HFe_3(CO)_{11}]^-$ within the first minutes of irradiation. Over the course of the reaction, another two species were found by IR spectroscopy to evolve while the gas evolution rate as well as the concentration of $[HFe_3(CO)_{11}]^-$ gradually decrease.

One of the two unknown species was generated upon reduction of $[HFe_3(CO)_{11}]^-$ and was found to be in photoinduced equilibrium with the latter. The species was assigned tentatively as a solvent-stabilized mononuclear species $[Fe(CO)_2(THF)_3]$. This assignment was affirmed by DFT calculations. However, the calculated wavenumbers deviated vigorously from the experimental IR spectrum even after application of a scaling factor that was suitable to bring the computed spectrum of $[HFe_3(CO)_{11}]^-$ in agreement with the experimental one.

Over the course of the reaction, CO_2 was neither detected by IR spectroscopy nor by gas chromatography. It was concluded that the water-gas shift reaction does not contribute to hydrogen generation. However, parallel to the production of hydrogen, acetaldehyde was found to evolve. The latter contributes characteristic bands to the IR spectrum and is, besides diethylamine, the product of the oxidation and decomposition of TEA.[23,81–86]

Based on the findings of the NMR- and IR spectroscopic investigation, a catalytic mechanism was proposed: From either of the precursors $[Fe(CO)_5]$, $[Fe_2(CO)_9]$ or $[Fe_3(CO)_{12}]$, under reaction conditions, the trinuclear $[HFe_3(CO)_{11}]^-$ was assumed to be generated (but not yet confirmed), with the latter species in equilibrium with $[Fe(CO)_2(THF)_3]$. $[HFe_3(CO)_{11}]^-$ was proposed to be the key intermediate in the catalytic cycle.

1.5.4 Simple Iron Carbonyl Catalyst with Phosphine Co-Catalyst (System B)

Various mono-dentate phosphine and phosphite ligands were added as co-catalyst to the reaction mixture described above in order to test for stabilization of the iron metal center and an increase in activity relative to the standard reaction with no ligand.[78] Electron-withdrawing phosphine ligands like $P(C_6H_3\text{-}3,5\text{-}(CF_3)_2)_3$ and $P(C_6H_4\text{-}4\text{-}CF_3)_3$ (Figure I.7, bottom, right) were found to increase the activity of the catalyst by 50% reaching a TON of 675 after three hours and 1080 TONs after ten hours. Other ligands like $P(C_6F_5)_3$ or PPh_3 had no effect on the reaction. A worse activity was observed in case of application of electron rich $P(C_6H_4\text{-}4\text{-}OMe)_3$, alkylphosphines like Pcy_3 (cy = cylcohexane) or phosphites like $P(OPh)_3$.

Further, the influence of the iron-to-ligand ratio on the activity was analyzed using $P(C_6H_4\text{-}4\text{-}CF_3)_3$ as ligand. While application of an $[Fe_3(CO)_{12}]/PR_3$ ratio of 1/1 and 1/1.5 increased the activity relative to the reaction without ligand, a ratio of 1/2 had no effect and a ratio of 1/3 had a worsening impact on the activity. It was deduced that polynuclear iron clusters participate in the reaction and that the catalyst center is blocked in case of excessive amounts of phosphines.

By optimization of the reaction conditions, the performance of the system could be further improved. In 10 mL THF/TEA/H_2O with a ratio of 3/2/1 (pH 12), 15 µmol **Ir*PS***, 3.3 µmol $[Fe_3(CO)_{12}]$ and 5 µmol $P(C_6H_3\text{-}3,5\text{-}(CF_3)_2)_3$ under Xe-light irradiation (300 W, no filter) at 25 °C, a TOF of 260 h^{-1} within the first three hours and a TON of 1610 after 24 hours was achieved. Notably, the reaction could be driven with visible light only. This was shown by the application of 385 and 420 nm UV cut-off filters, which led to a decrease of the TON by no more than respectively 5 and 10% as compared to the measurements with unfiltered Xe-light. In experiments carried out with monochromatic light (440 nm), a quantum yield of 13.4% could be determined. The hydrogen flow of this system was shown to be sufficient to run small-scale electric devices in combination with a fuel cell.

In a preliminary experiment, from a solution of $[Fe_3(CO)_{12}]$ and $P(C_6H_3\text{-}3,5\text{-}(CF_3)_2)_3$ in THF/TEA/H_2O, the solvent was reduced and the remaining solid dissolved in $CDCl_3$. The ^{31}P-NMR spectrum showed a sole signal at δ = 84.7 ppm. This signal was observed also under catalytic conditions after 20 minutes of light irradiation. It was assigned tentatively to the species $[Fe_3(CO)_{11}(P(C_6H_3\text{-}3,5\text{-}(CF_3)_2)_3)]$. However, the role of the phosphine ligand could not be identified unambiguously.

The Beller group accomplished further improvements of the system by modifying the PS.[87] More specifically, they added an alkylgroup like sec-Butyl or iso-Propyl to the bpy ligand (**Ir*PS*$_{i\text{Pr}}$**, Figure I.3). By this, they achieved the highest performance for the $[Fe_3(CO)_{12}]$ catalyst - $P(C_6H_3\text{-}3,5\text{-}(CF_3)_2)_3$ co-catalyst pair with 2770 TONs after 20 hours of irradiation with blue light (440 nm).The initial quantum yield of this system amount to astonishing 16.4%.

1.5.5 Iron Carbonyl Catalyst with Copper Photosensitizers (System C)

One of the first molecular-defined systems for photocatalytic water reduction that was composed exclusively of earth-abundant metals was developed by the Beller-group in 2013.[39,88] In contrast to the system described above, copper complexes of type $[Cu(N^N)(P^P)]^+$ were applied as photosensitizer. Previously, this type of complexes had been described in literature as components in organic light emitting diodes. Additionally to the PS (3.5 µmol), again $[Fe_3(CO)_{12}]$ was used as catalyst (5 µmol) in THF/TEA/H_2O (10 mL, volumetric ratio 4/1/1) with TEA as SR, irradiated by 1.5 W Xenon light.

The $[Cu(N^N)(P^P)]PF_6$ complexes were synthesized in a one-pot tandem ligand-substitution method. They comprise bathocuproine or derivates thereof (N^N) and a diphosphide (P^P) respectively as bidentate and chelating ligands. By modification of either ligands, advances in the system's catalytic performance could be accomplished. Since in all experiments, the same amount of $[Fe_3(CO)_{12}]$ was applied, the performance improvements are also reflected in an increased TON of the iron catalyst.

The initial system[39] included a copper PS with a DPEphos ligand. Substitution of the latter with the more rigid Xantphos ligand resulted in the complex that is denoted as **Cu*PS*** throughout this work (Figure I.3). Application of **Cu*PS*** enhanced the catalytic activity and stability of the system by 64% resulting in an iron catalyst TON of 273.[5] If instead of xantphos, a thixantphos derivate was used, which is equally rigid but electron-enriched, the hydrogen evolution rate was increased by the expense of the system's stability. As a result, a similar hydrogen yield was achieved in a shorter amount of time. Notably, both the xantphos and thixantphos containing copper complex outperform the **Ir*PS*** at the same reaction conditions.

The performance of the system could be further improved by changing the volumetric ratio of the THF/TEA/H_2O mixture. At a ratio of 4/3/1, the system with the xantphos containing **Cu*PS*** achieved a TON of 310 for the iron catalyst.

In the subsequent work of the Beller group[88], the hydrogen yield of the system was increased even further to a TON of 466 for the iron catalyst. This was accomplished by replacing the methyl groups next to the nitrogen atoms of the bathocuproine ligand with bulky n-Butyl groups. Thereby, the stability of the system was increased and hydrogen evolution was monitored still after 60 hours while in case of the other copper complexes it was ceasing after less than 35 hours.

The Beller group confirmed that there is a positive correlation between the activity of the system and the lifetime of the excited PS, which in turn was extended by the modification of the ligands: In the ground state, the Cu complexes show a distorted tetrahedral geometry. Upon

[5] please note that, the TON specified in the paper had to be recalculated in order to refer to molecules of H_2 per iron catalyst instead of atoms of H per **Cu*PS***

excitation, the formally $3d^9$ metal center tends to adopt a pseudo-square-planar geometry with two open coordination positions, both to which solvent molecules can coordinate. This species has a smaller energy gap to the ground state favoring the non-radiative decay pathway and shortening the lifetime of the excited state. The rigid diphosphine ligands and phenanthroline derivates with bulky substituents (like bathocuproine) inhibit the flattening of the molecule and conserve the tetrahedral geometry upon excitation. This shields the metal atom and increases the energy gap as well as the lifetime of the excited state.

Notably, the performance of the **Cu*PS***/$[Fe_3(CO)_{12}]$ system could not be improved by addition of electron withdrawing phosphine ligands to the reaction solution as it was the case for the **Ir*PS***/$[Fe_3(CO)_{12}]$ system (see above). On the contrary, the application of $P(C_6H_3\text{-}3,5\text{-}(CF_3)_2)_3$ as co-catalyst led to a slightly decreased activity.

Control experiments showed that proton reduction also takes place in the absence of UV light (395 nm cut-off filter), although at a lower rate. However, at these conditions, the system shows an improved stability of up to three days. Further, it was confirmed that all three components of the system (**Cu*PS***, catalyst and SR) are necessary for hydrogen generation. Moreover, the general applicability of the copper photosensitizer was demonstrated: hydrogen evolution was also observed with K_2PtCl_6 as catalyst or ascorbic acid and triethanolamine as alternative SR.

First mechanistic investigations by photoluminescence spectroscopy and electrochemistry focused on the **Cu*PS*** cycle:

The lifetime of the exited **Cu*PS*** in pure THF is 6.4 µs. In THF/TEA/H_2O (4/1/1) without the catalyst, the lifetime decreases to 730 ns, thus reflecting the quenching rate by TEA which probably corresponds to a reductive electron transfer step from the TEA to the PS. If the catalyst is added as well, the lifetime of the excited PS is further decreased by 4-fold to 180 ns. This means that the presence of the catalyst provides a second efficient quenching pathway, which corresponds to the oxidative quenching of the PS by the catalyst.

Electrochemistry experiments confirm that both the oxidative and reductive quenching pathways are feasible.[88,89] The excited state of the **Cu*PS*** has an oxidation potential E(**Cu*PS*$^+$**/**Cu*PS****) of −1.75 V vs. $Fc^{+/0}$. This is low enough for oxidative quenching and electron transfer to the catalyst $[HFe_3(CO)_{11}]^-$, which has a potential E($[HFe_3(CO)_{11}]^-$/ $[HFe_3(CO)_{11}]^{2-}$) of −1.70 vs. $Fc^{+/0}$. Likewise, the oxidation potential of TEA with E(TEA^+/TEA) = +0.44 V vs $Fc^{+/0}$ is below the reduction potential of the excited **Cu*PS*** with E(**Cu*PS****/**Cu*PS*$^-$**) = +0.63 V vs. $Fc^{+/0}$ allowing for a reductive quenching. In the latter case, the reduced **Cu*PS*** (E(**Cu*PS***/**Cu*PS*$^-$**) = −2.05 vs $Fc^{+/0}$) would also be thermodynamically capable of reducing the catalyst. It has to be noticed that in cyclovoltammetry experiments, the reduction of the ground sate of the **Cu*PS*** was found to be reversible while the oxidation was irreversible.

Further investigations on the degradation mechanism of the **Cu*PS*** had not been carried out at this point in time.

1.6 Homogeneous Water Oxidation - Examples

Out of both half reactions, water oxidation is more difficult to be accomplished artificially. The reason for this is the requirement of a high thermodynamic potential ($\Delta G \approx 237$ kJ mol^{-1} and $E_0 \approx 1.23$ V) and a high overpotential to overcome the kinetic barrier involved in the transfer of four protons and four electrons.[22]

In nature, water oxidation is catalyzed by the oxygen-evolving complex in Photosystem II. The active site of the complex consists of a Mn_4CaO_5 cluster that is surrounded by amino acid residues, Cl^- ions and H_2O molecules (see Figure I.8**)**.[90–92]

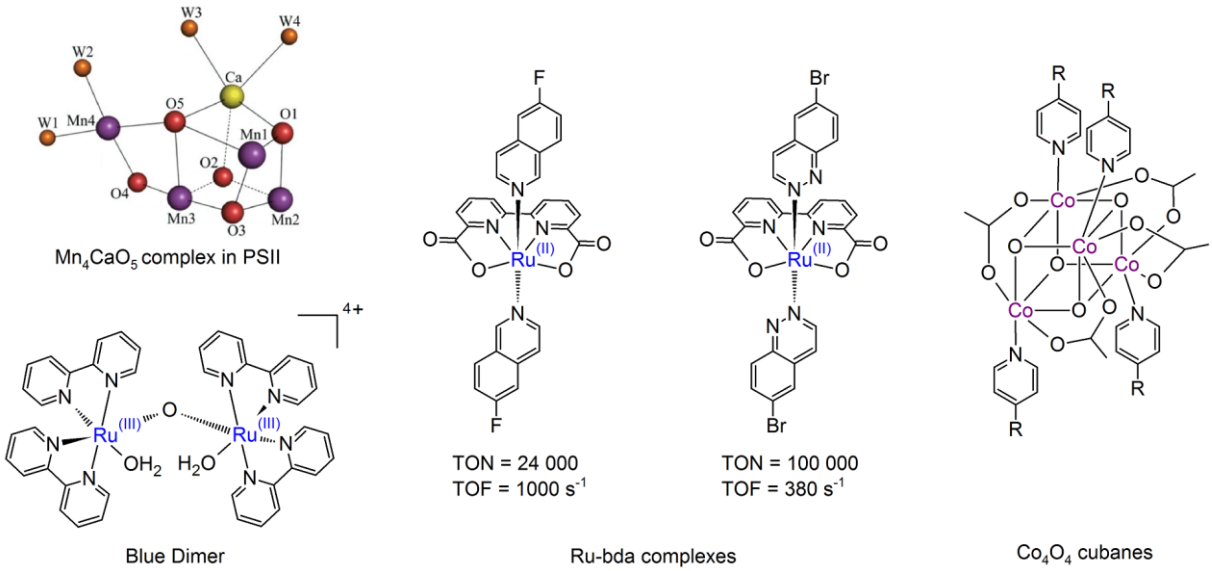

Figure I.8. WOC catalysts in nature and in artificial photocatalytic water oxidation systems. The structure of the Mn_4CaO_5 complex was reprinted with permission from ref. [90]. Copyright Macmillan Publishers 2011.

For artificial water oxidation, Meyer and co-workers introduced the famous ‘‘blue dimer’’ cis,cis-$[Ru^{II}(bpy)_2(H_2O)]_2(\mu\text{-}O)$ in 1982 with a TON of 13 and a TOF of 0.004 s^{-1} (see Figure I.8**)**.[93] These numbers were strongly improved with state of the art catalysts that are Ru complexes comprising a bda ligand (bda = 2,2’-bipyridine-6,6’-dicarboxylate) (see Figure I.8**)**. Those complexes were introduced by the working group of Sun and produce O_2 via a bimolecular pathway. Using Ce^{4+} as chemical oxidant in aqueous media at pH 1.0, such Ru-bda complexes can achieve TONs of >100 000 and TOFs of > 1000 s^{-1} at overpotential of less than 200 mV.[94–96]. The Ru-bda complexes were also proven to catalyze water oxidation under photocatalytic conditions with $[Ru(bpy)_3]^{2+}$ as a sensitizer and $S_2O_8^{2-}$ as a sacrificial electron acceptor[97].

Molecular WOCs based on earth abundant transition-metals have also been investigated. Complexes comprising Mn, Co, Cu, Ni and Fe have been found[22]. One of those many worth to mention is the class of Co_4O_4 cubane catalysts that have been applied successfully in photochemical water oxidation (see Figure I.8**)**. With $[Ru(bpy)_3]^{2+}$ as photo sensitizer and $S_2O_8^{2-}$ as a sacrificial electron acceptor, a quantum efficiency of impressive 80% at λ > 400 nm and a TON of > 140 was achieved.[98,99]

1.7 Dye Sensitized Photo Electrochemical Cells

For dispensation with sacrificial reagents and application on a large scale, molecular photocatalytic reduction- and oxidation systems can be recombined in Dye Sensitized Photoelectrochemical Cells (DSPEC).[13,22] In these devices, the PS and catalyst are immobilized at the surface of mesoporous semiconductors (SC) that are attached to transparent electrodes. DSPECs arose from the concept of dye-sensitized solar cells[100] extended to the field of photosynthetic cells. Instead of simply generating electricity, the cells use the electron flow to drive the water splitting reaction. Advantageously, the H_2 and the O_2 are generated at separated locations, which avoids the production of oxyhydrogen.

A DSPEC device may contain only one photoactive electrode, meaning a photocathode for proton reduction or photoanode for water oxidation, which is used together with a platinized counter electrode. In such an assembly, an auxiliary voltage (external bias) is most often applied since the photo-potential generated by light in the visible range might not be sufficient enough to drive the overall water splitting reaction.

A DSPEC is referred to as a tandem device in case both, the cathode and the anode are photoactive. Such a device is faintly reminiscent of nature's Z-scheme with the separated photosystems II and I. Light in a broad wavelength range can be harvested if the two PS's are chosen that way that they absorb light in different parts of the solar spectrum. Thereby, a theoretical maximum efficiency of 40% can be achieved.[13] It was calculated that the photo-generated current densities of the DSPEC's have to meet a value of 10 mA cm^{-2} and a solar-to-fuel efficiency of $\eta_{STH} \geq 10\%$ for an economic application in the year 2050. Furthermore, the devices should be stable for 20 to 30 years. To reach that goal, various proof-of-concept devices have been developed.[13]

For the photocathodes, which drive the hydrogen production, traditionally NiO is applied as SC material. It is important that the valance band of the SC must be more negative than the HOMO of the PS to allow for electron transfer from the cathode to the PS. The PS (and the catalyst) is usually attached to the SC surface via anchoring groups. In an example system of Wu and co-workers[101], the molecular components, a Ruthenium based PS and a cobaloxime catalyst, were covalently linked to each other to form a dyad (Figure I.9). This dyad was applied via a carboxylic acid anchoring group to an alumina coated nonoporous NiO. With this electrode design, a photocurrent density of 9 µA cm^{-2} could be measured over one hour with a faradaic efficiency of 68% at a bias of 0.1 V vs NHE and 300 W xenon irradiation. The system's low performance was mostly attributed to the low stability of the dyad and the deficiency of the NiO SC. Please note that, in solution, such dyads show considerable worse performance compared to the multi component systems.[50] Under catalytic conditions, the cobaloxime tends to dissociate from the pyridine ligand of the PS. Furthermore, the coordination of the glyoxime ligands to the cobalt were found to be unstable under the same conditions. The disadvantage of NiO

is its absorption of light by itself and its low hole/electron mobility. Hence, there is a need of using alternative and more transparent SC's with a higher hole mobility.

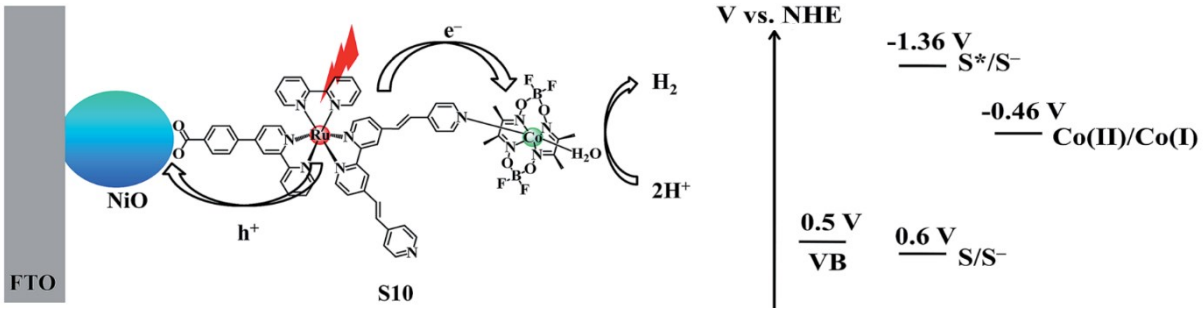

Figure I.9. DSPEC photocathode as described by Wu and co-workers. Reprinted with permission from ref. [101]. Copyright the American Chemical Society 2013.

Instead of applying dyads, also co-absorption of the PS and the catalyst on the SC have been proven to be effective. Best performance with such a design was achieved with an organic push-double-pull dye BH_4-sensitized NiO photocathode and a $[Mo_3S_4]^{4+}$ cluster as catalyst with a photocurrent of 183 µA cm^{-2}.[102]

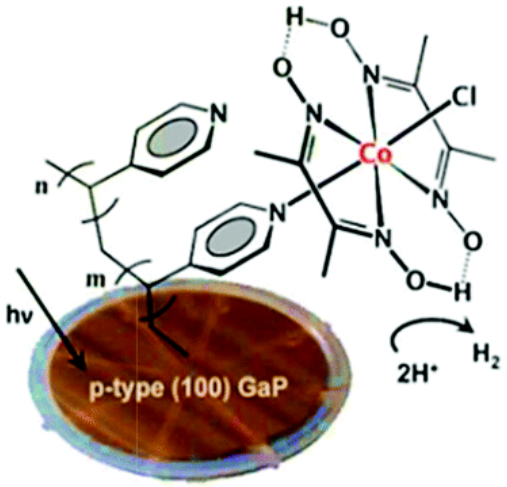

Figure I.10. DSPEC photocathode as described by Moore and co-workers. The catalyst is directly immobilized at the SC material by polymers that coat the electrode at the same time. Reprinted with permission from ref. [103]. Copyright the American Chemical Society 2013.

One can also omit the usage of a PS and directly use heterogeneous and visible-light absorbing SC electrodes with a molecular catalyst attached to it for acceleration of the reaction rate. Such a device constitutes a hybrid system. A successful example of such a system was presented by Moore and co-workers (Figure I.10). Thy used p-type GaP as visible light absorbing SC. The SC was coated with a polymer that served as protective layer and at the same time immobilized a cobaloxime catalyst via pyridyl or imidazolyl groups coordinating the Co-complex center. A photocurrent density of 2.4 mA cm^{-2} was measured at 0.31 V bias in 1 M phosphate buffer solution under 100 mW cm^{-2} illumination.[103]

Notably, with such polymers, the electrode can theoretically be loaded with the catalyst to levels higher than that of a monomolecular layer.[22]

The best hybrid photocathode constitutes a $GaInP_2$-TiO_2-cobaltoxime-TiO_2 device. In 0.1 NaOH solution, at 100 mW cm^{-2} illumination, a photocurrent density of 11 mA cm^{-2} at 0 V vs RHE and an onset potential at 0.75 V vs RHE was measured. For the catalyst, a TON of 1.4 * 10^5 was achieved after 16 h. The performance is comparable with a Pt-modified $GaInP_2$ electrode.[104]

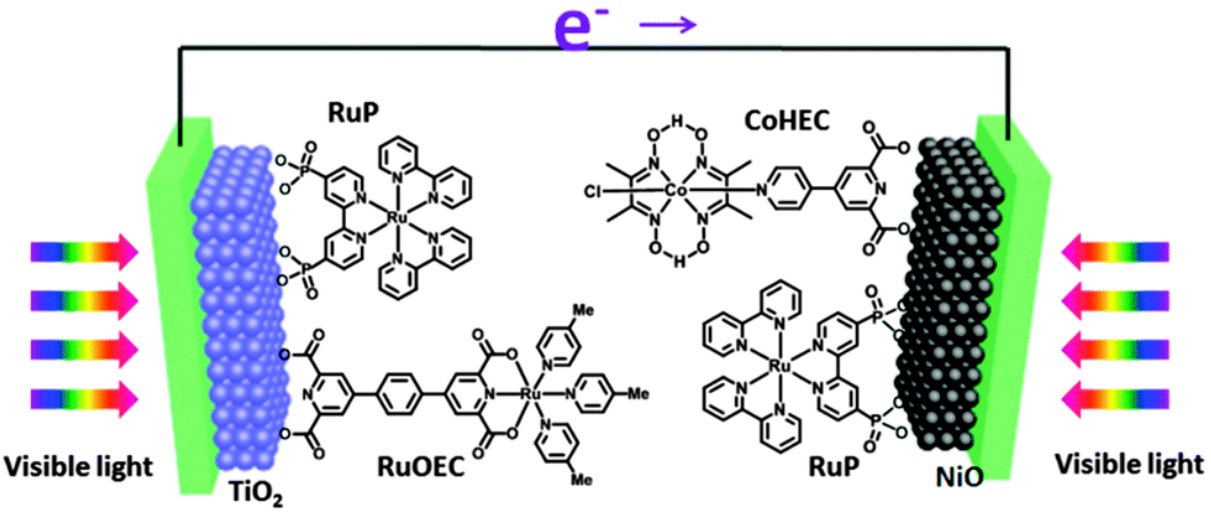

Figure I.11. Full Pt-free DSPEC tandem devise with a dye sensitized photoanode and -cathode as described by Sun and co-workers. Reprinted with permission from ref. [105]. Copyright the Royal Society of Chemistry 2014.

A proof of concept for a tandem device was presented by Sun and co-workers[105]: The photocathode comprised a Ruthenium based PS and a cobaloxime proton reduction catalyst co-absorbed onto a NiO SC (Figure I.11). In case of the photoanode, a PS and a water oxidation catalyst, both based on Ruthenium were co-absorbed on a TiO_2 SC. Notably, no external bias was necessary to drive water splitting. However, an average photocurrent density of only ~40 µA cm^{-2} was measured under 300 mW cm^{-2} irradiation, thus being far away from economic applications. As in the example above, the NiO photocathode was tracked down to be the bottleneck of the device.

In general, Sun et al. concluded that the regeneration of the PS by the catalyst tends to be too slow to compete with the back-electron transfer between PS and SC. Better immobilized PS and catalysts with a higher TOF and stability should be explored as well as more transparent SCs with a higher hole mobility. Also, the use of QDs as PS and the application of redox mediators might improve the system. A deep understanding on the molecular level of the underlying interfacial charge transfer dynamics at the interface of SC, PS and catalyst is recommended.[13]

II. OBJECTIVES OF THIS WORK

Considering the small price and low effort involved in the synthesis of simple iron carbonyls, the catalysts introduced by Beller and co-workers constitute a step in the development towards an ideal proton reduction catalyst. However, their stability and activity (expressed in terms of TON and TOF) are still far away from industrial application. A basis for future improvements is a deeper understanding of the catalytic reaction's mechanism and deactivation paths. This helps to recognize the strong and weak points of the system and gather new ideas for adjustments. To identify transformation processes of the catalyst precursor into catalytic relevant key intermediates or inactive species, the catalyst has to be monitored with spectroscopic methods *in-situ* under working conditions. In order to evaluate the activity of the observed catalyst species and to determine the structure-activity relationship, the production of H_2 has to be monitored simultaneously to the acquisition of spectroscopic data.

In this work, three systems for the photocatalytic water reduction were investigated: The phosphine free **Ir*PS***/[$Fe_3(CO)_{12}$] system (**A**), the phosphine modified **Ir*PS***/[$Fe_3(CO)_{12}$]/$P(R)_3$ system (**B**) and the noble metal free **Cu*PS***/[$Fe_3(CO)_{12}$] system (**C**). The investigation focused mainly on the iron carbonyl proton reduction catalyst with the principle objective to identify all major iron species and to investigate their role and performance in the catalytic reaction. Another general goal was to examine the transformation and deactivation processes of these species and to detect the influence of the reaction conditions thereon.

Additional interrogations were addressed with regard to the specific systems: Since system **A** had been found to be similarly active in case iron carbonyls different than [$Fe_3(CO)_{12}$] like [$Fe(CO)_5$] or [$Fe_2(CO)_9$] were applied, it was the task to examine whether all these precursors are transformed into the same key species. Further, the rate determining catalytic step or sub cycle of this system had to be determined.

With regards to the phosphine modified system **B**, the reason for the enhancing effect of added electron withdrawing phosphine ligands $P(R)_3$ had not been known prior to this work as pointed out in a review article by Du and Eisenberg[49]. Therefore, it was a task to elucidate this effect and to prove if it can be ascribed to the formation of iron phosphides. Further, it had to be investigated why certain phosphine ligands enhance the performance, while others have no or a negative impact on the system. It was also part of the study to detect the reason for the decreasing performance in case [$Fe_3(CO)_{12}$] was applied together with excessive amounts of phosphine.

System **C** was investigated to find out whether exchanging the photosensitizer from **Ir*PS*** to **Cu*PS*** affects the catalyst's transformation processes compared to those of system **A**. Since the heteroleptic copper photosensitizer $[Cu(P\hat{}P)(N\hat{}N)]^+$ is expected to be in equilibrium with its homoleptic form $[Cu(N\hat{}N)_2]^+$,[106] the mechanistic studies should also help to identify which of the two structures is the active copper photosensitizer.

To accomplish all of these objectives, the reaction was primarily analyzed by in-situ continuous-flow FTIR spectroscopy (Fourier-Transform InfraRed spectroscopy) coupled with gas volumetry. The combination of the two techniques is referred to as operando IR spectroscopy. To support experimental findings, further methods were applied like *in-situ* XAS (X-Ray Absorption Spectroscopy), ESI-MS (ElectroSpray Ionization - Mass Spectrometry), NMR spectroscopy (Nuclear Magnetic Resonance spectroscopy) and CV (cyclic voltammetry).
The use of all mentioned analytical methods is discussed in the following chapter. Subsequently, the published experimental results are summarized. In the conclusive chapter, it is discussed how the findings can help to improve the iron carbonyl based photocatalytic water reduction systems and how they can be a starting point for future research.

III. ANALYTICAL AND COMPUTATIONAL METHODS

3.1 Operando IR Spectroscopy

IR spectroscopy is a very suitable and sensitive method for the elucidation and monitoring of metal carbonyl complexes. These complexes show contributions of carbonyl stretching vibrations between 2125 and 1700 cm^{-1}. Depending on the IR active vibrational modes, each complex can contribute either one or multiple IR bands. The latter form a compound characteristic pattern which is dependent on the geometry of the complex and the distribution of electron density. The band position or wavenumber ($\tilde{\nu}$) is determined by the electron density at the metal center, since electron back transfer into the antibonding C-O orbital weakens the carbonyl bond and thus the force constant k (see Equation 7, μ = reduced mass). Hence, the contributions are shifted to lower wavenumbers for anions or compounds bearing electron-rich ligands. Please note that in anionic, multinuclear complexes, the charge is distributed across the nuclei. Hence, the bathochromic shift caused by the negative charge is attenuated with increasing number of metal atoms. Furthermore, terminal carbonyl vibration bands can be found at higher wavenumbers (2125 - 1850 cm^{-1}) whereas contributions of bridging carbonyls are found in the lower part of the spectrum (1850 - 1700 cm^{-1}). The structure of unknown complexes that are present at catalytic conditions can be elucidated by comparing their experimental spectra with those from quantum mechanical calculations or with spectra published in literature.[107,108]

$$\tilde{\nu} \sim \sqrt{\frac{k}{\mu}} \qquad (7)$$

The extinction (E) or magnitude of the IR contributions at a definite wavelength (λ) is proportional to the concentration (c) of the complexes and follows the Beer–Lambert law (Equation 8). However, the proportionality factor depends on the extinction coefficient (ε), which is compound and wavelength specific and the optical pathlength (d). Hence, an intensity-concentration calibration is necessary for each complex. The pathlength of the IR cell has to be chosen so that it is wide enough for a high sensitivity. At the same time, it has to be sufficiently narrow to prevent occultation of carbonyl bands by intensive contributions of the solvent, which can cause the IR-light intensity to drop below the detection limit of the detector (= total absorption).[107,108]

$$E_\lambda = \varepsilon_\lambda \, d \, c \qquad (8)$$

Notably, the contributions originating from a mixture of compounds and the solvent are additive. This allows for the subtraction of the of the pure solvent spectrum from the experimental

one (background subtraction). Furthermore, a quantitative measurement of the compounds is possible if the spectra of all pure compounds are known and can be fit to the mixed spectrum via the method of least squares. Especially during the investigations presented in publication 6.2, this analysis method was used. If the individual pure component spectra are unknown, they can be estimated together with the corresponding absorption-time curves via the model free Pure Component Decomposition (PCD) algorithm, which was developed by Neymeyr et al[109].

For this work, a new setup was built for experiments that allow for analysis of the irradiated reaction solution by continuous flow FTIR spectroscopy and synchronous monitoring of gas evolution. It consists of a customized reaction vessel that is connected to a mercury vapour lamp, a FTIR-spectrometer, an automatic gas burette and a custom holder for a small pot that contains the catalyst. The apparatus constitutes an updated version of the setup that was used in the work of Barsch and Gärtner in 2011[78,110,111] (see Figure III.1).

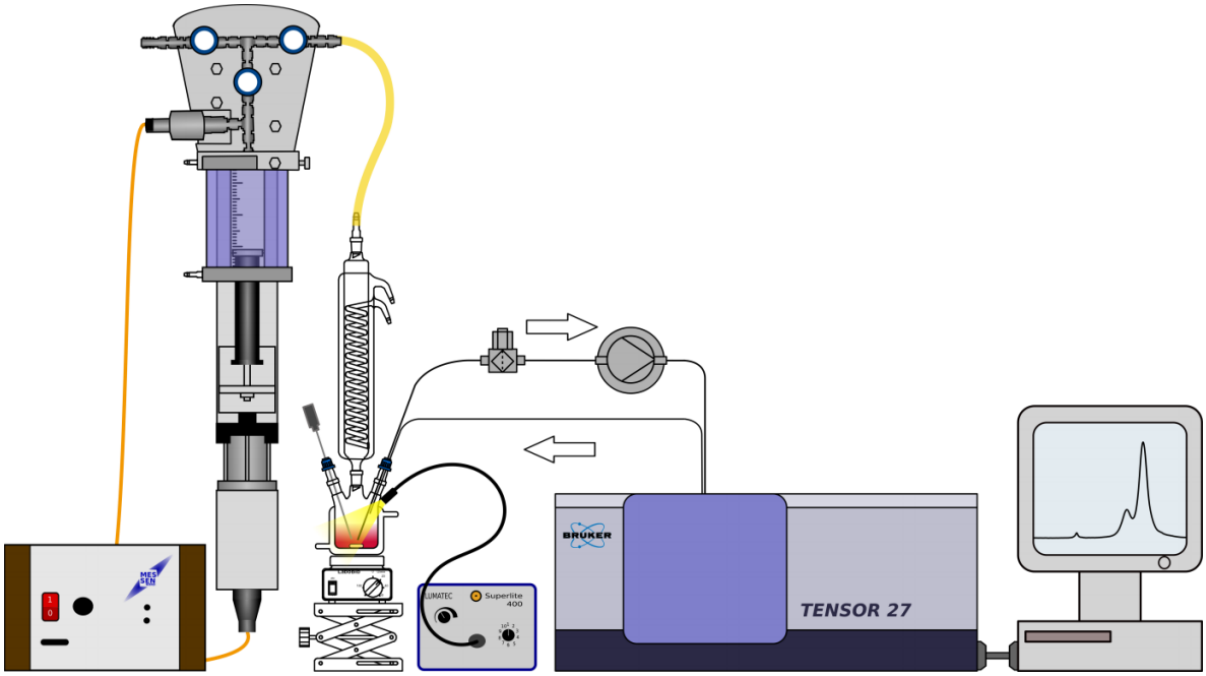

Figure III.1. Experimental setup for the operando IR spectroscopy. The setup is consisting of the automatic gas burett (left), the reaction vessel (center) as well as the FTIR spectrometer (right) connected via the micro annular gear pump.

The mercury vapour lamp (brand: LUMATEC) is attached to the double-walled reaction vessel at a fixed position via a fibre optic cable. The reaction vessel is kept at 25 °C. The lamp emits visible light between 380 and 700 nm with a power of 1500 W and is calibrated before each experiment.

The reaction solution is stirred by a magnetic stirrer at constant and reproducible speed and is continuously circulated by a micro annular gear pump (brand: HNP) through the cell in the IR-spectrometer. The cell is equipped with CaF_2 windows, has an optical pathlength of 100 µm and is kept at a constant temperature of 25 °C. This small path length allows for volumetric share of water in the solvent mixture of 20% (1:5) without total absorption in the spectral range of metal carbonyl contributions. The FTIR-measurements are carried out on a Bruker Tensor 27 spectrometer with a mercury-cadmium-telluride (MCT) detector that needs to be loaded with liquid nitrogen twice a day.

Tracking of gas evolution is realized by an automatic gas burette (brand: MESSEN NORD) at a constant pressure of 1020 mbar. Its temperature is kept constant at 25 °C. A condenser is installed in between the reaction vessel and the gas burette and runs at 5 °C to retain volatile solvent.

A typical experiment is carried out as follows: The whole apparatus is evacuated and purged with argon five times to provide oxygen-free conditions. 20 mL solvent are added to the reaction vessel against a flow of argon. Likewise, the **Ir*PS*** is added to the solution while a small pot containing the catalyst is placed in the customized holder that is attached to a Teflon joint. The apparatus is closed, and the solution is circulated by the pump through the IR-cell. After temperature adjustment of the solution, an IR-spectrum is recorded and used as background. The solid catalyst is added to the solution by a twist of the joint. After the thermal equilibrium between gas- and condensed phase (10 min) is reached, the reaction is started by turning on the light source. An IR-spectrum with 64 scans is taken every two minutes.

3.2 NMR Spectroscopy

In parallel to the IR spectroscopic investigations, Nuclear Magnetic Resonance spectroscopy (NMR) was applied ex-situ. With the focus on phosphorus containing complexes, proton decoupled $^{31}P\{H\}$-NMR spectra were acquired. ^{31}P is considered as NMR-sensitive nucleus since it has an isotopic abundance of 100% and a relatively large gyromagnetic ratio.[112] Metal complexes with only one monodentate phosphine ligand show a single singlet ^{31}P NMR signal. The chemical shift δ of that signal is the resonant frequency of the phosphorous nucleus in a magnetic field relative to that of phosphoric acid as standard. It correlates with the dia- and paramagnetic shielding of the phosphorous nuclei and is influenced by bond angles, electronegativity effects and π-electron overlap. Thus, it is very sensitive to structural changes.[112–114] Complexes with two phosphorous nuclei in geminal position show a $^2J(PMP)$ coupling and splitting of each of the signals into doublets. Even though prediction of the chemical shift and coupling constant is not trivial [112–114], $^{31}P\{H\}$-NMR spectroscopy is very useful to distinguish and to estimate the number of distinct phosphorus containing complexes in the reaction solution as well as to support or validate structural assignments.

3.3 XAS Spectroscopy

In X-ray absorption spectroscopy (XAS), the absorption of synchrotron X-ray radiation by atoms of a specific element is measured. At a critical wavelength, core electrons from the K-shell of that element are excited into the continuum resulting in the generation of photoelectrons and an abrupt increase of the absorption. The latter is referred to as absorption edge. The position of the edge is element specific and is shifted to higher energies with increasing oxidation number. Hence, the analysis of the pre-edge and the X-ray absorption near edge structure (XANES) reveals information about the oxidation state and additionally about the coordination geometry around the central atom.[115]

The ejected photoelectrons can be described as waves. The surrounding atoms scatter those waves leading to interference between the backscattered- and forward-propagating waves. The resulting interference pattern is reflected in the extended X-ray absorption fine structure (EXAFS) at energies higher than 30 eV after the absorption edge.[116] Analysis of the EXAFS provides information about the type and the number of neighbouring atoms and their distances from the central atom.[115] However, the analysis of EXAFS spectra is complicated by the fact that the structural parameters of all species in the reaction solution are averaged in the spectral signal.[117,118]

The X-ray absorption measurements were carried out at the synchrotron ANKA. The synchrotron beam current was between 80–140 mA at 2.5 GeV storage ring energy. A Si(111) double crystal monochromator was used for measurements at the Fe K-edge (7.112 keV). The second monochromator crystal was tilted for optimal harmonic rejection. To perform operando studies, the spectra were recorded in fluorescence mode using a hyper-pure germanium detector. Energy calibration was performed with an iron metal foil prior to the measurements. Samples in solution were measured in a specially designed fluorescence cell, which allowed securation and filling under inert gas flow.[119] An argon atmosphere was applied to the cell in course of the measurements in order to allow evolving gas to escape the cell. Details of the analysis are described elsewhere.[120]

EXAFS data analysis was performed according to the curved wave formalism of the EXCURV98 program with XALPHA phase and amplitude functions.[121] The amplitude reduction factor (AFAC) was allowed to float in the fit. The spectra were Fourier filtered (in the range between 1.0 – 3.2 Å), back-transformed and analysed in k-space

3.4 Cyclic Voltammetry

Cyclic Voltammetry (CV) was used to determine the electrochemical potentials and the reversibility of redox events of the catalysts and the PS. Both, the potential and the reversibility, are derived from the shape of the cyclic voltammogram. The redox potential $E_{1/2}$ is calculated from

equation 9 with $E_{p(a)}$ and $E_{p(c)}$ being the potential at the peak of the anodic and the cathodic current. Irreversible redox events show a high current during the forward reaction while a smaller or no current is observed at the expected potential of the back reaction.[122]

$$E_{1/2} = \frac{E_{p(a)} + E_{p(c)}}{2} \quad (9)$$

Cyclic voltammetry measurements were carried out at oxygen-free conditions in dry THF with $[NBu_4][PF_6]$ or $[NBu_4][ClO_4]$ added as electrolyte to decrease the electrical resistance of the solvent and the ohmic drop. A 2 mm^2 glassy carbon electrode was used as working electrode because this material does not catalyze the reduction of protons by itself and thus shows a very high over potential for this reaction.[123] Since redox potentials can only be measured against a reference, a nonaqueous $Ag/AgNO_3$ reference electrode was applied with a fixed potential that is stable over the time of the experiment (silver wire in 0.01 M $AgNO_3$/ 0.1 M $[NBu_4][ClO_4]$/ acetonitrile, separated from the experimental solution via a Vycor frit). However, the potential of such nonaqueous electrodes can vary from one experiment to another.[124] That is why ferrocene was added and measured as internal reference at the end of each experiment. This allows for reporting redox potentials against that of the ferrocene/ferrocenium couple ($Fc^{+/0}$). As counter electrode, a platinum wire was used.

3.5 ESI-MS Spectrometry

In ESI-MS spectrometry, molecules are separated and identified by their mass over charge ratio (m/z). For the ex-situ ESI-MS measurements, small volumes of the reaction solution were sampled periodically over the time of hydrogen production via a rubber septum and a syringe from the reaction vessel. In parallel, the solution was investigated by operando IR spectroscopy. Before and after each injection of a sample into the ESI-MS spectrometer, the latter was calibrated for a robust quantification of sensitive reaction intermediates like the copper photosensitizers. The instrument was running in positive ion-mode. By carrying out ex-situ ESI-MS and operando IR spectroscopy, the concentration of both, the PS and the catalyst species could by monitored over time.

3.6 Quantum-Chemical Computation

To confirm spectral assignments, quantum chemical calculations have been performed with Gaussian 09[125] with B3LYP/6-31+G** levels of theory[126–129]. The calculated frequencies have been corrected with a scaling factor of 0.97 to compensate for the harmonic approximation. This factor gives best agreement of experimental and calculated frequencies for all

$[Fe_2(CO)_6(\mu\text{-}CO)(\mu\text{-}P(R)_2)]^-$ species. The factor is also very similar to those specified in literature that were obtained for such iron cluster anions (0.9672)[130] and an even larger set of related molecules[131].

IV. SUMMARY OF THE WORK

In the following, the published work is summarized. The author dispenses with citing the literature that substantiate the findings. To look up underlying literature, the reader may refer to the publications itself that are exposed in chapter VI.

4.1 Investigation of System A (Publications 6.1. and 6.5.)

The **Ir*PS***/$Fe_3(CO)_{12}$ System **A** presented by F. Gärtner et al. supervised by M. Beller had already been investigated in preliminary mechanistic studies prior to this work. As stated in section 1.5.3 and chapter II, certain obscurities had been remained and were addressed in this work to give an even deeper understanding of the system and its catalytic cycle:

In stopped-flow IR experiments, carried out by Enrico Barsch and Bastian Hoffmann, supported by the author of this work, The third component that emerges after adding $[Fe_3(CO)_{12}]$ to THF/TEA/H_2O in the absence of light was identified as $[Fe(CO)_5]$. Thus, the catalyst starting material before initiation of the catalytic reaction was found to consist of a mixture of $[Fe_3(CO)_{11}]^{\bullet-}$, $[Fe_2(CO)_8]^{\bullet-}$ and $[Fe(CO)_5]$.

In the continuing work of the author, the assignment of the “monomeric intermediate” that evolves besides $[HFe_3(CO)_{11}]^-$ after addition of **Ir*PS*** and initiation of light irradiation was revised and corrected. It was identified to be the $[HFe(CO)_4]^-$ complex. This was found by comparison of the experimental IR spectrum with literature data, DFT calculated frequencies and the spectrum of synthesized $[NEt_4][HFe(CO)_4]$ in THF/TEA/H_2O (Figure IV.5, middle, blue).

Preliminary mechanistic studies had been carried out with a solvent mixture of THF/TEA/H_2O with a volumetric ratio of 16/4/1. However, the performance experiments by F. Gärtner et al. had been carried out with a solvent mixture with a ratio of 4/1/1. Therefore, the dependence of the water content on the transformation process of precursor $Fe_3(CO)_{12}$ was investigated. Experiments show that $[HFe_3(CO)_{11}]^-$ and $[HFe(CO)_4]^-$ are in equilibrium, which is shifted towards the latter with increasing water concentration. Thus, In a THF/TEA/H_2O ratio of 4/1/1, $[HFe_3(CO)_{11}]^-$ is quasi fully converted into $[HFe(CO)_4]^-$ within one hour. This solvent ratio[6] had been used for all further spectroscopic investigation of system **A** and **B**.

Further on, the transformation processes of the precursors $Fe(CO)_5$, $Fe_2(CO)_9$ and $[NEt_4][Fe(NO)(CO)_3]$ have been studied under catalytic conditions. All precursors were found to be transformed into $[HFe(CO)_4]^-$. This finding explains the similar catalytic performances of the iron carbonyl precursors and indicates $[HFe(CO)_4]^-$ to be a catalytically relevant species.

Notably, hydrogen production only occurs as long as $[HFe(CO)_4]^-$ is present in solution and terminates as soon as the complex is consumed (Figure IV.1). This is another evidence for the

[6] Carrying out IR spectroscopic experiments at this high water content (1:5) without total absorption in the spectral region of carbonyl vibrations was only possible because of the narrow pathlength of the IR cell (100 µm) that was used in this work.

important role of $[HFe(CO)_4]^-$. However, two findings point out that the complex is not the catalytically active species: a) its electrochemical reduction potential ($E_{1/2}$ = −2.52 V vs. $Fc^{+/0}$)[24,132] is too low for the species to be reduced by **Ir*PS***$^-$ ($E_{1/2}$ = −1.80 V vs. $Fc^{+/0}$)[24,31] b) TDDFT calculations (Time-Dependent Density Functional Theory calculations) carried out by O. Bokareva show that electron transfer from the reduced **Ir*PS*** towards the catalyst is only possible for the complexes $[HFe_2(CO)_8]^-$ (5.3% probability) and $[HFe_3(CO)_{11}]^-$ (18% probability) rather than $[HFe(CO)_4]^-$ (0% probability). Indeed, $[HFe_3(CO)_{11}]^-$ has a reduction potential ($E_{1/2}$ = −1.71 V vs. $Fc^{+/0}$)[24,132] high enough for the complex to be reduced by **Ir*PS***$^-$. Further, DFT calculations of O. Bokareva predict negative values for the changes in the Gibbs free energy for all steps in the catalytic water reduction subcycle starting with $[HFe_3(CO)_{11}]^-$. This indicates $[HFe_3(CO)_{11}]^-$ to be capable of running a full catalytic cycle and to be the catalytically active species.

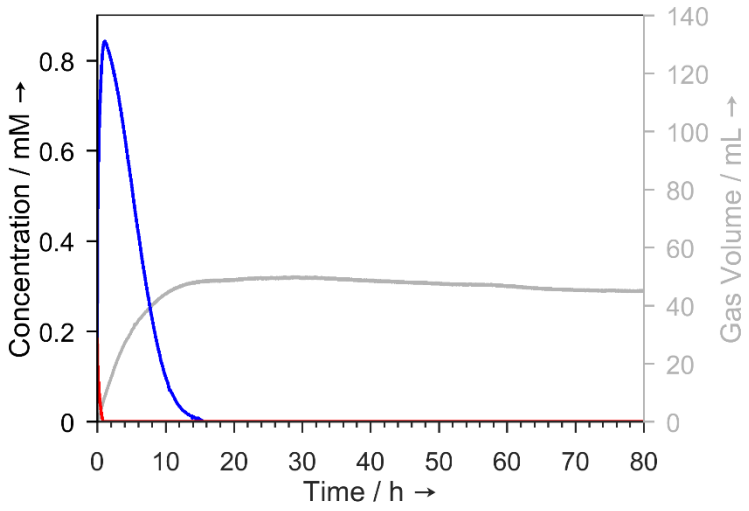

Figure IV.1. Gas evolution curve and concentration curves for iron carbonyl species observed in system **A**. The data was obtained in an operando FTIR experiment monitoring an irradiated solution of THF/TEA/H_2O (4/1/1) with added **Ir*PS*** and catalyst [$Fe_3(CO)_{12}$]. The gas evolution curve is shown in grey. The concentration curves for the complexes $[HFe_3(CO)_{11}]^-$ (red curve) and $[HFe(CO)_4]^-$ (blue curve) are also illustrated. For reaction conditions, please refer to publication 6.2., Figure 2a.

As confirmed by DFT calculations $[HFe_3(CO)_{11}]^-$ can decompose in a possible side reaction into $[HFe(CO)_4]^-$ and $[Fe_2(CO)_8]^{\bullet-}$ after having been reduced. The $[Fe_2(CO)_8]^{\bullet-}$ species can be converted into $[HFe(CO)_4]^-$ upon further reduction. This is in accordance to the above mentioned conversion of $[HFe_3(CO)_{11}]^-$ into $[HFe(CO)_4]^-$ under catalytic conditions in a reductive environment. However, this process was found to be reversible: Irradiating a solution of $[NEt_4][HFe(CO)_4]$ in THF/TEA/H_2O (ratio 4/1/1) in the absence of **Ir*PS*** affords conversion of $[HFe(CO)_4]^-$ back into $[HFe_3(CO)_{11}]^-$. This back reaction is initiated by light and can be considered to also occur under catalytic conditions, permanently regenerating very small amounts of $[HFe_3(CO)_{11}]^-$, which are undetectable by IR. Thus, $[HFe(CO)_4]^-$ can be assigned to be the dormant- or resting state of the catalytically active complex $[HFe_3(CO)_{11}]^-$.

In kinetic investigations, the rate limiting step or rate limiting cycle of the system was determined. $[NEt_4][HFe(CO)_4]$ was directly applied as catalyst and added to the reaction solution to omit pre-formation reactions. The initial hydrogen evolution rate was found to be independent from the applied catalyst amount. It was concluded that the catalyst is not involved in the major rate limiting process. Apart from that, the hydrogen yield grows and the stability of the system improves with increasing initial catalyst concentration.

In contrast, the initial hydrogen evolution rate does depend on the applied amount of **Ir*PS***. Linear dependence and pseudo-first-order kinetics were found in a range between 0.01 and 0.08 mM for the initial **Ir*PS*** concentration. This is in accordance with the results of Neubauer et al. who investigated the **Ir*PS*** subcycle by photoluminescence spectroscopy. They found that the **Ir*PS*** is dominantly quenched reductively. Furthermore, they found that the reductive quenching of the excited **Ir*PS*** by TEA is rate determining. By the findings stated above, it was confirmed that the mentioned process is the rate limiting step of the whole system.

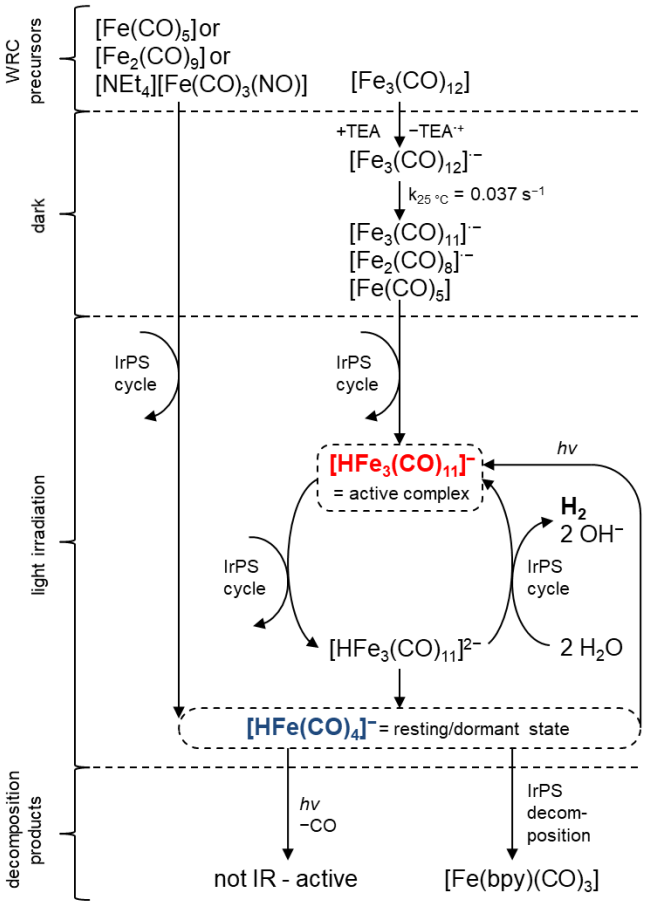

Figure IV.2. Catalyst transformation and deactivation processes in system A in the absence of light and during photocatalytic water reduction conditions.

The deactivation process of $[HFe(CO)_4]^-$ was also investigated: At low initial **Ir*PS*** concentrations (Ir/Fe ratio < 0.4), decomposition of $[HFe(CO)_4]^-$ was attributed to light induced CO-dissociation and an additional unspecified deactivation mechanism within the catalytic cycle. Both

loss channels lead to IR inactive products. Notably, at these low Ir/Fe ratios, the hydrogen yield rises with increasing initial **Ir*PS*** concentrations (Figure IV.3., grey gas evolution curves; highest $TON_{cat,18\ h}$ = 186 found at 0.16 mM **Ir*PS*** and 0.4 mM $[NEt_4][HFe(CO)_4]$).

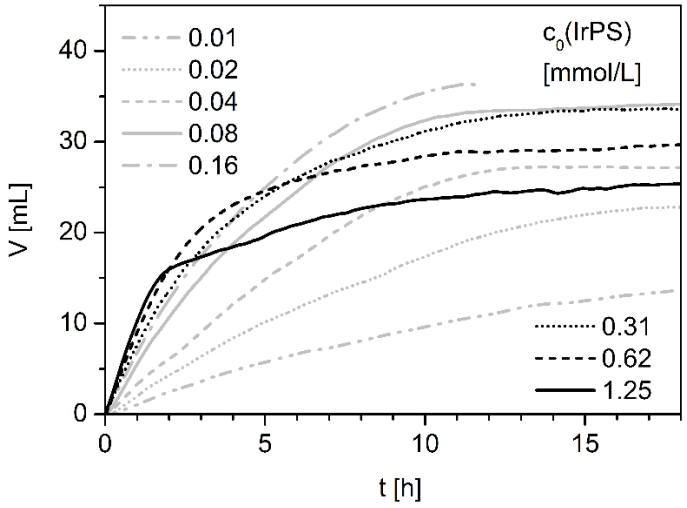

Figure IV.3. Gas evolution curves of system **A** monitored upon application of preformed catalyst $[NEt_4][HFe(CO)_4]$ and varying initial concentrations of **Ir*PS***. For reaction conditions, please refer to publication 6.1., Figure 6a.

However, the hydrogen yield again declines with increasing amounts of **Ir*PS*** at high initial **Ir*PS*** concentrations (Ir/Fe ratio > 0.4; Figure IV.3., black gas evolution curves). This is due to an additional deactivation mechanism taking effect: The bipyridine ligand is transferred from the **Ir*PS*** onto the catalyst. This results in poisoning of the catalyst and formation of $[Fe(bpy)(CO)_3]$. As a consequence, at high **Ir*PS*** concentrations, the catalyst is rapidly consumed at an early stage of the reaction leading to a sudden decrease of the hydrogen evolution.

The spectroscopic investigations have contributed to a more detailed understanding of the catalytic mechanism of system **A**. The mechanism is summarized in Figure IV.2.

4.2 Investigation of System B (Publications 6.2. and 6.5.)

Investigation on the phosphine modified **Ir*PS***/$Fe_3(CO)_{12}$/$P(R)_3$ system **B** focused on the elucidation of the role of the phosphine ligand. The effect of various types of phosphine ligand with different electron acceptor/donor properties was studied, starting with electron poor $P(OPh)_3$ {P(**a**)$_3$} towards the electron rich alkyl phosphine $P(Bu)_3$ {P(**i**)$_3$} (Figure IV.4.). In the upcoming text, the effect of the phosphines on the reaction is first illustrated with ligand $P(C_6H_4\text{-}4\text{-}CF_3)_3$ {P(**d**)$_3$} as an example, which had been found to enhance the performance. Later on, the impact of the other phosphines and deactivation mechanisms are discussed.

As in the phosphine free system **A**, $Fe_3(CO)_{12}$ is converted into $[Fe_3(CO)_{11}]^{\bullet-}$, $[Fe_2(CO)_8]^{\bullet-}$, and $[Fe(CO)_5]$ after being dissolved in THF/TEA/H_2O in the dark. Upon addition of P(**d**)$_3$, furthermore $[Fe(CO)_4P(\mathbf{d})_3]$ emerges by quantitative coordination of the phosphine to the iron. This was found by ^{31}P-NMR spectroscopy with a signal at δ 76.1 ppm consistent with literature

values.[7] The assignment was further supported by XAS spectroscopy, detecting an emerging Fe-P coordination shell and a reduced Fe-Fe coordination number.

As soon as hydrogen evolution starts after addition of IrPS and irradiation by light, $[Fe_3(CO)_{11}]^{\bullet-}$, $[Fe_2(CO)_8]^{\bullet-}$, and $[Fe(CO)_5]$ are transformed into $[HFe_3(CO)_{11}]^-$ and $[HFe(CO)_4]^-$ (Figure IV.5. left, b, 2 min, red and blue contributions), whereas $[Fe(CO)_4P(\mathbf{d})_3]$ remains in the solution during the starting phase of the catalytic reaction (Figure IV.5. left, b, 2min, green contributions). The single component IR spectrum of $[Fe(CO)_4P(\mathbf{d})_3]$ (Figure IV.5, middle, green spectrum) could be obtained by subtraction of the known component's spectra from the sum spectrum, which was recorded two minutes after initiation of light irradiation. The wavenumbers of the resulting spectrum are in agreement with literature data (see paper 6.2, supporting information, Figure SI1). Since $[HFe(CO)_4]^-$ is also the major species in the starting phase of system **B**, the composition of the reaction solution is broadly similar to that of system **A.** Accordingly, same initial gas evolution rates are observed.

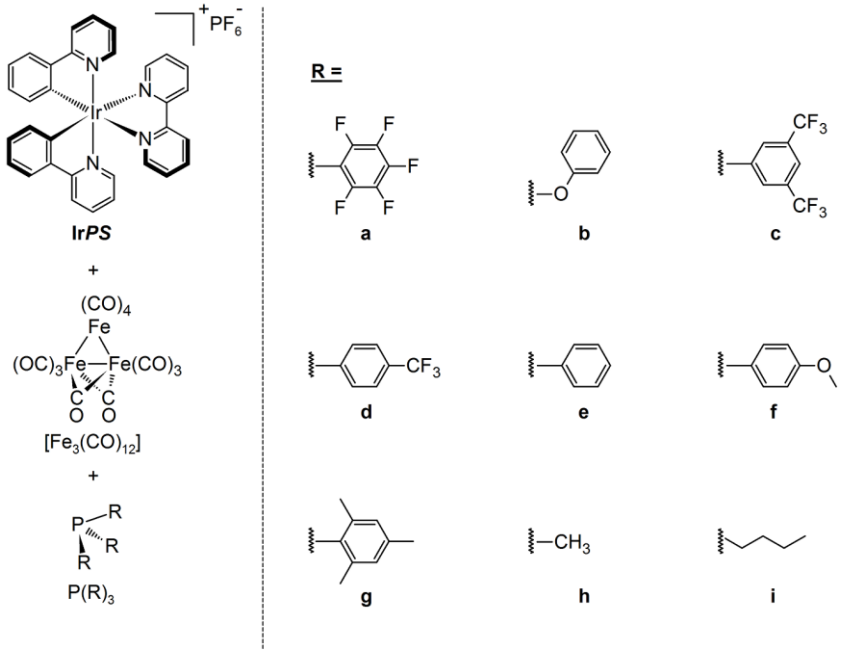

Figure IV.4. Components of System **B**.

During the first 10 hours of the reaction, all iron material was found to be converted into $[Fe_2(CO)_6(\mu\text{-}CO)(\mu\text{-}P(\mathbf{d})_2)]^-$. This complex is a diferrate with one bridging and six terminal carbonyls as well as one bridging phosphido ligand (Figure IV.5, right, structure of $2COP(R)_2^-$). The assignment is based on IR, NMR and XAS spectroscopy. The in-situ IR spectrum that was recorded after 15 hours of light irradiation shows the spectra of the known complex $[Fe_2(CO)_6(\mu\text{-}CO)(\mu\text{-}PPh_2)]^-$, shifted by an average of 6 cm^{-1} to higher wavenumbers (see Publication 6.2, Table 1). The spectral shift is caused by the electron withdrawing CF_3 substituent

[7] Hence, the assignment by Felix Gärtner et al., who assumed the formation of $[Fe_3(CO)_{11}(PPh_3)]$ under similar reaction conditions, was rejected and corrected.

at the aryl group of the phosphide ligand. The NMR spectrum of a sample of the solution taken at the same time shows a singlet at δ 123 ppm for $[Fe_2(CO)_6(\mu\text{-}CO)(\mu\text{-}P(\mathbf{d})_2)]^-$ again close to the signal specified in literature for $[Fe_2(CO)_6(\mu\text{-}CO)(\mu\text{-}PPh_2)]^-$ (δ 127 ppm in CD_3CN). Fe-C and Fe-P coordination numbers measured by XAS of respectively 3.5 ± 0.4 and 0.8 ± 0.2 are also consistent with the formation of this species. Synthesis and spectral characterization of $[NEt_4][Fe_2(CO)_6(\mu\text{-}CO)(\mu\text{-}P(\mathbf{d})_2)]$ reaffirmed the assignment, since this preformed complex shows the same contributions as in the in-situ IR and ex situ NMR spectra.

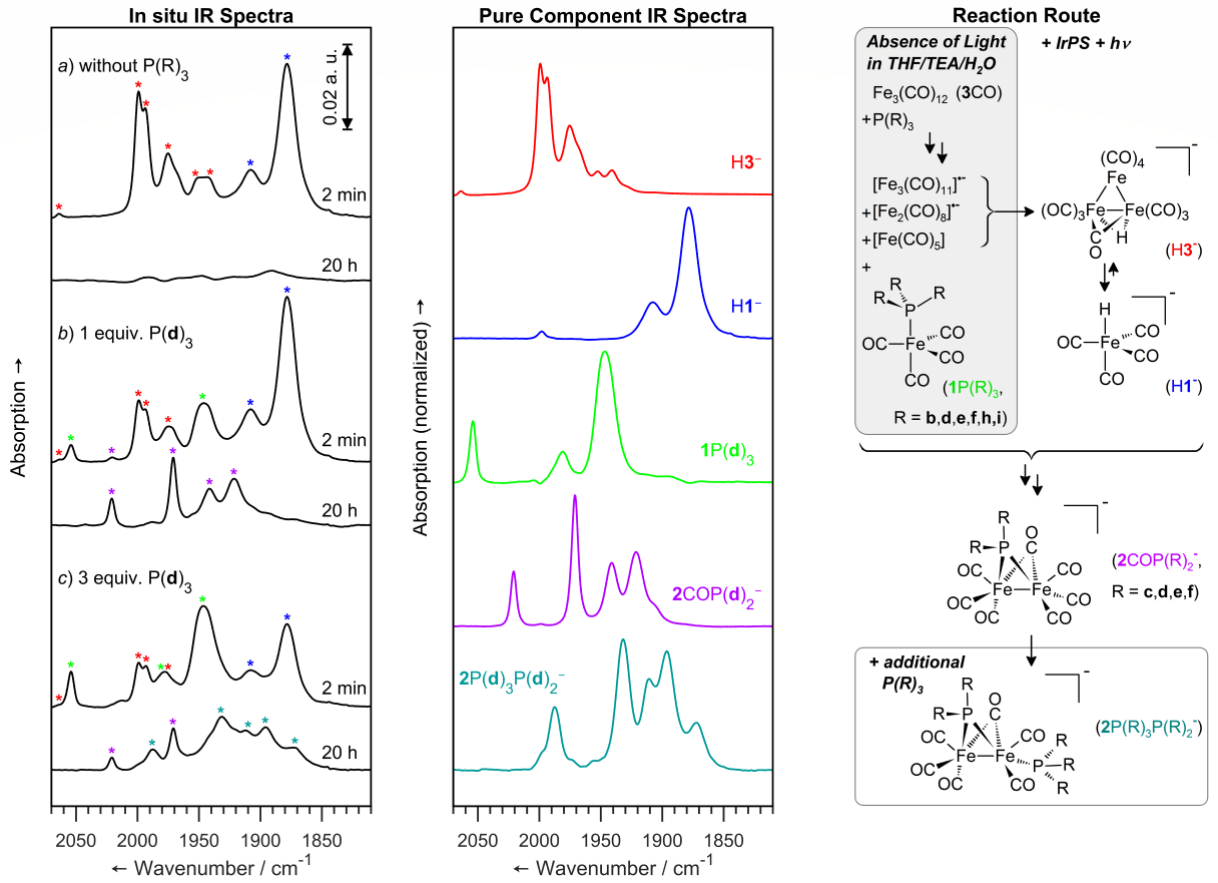

Figure IV.5. In situ and pure component IR spectra as well as the reaction route of system **B**. Left: experimental *in-situ* IR spectra of an irradiated solution of THF/TEA/H_2O (4/1/1) with added catalyst $[Fe_3(CO)_{12}]$, **Ir*PS***, and a) without phosphine, b) with one equivalent of P(**d**)$_3$, c) with three equivalents of P(**d**)$_3$. The spectra were recorded respectively after 2 min and 20 h. Middle and Right: pure component IR spectra and structures of $[HFe_3(CO)_{11}]^-$ ($H3^-$, red), $[HFe(CO)_4]^-$ ($H1^-$, blue), $[Fe(CO)_4(P(\mathbf{d})_3)]$ (1P(**d**)$_3$, green), $[Fe_2(CO)_6(\mu\text{-}CO)(\mu\text{-}P(\mathbf{d})_2)]^-$ (2COP(**d**)$_2^-$, violet) and $[Fe_2(CO)_5(P(\mathbf{d})_3)(\mu\text{-}CO)(\mu\text{-}P(\mathbf{d})_2)]^-$ (2P(**d**)$_3$P(**d**)$_2^-$, turquoise). For reaction conditions, please refer to publication 6.2, Figure 1.

As $[Fe_2(CO)_6(\mu\text{-}CO)(\mu\text{-}P(\mathbf{d})_2)]^-$ emerges during the catalytic reaction, it progressively contributes to hydrogen evolution (Figure IV.6). The complex is more stable than $[HFe(CO)_4]^-$ and maintains H_2 production even after decomposition of the latter. Hence, $[Fe_2(CO)_6(\mu\text{-}CO)(\mu\text{-}P(\mathbf{d})_2)]^-$ stabilizes the system and increases the H_2 yield by 200% after 80 hours of light irradiation as compared to system **A**.

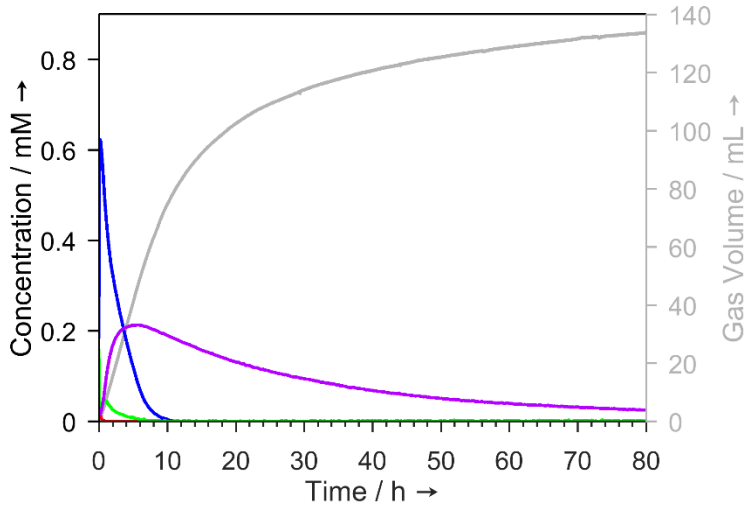

Figure IV.6. Gas evolution curve and concentration curves for iron carbonyl species observed in system **B**. The data was obtained in an operando FTIR experiment monitoring an irradiated solution of THF/TEA/H_2O (4/1/1) with added **Ir*PS***, catalyst [$Fe_3(CO)_{12}$] and one equivalent of P(**d**)$_3$. The gas evolution curve is shown in grey. The concentration curves for the complexes [$HFe_3(CO)_{11}]^-$ (red curve), [$HFe(CO)_4]^-$ (blue curve), [$Fe(CO)_4$(P(**d**)$_3$)] (green curve) and [$Fe_2(CO)_6$(μ-CO)(μ-P(**d**)$_2$)]$^-$ (violet curve) are also illustrated. For reaction conditions, please refer to publication 6.2, Figure 2b.

Application of preformed, molecularly defined [NEt_4][$Fe_2(CO)_6$(*μ*-CO)(*μ*-P(**d**)$_2$)] (molecularly defined **Ir*PS***/[NEt_4][$Fe_2(CO)_6$(*μ*-CO)(*μ*-P(R)$_2$)] system **B$_{MD}$**; Figure IV.7., black curve) results in a gas curve broadly similar to that of the in-situ system **B** (Figure IV.7., grey curve). Especially at extended reaction times, the slopes of the gas curves are equal because then, all iron material of system **B** has been converted into [$Fe_2(CO)_6$(*μ*-CO)(*μ*-P(**d**)$_2$)]$^-$ and the solution composition is similar to that of system **B$_{MD}$**. However, direct application of the molecular defined catalyst leads to an initial gas evolution rate being increased by 80%.

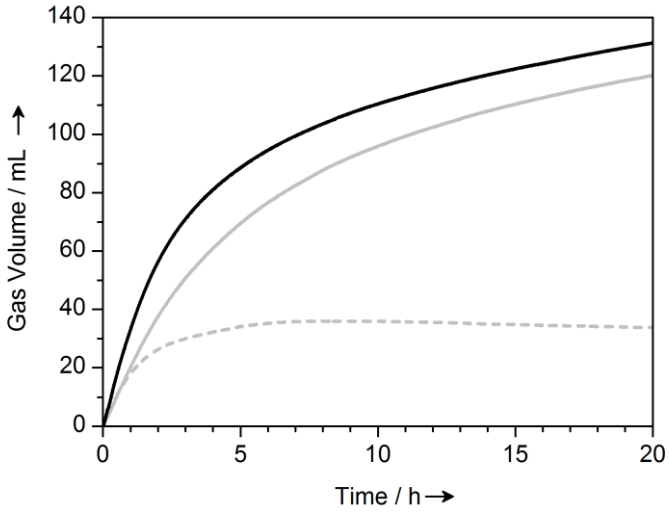

Figure IV.7. Gas evolution curves measured applying various starting catalyst material: the preformed [NEt_4][$Fe_2(CO)_6$(μ-CO)(μ-P(**d**)$_2$)] species (black, solid, system **B$_{MD}$**), the in-situ forming catalyst starting with [$Fe_3(CO)_{12}$] and co-catalyst P(**d**)$_3$ (grey, solid, system **B**), or plain [$Fe_3(CO)_{12}$] without phosphine (grey, dashed, system **B**) were applied together with the **Ir*PS*** in an illuminated THF/TEA/H_2O (3/2/1) solution. For the exact reaction conditions, please refer to publication 6.2, Figure 4.

It was therefore concluded that photons and thus electrons coming from the **Ir*PS*** are more efficiently used for hydrogen production by $[Fe_2(CO)_6(\mu\text{-}CO)(\mu\text{-}P(\mathbf{d})_2)]^-$ than by the $[HFe_3(CO)_{11}]^-/[HFe(CO)_4]^-$ couple which is primarily present in system **A** and in the starting phase of system **B**. Notably, due to the higher initial rates, system $\mathbf{B_{MD}}$ constitutes an improvement compared to system **B** with an H_2 yield increased by 10% (Figure IV.7). On the basis of these experiments, $[Fe_2(CO)_6(\mu\text{-}CO)(\mu\text{-}P(\mathbf{d})_2)]^-$ is confirmed to be a catalytically highly important key species. It was concluded that the complex can be regarded as a self assembling mimic of the [FeFe]-H_2ase active site, since it is a dinuclear iron complex with two bridging ligands in butterfly conformation and shows activity in photocatalytic proton reduction.

Different or similar effects on the catalytic system were observed by operando IR spectroscopy, if phosphines other than $P(\mathbf{d})_3$ had been applied as co-catalyst. The formation of $[Fe(CO)_4P(R)_3]$ or $[Fe_2(CO)_6(\mu\text{-}CO)(\mu\text{-}P(R)_2)]^-$ was found to be respectively determined by requirements on the ligand R, which will be specified in the following:

No impact on the catalytic reaction was observed in case sterically demanding phosphines like $P(\mathbf{a})_3$ and $P(\mathbf{g})_3$ were applied. They have Tolman cone angles bigger than 160° and do not show any interaction with the iron species. Hence, there are no differences in the process and H_2 yield compared with system **A**.

If the phosphite $P(\mathbf{b})_3$ or the alkylphosphines $P(\mathbf{h})_3$ and $P(\mathbf{i})_3$ were applied, exclusively $[Fe(CO)_4P(R)_3]$ emerged, which did not contribute to H_2 production. However, it caused a small negative effect on the system, most notably in case of the alkylphosphines. Due to formation of $[Fe(CO)_4P(R)_3]$, less iron material is available for transformation into $[HFe_3(CO)_{11}]^-/[HFe(CO)_4]^-$. Thereby, the latter species are used up sooner and H_2 production stops at an earlier stage with a decline of the H_2 yield by down to 16% as compared to system **A**.

Formation of $[Fe_2(CO)_6(\mu\text{-}CO)(\mu\text{-}P(R)_2)]^-$ was only detected in case $P(\mathbf{c})_3$, $P(\mathbf{d})_3$, $P(\mathbf{e})_3$ or $P(\mathbf{f})_3$ were applied. Further, all components of the system (catalyst, co-catalyst, THF/TEA/H_2O and light) except the **Ir*PS*** were found to be necessary for the generation of this complex. It was concluded that the phosphine has to meet two requirements to allow for formation of $[Fe_2(CO)_6(\mu\text{-}CO)(\mu\text{-}P(R)_2)]^-$:

(i) the phosphine belongs to the class of arylphosphines

(ii) the ortho positions of the aryl groups are unsubstituted

Most probably, these requirements are attributable to the P-C cleavage reaction prior to the formation of the $P(R)_2$ subunit. The reactivity for this process follows the order $P\text{-}C_{sp} > P\text{-}C_{sp2} > P\text{-}C_{sp3}$, which explains the formation of $[Fe_2(CO)_6(\mu\text{-}CO)(\mu\text{-}P(R)_2)]^-$ in case of arylphosphines rather than alkylphosphines. Formation of the diferrate in case of application of phosphites is also inhibited since the presence of water suppresses analogous P-O cleavage reactions and can cause decomposition of the ligands due to hydrolysis. As discussed in literature, P-C

cleavage is supposed to be activated by oxidative addition of the P-C bond to the metal center. Orthometallation, is argued to occur in a preceding process. This mechanism together with steric drawbacks might be the reason why ortho substituted phosphines like P(**a**)$_3$ and P(**g**)$_3$ do not afford $[Fe_2(CO)_6(\mu\text{-}CO)(\mu\text{-}P(R)_2)]^-$.

In case of formation of both electron poor complexes $[Fe_2(CO)_6(\mu\text{-}CO)(\mu\text{-}P(\mathbf{c})_2)]^-$ and $[Fe_2(CO)_6(\mu\text{-}CO)(\mu\text{-}P(\mathbf{d})_2)]^-$, the performance of the system was found to be improved as compared to system **A**, while it was declining in case the electron rich complexes $[Fe_2(CO)_6(\mu\text{-}CO)(\mu\text{-}P(\mathbf{e})_2)]^-$ and $[Fe_2(CO)_6(\mu\text{-}CO)(\mu\text{-}P(\mathbf{f})_2)]^-$ were generated. The same trend was found if these complexes were directly applied as preformed, molecularly defined catalysts $[NEt_4][Fe_2(CO)_6(\mu\text{-}CO)(\mu\text{-}P(R)_2)]$ (system $\mathbf{B_{MD}}$) with an increasing H_2 yield and TON the more electron poor substituent R gets(see Publication 6.2, Table 3). Therefore, to improve the performance of system **A** by addition of P(R)$_3$, the substituent R has to meet a further requirement:

(iii) the arylgroups R have to be electron withdrawing

It is supposed that the activity dependence of R is associated with the electron density of the central iron atoms in $[Fe_2(CO)_6(\mu\text{-}CO)(\mu\text{-}P(R)_2)]^-$. Electron density decreases with an increasing electron withdrawing effect of R, which is indicated by an IR shift to higher wavenumbers. Parallel to that, the electrochemical reduction potential rises, which facilitates reduction of $[Fe_2(CO)_6(\mu\text{-}CO)(\mu\text{-}P(R)_2)]^-$. However, the reduction potential is still too low ($[Fe_2(CO)_6(\mu\text{-}CO)(\mu\text{-}P(\mathbf{d})_2)]^-$: $E_{p(c)}$ = −2.6 V vs. $Fc^{+/0}$) to enable reduction by onefold negatively charged **Ir-*PS*** ($E_{1/2}$ = −1.80 V vs $Fc^{+/0}$). Hence, the exact mechanism of a proton reduction cycle involving $[Fe_2(CO)_6(\mu\text{-}CO)(\mu\text{-}P(R)_2)]^-$ and the included reaction steps (e.g. protonation of $[Fe_2(CO)_6(\mu\text{-}CO)(\mu\text{-}P(R)_2)]^-$ prior to reduction) need still to be investigated in future studies.

The best performance of system $\mathbf{B_{MD}}$ at optimized reaction conditions (see section 1.5.4 for conditions) was found for $[NEt_4][Fe_2(CO)_6(\mu\text{-}CO)(\mu\text{-}P(\mathbf{c})_2)]$ with an initial TOF of 309 h^{-1} (within the first 0.5 h) and a TON[8] of 1111 (after 20 h).

Investigation of the deactivation mechanisms of system $\mathbf{B/B_{MD}}$ was also part of the research. Catalyst poisoning at high **Ir*PS*** concentrations by bipyridine ligand transfer from the *PS* to the catalyst was not observed for $[Fe_2(CO)_6(\mu\text{-}CO)(\mu\text{-}P(R)_2)]^-$. This is a major reason for the high stability of system **B** in comparison with system **A**. However, $[Fe_2(CO)_6(\mu\text{-}CO)(\mu\text{-}P(R)_2)]^-$ is exposed to other slower light-induced decomposition processes such as CO dissociation. The decomposition was found to be attenuated under catalytic conditions in the presence of the **Ir*PS*** in THF/TEA/H_2O and was observed to proceed more quickly without **Ir*PS*** in pure THF. Hence, $[Fe_2(CO)_6(\mu\text{-}CO)(\mu\text{-}P(R)_2)]^-$ is stabilized by catalytic turnover.

Due to the slow rate of decomposition, $[Fe_2(CO)_6(\mu\text{-}CO)(\mu\text{-}P(R)_2)]^-$ is present in solution for more than 80 hours (in comparison, $[HFe(CO)_4]^-$ is consumed after 16 hours). Simultaneous

[8] Please note that in contrary to the work of F. Gärtner et al.[78,87], the TON in this work was calculated as $n(H_2)/n(Fe_2)$ rather than $n(H_2)/n(Fe_3)$

to the degradation of the catalyst, the **Ir*PS*** is decomposed. This is the reason for the steadily declining hydrogen evolution rate during the reaction time. Accordingly, by addition of a second **Ir*PS*** batch at extended reaction times, gas evolution could be restored for at least four hours.

A worse performance of system **B** was found if $[Fe_3(CO)_{12}]$ was applied as catalyst with more than one equivalent of P(**d**)$_3$ as co-catalyst. At these high phosphine concentrations, a terminal carbonyl ligand of $[Fe_2(CO)_6(\mu\text{-CO})(\mu\text{-P}(\mathbf{d})_2)]^-$ is substituted by P(**d**)$_3$ in a consecutive reaction and the complex $[Fe_2(CO)_5(P(\mathbf{d})_3(\mu\text{-CO})(\mu\text{-P}(\mathbf{d})_2)]^-$ emerges (Figure IV.5., right, structure of $2P(R)_3P(R)_2^-$). The species was assigned based on the agreement of its IR spectrum (Figure IV.5., middle, turquoise spectrum) with those of similar complexes described in literature like $[Fe_2(CO)_5(P(Me)(Ph)_2)(\mu\text{-CO})(\mu\text{-P}(Ph)_2)]^-$ and $[Fe_2(CO)_5(PH(Ph)_2)(\mu\text{-CO})(\mu\text{-P}(Ph)_2)]^-$ (see publication 6.2., Supporting Information). In the ^{31}P-NMR spectrum, the complex shows two doublet signals at δ 131.6 (for μ-P(**d**)$_2$) and 81.7 ppm (for *t*-P(**d**)$_3$) with a coupling constant of $^2J_{P\text{-}P}$ = 36.6 Hz, which is consistent with the proposed structure. Furthermore, DFT calculations support the assignment and indicate the terminal phosphine ligand to be in trans position to the phosphido bridge. The additional phosphine ligand in $[Fe_2(CO)_5(P(\mathbf{d})_3(\mu\text{-CO})(\mu\text{-P}(\mathbf{d})_2)]^-$ increases the electron density on the iron, which is subsequently even higher than on the iron atoms in the bad performing complexes $[Fe_2(CO)_6(\mu\text{-CO})(\mu\text{-P}(\mathbf{e})_2)]^-$ and $[Fe_2(CO)_6(\mu\text{-CO})(\mu\text{-P}(\mathbf{f})_2)]^-$ (vide supra). This was concluded from the IR contributions of $[Fe_2(CO)_5(P(\mathbf{d})_3(\mu\text{-CO})(\mu\text{-P}(\mathbf{d})_2)]^-$ observed at lower wavenumbers than those of the electron rich complexes $[Fe_2(CO)_6(\mu\text{-CO})(\mu\text{-P}(\mathbf{e})_2)]^-$ and $[Fe_2(CO)_6(\mu\text{-CO})(\mu\text{-P}(\mathbf{f})_2)]^-$. Hence, $[Fe_2(CO)_5(P(\mathbf{d})_3(\mu\text{-CO})(\mu\text{-P}(\mathbf{d})_2)]^-$ is a complex with a bad catalytic activity, which emerges in significant amounts in case of application of excessive quantities of P(**d**)$_3$ and lowers the performance of the system by competing with $[Fe_2(CO)_6(\mu\text{-CO})(\mu\text{-P}(\mathbf{d})_2)]^-$ for electrons.

4.3 Investigation of System C (Publications 6.3., 6.4. and 6.5.)

Basis for the investigation of the noble metal free **Cu*PS***/$[Fe_3(CO)_{12}]$ system **C**, has been a work by Armaroli et al. who studied the dissociation of phosphine ligands in copper complexes akin to the **Cu*PS***. Therein, the heteroleptic starting compound [Cu(bathocuproine)(xantphos)]$^+$ (**Cu*PS*$_{\text{heteroleptic}}$**) was found to be in equilibrium with the homoleptic complex $[Cu(bathocuproine)_2]^+$ (**Cu*PS*$_{\text{homoleptic}}$**)[106] (Figure IV.8.). This is in line with experimental findings by means of UV/vis spectroelectrochemistry experiments carried out by S. Tschierlei. During alternating oxidation and re-reduction of the **Cu*PS***, S. Tschierlei observed a decline of the spectroscopic band for **Cu*PS*$_{\text{heteroleptic}}$** and an increasing band for **Cu*PS*$_{\text{homoleptic}}$**. EPR measurements by D. Hollmann showed, that the **Cu*PS**** can be subject to both, the reductive- and oxidative quenching. However, no oxidized copper could be observed after CuPS* reduced $[Fe_3(CO)_{12}]$, which

indicates an unexpected reaction pathway. It was concluded that CuPS decomposes when being oxidized. This is supported by cyclic voltammetry data.

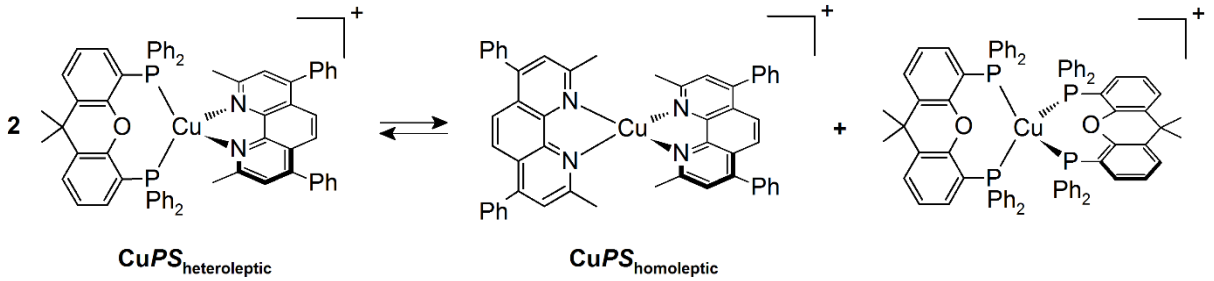

Figure IV.8. Equilibrium between the heteroleptic CuPS and the homoleptic CuPS as described by Armaroli et al..[106]

Hence, the diphosphine ligand is loosely bond to the **Cu*PS***. After dissociation, it is located in a $[Cu(xantphos)_2]^+$ complex or remains free in solution. With $[Fe_3(CO)_{12}]$ and a (di)phosphine ligand being present, the composition of the starting solution of system **C** is broadly similar to that of system **B**. Therefore, the effects of the ligand dissociation reaction of the **Cu*PS*** on the catalyst $Fe_3(CO)_{12}$ in THF/TEA/H_2O (4/1/1) under light irradiation, were investigated by operando IR spectroscopy in this work. As in system **A** and **B**, $[HFe_3(CO)_{11}]^-$ emerges at the beginning of the solution. As the reaction proceeds, it is transformed into $[Fe_2(CO)_6(\mu\text{-}CO)(\mu\text{-}P(Ph)_2)]^-$, the same species which had been observed in system **B** by application of PPh_3 (P(**e**)$_3$) as ligand. After 35 hours reaction time, $[Fe_2(CO)_6(\mu\text{-}CO)(\mu\text{-}P(Ph)_2)]^-$ is the only iron carbonyl complex present in solution. At that time, H_2 evolution is ongoing, which indicates that $[Fe_2(CO)_6(\mu\text{-}CO)(\mu\text{-}P(Ph)_2)]^-$ is catalytically active in system **C**. These findings reveal that xantphos also undergoes P-C cleavage. Similar to the $[Fe_3(CO)_{12}]$/P(**d**)$_3$ couple, formation of $[Fe_2(CO)_6(\mu\text{-}CO)(\mu\text{-}P(Ph)_2)]^-$ is also observed on the absence of the **Cu*PS*** in a solution of $[Fe_3(CO)_{12}]$ and xantphos in THF/TEA/H_2O. However, this occurs at much slower speed, which is reduced by the factor 7 as compared to the corresponding reaction with the monophosphine P(**d**)$_3$. Notably, the presence of the **Cu*PS*** and light irradiation accelerate the formation $[Fe_2(CO)_6(\mu\text{-}CO)(\mu\text{-}P(Ph)_2)]^-$. It was concluded that reductive conditions promote the P-C cleavage reaction of xantphos.

Based on the finding that system **C** is very dynamic and implies several rearrangement reactions, the **Cu*PS*$_{homoleptic}$** was tested as PS together with free xantphos and $[Fe_3(CO)_{12}]$ (system **C$_H$**) by Beller and co-workers for photocatalytic proton reduction. The Beller group also designed a system that omits time consuming synthesis and provides in-situ formation of the **Cu*PS*.** This system consists of the components $[Cu(MeCN)_4]PF_6$, bathocuproine, xantphos and $[Fe_3(CO)_{12}]$ as starting material(system **C$_{IS}$**). In both cases (system **C$_H$** and **C$_{IS}$**), H_2 yields were observed, which are similar to those of system **C**.

In all three systems, the **Cu*PS*$_{heteroleptic}$** was found to be present in solution under catalytic conditions, as observed by ^{31}P-NMR spectroscopy. Considering the equilibrium between **Cu*PS*$_{heteroleptic}$** and **Cu*PS*$_{homoleptic}$**, it was studied which of these complexes is the active photosensitizer. Investigation showed that **Cu*PS*$_{homoleptic}$** neither shows activity in combination with $[Fe_3(CO)_{12}]$ nor with pre-synthesized $[NEt_4][Fe_2(CO)_6(\mu\text{-CO})(\mu\text{-P(Ph)}_2)]$, while the **Cu*PS*$_{heteroleptic}$** does. Hence, the latter was confirmed to be the active photosensitizer, which is in line with the experimental results of Amaroli and co-workers, who found the **Cu*PS*$_{homoleptic}$** to be inactive.

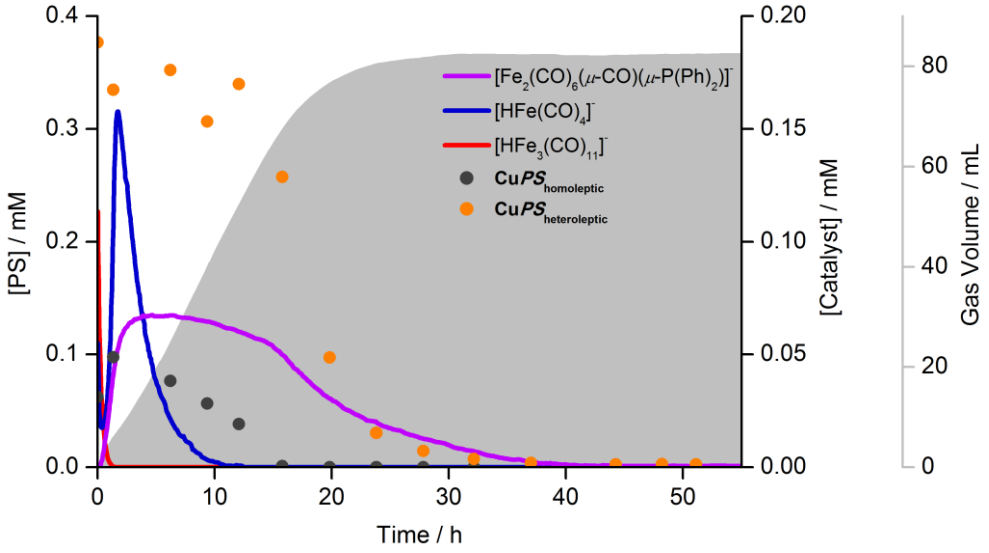

Figure IV.9. Operando IR/ex-situ ESI-MS measurements of system C. The concentration curves ([Catalyst]) of the iron complexes $[HFe_3(CO)_{11}]^-$ (red curve), $[HFe(CO)_4]^-$ (blue curve), and $[Fe_2(CO)_6(\mu\text{-CO})(\mu\text{-PPh}_2)]^-$ (violet curve) are illustrated. Furthermore, the concentrations ([PS]) as function of time are shown for the homoleptic **Cu*PS*** (black dots) and the heteroleptic **Cu*PS*** (orange dots). The gas evolution curve is depicted as shaded area. For the exact reaction conditions, please refer to publication 6.4, figure 6.

To simultaneously monitor the conversion and deactivation processes of the catalyst and the photosensitizer, an experiment was carried out with operando IR applied in parallel to *ex-situ* ESI-MS (Figure IV.9.). It was found that over the course of the reaction, **Cu*PS*$_{homoleptic}$** decays first, while **Cu*PS*$_{heteroleptic}$** is relatively stable during the first 15 hours. As soon as **Cu*PS*$_{homoleptic}$** is decomposed, rapid degradation of **Cu*PS*$_{heteroleptic}$** occurs. It was concluded that dissociation of the bathocuproine ligand is the major degradation pathway of the photosensitizer. The **Cu*PS*$_{homoleptic}$** serves as reservoir of bathocuproine and regenerates **Cu*PS*$_{heteroleptic}$** through adjustment of the equilibrium. This finding is in line with the observation that higher TONs are achieved with increased amounts of bathocuproine added at the beginning of the reaction.

As was found for system **B**, $[Fe_2(CO)_6(\mu\text{-CO})(\mu\text{-P(R)}_2)]^-$ is stabilized by catalytic turnover. As soon as **Cu*PS*$_{heteroleptic}$** is consumed, H_2 evolution stops and consequently rapid decomposition of $[Fe_2(CO)_6(\mu\text{-CO})(\mu\text{-P(Ph)}_2)]^-$ follows. Hence, the degradation reactions of both components are linked to each other and the decomposition of the photosensitizer is the yield limiting process of the system.

V. CONCLUSION AND OUTLOOK

This work demonstrates the potential of spectroscopic and quantum computational techniques for the investigation of the mechanism of catalytic reactions. For the photocatalytic water reduction systems **A**, **B** and **C**, the understanding of such a mechanism has been substantially improved:

The monomeric intermediate, which was detected in previous studies, has now been identified as $[HFe(CO)_4]^-$. This complex was found to be formed irrespectively of the applied iron carbonyl precursor and to be the dormant species of the system in equilibrium with the active species $[HFe_3(CO)_{11}]^-$. Due to the self-assembling nature of these hydride species, they might be expected to be present, at least in small amounts, in many systems that include carbonyl comprising iron-based catalysts.

It is pointed out that optimization of the **Ir*PS*** has to be prioritized in order to improve system **A** and **B**. This is concluded from the finding that in system **A** the quenching of the **Ir*PS*** by TEA constitutes the rate determining step and that the catalyst is poisoned by bpy ligands that were dissociated from the **Ir*PS***. As shown in this work, application of electronic withdrawing phosphines results in the formation of the sulfur-free hydrogenase mimic $[Fe_2(CO)_6(\mu\text{-}CO)(\mu\text{-}P(R)_2)]^-$, which is inert to poisoning by bpy. The complex $[Fe_2(CO)_6(\mu\text{-}CO)(\mu\text{-}P(R)_2)]^-$ is furthermore stabilized by catalytic turnover and has a better catalytic performance than the $[HFe_3(CO)_{11}]^-$ / $[HFe(CO)_4]^-$ species. Due to these properties of the complex, the stability of the system is improved and is subsequently limited mainly by the degradation of the **Ir*PS***. These findings answer the question of the role of the phosphine that had been brought up in a review article by Du and Eisenberg[49].

Other iron phosphines were identified in this work like $[Fe(CO)_4P(R)_3]$, which is present at the beginning of the reaction, and the inactive $[Fe_2(CO)_5(P(R)_3)(\mu\text{-}CO)(\mu\text{-}P(R)_2)]^-$ species, which is generated at excessive amounts of $P(R)_3$. Moreover, the requirements on the phosphine and the reaction conditions that allow for the formation of the active $[Fe_2(CO)_6(\mu\text{-}CO)(\mu\text{-}P(R)_2)]^-$ species were presented. This narrows down the list of other potential phosphines that might be tested in the future to improve the system. It has to be highlighted that due to the self-assembly of the complex, time-consuming synthesis is omitted. This allows for easy regeneration of the catalyst, which is important for the longevity of modern solar fuel devices.[10] However, it was also shown that direct application of pre-synthesized $[NEt_4][Fe_2(CO)_6(\mu\text{-}CO)(\mu\text{-}P(R)_2)]$ increases the initial TOF by 80% and the final H_2 yield by 10% due to the shortcut for the assembling reaction during the induction phase. The exact proton reduction cycle of $[Fe_2(CO)_6(\mu\text{-}CO)(\mu\text{-}P(R)_2)]^-$ including expected hydride-intermediates have to be elucidated in future works.

With focus on the PS, the system might be improved by substituting the former with an iridium based PS that comprises tridentate ligands.[133,134] The dissociation of these ligands and subsequent catalyst poisoning could possibly be prevented due to the enhanced chelate effect. The use of quantum dots as photosensitizer is also very promising, since they are known to boost the system's performance significantly, as shown in combination with other iron-, cobalt- and nickel catalysts (see section 1.5).
There are also starting points to improve the performance of the $[Fe_2(CO)_6(\mu\text{-}CO)(\mu\text{-}P(R)_2)]^-$ catalyst or make use of it in other applications: E.g. usage of sulfonated phosphines like $P(C_6H_4SO_3Na)_3$ (TPPTS), might increase the water-solubility of the complex and allow for a higher water content in the solvent mixture. Also, diferrates that are not accessible by the self-assembly reaction, like $[Fe_2(CO)_6(\mu\text{-}CO)(\mu\text{-}P(O\text{^}O))]^-$ with an electron-poor bridging phosphite ligand (e.g. dioxaphospholane), might show a good catalytic performance. For integration in dye-sensitized photoelectrochemical cells, the catalytic complex would need to be immobilized at the electrode surface (see section 1.6). This immobilization could be realized in-situ e.g. by application of diarylphosphine-functionalized polystyrene instead of molecular $P(R)_3$.[135] This polymer would in the same time constitute a protective layer for the electrode and allow for hyper-quantitative catalyst loading (see section 1.6).

For system C, which makes use of a copper-based PS, the conversion processes of the PS and the catalyst could also be elucidated and monitored in this work. The finding by Armaroli and co-workers, that the diphoshine ligand (xantphos) is loosely coordinated to the Copper was confirmed. It was further found by IR and NMR spectroscopy that the dissociated ligand degrades, resulting in the formation of $[Fe_2(CO)_6(\mu\text{-}CO)(\mu\text{-}P(Ph)_2)]^-$.
Based on this knowledge, the Beller group designed an in-situ system where the **Cu*PS*** self-assembles from inexpensive $[Cu(MeCN)_4]PF_6$ and respectively bare diphosphide and bathocuproine. This in-situ system dispenses with the **Cu*PS*** synthesis and allows for an easy and economic screening of potential ligands and optimizing of reaction conditions. By the latter, the Beller group could increase the systems activity by 30%.
Regardless of the starting material, both, the homoleptic complex $[Cu(N\text{^}N)_2]^+$ and the heteroleptic **Cu*PS*** $[Cu(N\text{^}N)(P\text{^}P)]^+$ were found to be present in solution and confirmed to be in equilibrium with each other over the reaction time. This was shown in this work by quantitative ex-situ ESI-MS measurements that were carried out parallel to operando IR experiments. However, control experiments starting with pre-synthesized components revealed that the heteroleptic **Cu*PS*** $[Cu(N\text{^}N)(P\text{^}P)]^+$ and the catalyst $[Fe_2(CO)_6(\mu\text{-}CO)(\mu\text{-}P(Ph)_2)]^-$ exclusively constitute the active components of the system. Similar to the systems A and B, the degradation of the **Cu*PS***, more precisely the dissociation and degradation of the bathocuproine ligand from the ligand was found to be the stability limiting process of the system.

Research addressing the photostability of the copper-based photosensitizer is ongoing in the scientific community. E.g. homoleptic Cu complexes with heteronuclear ligands like $[Cu(N\hat{}P)_2]^+$ are tested. [136,137] Also, the application of multidentate ligands is investigated resulting in complexes like $[Cu(X\hat{}N\hat{}N\hat{}X)_2]^+$ (X = O or S),[138,139] $[Cu(P\hat{}N\hat{}N\hat{}P)]^+$,[140] or macrocyclic $[Cu(N\hat{}N\hat{}N\hat{}N)]^+$.[141] These complexes make use of the chelate effect and aim for conserving the tetrahedral coordination sphere upon excitation or for shielding the flattened excited state from nucleophilic attack by solvent molecules.

Please note that with regards to the catalyst, the **Cu*PS***/differate couple might be a promising candidate to be the template for a Cu/Fe dyad. In literature, related complexes like $[\{Fe_2(CO)_6(\mu\text{-}CO)(\mu\text{-}P(R)_2)Cu\}_2(P\hat{}P)]$ have already been described.[142]

The sum of the ideas presented here, illustrate the potential of $Fe_2(CO)_6(\mu\text{-}CO)(\mu\text{-}P(R)_2)]^-$ as catalyst and its relevance in future applications.

VI. PUBLICATIONS

Nr.	Publication	Contribution
1	Steffen Fischer, Olga S. Bokareva, Enrico Barsch, Sergey I. Bokarev, Oliver Kühn, and Ralf Ludwig, “Mechanistic Study of Photocatalytic Hydrogen Generation with Simple Iron Carbonyls as Water Reduction Catalysts” *ChemCatChem*, **2016**, *8* (2), 404-411	Full Paper 50%
2	Steffen Fischer, Arend Rösel, Matthias Bauer, Anja Kammer, Enrico Barsch, Roland Schoch, Henrik Junge, Matthias Beller and Ralf Ludwig, „Diferrate $[Fe_2(CO)_6(\mu\text{-}CO)(\mu\text{-}P(aryl)_2)]^-$ as Self-Assembling Iron/Phosphor Based Catalyst for the Hydrogen Evolution Reaction in Photocatalytic Proton Reduction – Spectroscopic Insights“ *Chem. Eur. J.*, **2018**, *24* (60), 16052-16065	Full Paper 50%
3	Steffen Fischer, Dirk Hollmann, Stefanie Tschierlei, Michael Karnahl, Nils Rockstroh, Enrico Barsch, Patrick Schwarzbach, Shu-Ping Luo, Henrik Junge, Matthias Beller, Stefan Lochbrunner, Ralf Ludwig, and Angelika Brückner, “Death and Rebirth: Photocatalytic Hydrogen Production by a Self-Organizing Copper-Iron System” *ACS Catal.*, **2014**, *4* (6), 1845-1849	Communication 25%
4	Alastair J. J. Lennox, Steffen Fischer, Mark Jurrat, Shu-Ping Luo, Nils Rockstroh, Henrik Junge, Ralf Ludwig, and Matthias Beller, “Copper-Based Photosensitizers in Water Reduction: A More Efficient In Situ Formed System and Improved Mechanistic Understanding” *Chem. Eur. J.*, **2016**, *22* (4), 1233-1238	Communication 30%
5	Henrik Junge, Nils Rockstroh, Steffen Fischer, Angelika Brückner, Ralf Ludwig, Stefan Lochbrunner, Oliver Kühn and Matthias Beller, “Light to Hydrogen: Photocatalytic Hydrogen Generation from Water with Molecularly-Defined Iron Complexes” *Inorganics*, **2017**, *5* (1), 14	Review 15%

6.1 Mechanistic Study of Photocatalytic Hydrogen Generation with Simple Iron Carbonyls as Water Reduction Catalysts

Steffen Fischer, Olga S. Bokareva, Enrico Barsch, Sergey I. Bokarev, Oliver Kühn, and Ralf Ludwig

Full Paper: *ChemCatChem*, **2016**, *8* (2), 404-411
DOI: 10.1002/cctc.201500872

Shortened Abstract

Mechanisms of water reduction: This mechanistic study provides new detailed insights into homogeneous photocatalytic water reduction using an iridium dye/iron carbonyl system. It shows the system's loss channels and reveals the nature of the catalytically active complex by application of stopped-flow rapid-scan and operando continuous-flow FTIR spectroscopy as well as time-dependent density functional theory. SR = Sacrificial reductant, IrPS = Iridium photosensitizer, WRC = Water reduction catalyst.

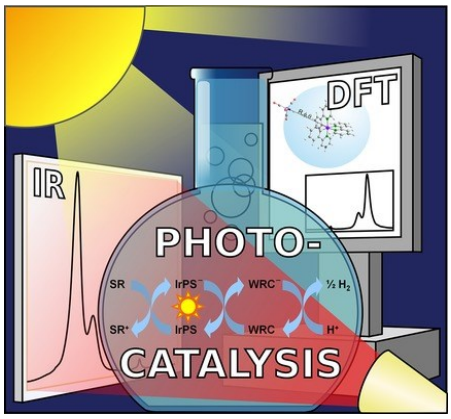

Contribution to this work (50%)

Steffen Fischer designed and performed all operando continuous-flow FTIR experiments and analyzed the spectroscopic data thereby obtained. He led the discussion of the experimental results and wrote the manuscript. The overall contribution is about 50%.

ChemPubSoc Europe

DOI: 10.1002/cctc.201500872

CHEMCATCHEM Full Papers

Mechanistic Study of Photocatalytic Hydrogen Generation with Simple Iron Carbonyls as Water Reduction Catalysts

Steffen Fischer,[a] Olga S. Bokareva,[b] Enrico Barsch,[a, c] Sergey I. Bokarev,[b] Oliver Kühn,*[b] and Ralf Ludwig*[a, c]

This study provides new insights into light-driven hydrogen generation using an iridium photosensitizer (IrPS) and simple iron carbonyls as water reduction catalysts (WRCs). Stopped-flow rapid-scan FTIR and operando continuous-flow FTIR spectroscopy as well as time-dependent density functional theory (TD-DFT) has been applied to study the reaction. The conversion of the WRC precursor $[Fe_3(CO)_{12}]$ into the radicals $[Fe_3(CO)_{11}]^{\bullet-}$ and $[Fe_2(CO)_8]^{\bullet-}$ as well as $[Fe(CO)_5]$ in the absence of light in a solvent mixture of tetrahydrofuran, triethylamine, and water has been studied quantitatively. During light-induced hydrogen production in the presence of the IrPS, the trimeric $[HFe_3(CO)_{11}]^-$ and the monomeric $[HFe(CO)_4]^-$ anion could be identified as major WRC species. The equilibrium between both species can be shifted completely towards $[HFe(CO)_4]^-$ by increasing the water content of the solvent mixture. Application of other iron(0) carbonyl compounds as WRC precursors also results in the exclusive formation of $[HFe(CO)_4]^-$. Kinetic experiments show that the stability of the system is primarily influenced by the applied amount of WRC precursor, whereas the reaction rate is mainly determined by the concentration of the IrPS. At least two loss channels could be identified: light-induced CO dissociation from the WRC and decomposition of the IrPS at high IrPS/WRC ratios, accompanied by a ligand transfer from the iridium towards the iron center of the WRC. To reveal the nature of the catalytically active complex, binding energies and charge-transfer probabilities of all coordination geometries of various IrPS···WRC complexes have been calculated. These computations indicate an increased probability of charge transfer for dimeric and trimeric iron carbonyl species.

Introduction

Efficient conversion and storage of solar energy in a convenient chemical form such as hydrogen is one of the most prominent challenges of modern "green energy" research. From this perspective, photocatalytic water splitting represents a very promising reaction to produce hydrogen with an estimated theoretical efficiency of more than 15%, generating a product that can be used in fuel cells without emission of greenhouse gases.[1] The water-splitting process is usually divided into the oxidation and reduction half reactions. By adding sacrificial oxidants or reductants, these half-reactions can be investigated separately.[2] Accordingly, a homogeneous photocatalytic water reduction system consists of a sacrificial reductant (SR) as the electron donor, a photosensitizer (PS) as the light-absorbing and primary charge-separating unit, as well as a water reduction catalyst (WRC) as an agent for reducing aqueous protons and assembling them into molecular hydrogen.[3] For industrial applications, such a system must be active and stable in the long-term and be based on low-cost ingredients.[4] To satisfy the latter requirement, noble-metal-free complexes of Co, Ni, and Fe have been suggested as active WRCs.[3,5] However, a sophisticated and time-consuming synthesis of these complexes is often necessary.

Beller and co-workers have reported the first photocatalytic water reduction system utilizing simple iron carbonyls as the WRC.[6] The iridium complex $[Ir(bpy)(ppy)_2]PF_6$ (IrPS; bpy = 2,2′-bipyridine; ppy = 2-phenylpyridine) is used as a PS and triethylamine (TEA) as the SR in a THF/TEA/H_2O solvent mixture (Scheme 1). If $[Fe_3(CO)_{12}]$ is applied as the WRC, a turnover number (TON) of 200 hydrogen molecules per Fe is achieved after 3 h of light irradiation. This system has been further modified by replacing the IrPS by a heteroleptic copper complex with bathocuproin and xantphos ligands, resulting in a photocatalytic water reduction system exclusively consisting of earth-abundant elements.[7]

The present mechanistic study combines experimental and theoretical methods such as IR spectroscopy and DFT calculations to focus on the homogeneous photocatalytic system based on IrPS and iron carbonyl WRC and to continue previous

[a] S. Fischer, E. Barsch, Prof. Dr. R. Ludwig
Abteilung für Physikalische Chemie
Institut für Chemie
Universität Rostock
Dr.-Lorenz-Weg 1, 18059 Rostock (Germany)
Fax: (+49) 381-498-6524
E-mail: ralf.ludwig@uni-rostock.de

[b] Dr. O. S. Bokareva, Dr. S. I. Bokarev, Prof. Dr. O. Kühn
Institut für Physik, Universität Rostock
Albert-Einstein-Str. 23-24, 18059 Rostock (Germany)
E-mail: oliver.kuehn@uni-rostock.de

[c] E. Barsch, Prof. Dr. R. Ludwig
Leibniz-Institut für Katalyse an der Universität Rostock e.V.
Albert-Einstein-Str. 29a, 18059 Rostock (Germany)

Supporting information and ORCID(s) from the author(s) for this article are available on the WWW under http://dx.doi.org/10.1002/cctc.201500872.

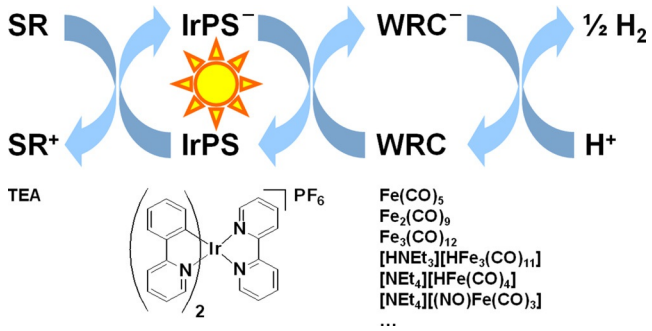

Scheme 1. Principle scheme of photocatalytic water reduction making use of a sacrificial reductant (SR), an iridium photosensitizer (IrPS), and a water reduction catalyst (WRC).[6]

investigations of the IrPS[8] and WRC subcycles.[6b,9] The particular focus is put on elucidating the light-induced transformation of the WRC precursor into catalytically active iron carbonyl complexes and their degradation mechanism.

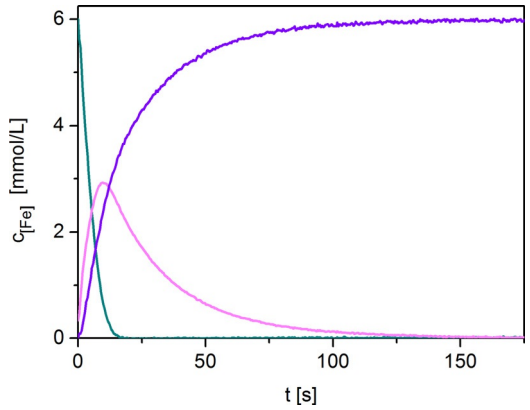

Figure 2. Conversion of $[Fe_3(CO)_{12}]$ into a mixture of $[Fe_3(CO)_{11}]^{\bullet-}$, $[Fe_2(CO)_8]^{\bullet-}$, and $[Fe(CO)_5]$ in the presence of TEA and H_2O. Iron concentration determined by $c\times$(number of Fe per molecule) of the species $[Fe_3(CO)_{12}]$ (turquoise), $[Fe_3(CO)_{12}]^{\bullet-}$ (magenta), and the mixture of $[Fe_3(CO)_{11}]^{\bullet-}$, $[Fe_2(CO)_8]^{\bullet-}$, and $[Fe(CO)_5]$ (violet). Conditions: 2 mmol L^{-1} $[Fe_3(CO)_{12}]$ in THF/TEA/H_2O 8:2:1, 25 °C.

Results and Discussion

Dark-phase WRC activation

$[Fe_3(CO)_{12}]$ is the standard WRC precursor in the photocatalytic water reduction system as it shows a good activity and can be handled conveniently. Belousov et al. have intensively investigated the reaction of $[Fe_3(CO)_{12}]$ with various Lewis bases.[10] Dissolving $[Fe_3(CO)_{12}]$ in a mixture of THF, TEA, and H_2O leads to the radical anions $[Fe_3(CO)_{12}]^{\bullet-}$, $[Fe_3(CO)_{11}]^{\bullet-}$, and $[Fe_2(CO)_8]^{\bullet-}$ with a ratio of 1:66:32, which has been studied by using EPR in our previous work[9].

In the present study, we have followed this first electron-transfer reaction by means of stopped-flow rapid-scan FTIR. Initially, $[Fe_3(CO)_{12}]$ with vibrational bands at 2106 (vw), 2047 (s), 2025 (m), 1860 (vw), and 1825 (w) cm^{-1} (Figures 1 and 2, turquoise spectrum and concentration curve) is converted into the rather unstable radical $[Fe_3(CO)_{12}]^{\bullet-}$ (Figure 2, magenta concentration curve).

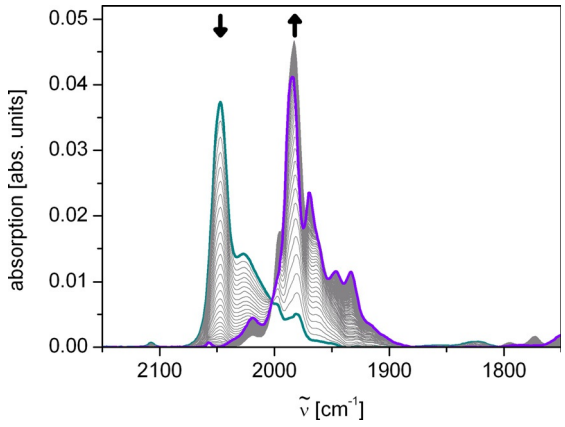

Figure 1. Absorption spectra showing the conversion of $[Fe_3(CO)_{12}]$ (turquoise) into a mixture of $[Fe_3(CO)_{11}]^{\bullet-}$, $[Fe_2(CO)_8]^{\bullet-}$, and $[Fe(CO)_5]$ (violet). Conditions: 2 mmol L^{-1} $[Fe_3(CO)_{12}]$ in THF/TEA/H_2O 8:2:1, 25 °C, $\Delta t_{spectra} = 0.45$ s.

The reaction rate is strongly accelerated by an increasing water concentration (Supporting Information, Figure SI1). In a consecutive reaction of pseudo-first-order type, $[Fe_3(CO)_{12}]^{\bullet-}$ decomposes into $[Fe_3(CO)_{11}]^{\bullet-}$, $[Fe_2(CO)_8]^{\bullet-}$, and $[Fe(CO)_5]$ (Figures 1 and 2, violet resulting spectrum and concentration curve; for spectral assignments, see Figure SI3 in the Supporting Information). The latter species has been identified to be the dominant EPR-silent iron species through the work of Hollmann et al.[9] The rate constant of the decomposition reaction at 25 °C has been determined to be $k_{25\,°C} = 0.038\ s^{-1}$ (Figure SI4 in the Supporting Information).

Light-induced formation of $[HFe(CO)_4]^-$

We have studied the following reaction processes under water reduction conditions by means of operando continuous-flow FTIR spectroscopy on a longer time scale. After adding IrPS to the activated reaction mixture, hydrogen evolution starts under exposure to visible light (380–700 nm). The IrPS is excited by irradiation and subsequently quenched reductively[8] by the SR triethylamine. This results in the reduced IrPS and the decomposition products diethylamine and acetaldehyde. The latter is observed in the IR spectra at 1724 cm^{-1}.[6b,9]

Owing to the subsequent reduction by the reduced IrPS, all of the iron carbonyl species $[Fe_3(CO)_{11}]^{\bullet-}$, $[Fe_2(CO)_8]^{\bullet-}$ and $[Fe(CO)_5]$ are transformed within one minute into $[HFe_3(CO)_{11}]^-$, with IR-absorption features at 2064 (vw), 1999 (s), 1993 (s), 1975 (m), 1953 (w), 1941 (w), and 1748 (w) cm^{-1} (Figures 3 and 4, red spectrum and concentration curve),[6b,9,11] and the monomeric anion $[HFe(CO)_4]^-$, with contributions at 1998 (w), 1908 (m), and 1878 (s) cm^{-1} (Figures 3 and 4, blue spectrum and concentration curve). The assignment of $[HFe(CO)_4]^-$ is supported by comparison with literature values,[12] DFT calculated spectra, and the IR spectrum of synthesized $[NEt_4][HFe(CO)_4]$[13] (Table SI1 in the Supporting Information). In our previous work,[6b] this complex was assigned as a monomeric intermediate.

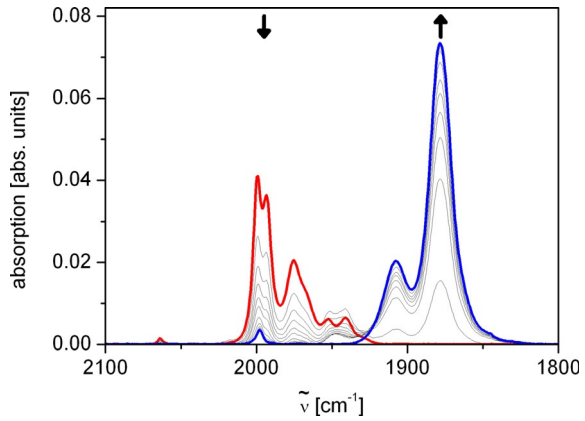

Figure 3. Conversion of $[HFe_3(CO)_{11}]^-$ (red) into $[HFe(CO)_4]^-$ (blue) during the first 1.5 h of light irradiation as tracked by operando continuous-flow FTIR. Conditions: 10.0 μmol of IrPS, 6.1 μmol of $[Fe_3(CO)_{12}]$, 20 mL of THF/TEA/H_2O 4:1:1, visible light (1.5 W), 25 °C, $\Delta t_{spectra} = 8$ min.

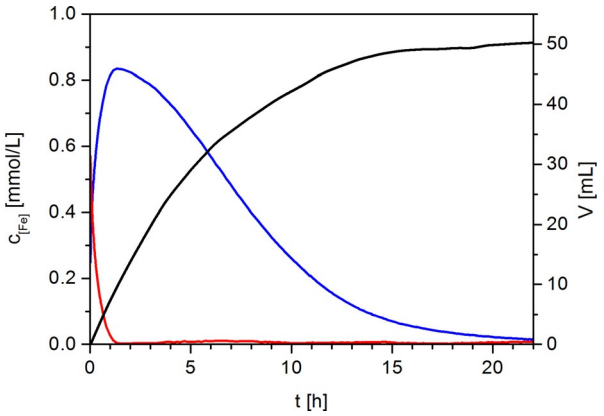

Figure 4. Concentration curves ($c \times$(number of Fe per molecule)) of iron species $[HFe_3(CO)_{11}]^-$ (red) and $[HFe(CO)_4]^-$ (blue) as well as hydrogen evolution curve (black) in a standard water reduction experiment. Conditions: 10.0 μmol of IrPS, 6.1 μmol of $[Fe_3(CO)_{12}]$, 20 mL of THF/TEA/H_2O 4:1:1, visible light (1.5 W), 25 °C.

The equilibrium between $[HFe_3(CO)_{11}]^-$ and $[HFe(CO)_4]^-$ strongly depends on the water content of the THF/TEA/H_2O mixture. For the volumetric ratio of 4:1:0.25, which was applied in our previous in situ FTIR study,[6b] both carbonyls are present throughout the whole reaction time. At higher water concentrations, this equilibrium is shifted towards $[HFe(CO)_4]^-$. Thus, at a THF/TEA/H_2O ratio of 4:1:1, the $[HFe_3(CO)_{11}]^-$ complex is converted completely into $[HFe(CO)_4]^-$ within 1.5 h. Notably, hydrogen evolution continues for a further 15 h as long as $[HFe(CO)_4]^-$ is present in solution (Figure 4). In addition, the higher water content slightly increases the hydrogen evolution rate (Figure SI5 in the Supporting Information). All further studies were carried out with a THF/TEA/H_2O 4:1:1 mixture, as this is the standard ratio of catalytic experiments in the literature.[6]

In addition to $[Fe_3(CO)_{12}]$, various other iron(0) carbonyls show catalytic activity as WRC precursors.[6] $[Fe(CO)_5]$, $[Fe_2(CO)_9]$, $[HNEt_3][HFe_3(CO)_{11}]$, and $[NEt_4][Fe(NO)(CO)_3]$ have been applied in operando continuous-flow FTIR experiments. In all cases we observed a complete conversion into $[HFe(CO)_4]^-$ under water reduction conditions (Figure SI6 in the Supporting Information). The time needed for full conversion ranges between 1.5 h for $[Fe_3(CO)_{12}]$ and $[HNEt_3][HFe_3(CO)_{11}]$ and 12 min for $[Fe(CO)_5]$. In the case of $[Fe(CO)_5]$, transformation even partly occurs in the dark, which conforms to the water gas shift reaction.[14]

Note that after the preformation reactions, $[HFe(CO)_4]^-$ is the only observable catalyst intermediate during water reduction. To exclude these preformation reactions, $[NEt_4][HFe(CO)_4]$ was directly applied as the WRC precursor in the following kinetic experiments.

Rate-limiting step and loss channels

As seen in Scheme 1, the photocatalytic water reduction system consists of two catalytic subcycles: the IrPS subcycle and the WRC subcycle. To determine which one is rate-limiting, the initial concentration of each catalyst was varied in kinetic experiments. First, the WRC was brought into focus by varying the initial concentration of $[NEt_4][HFe(CO)_4]$ from 0.12 to 0.45 mmol L^{-1}, while the concentration of IrPS was kept constant at 0.62 mmol L^{-1}. Experiments show that within the chosen concentration range, increasing amounts of WRC do not affect the initial hydrogen evolution rate, which does not exceed a value of 10.8 mL h^{-1} (Figure 5). The zeroth reaction

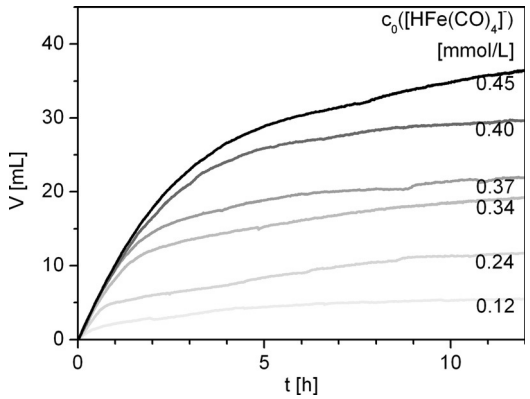

Figure 5. Hydrogen evolution curves for different initial WRC concentrations in the water reduction experiments. Conditions: 12.5 μmol of IrPS, 2.4 to 9.0 μmol of $[NEt_4][HFe(CO)_4]$, 20 mL of THF/TEA/H_2O 4:1:1, visible light (1.5 W), 25 °C.

order shows that the major rate-limiting step of the whole catalytic system is independent of the WRC. Apart from that, it is shown that the overall hydrogen yield grows significantly and, thus, the system's stability improves by applying higher amounts of WRC (for TONs, see Figure SI8 and Table SI2 in the Supporting Information).

Next, the IrPS subcycle was analyzed. Kinetic experiments with an initial concentration of IrPS in the range from 0.01 to 1.25 mmol L^{-1} and a constant WRC concentration of 0.40 mmol L^{-1} were performed. The experiments showed an increasing initial hydrogen evolution rate with increasing amounts of IrPS (Figure 6a). Between 0.01 and 0.08 mmol L^{-1}, a linear dependence on IrPS is found, which shows a pseudo-

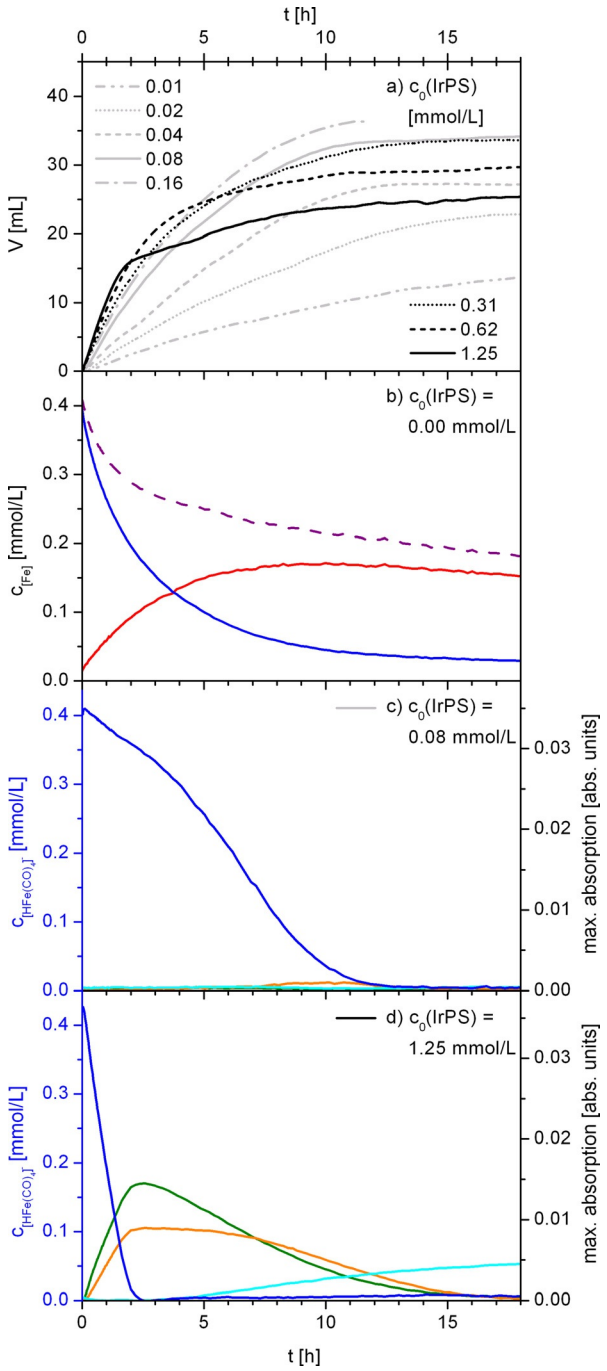

Figure 6. Hydrogen evolution curves (a) and concentration ($c\times$(number of Fe per molecule)/absorption curves (b, c, d) of experiments with varying initial concentrations of IrPS. Iron carbonyl species: $[HFe(CO)_4]^-$ (blue), $[Fe(CO)_3(bpy)]$ (green), **y** (orange), **z** (cyan), $[HFe_3(CO)_{11}]^-$ (red); 3·$[HFe_3(CO)_{11}]^-$ + $[HFe(CO)_4]^-$ (dashed violet). Conditions: 0.0 (b), 1.6 (c), or 25.0 μmol (d) of IrPS, 8.0 μmol of $[NEt_4][HFe(CO)_4]$, 20 mL of THF/TEA/H_2O 4:1:1, visible light (1.5 W), 25 °C.

first-order behavior with respect to the IrPS (Figure SI11 in the Supporting Information). In this range, the experimental results are congruent with the findings of Neubauer et al.[8] They exclusively investigated the IrPS subcycle by theoretical methods and photoluminescence spectroscopy at a IrPS concentration of 0.013 mmol L^{-1} and found the quenching of the excited IrPS by TEA to be the rate-limiting step. Considering the results of this work, it can be concluded that this process is the rate-limiting step of the whole system. However, for IrPS amounts higher than 0.08 mmol L^{-1}, we observed deviations from pseudo-first-order kinetics (Figure SI12 and Table SI3 in the Supporting Information). The reason for this may be the solution's increased light absorption at a concentration range in which the Lambert–Beer law is not valid anymore.

At low IrPS concentrations, from 0.01 to 0.16 mmol L^{-1} (Figure 6a, grey curves), an increasing hydrogen yield is observed and $[HFe(CO)_4]^-$ is the only IR-active species observed throughout the whole reaction (Figure 6c). At these conditions, the decomposition of $[HFe(CO)_4]^-$ is considered to be partly induced by light irradiation, which causes CO dissociation from the metal center[15] and leads to IR-inactive decomposition products.

To study the WRC behavior independently from the IrPS, $[NEt_4][HFe(CO)_4]$ was dissolved in the THF/TEA/H_2O mixture. In the dark, this solution is stable for at least 20 h. Irradiation of this solution initiates the formation of $[HFe_3(CO)_{11}]^-$ from the monomeric anion (Figure 6b). Note that with $[NEt_4][HFe(CO)_4]$ as the WRC precursor, the trimeric species is only observable in the absence of IrPS. The presence of even small amounts of IrPS results in a fragmentation of the trimers , which again leads to $[HFe(CO)_4]^-$ as the only observable complex (Figure 6c). The overall iron concentration curve in the absence of IrPS (Figure 6b, dashed violet) still differs from the $[HFe(CO)_4]^-$ concentration curve in the case of low IrPS concentration (Figure 6c, blue). This implies an additional loss channel within the catalytic cycle.

At high IrPS concentrations, from 0.16 to 1.25 mmol L^{-1} (Figure 6a, black curves), the decomposition of $[HFe(CO)_4]^-$ is even more accelerated by increasing amounts of IrPS. When $[HFe(CO)_4]^-$ disappears, the hydrogen evolution rate decreases dramatically. For the highest IrPS concentration, this happens after 2 h (Figure 6d). In that time, $[HFe(CO)_4]^-$ is mainly converted into $[Fe(bpy)(CO)_3]$ (1972.5 (s), 1890 (s) cm^{-1}; Figure 7, green spectrum) and the unidentified species **y** (1965 (m), 1883 (s) cm^{-1}; Figure 7, orange spectrum). Both show a considerably lower activity. In a consecutive reaction, the iron complex **z** is formed (2033.5 (w), 1989.5 (s), 1892(w) cm^{-1}; Figure 7, cyan spectrum), which does not show any catalytic activity. The accelerated decomposition of $[HFe(CO)_4]^-$ at these high IrPS concentrations leads to a declining overall hydrogen yield (Figure 6a, black curves) and can be attributed to the destruction of the IrPS and a transfer of the bipyridine ligand from the IrPS to the iron center of the WRC. This is supported by a study by Bernhard and co-workers.[16] They observed a loss of the bpy ligands from the IrPS to form $[Ir(ppy)_2]^+$. Furthermore, the formation and assignment of $[Fe(bpy)(CO)_3]$ is supported by spectroscopic data[17] (Table SI5 in the Supporting Information) and DFT frequency calculations (Figure 7, calculated spectrum, dashed green).

The catalytically active complex

$[HFe(CO)_4]^-$ cannot be the catalytically active complex as its reduction potential (−1.98 V[18]) is too low for it to be reduced

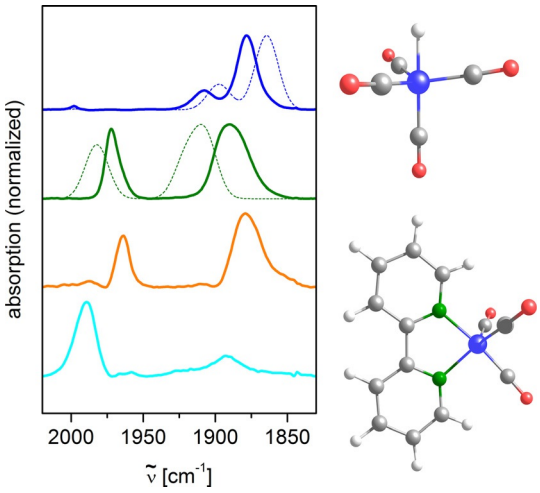

Figure 7. Extracted experimental (solid) and calculated (dashed) pure component spectra and calculated structures of species observed during photocatalytic water reduction when applying $[NEt_4][HFe(CO)_4]$ as the WRC. Species: $[HFe(CO)_4]^-$ (blue, top structure), $[Fe(bpy)(CO)_3]$ (green, bottom structure), **y** (orange), **z** (cyan).

by the IrPS (reduction potential −1.38 V[19]). Instead, it can be considered to be the resting state of the catalytically active complex.

Irradiating a $[HFe(CO)_4]^-$ solution without IrPS results in the formation of dimers and trimers. Experiments show that these species are highly reactive towards the reduced IrPS. As observed by IR spectroscopy, they are rapidly reduced and converted into $[HFe(CO)_4]^-$ under water reduction conditions (Figure SI14 in the Supporting Information) and possibly remain present in amounts below the detection limit.

This first electron transfer onto the WRC is a crucial reaction step for the catalytically active species and was further investigated by computational studies of IrPS···WRC complexes with $[HFe(CO)_4]^-$, $[HFe_2(CO)_8]^-$, and $[HFe_3(CO)_{11}]^-$ as the WRC. Binding energies and probabilities of charge transfer (CT) have been calculated for all configurations of the IrPS···WRC complexes with a Ir···WRC-center distance of 10 Å (Figure 8). The binding maps of IrPS with the three iron carbonyl catalysts have maxima or minima at the ligand positions. For the monomer and dimer, the points indicating the catalyst position near the ligand correspond to attractive regions with binding energies up to −0.08 eV for the monomer and −0.12 eV for the dimer; the cavities between ligands provide unbound regions. In contrast, for the trimer, the binding energies in the cavities reach values up to −0.17 eV, whereas the other areas are repelling as a result of the larger size of the iron complex. The probability of CT from the IrPS to the WRC has been evaluated on the basis of TD-DFT calculations of the lowest doublet excited states. The spin-density of the IrPS···WRC complex in the ground doublet state is always located on the π_1*(bpy) orbitals, pointing to no CT without irradiation.

If we compare the probability of electron transfer from IrPS to the Fe catalyst, the WRCs can be organized by their increasing photoactivity: $[HFe(CO)_4]^-$ (0%) < $[HFe_2(CO)_8]^-$ (5.3%) < $[HFe_3(CO)_{11}]^-$ (18%), where the percentage of points where the first excited state is of long-range CT nature is given in parenthesis. In addition, if we consider the trimer placed on a sphere of 11 Å (Figure SI16 in the Supporting Information),

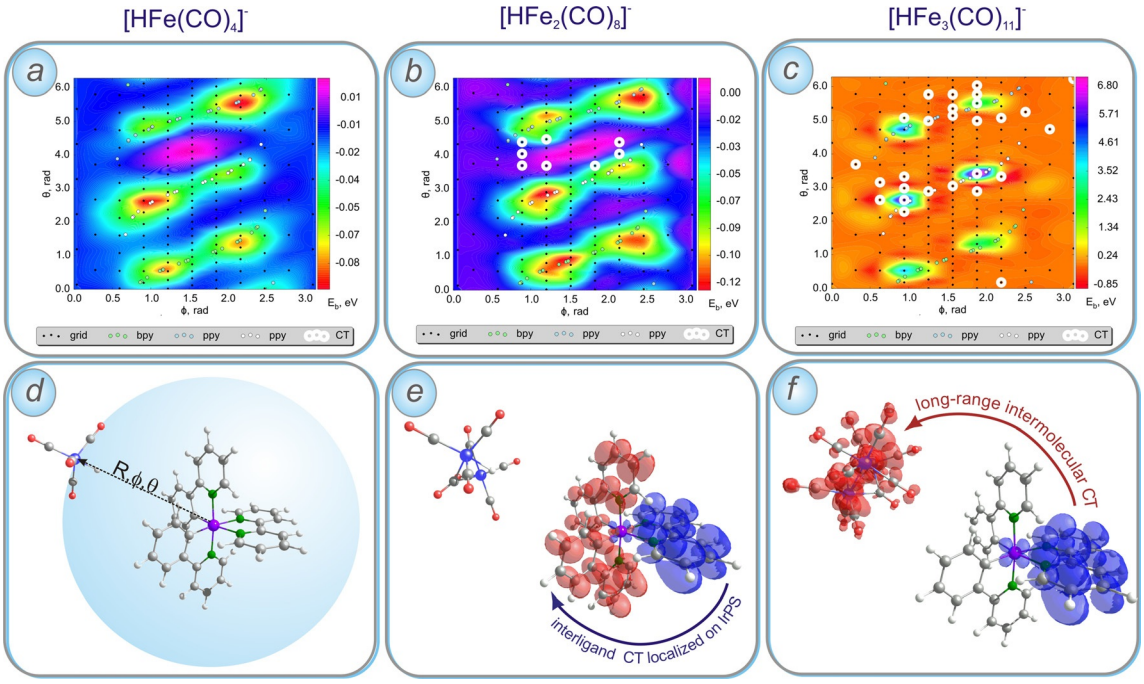

Figure 8. Calculated binding energies and charge-transfer configurations (white hollow circles) of IrPS···WRC complexes (a, b, and c); the WRC is located on a sphere around the IrPS at the distance $R = 10$ Å, as shown in (d) for the example of WRC = $[HFe(CO)_4]^-$. The projections of atoms of the bpy and ppy ligands onto the sphere are also given. (e) and (f) Examples of transition density differences for IrPS-localized and intermolecular transitions are shown. Blue and red colors indicate regions of electron loss and gain, respectively.

the repelling areas near the ligand positions disappear and the binding map is similar to those of the monomer and dimer at a distance of $R = 10$ Å. However, increasing the distance between IrPS and $[HFe_3(CO)_{11}]^-$ leads to a decreasing number of points where CT is the first excited state, from 18 to 5.3%, which is again similar to the dimer case. Note that despite the absence of CT-favorable points in the case of the monomer, the reaction could nevertheless take place because higher excited states can be involved or the reaction can be assisted by direct solvent complexation as proposed in previous work.[6b] For the monomer placed on a sphere of 7 Å, the percentage of favorable combinations (15%) is comparable with that of the trimer. However, a situation in which the WRC comes very close to IrPS, "pushing aside" the solvent molecules, can hardly be achieved.

These results confirm that the active complex can only be a dimeric or trimeric iron carbonyl species. DFT calculations predict negative values for the changes in the Gibbs free energy (ΔG) for all steps in a water reduction catalytic subcycle (Figure 9) starting with $[HFe_3(CO)_{11}]^-$. This shows that the trimeric species can be considered to be a catalytically active complex.[6b,9] Fragmentation into the dimer $[Fe_2(CO)_8]^{\bullet-}$ and monomer $[HFe(CO)_4]^-$ can occur after the first reduction step. The small negative ΔG value for this process suggests that the fragmentation products are thermodynamically favored. Subsequently, $[Fe_2(CO)_8]^{\bullet-}$ can be further reduced and converted into the resting state, $[HFe(CO)_4]^-$, as shown experimentally (Figure SI14 in the Supporting Information).

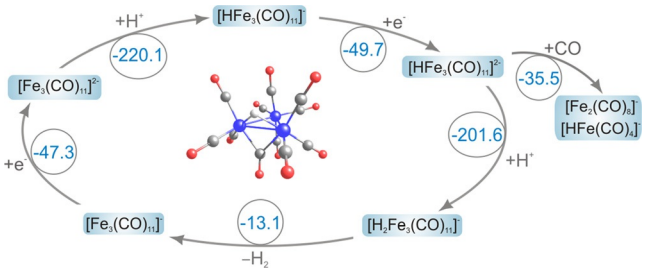

Figure 9. Evolution of $[HFe_3(CO)_{11}]^-$ in THF solution in the course of catalysis as predicted theoretically. The scheme does not consider a particular source of free electrons. For all reactions, the corresponding change in Gibbs free energy, ΔG (in kcal mol^{-1}), is provided by the numbers in the circles. Inset: the structure of $[HFe_3(CO)_{11}]^-$.

Conclusions

In this work, the mechanistic understanding of the WRC cycle in the photocatalytic water reduction system has been further improved. The emerging picture is summarized in Scheme 2.

By means of stopped-flow rapid-scan FTIR spectroscopy, transformation processes of the precursor $[Fe_3(CO)_{12}]$ in the dark, in the solvent mixture of THF/TEA/H_2O has been quantitatively determined. Owing to reduction by TEA, the unstable radical $[Fe_3(CO)_{12}]^{\bullet-}$ is formed and rapidly converted in a pseudo-first-order reaction ($k_{25\,°C} = 0.038$ s^{-1}) into a mixture of $[Fe_3(CO)_{11}]^{\bullet-}$, $[Fe_2(CO)_8]^{\bullet-}$, and $[Fe(CO)_5]$.

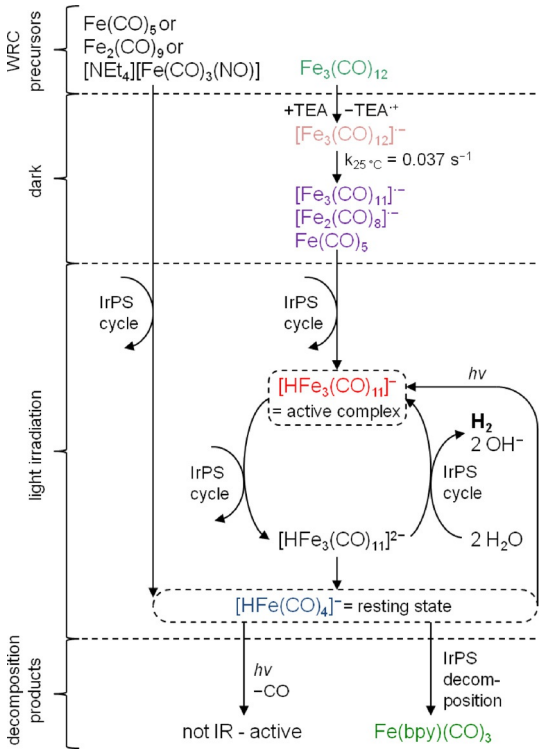

Scheme 2. Transformation and deactivation processes of the WRC in the absence of light and during photocatalytic water reduction.

By using operando continuous-flow FTIR spectroscopy, the WRC species present under water reduction conditions have been identified and their catalytic role and decomposition processes have been elucidated. By adding IrPS and irradiation of the reaction mixture, all the iron carbonyls originating from $[Fe_3(CO)_{12}]$ are converted into $[HFe_3(CO)_{11}]^-$, which in turn is transformed into $[HFe(CO)_4]^-$. The latter conversion proceeds completely only at relatively high water concentrations such as in a THF/TEA/H_2O mixture with a ratio of 4:1:1. The exclusive formation of $[HFe(CO)_4]^-$ also takes place if other WRC precursors such as $[Fe_2(CO)_9]$, $[Fe(CO)_5]$, or $[NEt_4][Fe(NO)(CO)_3]$ are applied. Remarkably, hydrogen evolution can only be observed as long as $[HFe(CO)_4]^-$ is present in solution, a species that is decomposed over the reaction time, partly as a result of light-induced CO dissociation. However, this species can only be considered to be the resting state of the catalytically active water reduction complex as its electrochemical potential is too low to allow an electron transfer from the IrPS.[6b]

Kinetic experiments showed that the WRC is not involved in the system's rate-limiting step. Thus, an increase in the initial concentration of the precursor $[NEt_4][HFe(CO)_4]$ does not lead to an enhanced hydrogen evolution rate, but to a higher hydrogen yield, owing to the larger WRC reservoir. If the concentration of the IrPS is increased, the initial hydrogen evolution rate rises. As first-order kinetics with respect to the IrPS were found for IrPS concentrations between 0.01 and 0.08 mmol L^{-1}, the quenching of the excited IrPS by TEA can be considered to be the rate-limiting step of the overall system, as also found by Neubauer et al. for the IrPS subcycle.[8] However, with in-

creasing initial IrPS concentration, the hydrogen yield passes through a maximum at 0.16 mmol L^{-1} ($TON_{[Fe]} = 186$) and decreases at very high concentrations of IrPS. The accelerated deactivation of the catalytic system at these high IrPS concentrations is due to the bpy ligand transfer from the IrPS onto $[HFe(CO)_4]^-$, resulting in the much less active $[Fe(bpy)(CO)_3]$.

TD-DFT calculations show that charge transfer from the IrPS to the WRC is only possible for dimeric or trimeric iron species. As calculated, $[HFe_3(CO)_{11}]^-$ is theoretically able to run a WRC subcycle as the catalytically active complex, producing hydrogen or decomposing into the resting state $[HFe(CO)_4]^-$ and $[Fe_2(CO)_8]^{\bullet-}$ after the first reduction step. The latter species can also be reduced and converted subsequently to form $[HFe(CO)_4]^-$ as shown experimentally. Finally, the resulting resting state, $[HFe(CO)_4]^-$, can be considered as a WRC reservoir to continuously produce the catalytically active dimeric and trimeric species upon light irradiation, which is observed in experiments without IrPS.

Concluding, the photocatalytic system with simple iron carbonyls as the WRC is very dynamic. For further improvement of the system, at least two directions should be explored: design of light-resistant trimeric or dimeric WRC compounds to increase the system's stability (e.g., addition of CO-substituting phosphine ligands[6b]) and improvement of the performance of the IrPS to enhance the system's activity. Furthermore, the ground, excited, and reduced states of the IrPS should be inert towards ligand dissociation (for example, see reference [20]) to allow reaction conditions with an excess of IrPS.

Experimental Section

All experiments were carried out in an argon atmosphere and under exclusion of air. Solvents were purified and degassed by standard procedures prior to use. The catalyst precursors were purchased from a commercial supplier (Sigma–Aldrich). $[Ir(bpy)(ppy)_2]PF_6$,[21] $[HNEt_3][HFe_3(CO)_{11}]$,[22] $[NEt_4][HFe(CO)_4]$,[13] and $[NEt_4][(NO)Fe(CO)_3]$[23] were synthesized according to literature procedures.

The time-resolved infrared experiments for the dark phase were carried out on a stopped-flow unit (TgK Scientific, UK) combined with a VERTEX 80 (Bruker) with rapid-scan extension. The solutions and the IR cell were thermostated to 25 °C. The IR cell has CaF_2 windows. The optical path length was specified by the supplier as 100 μm. The spectra (2 scans per spectrum) were taken with a resolution of 2 cm^{-1}. At a mirror velocity of 320 kHz, we were able to record an IR spectrum every 116 ms.

The experimental setup (Scheme SI1) for time-resolved operando continuous-flow FTIR experiments under light irradiation consists of a reaction vessel connected to a FTIR-spectrometer and to an automatic gas burette. Hence, this setup provides the tracking of gas evolution and the simultaneous acquisition of IR spectra and differs from the setup of the Beller group[6] only by the additional IR unit.

A mercury vapor lamp (LUMATEC) was attached to the double-walled thermostatically controlled reaction vessel at a fixed position by a fiber optic cable. This lamp emits visible light between 380 and 700 nm. The reaction solution was stirred by a magnetic stirrer at constant and reproducible speed and was continuously circulated by a microannular gear pump (HNP) through the thermostated measuring cell of the IR spectrometer. The cell was equipped with CaF_2 windows and has an optical path length of 100 μm. The FTIR measurements were carried out with a Bruker Tensor 27 spectrometer with a mercury–cadmium–telluride (MCT) detector. Tracking of gas evolution was realized by an automatic gas burette (MESSEN NORD). Its temperature was kept constant at 25 °C. A condenser was installed in between the reaction vessel and the gas burette and operated at 5 °C to retain volatile solvent.[24]

A typical experiment was carried out as follows: the whole apparatus was evacuated and purged with argon five times to provide oxygen-free conditions. The reaction vessel was filled with 20 mL of solvent. After temperature adjustment, an IR spectrum was taken and used as the background. The solid catalysts were added to the system. After reaching thermal equilibrium between the gas and condensed phases (10 min), the reaction was started by irradiating the solution (1500 mW). An IR spectrum with 20 scans was taken every 30 s. The monitored hydrogen evolution curve was corrected for the system's blind value, which was obtained in an experiment without catalysts.

The pure component spectra and the associated absorption and concentration profiles were extracted with an algorithm based on factor analysis.[25] In Figures 2, 4, and 6b, the concentrations of the complexes were multiplied by the number of their iron atoms to facilitate identification of conversion processes. This is indicated with the entry "$c\times$(number of Fe per molecule)". In Figure 6c and 6d, the absorption curves indicate the maximum of each species' absorption spectrum as a function of time.

Theoretical methods

Quantum chemical calculations have been performed with (TD)-DFT by using the long-range corrected density functional approach (LC-BLYP) to correctly account for charge-transfer excitations.[26] This approach has previously been used to investigate the vertical excitation energies of the bare IrPS[27] and it was applied further to describe other steps of the photocatalytic cycle.[28] An important aspect concerns the choice of the so-called range separation parameter, ω, which defines the switching between short- and long-range parts in the exchange-correlation potential. Following the strategy put forward in Ref. [29], this parameter was tuned such as to guarantee the fulfilment of Koopmans' theorem; the details can be found in a separate publication.[30] The value $\omega = 0.18$ $bohr^{-1}$ has been applied for all calculations.

Numerical calculations and frequency calculations were performed by using the Gaussian 09[31] program with the LANL2DZ ECP[32] and basis set for Ir and Fe and the 6-31G(d)[33] basis set for all other atoms. For DFT/TD-DFT calculations, no symmetry restrictions were applied. The environment effects of THF solvent have been included through the Polarizible Continuum Model (IEFPCM).[34] Calculated IR bands were plotted with a half width of 8 cm^{-1} and harmonic IR frequencies were corrected by a scaling factor $f = 0.9795$, which was chosen to give best agreement of calculated with experimental data.

As no stable complexes between IrPS and WRC are supposed to be formed in solution, the binding energies and energies of the 10 lowest excited states have been calculated for 152 configurations for each WRC, similar to our previous study of interaction between IrPS and TEA.[8] The center of masses of the iron catalysts (M_c) were

placed on spherical grids around the IrPS. The relative orientation of iron catalyst towards the Ir–M_c axis was kept fixed; no geometry relaxation was included. The distance between Ir and M_c was 10 Å (Figure 9). For the monomeric WRC, this study was repeated for a distance of 7 Å (Figure SI13 in the Supporting Information); owing to steric hindrance, it was not done for the dimer and trimer forms.

Acknowledgements

This work has been partly supported by the BMBF within the project "Light2Hydrogen" (Spitzenforschung und Innovation in den Neuen Ländern), by the European Union (European Social Funds, ESF) within the project "PS4H" and by the Ministry for Education, Science and Culture of Mecklenburg-Vorpommern. We thank Matthias Beller, Henrik Junge, Felix Gärtner, Michael Karnahl, Nils Rockstroh, and Petra Bartels for providing chemicals and expertise, Fabio Ragaini for helpful hints, Peter Kumm and Martin Riedel for technical support, as well as Bastian Hoffmann for supporting the stopped-flow experiments.

Keywords: homogeneous catalysis · photocatalysis · proton reduction · time-resolved IR spectroscopy · water reduction

[1] a) S. Chu, H. Michel, H. Dotan, H. Mayes, S. Sheehan, *Nature* **2013**, *502*, S60 – S61; b) F. E. Osterloh, *J. Phys. Chem. Lett.* **2014**, *5*, 2510 – 2511.
[2] R. Eisenberg, *Science* **2009**, *324*, 44 – 45.
[3] Z. Han, R. Eisenberg, *Acc. Chem. Res.* **2014**, *47*, 2537 – 2544.
[4] J. Marshall, *Nature* **2014**, *510*, 22 – 24.
[5] P. Du, R. Eisenberg, *Energy Environ. Sci.* **2012**, *5*, 6012 – 6021.
[6] a) F. Gärtner, B. Sundararaju, A.-E. Surkus, A. Boddien, B. Loges, H. Junge, P. H. Dixneuf, M. Beller, *Angew. Chem. Int. Ed.* **2009**, *48*, 9962 – 9965; *Angew. Chem.* **2009**, *121*, 10147 – 10150; b) F. Gärtner, A. Boddien, E. Barsch, K. Fumino, S. Losse, H. Junge, D. Hollmann, A. Brückner, R. Ludwig, M. Beller, *Chem. Eur. J.* **2011**, *17*, 6425 – 6436.
[7] a) S.-P. Luo, E. Mejía, A. Friedrich, A. Pazidis, H. Junge, A.-E. Surkus, R. Jackstell, S. Denurra, S. Gladiali, S. Lochbrunner, M. Beller, *Angew. Chem. Int. Ed.* **2013**, *52*, 419 – 423; *Angew. Chem.* **2013**, *125*, 437 – 441; b) E. Mejía, S.-P. Luo, M. Karnahl, A. Friedrich, S. Tschierlei, A.-E. Surkus, H. Junge, S. Gladiali, S. Lochbrunner, M. Beller, *Chem. Eur. J.* **2013**, *19*, 15972 – 15978; c) S. Fischer, D. Hollmann, S. Tschierlei, M. Karnahl, N. Rockstroh, E. Barsch, P. Schwarzbach, S.-P. Luo, H. Junge, M. Beller, S. Lochbrunner, R. Ludwig, A. Brückner, *ACS Catal.* **2014**, *4*, 1845 – 1849.
[8] A. Neubauer, G. Grell, A. Friedrich, S. I. Bokarev, P. Schwarzbach, F. Gärtner, A.-E. Surkus, H. Junge, M. Beller, O. Kühn, S. Lochbrunner, *J. Phys. Chem. Lett.* **2014**, *5*, 1355 – 1360.
[9] D. Hollmann, F. Gärtner, R. Ludwig, E. Barsch, H. Junge, M. Blug, S. Hoch, M. Beller, A. Brückner, *Angew. Chem. Int. Ed.* **2011**, *50*, 10246 – 10250; *Angew. Chem.* **2011**, *123*, 10429 – 10433.
[10] a) Y. A. Belousov, T. A. Kolosova, V. N. Babin, *Polyhedron* **1989**, *8*, 603 – 611; b) Y. A. Belousov, T. A. Belousova, *Polyhedron* **1999**, *18*, 2605 – 2608; c) Y. A. Belousov, E. F. Brin, *Polyhedron* **2001**, *20*, 2765 – 2769; d) A. B. Yurii, *Russ. Chem. Rev.* **2007**, *76*, 41 – 58; e) P. J. Krusic, J. San Filippo, B. Hutchinson, R. L. Hance, L. M. Daniels, *J. Am. Chem. Soc.* **1981**, *103*, 2129 – 2131; f) P. J. Krusic, *J. Am. Chem. Soc.* **1981**, *103*, 2131 – 2133; g) F. Ragaini, D. L. Ramage, S. Song Jeong, G. L. Geoffroy, A. L. Rheingold, *J. Am. Chem. Soc.* **1993**, *115*, 12183 – 12184; h) F. Ragaini, *Organometallics* **1996**, *15*, 3572 – 3578.
[11] K. Farmery, M. Kilner, R. Greatrex, N. N. Greenwood, *J. Chem. Soc. A* **1969**, 2339 – 2345.
[12] M. Y. Darensbourg, D. J. Darensbourg, H. L. C. Barros, *Inorg. Chem.* **1978**, *17*, 297 – 301.
[13] I. Y. Guzman-Jimenez, J. W. van Hal, K. H. Whitmire, *Organometallics* **2003**, *22*, 1914 – 1922.
[14] R. G. Pearson, H. Mauermann, *J. Am. Chem. Soc.* **1982**, *104*, 500 – 504.
[15] a) M. Poliakoff, J. J. Turner, *J. Chem. Soc. Dalton Trans.* **1974**, 2276 – 2285; b) R. L. Whetten, K. J. Fu, E. R. Grant, *J. Chem. Phys.* **1983**, *79*, 4899 – 4911; c) P. J. Krusic, D. J. Jones, D. C. Roe, *Organometallics* **1986**, *5*, 456 – 460; d) L. Bañares, T. Baumert, M. Bergt, B. Kiefer, G. Gerber, *Chem. Phys. Lett.* **1997**, *267*, 141 – 148; e) L. Bañares, T. Baumert, M. Bergt, B. Kiefer, G. Gerber, *J. Chem. Phys.* **1998**, *108*, 5799 – 5811; f) P. Portius, J. Yang, X.-Z. Sun, D. C. Grills, P. Matousek, A. W. Parker, M. Towrie, M. W. George, *J. Am. Chem. Soc.* **2004**, *126*, 10713 – 10720.
[16] L. L. Tinker, N. D. McDaniel, P. N. Curtin, C. K. Smith, M. J. Ireland, S. Bernhard, *Chem. Eur. J.* **2007**, *13*, 8726 – 8732.
[17] a) M. DelaVarga, R. Costa, R. Reina, A. Núñez, M. Ángel Maestro, J. Mahía, *J. Organomet. Chem.* **2003**, *677*, 101 – 117; b) F. Calderazzo, S. Falaschi, F. Marchetti, G. Pampaloni, *J. Organomet. Chem.* **2002**, *662*, 137 – 143; c) H. K. van Dijk, D. J. Stufkens, A. Oskam, *J. Organomet. Chem.* **1988**, *340*, 227 – 238.
[18] A. M. Bond, P. A. Dawson, B. M. Peake, B. H. Robinson, J. Simpson, *Inorg. Chem.* **1977**, *16*, 2199 – 2206.
[19] J. I. Goldsmith, W. R. Hudson, M. S. Lowry, T. H. Anderson, S. Bernhard, *J. Am. Chem. Soc.* **2005**, *127*, 7502 – 7510.
[20] a) L. L. Tinker, S. Bernhard, *Inorg. Chem.* **2009**, *48*, 10507 – 10511; b) D. N. Chirdon, W. J. Transue, H. N. Kagalwala, A. Kaur, A. B. Maurer, T. Pintauer, S. Bernhard, *Inorg. Chem.* **2014**, *53*, 1487 – 1499.
[21] E. D. Cline, S. E. Adamson, S. Bernhard, *Inorg. Chem.* **2008**, *47*, 10378 – 10388.
[22] W. McFarlane, G. Wilkinson, W. Hübel, in *Inorganic Syntheses* (Ed.: H. F. Holtzlaw), Wiley, **2007**, pp. 181 – 183.
[23] B. Plietker, A. Dieskau, *Eur. J. Org. Chem.* **2009**, 775 – 787.
[24] a) B. Loges, H. Junge, B. Spilker, C. Fischer, M. Beller, *Chem. Ing. Tech.* **2007**, *79*, 741 – 753; b) A. Boddien, B. Loges, H. Junge, M. Beller, *ChemSusChem* **2008**, *1*, 751 – 758.
[25] K. Neymeyr, M. Sawall, D. Hess, *J. Chemom.* **2010**, *24*, 67 – 74.
[26] a) M. Chiba, T. Tsuneda, K. Hirao, *J. Chem. Phys.* **2006**, *124*, 144106; b) H. Iikura, T. Tsuneda, T. Yanai, K. Hirao, *J. Chem. Phys.* **2001**, *115*, 3540 – 3544; c) Y. Tawada, T. Tsuneda, S. Yanagisawa, T. Yanai, K. Hirao, *J. Chem. Phys.* **2004**, *120*, 8425 – 8433.
[27] S. I. Bokarev, O. S. Bokareva, O. Kühn, *J. Chem. Phys.* **2012**, *136*, 214305.
[28] a) S. I. Bokarev, D. Hollmann, A. Pazidis, A. Neubauer, J. Radnik, O. Kuhn, S. Lochbrunner, H. Junge, M. Beller, A. Bruckner, *Phys. Chem. Chem. Phys.* **2014**, *16*, 4789 – 4796; b) S. I. Bokarev, O. S. Bokareva, O. Kühn, *Coord. Chem. Rev.* **2015**, *304-305*, 133 – 145.
[29] T. Stein, L. Kronik, R. Baer, *J. Am. Chem. Soc.* **2009**, *131*, 2818 – 2820.
[30] O. S. Bokareva, G. Grell, S. I. Bokarev, O. Kühn, *J. Chem. Theory Comput.* **2015**, *11*, 1700 – 1709.
[31] Gaussian 09, revision D.01, M. J. Frisch, G. W. Trucks, H. B. Schlegel, G. E. Scuseria, M. A. Robb, J. R. Cheeseman, G. Scalmani, V. Barone, B. Mennucci, G. A. Petersson, H. Nakatsuji, M. Caricato, X. Li, H. P. Hratchian, A. F. Izmaylov, J. Bloino, G. Zheng, J. L. Sonnenberg, M. Hada, M. Ehara, K. Toyota, R. Fukuda, J. Hasegawa, M. Ishida, T. Nakajima, Y. Honda, O. Kitao, H. Nakai, T. Vreven, J. A. Montgomery Jr., J. E. Peralta, F. Ogliaro, M. J. Bearpark, J. Heyd, E. N. Brothers, K. N. Kudin, V. N. Staroverov, R. Kobayashi, J. Normand, K. Raghavachari, A. P. Rendell, J. C. Burant, S. S. Iyengar, J. Tomasi, M. Cossi, N. Rega, N. J. Millam, M. Klene, J. E. Knox, J. B. Cross, V. Bakken, C. Adamo, J. Jaramillo, R. Gomperts, R. E. Stratmann, O. Yazyev, A. J. Austin, R. Cammi, C. Pomelli, J. W. Ochterski, R. L. Martin, K. Morokuma, V. G. Zakrzewski, G. A. Voth, P. Salvador, J. J. Dannenberg, S. Dapprich, A. D. Daniels, Ö. Farkas, J. B. Foresman, J. V. Ortiz, J. Cioslowski, D. J. Fox, Gaussian, Inc., Wallingford, CT, USA, **2013**.
[32] P. J. Hay, W. R. Wadt, *J. Chem. Phys.* **1985**, *82*, 270 – 283.
[33] a) W. J. Hehre, R. Ditchfield, J. A. Pople, *J. Chem. Phys.* **1972**, *56*, 2257 – 2261; b) P. C. Hariharan, J. A. Pople, *Theor. Chim. Acta* **1973**, *28*, 213 – 222.
[34] J. Tomasi, B. Mennucci, R. Cammi, *Chem. Rev.* **2005**, *105*, 2999 – 3094.

Received: August 5, 2015
Revised: September 11, 2015
Published online on November 3, 2015

6.2 Diferrate $[Fe_2(CO)_6(\mu\text{-}CO)(\mu\text{-}P(aryl)_2)]^-$ as Self-Assembling Iron/Phosphor Based Catalyst for the Hydrogen Evolution Reaction in Photocatalytic Proton Reduction – Spectroscopic Insights

Steffen Fischer, Arend Rösel, Matthias Bauer, Anja Kammer, Enrico Barsch, Roland Schoch, Henrik Junge, Matthias Beller and Ralf Ludwig

Full Paper: *Chem. Eur. J.*, **2018**, *24* (60), 16052-16065
DOI: 10.1002/chem.201802694

Shortened Abstract

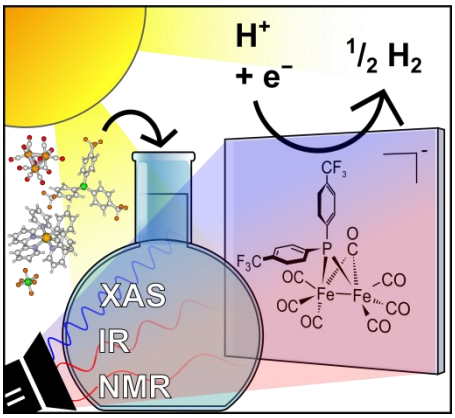

In this mechanistic study, Fischer et al. identified catalytically relevant key species in photocatalytic proton reduction through an iron carbonyl catalyst, an electronic withdrawing phosphine co-catalyst and an iridium dye. By means of operando FTIR, NMR and XAS spectroscopy, the sulfur free [FeFe]-Hydrogenase active site mimic $[Fe_2(CO)_6(\mu\text{-}CO)(\mu\text{-}P(aryl)_2)]^-$ was found to self assemble and to show good catalytic performance depending on the applied phosphine. The authors specified reaction conditions necessary for catalyst formation and deactivation mechanisms, thus providing a deeper understanding of the system for improvements in future applications.

Contribution to this Work (50%)

Steffen Fischer designed and carried out all NMR and operando continuous flow FTIR experiments as well as DFT calculations. He analyzed the spectroscopic data and identified all iron phosphides mentioned in this work. Further, he investigated the requirements for formation and activity of the diferrate $[Fe_2(CO)_6(\mu\text{-}CO)(\mu\text{-}P(aryl)_2)]^-$ and studied the deactivation mechanism of the system. He was involved in the synthesis and performance experiments of the molecularly defined $[NEt_4][Fe_2(CO)_6(\mu\text{-}CO)(\mu\text{-}P(aryl)_2)]$ catalysts. Steffen Fischer was also involved in design and implementation of the XAS experiments as well as in design and data analysis of the cyclic voltammetry measurements. He formed the concept of this work, led the discussion of the experimental results, and wrote the manuscript. The overall contribution is about 50%.

ChemPubSoc Europe

DOI: 10.1002/chem.201802694

CHEMISTRY A European Journal Full Paper

Photocatalytic Proton Reduction |Hot Paper|

Diferrate $[Fe_2(CO)_6(\mu\text{-}CO)\{\mu\text{-}P(aryl)_2\}]^-$ as Self-Assembling Iron/Phosphor-Based Catalyst for the Hydrogen Evolution Reaction in Photocatalytic Proton Reduction—Spectroscopic Insights

Steffen Fischer,[a, b] Arend Rösel,[a] Anja Kammer,[c] Enrico Barsch,[a] Roland Schoch,[d] Henrik Junge,[c] Matthias Bauer,[d] Matthias Beller,[c] and Ralf Ludwig*[a, b, c]

Abstract: This work is focused on the identification and investigation of the catalytically relevant key iron species in a photocatalytic proton reduction system described by Beller and co-workers. The system is driven by visible light and consists of the low-cost $[Fe_3(CO)_{12}]$ as catalyst precursor, electron-poor phosphines $P(R)_3$ as co-catalysts, and a standard iridium-based photosensitizer dissolved in a mixture of THF, water, and the sacrificial reagent triethylamine. The catalytic reaction system was investigated by operando continuous-flow FTIR spectroscopy coupled with H_2 gas volumetry, as well as by X-ray absorption spectroscopy, NMR spectroscopy, DFT calculations, and cyclic voltammetry. Several iron carbonyl species were identified, all of which emerge throughout the catalytic process. Depending on the applied $P(R)_3$, the iron carbonyl species were finally converted into $[Fe_2(CO)_6(\mu\text{-}CO)\{\mu\text{-}P(R)_2\}]^-$. This involves a P–C cleavage reaction. The requirements of $P(R)_3$ and the necessary reaction conditions are specified. $[Fe_2(CO)_6(\mu\text{-}CO)\{\mu\text{-}P(R)_2\}]^-$ represents a self-assembling, sulfur-free [FeFe]-hydrogenase active-site mimic and shows good catalytic activity if the substituent R is electron poor. Deactivation mechanisms have also been investigated, for example, the decomposition of the photosensitizer or processes observed in the case of excessive amounts of $P(R)_3$. $[Fe_2(CO)_6(\mu\text{-}CO)\{\mu\text{-}P(R)_2\}]^-$ has potential for future applications.

Introduction

The use of sunlight, more precisely, the storage of solar energy in the form of chemical energy carriers, represents one of the most promising options to approach current energy challenges.[1] Photocatalytic water splitting into oxygen and energy-containing hydrogen is very suitable for this purpose. Its two half-reactions, water oxidation and water reduction, are mostly studied separately. This allows for simplification of the system and facilitates a detailed understanding, which is beneficial for further improvements.[2] The photocatalytic water reduction reaction requires the application of a sacrificial reagent (SR) as electron donor. Furthermore, a light-harvesting and charge-separating photosensitizer (PS) is necessary. The PS transfers electrons to a catalyst, the proton reduction catalyst (also named as the water reduction catalyst), which combines them with protons from water to accomplish the hydrogen evolution reaction.[3] The catalyst is preferably made of abundant and low-cost metals, such as iron, cobalt, nickel, copper, or zinc, and must show long-term stability.[4] Molecular iron-based catalysts have mainly been inspired by the structure of the active site of [FeFe]-hydrogenase ([FeFe]-H_2ase;[5] (Figure 1, gray background), which has been the focus of numerous reviews.[2b,4d,6]

Embedded in a protein matrix, the diiron complex shows specific structure motifs, for example, terminal cyanide and carbonyl ligands as well as a bridging carbonyl and an azadithiolato ligand (adt^H). In adt^H, the nitrogen bridgehead acts as a pendant base and plays an important role in the biological catalytic cycle.

A successful [FeFe]-H_2ase active-site mimic applied in a photocatalytic water reduction reaction was introduced by Wang, Sun and co-workers.[7] They used $[Fe_2(adt^{Bz})(CO)_5\{P(Pyr)_3\}]$ (Pyr = *N*-pyrrolyl; Figure 1) as catalyst together with an iridium-based PS, $[Ir(bpy)(ppy)_2]PF_6$ (**Ir-PS**, bpy = 2,2′-bipyridine, ppy = 2-phenylpyridine; Figure 2), and triethylamine (TEA) as SR. The diiron complex achieved a turnover number (TON) of 466 molecules of H_2 per molecule of catalyst after 8 h of light irradiation.

[a] S. Fischer, A. Rösel, E. Barsch, Prof. Dr. R. Ludwig
Physical and Theoretical Chemistry Department
University of Rostock, Dr.-Lorenz-Weg 2, 18059 Rostock (Germany)
E-mail: ralf.ludwig@uni-rostock.de

[b] S. Fischer, Prof. Dr. R. Ludwig
Department of Life, Light & Matter, University of Rostock
Albert-Einstein-Straße 25, 18059 Rostock (Germany)

[c] A. Kammer, Dr. H. Junge, Prof. Dr. M. Beller, Prof. Dr. R. Ludwig
Leibniz-Institut für Katalyse e.V. (LIKAT Rostock)
Albert-Einstein-Straße 29a, 18059 Rostock (Germany)

[d] R. Schoch, Prof. Dr. M. Bauer
Department Chemie, Fakultät Naturwissenschaften
Paderborn University, Warburger Str. 100, 33098 Paderborn (Germany)

Supporting information and the ORCID identification number(s) for the author(s) of this article can be found under:
https://doi.org/10.1002/chem.201802694.

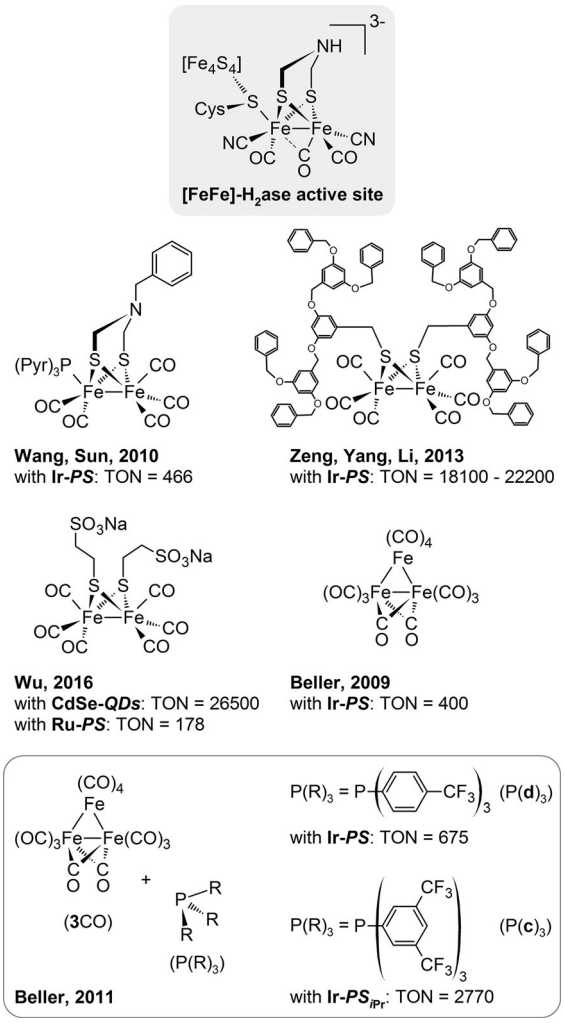

Figure 1. [FeFe]-H_2ase active-site structure and its mimics as catalysts in photocatalytic proton reduction.

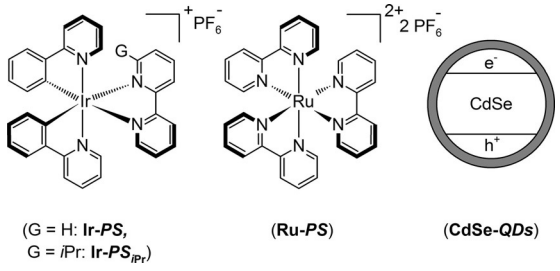

Figure 2. Photosensitizers employed in photocatalytic proton reduction.

Zeng, Yang, Li and co-workers employed the same PS and SR.[8] Concerning the catalyst, they made use of dendritic architectures that encapsulate the active-site model of the [FeFe]-H_2ase to mimic the protein matrix of the enzyme. For catalysts incorporating one to four dendrimer generations (as an example, the two-generation catalyst is depicted in Figure 1), TONs of 18100 to 22200 were observed. However, the system was only tested on a very small scale with 10 nM catalyst. Systems like these show that the nitrogen atom in the thiolate bridge of the catalyst is not indispensable, because abiological reaction mechanisms are also suitable for the reduction of protons.[6e]

With [FeFe]-H_2ase active-site mimics in combination with a different class of PS, namely quantum dots like CdTe, TONs of up to 52800 have been observed by Jian, Wu and co-workers.[9] The same group revealed that this high TON should mainly be attributed to the PS rather than the catalyst.[10] In fact, a similar system using $[Fe_2\{\mu\text{-}S(CH_2)_2SO_3Na\}_2(CO)_6]$ as catalyst (Figure 1) and ascorbic acid as SR showed a TON of 26500 if the quantum dot CdSe (Figure 2) was employed, but only a TON of 178 if a ruthenium-based PS $[Ru(bpy)_3][PF_6]_2$ (**Ru-PS**, Figure 2) was used, the latter belonging to the same class as **Ir-PS**.[11,12]

A thiolate-free photocatalytic system with a self-assembling catalyst was presented by Beller and co-workers.[13] This system consists of the **Ir-PS** and commercially available iron carbonyls such as $[Fe_3(CO)_{12}]$ (**3**CO) as catalyst precursor. Thus, time-consuming synthesis of the catalyst is avoided. The components are dissolved in a THF/TEA/H_2O mixture (4:1:1, v/v/v), and TEA again acts as the SR. After 6 h of irradiation by visible light, a TON of 400 was achieved. Extensive spectroscopic studies by our group and colleagues[14] revealed important mechanistic information, which will be summarized below.

The Beller system was later modified by the addition of specific electron-poor arylphosphines ($P(R)_3$) as co-catalysts (Figure 1, bottom).[14a] The addition of $P(C_6H_4\text{-}4\text{-}CF_3)_3$ ($P(\mathbf{d})_3$) led to an increased TON of approximately 50% up to 675 after 3 h. Under optimized reaction conditions and the application of $P[C_6H_4\text{-}3,5\text{-}(CF_3)_2]_3$ ($P(\mathbf{c})_3$) as co-catalyst, a TON of even 1610 was achieved after 24 h. Notably, the reaction can be driven by visible light only. This was shown by the application of 385 and 420 nm UV cutoff filters, which led to a decrease of the TON by not more than 5 and 10%, respectively, as compared with the measurements with unfiltered Xe light. Further improvement of the system was accomplished by use of an **Ir-PS** derivate with an isopropyl substituent (**Ir-PS**$_{iPr}$, Figure 2), which led to a final TON of 2770 after 20 h of irradiation with blue light (440 nm).[15]

Acknowledging these high TONs and taking into account the widely differing reaction scale or photosensitizer applied in the aforementioned systems, **3**CO together with $P(R)_3$ still represents an outstanding iron catalyst that combines easy access with a comparably high performance.

Du and Eisenberg highlighted the system of Beller and co-workers in a review and at the same time remarked on the obscurity of the role of phosphine.[4a] Moreover, it was not clear why phosphites or phosphines that differ from the above-mentioned do not enhance or even reduce the catalyst performance. Another unexplained issue is the decline in activity that was observed if the otherwise enhancing $P(\mathbf{d})_3$ was applied in amounts greater than one equivalent with respect to **3**CO.[14a]

In this work we have investigated these issues by monitoring the system by operando continuous-flow FTIR spectroscopy coupled with simultaneous measurement of the evolving H_2 volume. We therefore applied various types of $P(R)_3$ with

different electron-acceptor/donor properties, starting with the electron-poor $P(OPh)_3$ ($P(\mathbf{a})_3$) through to the electron-rich alkylphosphine $P(Bu)_3$ ($P(\mathbf{i})_3$; Table 1, first and second column). For the phosphine $P(\mathbf{d})_3$ we additionally performed a more detailed analysis by NMR spectroscopy, DFT calculations, and cyclic voltammetry. Furthermore, X-ray absorption spectroscopy (XAS) was carried out to substantiate our analysis. We start the following section by describing the species that emerge throughout the reaction if **3**CO and one equivalent of phosphine are applied. Subsequently, we present the results of our XAS study and specify the catalytic relevance of the identified species. At the end of this work, we discuss the deactivation processes of the system and illustrate the results of our electrochemistry experiments.

Results and Discussion

Emerging species due to the application of 3CO and one equivalent of phosphine

In the original phosphine-free system of Beller and co-workers, a preliminary reaction preceding light irradiation was observed: The moment the precursor $[Fe_3(CO)_{12}]$ (**3**CO) was dissolved in THF/TEA/H_2O, it started to convert within 2 min into a mixture of $[Fe_3(CO)_{11}]^{\bullet-}$, $[Fe_2(CO)_8]^{\bullet-}$, and $[Fe(CO)_5]$. This was caused by the presence of TEA and water and has been reported in our previous publications.[14b,d]

If the system was modified by the additional application of one of the phosphines $P(\mathbf{b})_3$, $P(\mathbf{d})_3$, $P(\mathbf{e})_3$, $P(\mathbf{f})_3$, $P(\mathbf{h})_3$, or $P(\mathbf{i})_3$ (Table 1), the same conversion reaction of **3**CO took place, but additionally a further species emerged, identified as $[Fe(CO)_4\{P(R)_3\}]$ (**1**$P(R)_3$; see Figure SI1 in the Supporting Information). The assignment of **1**$P(R)_3$ was supported by ^{31}P NMR analysis of a solution of **3**CO with one equivalent of $P(\mathbf{d})_3$ in THF/TEA/H_2O (4:1:1). The spectrum shows a singlet at $\delta =$ 76.1 ppm, which is in good agreement with the signal for **1**$P(\mathbf{d})_3$ reported by Howell et al.[16] at $\delta = 78.8$ ppm in $CDCl_3$.[17] Noteworthy, the phosphine ligand coordinates quantitatively to iron, because no signal is found for free $P(\mathbf{d})_3$ at $\delta =$ −5.6 ppm (see Figure SI2 in the Supporting Information).

The conversion of **3**CO and $P(R)_3$ into **1**$P(R)_3$ has already been reported to occur under significantly harsher conditions.[18] However, in these reports it was proposed to be initiated by CO loss from **3**CO[18c] and the formation of radicals,[19] as is also the case in the reaction presented here (see above).

Complexes **1**$P(R)_3$ were not formed when $P(\mathbf{a})_3$, $P(\mathbf{c})_3$, or $P(\mathbf{g})_3$ were applied. This might be explained by steric hindrance due to the wide cone angles of the phosphines (Table 1, second column). Although this argument holds for $P(\mathbf{a})_3$ and $P(\mathbf{g})_3$, this is not necessarily the case for $P(\mathbf{c})_3$, because this phosphine has a cone angle similar to those of $P(\mathbf{d})_3$ and $P(\mathbf{e})_3$, as reported by Howell et al.[16]

In the next step of the catalytic reaction, hydrogen gas was generated following the addition of the **Ir-PS** and initiation by light irradiation.[20] Our previous studies revealed that the **Ir-PS** is excited by light and reductively quenched by TEA. The decomposition of the latter gives rise to acetaldehyde, which shows an IR contribution at 1724 cm^{-1} (see Scheme SI2 in the Supporting Information).[14a–c]

Subsequently, the iron carbonyls $[Fe_3(CO)_{11}]^{\bullet-}$, $[Fe_2(CO)_8]^{\bullet-}$, and $[Fe(CO)_5]$ were converted into the hydride species $[HFe_3(CO_{11})]^-$ (H**3**$^-$) and $[HFe(CO)_4]^-$ (H**1**$^-$) within 1 min, due to electron transfer from the reduced **Ir-PS** and reaction with water (Figure 3, right).[14a,d] This happened in the phosphine-free as well as the phosphine-containing systems, as proven by IR spectroscopy. The resulting spectra (Figure 3, left, a and b, spectra at $t = 2$ min) show contributions of H**3**$^-$ at 2064 (vw), 1999 (s), 1993 (s), 1975 (m), 1953 (w), and 1941 cm^{-1} (w; Figure 3, middle, red spectrum) together with contributions of H**1**$^-$ at 1998 (w), 1908 (m), and 1878 cm^{-1} (s; Figure 3, middle, blue spectrum).

Because **1**$P(R)_3$ remains in solution during the beginning of the reaction of the phosphine containing system, its pure IR spectrum could be revealed by subtracting the pure spectra of the known compounds from the sum spectrum. The resulting spectrum of the observed **1**$P(R)_3$ species (e.g., **1**$P(\mathbf{d})_3$, Figure 3, middle, green spectrum) consists of three bands and shows the IR profile of the well-reported **1**$P(\mathbf{e})_3$.[21] This profile is shifted to higher or lower wavenumbers depending on the electron-acceptor/donor ability of the respective substituent R in the applied phosphine. The wavenumbers are listed in Table 1 and are in good agreement with literature values[16,18a,19,21c,22] (for direct comparison with the literature, see Table SI1 in the Supporting Information).

In the case of the application of $P(\mathbf{c})_3$, $P(\mathbf{d})_3$, $P(\mathbf{e})_3$, and $P(\mathbf{f})_3$, all the iron material was further converted into another iron phosphide species, which was identified as the diferrate $[Fe_2(CO)_6(\mu\text{-}CO)\{\mu\text{-}P(R)_2\}]^-$ (**2**$COP(R)_2^-$) and contains one bridging and six terminal CO ligands as well as one bridging phosphido ligand (Figure 3, right, violet-labeled structure). The complex shows four characteristic IR bands, which emerge during the catalytic process in the spectral region of the terminal carbonyl groups (e.g., R = **d** Figure 3, left, b, spectrum at $t = 20$ h). The contribution of the bridging carbonyl ligand cannot be detected because it overlaps with the broad and intense band of acetaldehyde, the decomposition product of TEA.

The wavenumbers of the bands observed for each **2**$COP(R)_2^-$ complex are listed in Table 1. Again, they are shifted depending on the electron-acceptor/donor ability of R. For **2**$COP(\mathbf{e})_2^-$, the experimental wavenumbers of this work match with the IR data reported in the literature.[22d,24] **2**$COP(\mathbf{e})_2^-$ was first described by Osterloh[25] and is the only one of the **2**$COP(R)_2^-$ compounds reported here that had been characterized[26] prior to this work (see Table SI2 in the Supporting Information). We further confirmed the assignment of **2**$COP(R)_2^-$ by DFT calculations of the IR spectra (see Figure SI12 in the Supporting Information) and synthesis of the pre-formed complexes $[NEt_4][\mathbf{2}COP(\mathbf{c})_2]$, $[NEt_4][\mathbf{2}COP(\mathbf{d})_2]$, $[NEt_4][\mathbf{2}COP(\mathbf{e})_2]$, and $[NEt_4][\mathbf{2}COP(\mathbf{f})_2]$. The IR spectra of these synthesized compounds (e.g., $[NEt_4][\mathbf{2}COP(\mathbf{d})_2]$, Figure 3, middle, violet) equal the corresponding in situ spectra observed in the catalytic process of the phosphine-containing system. Furthermore, they include the band of the bridging carbonyl[14b] (see Figure SI10 in the Supporting Information).

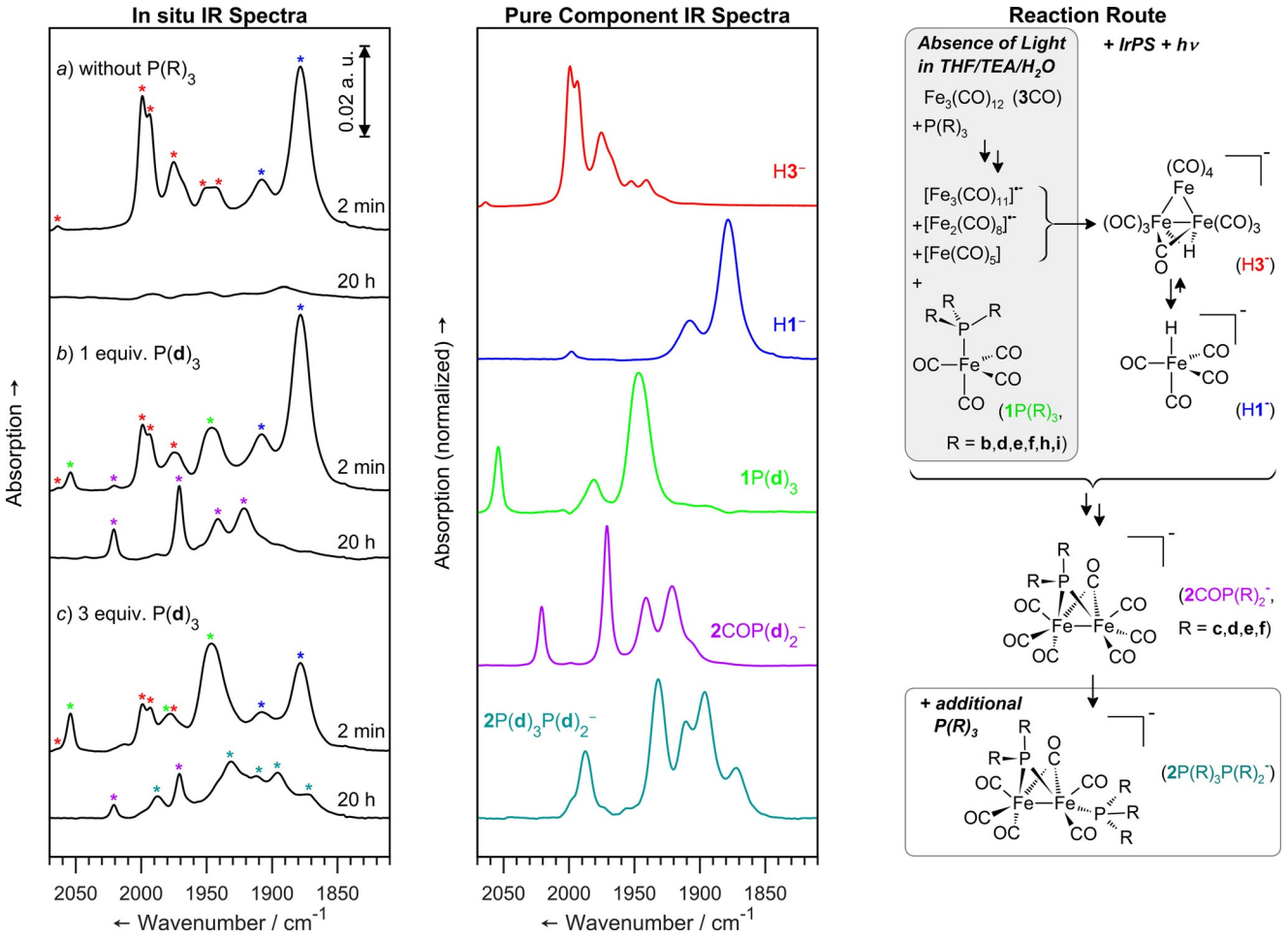

Figure 3. Left: In situ IR spectra of the reaction solution of a) the phosphine-free system with **3**CO as catalyst precursor, b) the phosphine-containing system with **3**CO and one equivalent of co-catalyst P(**d**)$_3$, and c) the phosphine-containing system with **3**CO and three equivalents of P(**d**)$_3$. For all three cases, two spectra are shown recorded at 2 min and 20 h after initiation of light irradiation. Reaction conditions: 0.5 mM **Ir-PS**, 0.305 mM **3**CO, 20 mL THF/TEA/H_2O (4:1:1, pH 12), visible light (380–700 nm, 1.5 W), 25 °C, a) 0 mM P(**d**)$_3$, b) 0.305 mM P(**d**)$_3$, and c) 0.915 mM P(**d**)$_3$. Middle: Pure component spectra of $[HFe_3(CO_{11})]^-$ (H**3**$^-$, red), $[HFe(CO_4)]^-$ (H**1**$^-$, blue), $[Fe(CO)_4\{P(\mathbf{d})_3\}]$ (**1**P(**d**)$_3$, green), $[Fe_2(CO)_6(\mu\text{-}CO)\{\mu\text{-}P(\mathbf{d})_2\}]^-$ (**2**COP(**d**)$_2^-$, violet), and $[Fe_2(CO)_5\{P(\mathbf{d})_3\}(\mu\text{-}CO)\{\mu\text{-}P(\mathbf{d})_2\}]^-$ (**2**P(**d**)$_3$P(**d**)$_2^-$, turquoise). The spectra of H**3**$^-$, H**1**$^-$, and **2**COP(**d**)$_2^-$ were recorded by measuring the respective synthesized compound dissolved in THF/TEA/H_2O (4:1:1, pH 12). The spectra of **1**P(**d**)$_3$ and **2**P(**d**)$_3$P(**d**)$_2^-$ were extracted by subtraction of the spectra of the known compounds from the in situ spectra. Contributions of all five species in the in situ IR spectra on the left of the figure are marked with * in the corresponding color. Right: Conversion of the precursor **3**CO + P(R)$_3$ as detected by IR spectroscopy throughout the reaction. The scheme starts with processes observed in the absence of light (gray background) and continues with the conversion of the phosphine-deficient species occurring within minutes of visible-light irradiation. Depending on the substituent R, on a time scale of hours, all the species were further converted into **2**COP(R)$_2^-$. If an excess of P(R)$_3$ was applied, **2**P(R)$_3$P(R)$_2^-$ was formed.

The formation of **2**COP(R)$_2^-$ was also confirmed by NMR spectroscopy. Thus, a sample was taken from the solution of the precursor system **3**CO + P(**d**)$_3$ after 15 h of light irradiation. At this time, all iron material has been converted into **2**COP(**d**)$_2^-$, as reflected in the IR spectra. Consistently, the ^{31}P NMR spectrum shows only one singlet signal at $\delta =$ 123.0 ppm, which corresponds to the signal of the synthesized [NEt$_4$][**2**COP(**d**)$_2$] in [D$_8$]THF (see Figures SI2 and SI3 in the Supporting Information). In the ^{19}F NMR spectrum, the signal arising from **2**COP(**d**)$_2^-$ appears at $\delta = -62.8$ ppm. An additional signal at $\delta = -62.7$ ppm could be assigned to trifluorotoluene (**d**H; see Figure SI4 in the Supporting Information). The latter derives from the cleavage of one of the substituents from phosphorus during the formation of the phosphido bridge in **2**COP(**d**)$_2^-$ (P–C cleavage reaction, see below).

To determine the conditions for the formation of **2**COP(R)$_2^-$, we carried out experiments successively excluding one of the system's components apart from **3**CO and P(R)$_3$ apart from **3**CO and P(R)$_3$ (represented by P(**d**)$_3$). The results show that the **Ir-PS** is not necessary for the formation of **2**COP(**d**)$_2^-$. On the other hand, the experiments indicate that all the other components, THF, TEA, and H_2O as well as light irradiation, are essential (see Figure SI14 in the Supporting Information). The need for TEA and H_2O is most probably attributable to the fact that they initiate the formation of radicals (see above).[14d] TEA and H_2O were found by Rahaman et al. to promote the generation of a phosphido-bridged diiron complex akin to **2**COP(R)$_2$ by treatment of **3**CO with Na$^+$[Ph$_2$CO]$^{\bullet-}$ and P(2-furyl)$_3$ in THF at room temperature.[27]

Table 1. Cone angles[a] (θ) of phosphines[b] and IR data[c] of the in situ generated iron phosphides.

R	Structure of R	θ [°] $P(R)_3$	$\tilde{\nu}$(*t*-CO) [cm^{-1}] $1P(R)_3$	$2COP(R)_2^-$
a		184	n.f.	n.f.
b		128	2064 (m) 1989 (m) 1958 (s)	n.f.
c	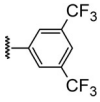	160[d]	n.f.	2025 (m) 1977 (s) 1947 (m) 1926 (m)
d	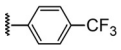	145 or 164[d]	2054 (m) 1981 (m) 1947 (s)	2021 (m) 1971 (s) 1941 (m) 1921 (m)
e		145 or 155[d]	2048 (m) 1971 (m) 1942 (s)	2016 (m) 1965 (s) 1934 (m) 1916 (m)
f	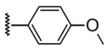	145	2045 (m) 1967 (m) 1938 (s)	2014 (m) 1963 (s) 1932 (m) 1913 (m)
g		212	n.f.	n.f.
h		118	2044 (m) 1964 (m) 1931 (s)	n.f.
i		132	2043 (m) 1964 (m) 1930 (s)	n.f.

[a] Cone angles reported by Tolman[23] unless stated otherwise. [b] The substituents R of the phosphines are listed according to their electron-withdrawing character, which decreases from top to bottom of the table. [c] Solvent: THF/TEA/H_2O, 4:1:1. *t*-CO = terminal carbonyls, n.f. = not formed, w = weak, m = medium, s = strong. [d] Cone angles reported by Howell et al.[16]

The choice of the ligand $P(R)_3$ was also found to be relevant: As concluded from our study, the formation of **2**$COP(R)_2^-$ is only observed if the phosphine meets the following two requirements: 1) $P(R)_3$ has to be an arylphosphine and 2) the *ortho* positions of the aryl group have to be unsubstituted.

These requirements are most probably attributable to the P–C or P–O cleavage reaction, prior to the formation of the phosphido bridge. Such transition-metal-mediated P–C cleavage reactions have been widely reported in the literature.[28] They occur even under mild conditions at temperatures as low as 25 °C.[28a,d] Consistent with our observations, they commonly include hydrido intermediates and yield bi- or higher-nuclear complexes featuring bridging phosphido groups.[28] The reactivity of the cleavage process decreases in the order $P–C_{sp} > P–C_{sp2} > P–C_{sp3}$,[28a] which explains the formation of **2**$COP(R)_2^-$ upon application of arylphosphines rather than alkylphosphines. For phosphites, analogous P–O cleavage reactions with subsequent formation of bridging ligands are also known.[29] However, the in situ formation of **2**$COP(R)_2^-$ by application of phosphites is inhibited, because the presence of water suppresses these P–O cleavage reactions[29a] and can also induce decomposition of the ligands due to hydrolysis.[30] The mechanism of the P–C cleavage reaction has not yet been completely investigated.[28c] Thus far, mechanistic studies point to the oxidative addition of the P–C bond to the metal center as the activating step.[28a,b,31] This requires a coordinatively unsaturated metal atom,[32] for example, provided by light-initiated CO dissociation. It is assumed that other processes precede the P–C cleavage reaction. These processes include, for example, η^6-coordination of the phosphine aryl rings to neighboring metal atoms in polynuclear complexes[33] or the oxidative addition of the *ortho*-C–H bond to the metal center, known as "orthometalation".[28a,b] These processes together with steric drawbacks might explain why *ortho*-substituted arylphosphines do not undergo P–C cleavage[34] and **2**$COP(R)_2^-$ is not observed when $P(\mathbf{a})_3$ and $P(\mathbf{g})_3$ are applied.

Results of the analysis by X-ray absorption spectroscopy

To further substantiate the results of the IR analysis of the formed species, XAS was carried out. Unlike IR spectroscopy, XAS directly provides bond distances and coordinating atoms in an element-specific manner by evaluation of the extended X-ray absorption fine structure (EXAFS) above the absorption edge. However, the analysis of EXAFS spectra is complicated by the fact that the structural parameters of all the species in the reaction solution are averaged in the spectral signal.[35]

Figure 4 shows the experimental Fourier-transformed EXAFS spectra, and the corresponding χ(k) functions and XANES (X-ray absorption near-edge structure) spectra are given as Figures SI 15–17 in the Supporting Information. Analysis was carried out on Fourier-filtered data in the range of 1–3.2 Å by using the radial distribution function approach, because the

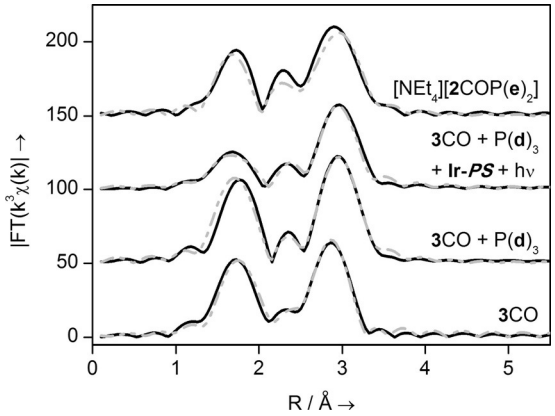

Figure 4. Fourier-transformed EXAFS function of the samples given in Table 2. The experimental spectra are shown as black solid lines and the fitted spectra are given as gray dashed lines.

nature of the formed species was unknown. Because mixtures of species were also expected, no multiple scattering analysis[36] was carried out and the rather intense multiple scattering signal of the CO ligands was fitted by using a single scattering Fe–O shell.[37] The signal in the case of **3**CO + P(**d**)$_3$ + **Ir-PS** + $h\nu$ is slightly reduced compared with the other spectra, as the fluorescence signal was superior to the absorption data due to the presence of the iridium photosensitizer. However, the signal is affected by self-absorption effects, which can be accounted for by an overall amplitude reduction factor of 0.68, whereas for all others it was 0.9. All the obtained structural parameters are summarized in Table 2.

Table 2. Structural parameters obtained by fitting the experimental EXAFS function with theoretical models.

	Abs–Bs[a]	N(Bs)[b]	R(Abs–Bs)[c] [Å]	σ[d] [Å]	R[e] [%]
3CO[f]	Fe–C	4.7 ± 0.5	1.80 ± 0.02	0.067 ± 0.002	20.91
	Fe–Fe	1.8 ± 0.3	2.51 ± 0.03	0.032 ± 0.001	
	Fe–O[g]	7.0 ± 1.4	2.99 ± 0.03	0.067 ± 0.002	
3CO + P(**d**)$_3$[h]	Fe–C	5.2 ± 0.5	1.75 ± 0.02	0.074 ± 0.002	16.88
	Fe–P	0.4 ± 0.1	2.23 ± 0.02	0.039 ± 0.001	
	Fe–Fe	0.6 ± 0.2	2.71 ± 0.03	0.097 ± 0.020	
	Fe–O[g]	15.0 ± 3.2	2.99 ± 0.03	0.077 ± 0.002	
3CO + P(**d**)$_3$ + **Ir-PS** + $h\nu$[i]	Fe–C	3.5 ± 0.4	1.78 ± 0.02	0.102 ± 0.020	18.22
	Fe–P	0.8 ± 0.2	2.13 ± 0.02	0.045 ± 0.009	
	Fe–Fe	1.6 ± 0.4	2.46 ± 0.03	0.110 ± 0.022	
	Fe–O[g]	9.1 ± 1.8	2.94 ± 0.03	0.074 ± 0.015	
[NEt$_4$][**2**COP(**e**)$_2$][k]	Fe–C	4[k]	1.75 ± 0.02	0.059 ± 0.012	22.73
	Fe–P	1[k]	2.16 ± 0.02	0.071 ± 0.002	
	Fe–Fe	1[k]	2.53 ± 0.03	0.107 ± 0.022	
	Fe–O[g]	15 ± 3.0	2.99 ± 0.03	0.077 ± 0.016	

[a] Abs = X-ray absorbing atom, Bs = Back-scattering atom. [b] Number of back-scattering atoms. [c] Distance between absorbing and back-scattering atom. [d] Debye–Waller factor. [e] Quality of fit. [f] 0.01 M **3**CO in THF/TEA/H_2O (4:1:1). [g] Although denoted as a single Fe–O scattering path, the underlying signal contains a significant amount of multiple scattering from the CO ligand. [h] 0.025 M **3**CO and 0.025 M P(**d**)$_3$ in THF/TEA/H_2O (4:1:1, pH 12), measured 3 h after preparation of the reaction solution. [i] 0.0033 M **3**CO, 0.0033 M P(**d**)$_3$, 0.0022 M **Ir-PS**, and $h\nu$ in THF/TEA/H_2O (4:1:1, pH 12), after 8 h of reaction time. [j] 0.05 M [NEt$_4$][**2**COP(**e**)$_2$] in THF/TEA/H_2O (4:1:1, pH 12). [k] Value fixed to the crystallographic number.

The parameters obtained for **3**CO in THF/TEA/H_2O (4:1:1) solution agree very well with previous EXAFS studies.[38] The Fe–Fe coordination number deviates slightly from the expected number of two, which is in line with the presence of iron species of lower nuclearity. Nonetheless, the bond distances agree very well with the crystal structure data of **3**CO.[39]

By adding one equivalent of P(**d**)$_3$, a characteristic Fe–P shell appears with a coordination number of 0.4. Together with the significantly reduced Fe–Fe coordination number of 0.6, it is in very good agreement with a quantitative coordination of P(**d**)$_3$ to iron (expected Fe–P coordination number 0.33). The average of 0.6 iron neighbors cannot be explained by only trinuclear phosphine-free species, as in this case an average value of >1 would be expected. Thus, a mixture of mono-, di-, and trinuclear iron carbonyl compounds ([Fe(CO)$_5$], [Fe$_2$(CO)$_8$]$^{\bullet-}$, and [Fe$_3$(CO)$_{11}$]$^{\bullet-}$) is confirmed, which is also in agreement with the Fe–C coordination number of 5.2.[40]

The reaction system (**3**CO + P(**d**)$_3$ + **Ir-PS** + $h\nu$) was subjected to a full EXAFS characterization after 8 h. It is clear that the nearest neighbor Fe–C coordination number is reduced to around four, whereas the Fe–P coordination number increases to nearly one. These coordination numbers and the distances of both shells agree very well within the error bar with those of the reference compound [NEt$_4$][**2**COP(**e**)$_2$] with one coordinating bridging phosphine and four CO ligands per iron center.[24b] The results thus confirm the formation of **2**COP(**d**)$_2^-$ previously concluded by IR analysis. However, due to the reduced reaction time and the high concentrations of the reaction components (concentrations are increased by a factor of 10 as compared with the other experiments of this work), full conversion to this species is not complete, which is evident from the Fe–Fe coordination number of 1.6, which is slightly too high even if the error is taken into account. The presence of other species contributing to the spectra is also recognizable from the large Debye–Waller factor and was confirmed by an analogous in situ IR experiment carried out under the same reaction conditions as applied in the XAS experiment. Accordingly, the IR spectrum measured at the same time shows H**3**$^-$, H**1**$^-$, and **1**P(**d**)$_3$ to be present in addition to the major species **2**COP(**d**)$_2^-$ that shows the biggest share of 43% (see Figure SI18 in the Supporting Information).

Influence of 1P(R)$_3$ and 2COP(R)$_2^-$ on the H_2 evolution

For a better understanding of the differing effects of specific phosphine co-catalysts, we start this section with a brief summary of the results of previous mechanistic studies on the phosphine-free system with **3**CO as exclusive precursor.

The catalytic cycle begins with the excitation of the **Ir-PS** by light and subsequent reductive quenching by TEA. The latter process was found by means of photoluminescence spectroscopy and kinetic analysis to be the rate-limiting step of the system.[14c,d] After that, the reduced **Ir-PS** transfers electrons to the active catalyst, which we proposed to be H**3**$^-$. This proposition was based on time-dependent DFT calculations and is supported by the finding that H**3**$^-$ shows a more positive reduction potential than the **Ir-PS**.[14a,d] The transferred electrons either are directly used within the catalytic cycle for proton reduction and H_2 generation or they induce the fragmentation of H**3**$^-$. Through the latter process, quasi-full conversion of H**3**$^-$ into the resting state H**1**$^-$ occurs within 1 h. However, both species are in equilibrium because a light-induced back reaction continually regenerates H**3**$^-$ in small amounts (Scheme 1).[14d] Over the further course of the reaction, H**1**$^-$ decomposes due to processes discussed in a following section of this article (Figure 5, top, blue concentration curve). After 16 h, H**1**$^-$ is fully consumed. As a consequence, catalysis ceases and gas evolution stops (Figure 5, top, gray gas evolution curve).[14d]

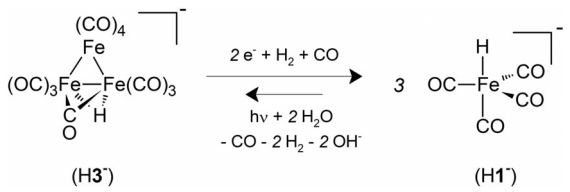

Scheme 1. Equilibrium between H**3**$^-$ and H**1**$^-$.

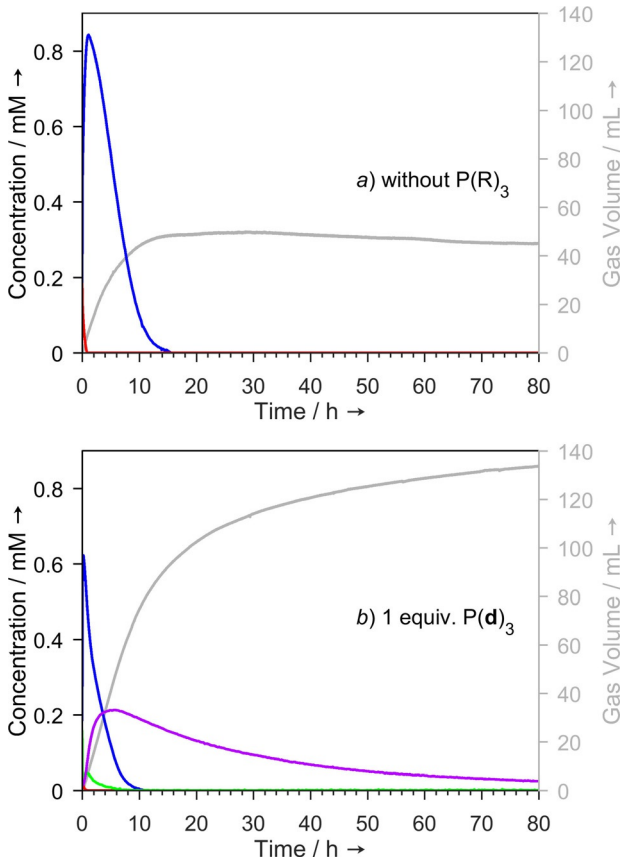

Figure 5. Gas evolution curves (gray) and concentration curves for H**3**$^-$ (red), H**1**$^-$ (blue), **1**P(**d**)$_3$ (green) and **2**COP(**d**)$_2^-$ (violet) in the original phosphine-free proton reduction system with **3**CO as catalyst precursor (top) and the phosphine-containing system with **3**CO and the co-catalyst P(**d**)$_3$ (bottom). Reagents and conditions: 0.5 mM **Ir-PS**, 0.305 mM **3**CO, 20 mL THF/TEA/H_2O (4:1:1, pH 12), visible light (380–700 nm, 1.5 W), 25 °C, (a) 0 mM P(**d**)$_3$, (b) 0.305 mM P(**d**)$_3$.

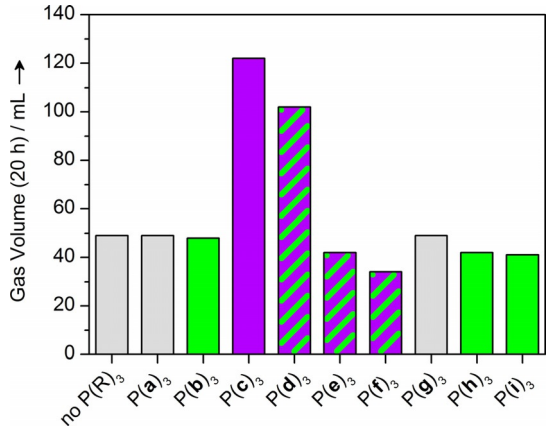

Figure 6. Evolved H_2 gas after 20 h of light irradiation in the original phosphine-free system (first data point) and the phosphine-containing system as a function of the applied co-catalyst P(R)$_3$. The formation of iron phosphides **1**P(R)$_3$ (green) and **2**COP(R)$_2^-$ (violet) is denoted by the color of the bar in the case of their formation during experiments with the respective co-catalyst; gray denotes no formation of **1**P(R)$_3$ or **2**COP(R)$_2^-$. Reagents and conditions: 0.5 mM **Ir-PS**, 0.305 mM **3**CO, 20 mL THF/TEA/H_2O (4:1:1, pH 12), visible light (380–700 nm, 1.5 W), 25 °C, first data point: 0 mM P(R)$_3$, other: 0.305 mM P(R)$_3$.

Modification of the system by application of one equivalent of phosphine ligand has varying effects on the production of H_2, depending on the choice of the phosphine ligand and the emerging iron phosphides associated therewith.

As described previously, sterically demanding P(**a**)$_3$ or P(**g**)$_3$ do not show any interaction with the iron species (see Figures SI20a and SI20g in the Supporting Information). Hence, their application has no impact on the catalytic process and the same amount of gas is produced as in the phosphine-free system (Figure 6).

The phosphite P(**b**)$_3$ and the alkylphosphines P(**h**)$_3$ and P(**i**)$_3$ do coordinate to iron and form exclusively **1**P(**b**)$_3$, **1**P(**h**)$_3$, and **1**P(**i**)$_3$, respectively. This has a small negative effect on the H_2 productivity of the system, most notably in the case of the alkylphosphines, with a decline in the yield of H_2 by 15% (Figure 6). Due to the formation of **1**P(R)$_3$, less iron material is available for transformation into the catalytically relevant species H**3**$^-$ and H**1**$^-$. As a consequence, these two species are present in lower amounts and are used up sooner over the reaction time. Because **1**P(R)$_3$ does not contribute to the production of H_2, gas evolution stops at an earlier stage as compared with the phosphine-free system (see Figures SI20h and SI20i in the Supporting Information).

In contrast, the application of the electron-poor arylphosphines P(**c**)$_3$ or P(**d**)$_3$ highly improves the system due to the formation of **2**COP(**c**)$_2^-$ and **2**COP(**d**)$_2^-$, respectively. We illustrate this for the example of P(**d**)$_3$ (Figure 5, bottom): At the beginning of the experiment, H**1**$^-$ (Figure 5, bottom, blue concentration curve) is the major iron species in solution. Thus, at this point, the system shows similar catalytic activity to the phosphine-free system. However, during the first 6 h of the reaction, **2**COP(**d**)$_2^-$ emerges (Figure 5, bottom, violet concentration curve) and progressively contributes to gas evolution (Figure 5, bottom, gray gas evolution curve). This complex is more stable than H**1**$^-$ and maintains H_2 production even after the decomposition of the latter. This reveals the catalytic activity of **2**COP(**d**)$_2^-$. Hence, the formation of **2**COP(**d**)$_2^-$ improves the stability of the system and increases the yield of H_2 by 108% after 20 h (Figure 6) and by even 155% after 48 h of light irradiation as compared with the phosphine-free catalytic reaction (see Table SI4 in the Supporting Information).

Direct application of the pre-formed molecularly defined [NEt_4][**2**COP(**c**)$_2$] or [NEt_4][**2**COP(**d**)$_2$] as catalyst results in a gas evolution curve broadly similar to that of the respective in situ system **3**CO + P(**c**)$_3$/P(**d**)$_3$ (Figure 7, black gas evolution curve for [NEt_4][**2**COP(**d**)$_2$], solid gray gas evolution curve for **3**CO + P(**d**)$_3$). Especially at extended reaction times, the slopes of the

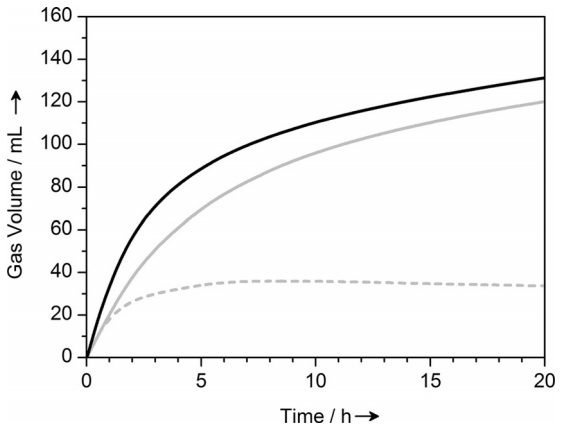

Figure 7. Comparison of the performances of the molecularly defined catalyst $[NEt_4][\mathbf{2}COP(\mathbf{d})_2]$ (solid black), the in situ system $\mathbf{3}CO + P(\mathbf{d})_3$ (solid gray), and **3**CO (dashed gray) in the light-driven generation of hydrogen under the optimized conditions: 1.5 mM **Ir-PS**, 10 mL THF/TEA/H_2O (3:2:1, pH 12), 20 h Xe light irradiation (1.5 W, no filter), 25 °C, solid black line: 0.5 mM $[NEt_4][\mathbf{2}COP(\mathbf{d})_2]$, solid gray line: 0.33 mM $\mathbf{3}CO + 0.5$ mM $P(\mathbf{d})_3$, dashed gray line: 0.33 mM **3**CO.

gas evolution curves are equal, because at this point all the iron material of the in situ assembly $\mathbf{3}CO + P(\mathbf{c})_3/P(\mathbf{d})_3$ has been converted into $\mathbf{2}COP(\mathbf{c})_2^-$ or $\mathbf{2}COP(\mathbf{d})_2^-$ and the solution composition is similar to that of the molecularly defined system. However, direct application of the molecularly defined catalyst leads to an initial gas evolution rate increased by 80% compared with the in situ system (Table 3). We can therefore conclude that photons and thus electrons coming from the **Ir-PS** are more efficiently used for proton reduction by $\mathbf{2}COP(\mathbf{c})_2^-$ or $\mathbf{2}COP(\mathbf{d})_2^-$ than by the $H\mathbf{3}^-/H\mathbf{1}^-$ couple, which is primarily present in the phosphine-free system and in the starting phase of the in situ $\mathbf{3}CO + P(\mathbf{c})_3/P(\mathbf{d})_3$ system. Notably, the higher initial rates derived from the application of the molecularly defined catalysts lead to yields of H_2 enhanced by up to 10% as compared with the in situ catalysts. For $[NEt_4][\mathbf{2}COP(\mathbf{c})_2]$, the highest TON[41] was found to be 1111 after 20 h under the optimized reaction conditions (for details, see Table 3). The IR spectrum of the reaction solution containing pre-formed $[NEt_4][\mathbf{2}COP(\mathbf{d})_2]$ shows predominant contributions from $\mathbf{2}COP(\mathbf{d})_2^-$ throughout the active phase of the system. Only minor, very weak IR bands at 2043, 1988, 1956, 1890, and 1871 cm^{-1} arising from as-yet unassigned species are observed in the same time span as well as $H\mathbf{1}^-$ in very low concentration at the beginning of the experiment (see Figures SI22z and SI23 in the Supporting Information). On the basis of these experiments, $\mathbf{2}COP(\mathbf{c})_2^-$ and $\mathbf{2}COP(\mathbf{d})_2^-$ are confirmed to be catalytically highly important key species. Our results suggest that these complexes can be regarded as a mimic of the [FeFe]-H_2ase active site, because they are dinuclear iron complexes that show catalytic activity and possess carbonyls as well as two bridging ligands in butterfly conformation.

Table 3. Precursor **3**CO, the in situ systems $\mathbf{3}CO + P(R)_3$, and the pre-formed catalysts $[NEt_4][\mathbf{2}COP(R)_2]$ used in the light-driven generation of hydrogen under the optimized conditions.[a] Initial rate of gas evolution and TOF of the catalyst during the first 0.5 h of light irradiation as well as evolved gas and TONs of the catalyst after 20 h of light irradiation.

Entry	Precursor or catalyst	0.5 h Initial rate [L h^{-1}]	0.5 h TOF_{cat}[b] [h^{-1}]	20 h Evolved gas [mL]	20 h TON_{cat}[b]
1	**3**CO	21	(260)	33	(408)
2[c]	$\mathbf{3}CO + P(\mathbf{c})_3$	21	172 (260)	130	1073 (1610)
3	$\mathbf{3}CO + P(\mathbf{d})_3$	21	172 (260)	120	980 (1485)
4	$[NEt_4][\mathbf{2}COP(\mathbf{c})_2]$	37	306	136	1111
5	$[NEt_4][\mathbf{2}COP(\mathbf{d})_2]$	38	309	134	1095
6	$[NEt_4][\mathbf{2}COP(\mathbf{e})_2]$	31	257	80	653
7	$[NEt_4][\mathbf{2}COP(\mathbf{f})_2]$	27	222	49	400

[a] Reagents and conditions: 1.5 mM **Ir-PS**, 10 mL THF/TEA/H_2O (3:2:1, pH 12), 20 h Xe light irradiation (1.5 W, no filter), 25 °C, entry 1: 0.33 mM **3**CO, entries 2 and 3: 0.33 mM **3**CO and 0.5 mM $P(R)_3$, entries 4–7: 0.5 mM $[NEt_4][\mathbf{2}COP(R)_2]$. [b] $TON = n_{H2}/n_{cat}$, $TOF = n_{H2}/n_{cat}/t$ with n_{cat} = amount of $\mathbf{2}COP(R)_2^-$ or $P(R)_3$, because the quantity of $P(R)_3$ determines the maximum possible amount of $\mathbf{2}COP(R)_2^-$ to be formed in the in situ system (in parentheses: n_{cat} = amount of **3**CO). [c] Values taken from ref.:[14a] TON after 24 h, TOF during first 3 h.

However, the activity of compounds with the $\mathbf{2}COP(R)_2^-$ structure is highly dependent on the electron-acceptor/donor ability of the substituent R. This is shown by application of the precursor **3**CO together with the co-catalysts $P(\mathbf{e})_3$ or $P(\mathbf{f})_3$. During the reaction, electron-rich $\mathbf{2}COP(\mathbf{e})_2^-$ or $\mathbf{2}COP(\mathbf{f})_2^-$ is formed. In contrast to their electron-poor counterparts $\mathbf{2}COP(\mathbf{c})_2^-$ and $\mathbf{2}COP(\mathbf{d})_2^-$, they cause a decrease in the yield of H_2 (Figure 6). Direct application of the pre-formed $[NEt_4][\mathbf{2}COP(\mathbf{e})_2]$ or $[NEt_4][\mathbf{2}COP(\mathbf{f})_2]$ accordingly results in lower TONs as compared with $[NEt_4][\mathbf{2}COP(\mathbf{c})_2]$ or $[NEt_4][\mathbf{2}COP(\mathbf{d})_2]$ (Table 3).

Hence, we conclude the formation of $\mathbf{2}COP(R)_2^-$ to be necessary but not sufficient to improve the performance of precursor **3**CO by the addition of $P(R)_3$. For the latter, R has to meet a further requirement: R must be electron-withdrawing.

This dependence of the activity on R is consistent with the findings described in the literature. Best and co-workers found $\mathbf{2}COP(\mathbf{e})_2^-$ to be an inactive side-product during electrochemical proton reduction by $[Fe_2(CO)_6\{\mu\text{-}P(Ph)_2\}_2]$.[24b,42] In our previous work, the formation of $\mathbf{2}COP(\mathbf{e})_2^-$ was also observed in photocatalytic proton reduction by a non-noble-metal-based system introduced by Beller and co-workers.[43] The system involves a copper complex as PS ([Cu(Xantphos)(Bathocuproine)]PF_6) and **3**CO as catalyst. The phosphorus ligand in $\mathbf{2}COP(\mathbf{e})_2^-$ originates from Xantphos, which was found to dissociate from the PS and undergo P–C cleavage. TONs similar to those of the phosphine-free **Ir-PS** system were observed.

Deactivation processes during photocatalytic water reduction

As described in our previous work, the phosphine-free system is deactivated by the decomposition of $H\mathbf{1}^-$ (Figure 8, top, blue curve). Decomposition mechanisms were found to be light-induced decarbonylation and poisoning of the catalyst by 2,2′-bipyridine (bpy). The latter process occurs at high concentrations of the **Ir-PS** (Ir/Fe ratio > 0.4), which degrades over reaction time and releases bpy as a result of light irradiation. This was shown by Bernhard and co-workers by means of ESI-MS.[44] The bpy ligand is transferred to the catalyst resulting in

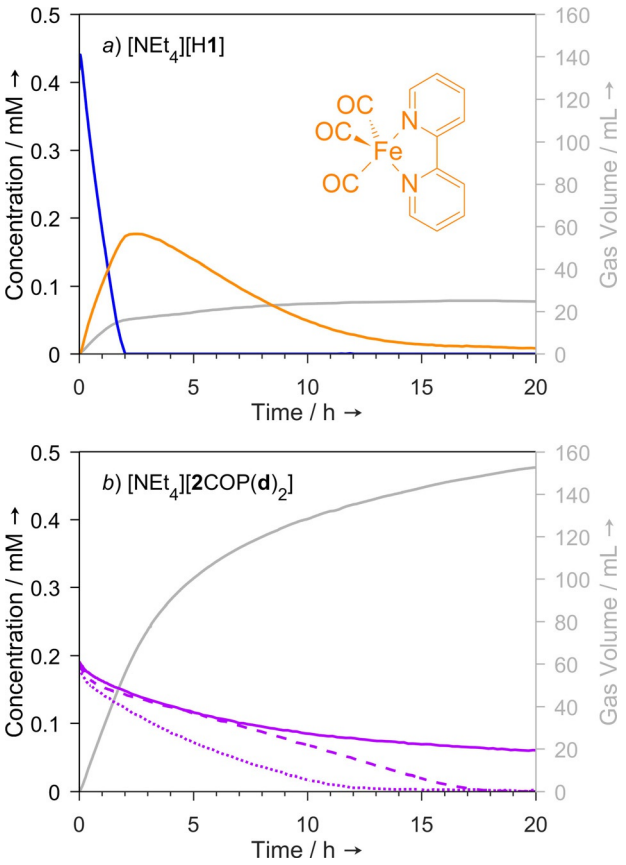

Figure 8. Top: Performance (gray gas evolution curve) of pre-formed $[NEt_4][H\mathbf{1}]$ (blue concentration curve) applied at high **Ir-PS** concentration. Deactivation occurs due to transformation of the catalyst into $[Fe(CO)_3bpy]$ (orange concentration curve and structure). Bottom: Performance (gray gas evolution curve) and concentration curve of the molecularly defined $[NEt_4][\mathbf{2}COP(\mathbf{d})_2]$ (violet) applied at high **Ir-PS** concentration in THF/TEA/H_2O (solid) and concentration curve of $[NEt_4][\mathbf{2}COP(\mathbf{d})_2]$ applied without **Ir-PS** in THF/TEA/H_2O (dashed) or in THF only (dotted). Reagents and conditions: 0.4 mM $[NEt_4][H\mathbf{1}]$ (top) or 0.2 mM $[NEt_4][\mathbf{2}COP(\mathbf{d})_2]$ (bottom), 1.25 mM **Ir-PS** (solid) or 0 mM **Ir-PS** (dashed, dotted), 20 mL THF/TEA/H_2O (4:1:1, pH 12, solid and dashed) or 10 mL THF (dotted), visible light (380–700 nm, 1.5 W), 25 °C.

the formation of the less-active $[Fe(CO)_3(bpy)]$ (Figure 8, top, orange curve). The assignment of this species was discussed in our previous work and is based on the good agreement between the wavenumbers of our in situ IR experiments and those quoted in the literature and obtained from DFT calculations.[14d]

In contrast to $H\mathbf{1}^-$, catalyst $\mathbf{2}COP(R)_2^-$ is inert to bpy poisoning because the formation of $[Fe(CO)_3(bpy)]$ is not observed in experiments at high **Ir-PS** concentration with $[NEt_4][\mathbf{2}COP(\mathbf{d})_2]$ as the pre-formed catalyst (Figure 8, bottom, solid curves). This property is a major reason for the high stability of the phosphine-containing system compared with the phosphine-free system. Nevertheless, $\mathbf{2}COP(R)_2^-$ is exposed to other slow light-induced decomposition processes such as CO dissociation:[45] Although stable in the dark, $[NEt_4][\mathbf{2}COP(\mathbf{d})_2]$ disintegrates upon light irradiation in pure THF in the absence of the PS (Figure 8, bottom, dotted curve). Remarkably, the process is attenuated in the THF/TEA/H_2O mixture (Figure 8, bottom, dashed curve).[46] Under the catalytic conditions with **Ir-PS** present, the decomposition further slows down at extended reaction times (Figure 8, bottom, solid violet curve).[47] Parallel to catalyst decomposition, the concentration of the **Ir-PS** decays due to light irradiation.[14a,44] That is why the rate of H_2 evolution steadily declines throughout the reaction while $\mathbf{2}COP(R)_2^-$ is still present. Accordingly, the activity can be restored by the addition of a second batch of **Ir-PS** at extended reaction times (see Figure SI24 in the Supporting Information).

Deactivation by excess of phosphine

Beller and co-workers[14a] observed a decline in activity if the catalytic reaction was performed with more than one equivalent of electron-poor phosphine with respect to **3**CO. To explore this issue in more depth we studied the system by applying **3**CO and three equivalents of $P(\mathbf{d})_3$. Under these conditions, we found that in a portion of the emerging $\mathbf{2}COP(\mathbf{d})_2^-$ complex a terminal carbonyl group was replaced by one $P(\mathbf{d})_3$ ligand (Scheme 2). As a consequence, the compound

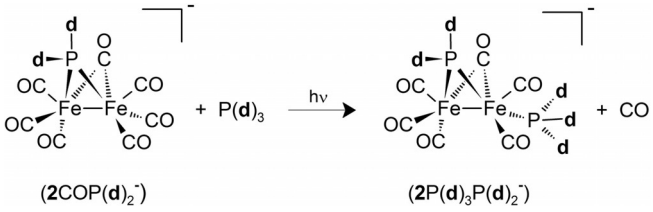

Scheme 2. Substitution of a terminal CO ligand in $\mathbf{2}COP(\mathbf{d})_2^-$ by $P(\mathbf{d})_3$ yields the complex $\mathbf{2}P(\mathbf{d})_3P(\mathbf{d})_2^-$. This reaction is induced by light irradiation.

$[Fe_2(CO)_5\{P(\mathbf{d})_3\}(\mu\text{-}CO)\{\mu\text{-}P(\mathbf{d})_2\}]^-$ ($\mathbf{2}P(\mathbf{d})_3P(\mathbf{d})_2^-$) was formed and shows IR bands at 1988 (m), 1932 (s), 1911 (m), 1896 (m), and 1872 cm^{-1} (sh; Figure 3, left, c, in situ spectrum at $t = 20$ h, Figure 3, middle, turquoise pure component spectrum, and Figure 3, right, turquoise-labeled structure). We could assign this species based on the agreement of its IR spectrum with those of similar complexes like $[Fe_2(CO)_5(PMePh_2)(\mu\text{-}CO)(\mu\text{-}PPh_2)]^-$ [48] or $[Fe_2(CO)_5(PHPh_2)(\mu\text{-}CO)(\mu\text{-}PPh_2)]^-$[24b,49] (see Table SI3 in the Supporting Information). DFT calculations of distinct isomers of $\mathbf{2}P(\mathbf{d})_3P(\mathbf{d})_2^-$ indicate that the position of the terminal phosphine ligand is in a *trans* position with respect to the phosphido bridge (see Figure SI13 in the Supporting Information).

We also generated a mixture of $\mathbf{2}P(\mathbf{d})_3P(\mathbf{d})_2^-$ and $\mathbf{2}COP(\mathbf{d})_2^-$ by another reaction route, namely by irradiating a solution of $[NEt_4][\mathbf{2}COP(\mathbf{d})_2]$ and $P(\mathbf{d})_3$ in pure THF with UV light (320–400 nm) for 30 min (see Figure SI5 in the Supporting Information). The ^{31}P NMR spectrum of this solution shows two doublet signals for $\mathbf{2}P(\mathbf{d})_3P(\mathbf{d})_2^-$ at $\delta = 131.6$ (for $\mu\text{-}P\mathbf{d}_2$) and 81.7 ppm (for $t\text{-}P\mathbf{d}_3$, *t* denotes a terminal ligand) with a coupling constant of $^2J_{P\text{-}P} = 36.6$ Hz (see Figure SI6 in the Supporting Information), which is consistent with the proposed structure and the NMR spectra of the aforementioned similar complexes.

Although $2P(d)_3P(d)_2^-$ was formed to only a minor extent with one equivalent of $P(d)_3$ with respect to **3**CO under the catalytic conditions (Figure 9, cyan solid absorption curve for $2P(d)_3P(d)_2^-$), three equivalents of $P(d)_3$ led to $2P(d)_3P(d)_2^-$ as the major species (Figure 9, cyan-dotted absorption curve for $2P(d)_3P(d)_2^-$). The additional phosphine ligand in this complex increases the electron density on the iron, which is indicated by the IR bands of $2P(d)_3P(d)_2^-$ being found at lower wavenumbers as compared with the $2COP(R)_2^-$ species.[50] Hence, the electron density on the iron in $2P(d)_3P(d)_2^-$ is even higher than those in the electron-rich complexes $2COP(e)_2^-$ and $2COP(f)_2^-$. As a consequence, H_2 evolution is reduced in the presence of significant amounts of $2P(d)_3P(d)_2^-$ (Figure 9, gray gas evolution curves). Thus, to achieve the highest possible yield of H_2, **3**CO and $P(R)_3$ need to be applied in equal quantities.

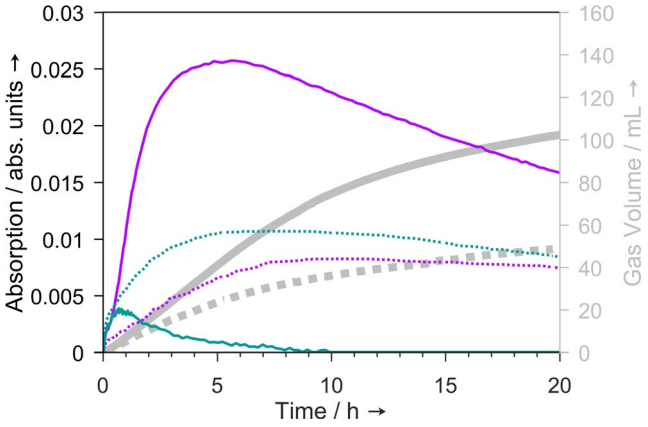

Figure 9. Gas evolution curves (gray) and absorption curves of $2COP(d)_2^-$ (violet) and $2P(d)_3P(d)_2^-$ (cyan) in the phosphine-containing system starting with precursor **3**CO and 1 equiv of $P(d)_3$ (solid) or 3 equiv of $P(d)_3$ (dotted). Reagents and conditions: 0.5 mM **Ir-PS**, 0.305 mM **3**CO, 0.305 mM $P(d)_3$ (solid) or 0.915 mM $P(d)_3$ (dotted), 20 mL THF/TEA/H_2O (4:1:1, pH 12), visible light (380–700 nm, 1.5 W), 25 °C.

Electrochemistry

To have an idea of the reasons for the differing performances of $[NEt_4][2COP(R)_2]$ depending on the substituent R, we investigated their electrochemical properties in a brief preliminary study. The violet graph in Figure 10 shows the cyclic voltammogram of $[NEt_4][2COP(d)_2]$ in THF containing $[NBu_4][ClO_4]$. It displays the electrochemical stability of the iron compound in the potential range between −2.3 and −0.8 V versus $Fc^{0/+}$ ($Fc^{0/+}$ = ferrocene/ferrocenium redox couple). At more positive potentials, a quasi-reversible oxidation occurs (E°_{redox1} = −0.58 V vs. $Fc^{0/+}$). At lower potentials, two reduction steps are found (peak potentials E_{red2} = −2.60 V and E_{red3} = −2.98 V vs. $Fc^{0/+}$). The same signals are found for the other $[NEt_4][2COP(R)_2]$ complexes, shifted to lower potentials the more electron-rich R becomes (see Table SI5 in the Supporting Information). A lower reduction potential corresponds to a lower electron-acceptor capability, which impedes the electron transfer from the **Ir-PS** to the catalyst. This might be one possible explanation for the poorer performances of the electron-rich $[NEt_4][2COP(e)_2]$ and $[NEt_4][2COP(f)_2]$ in the photocatalytic reactions.

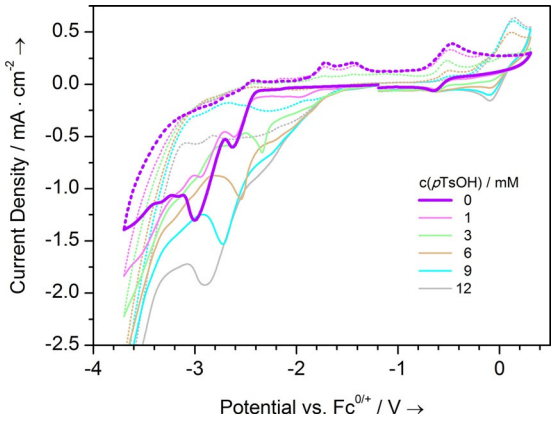

Figure 10. Cyclic voltammograms of $[NEt_4][2COP(d)_2]$ without (violet) and with additional amounts of tosylic acid (*p*TsOH). To provide an overview, the forward scan is denoted as a solid line and the backward scan as a dotted line. Parameters: 1 mM $[NEt_4][2COP(d)_2]$, 0–12 mM *p*TsOH, 0.1 M $TBAClO_4$/THF (TBA = tetrabutylammonium), ν = 100 mV s^{-1}, 2 mm^2 glassy carbon working electrode, Pt counter electrode, and $Ag/AgNO_3$ reference electrode. Potentials are reported with respect to the ferrocene/ferrocenium redox couple.

We conceive the reductions steps E_{red2} and E_{red3} to be irreversible, because we did not observe corresponding re-oxidation signals with the same magnitude of current density. The complexes $2COP(R)_2^-$ perhaps decomposed at these low potentials. Evidence for the degradation is indicated by an anodic signal that emerges during the back scan to positive potentials at −1.72 V in each of the cyclic voltammograms of the $2COP(R)_2^-$ complexes (see Figures SI26 and SI27 in the Supporting Information). The signal is also found at the same position in the cyclic voltammetric measurement of $[Fe(CO)_4]^{2-}$, which would be a potential decomposition product deriving from the degradation of $2COP(R)_2^-$ upon reduction.

We were also interested in the performance of $[NEt_4][2COP(d)_2]$ in electrocatalytic proton reduction. For similar complexes like $[Fe_2(CO)_6\{\mu\text{-}P(Ph)_2\}_2]$ and $[Fe_2(CO)_6\{\mu,\mu\text{-}PPh(CH_2)_3PPh\}]$, Best and co-workers observed catalytic currents at −2.25 V versus $Fc^{0/+}$ upon addition of tosylic acid (*p*TsOH).[24b,42] To obtain comparable results we applied the same proton source in the experiments with $[NEt_4][2COP(d)_2]$, although recent research has revealed that *p*TsOH has drawbacks in the sense that it starts to be directly reduced on glassy carbon working electrodes without a catalyst at −1.5 V.[51]

The addition of *p*TsOH changes the appearance of the cyclic voltammogram of $[NEt_4][2COP(d)_2]$. At three equivalents of *p*TsOH, the first reduction signal is shifted by 0.24 V to more positive values (−2.36 V vs. $Fc^{0/+}$). This indicates protonation of $2COP(d)_2^-$ prior to reduction, which is confirmed by NMR and IR spectroscopy. Namely, the spectra of a solution of $[NEt_4][2COP(d)_2]$ and *p*TsOH in pure THF show several signals and bands of as-yet unassigned species (see Figures SI7 and SI8 in the Supporting Information). However, the high number of these spectral contributions provides indication of a side-reac-

tion of **2**COP(**d**)$_2^-$ with the conjugated base of *p*TsOH.[52] With increasing concentration of the proton donor, the first reduction peak is again shifted cathodically. In parallel, the magnitude of the peak current rises. The latter can be attributed to both the electrocatalytic proton reduction by the catalyst and the direct reduction of *p*TsOH at the electrode overlapping in this potential range (see Figure SI29 in the Supporting Information). However, the performance of **2**COP(**d**)$_2^-$ in electrocatalytic proton reduction is rather low, and therefore the catalytic current increase should be higher. Also, the catalytic peak potential is expected to remain steady and should be closer to the thermodynamic potential for proton reduction at −0.95 V versus $Fc^{0/+}$ (estimated in THF, −0.65 V vs. $Fc^{0/+}$ in acetonitrile)[51,53] offset by only a small overpotential.

Hence, **2**COP(**d**)$_2^-$ in combination with *p*TsOH does not show an electrocatalytic performance as good as $[Fe_2(CO)_6\{\mu\text{-}P(Ph)_2\}_2]$ or $[Fe_2(CO)_6\{\mu,\mu\text{-}PPh(CH_2)_3PPh\}]$.

The electrocatalytic experiment was performed in acidic electrolyte whereas photocatalytic water reduction was carried out in basic solution. Hence, we suppose the differing catalytic activities of **2**COP(**d**)$_2^-$ can be attributed to the distinct solvent environments in which the two measurements were performed. Heterogeneous nickel alloys, for example, are known to catalyze electrocatalytic proton reduction only in an alkaline electrolyte.[54] Also, irradiation and photoexcitation of the protonated catalyst possibly improves the performance in electrocatalytic proton reduction.[55] We would like to point out that the processes observed in the electrochemistry experiments can be considered as only a few of the many processes occurring during photocatalysis. Further electrochemical studies with different reaction conditions have to be carried out in future work.

Conclusion

Through this detailed spectroscopic study we have determined the role of phosphines applied as co-catalysts together with $[Fe_3(CO)_{12}]$ in the photocatalytic proton reduction system of Beller and co-workers.[14a,15] By means of IR, NMR, and X-ray absorption spectroscopy, we detected $[Fe_2(CO)_6(\mu\text{-}CO)\{\mu\text{-}P(R)_2\}]^-$ as the key species in this system. In order that this complex can be formed in situ and show good catalytic activity, the phosphine co-catalyst has to meet the following requirements: 1) It must be an arylphosphine, 2) the *ortho* positions of the aryl groups have to be unsubstituted, and 3) the aryl groups should be electron poor, for example, with electron-withdrawing substituents in the *meta* or *para* positions. Furthermore, $[Fe_3(CO)_{12}]$ and $P(R)_3$ have to be applied in equal amounts because excessive $P(R)_3$ deactivates $[Fe_2(CO)_6(\mu\text{-}CO)\{\mu\text{-}P(R)_2\}]^-$ by substitution of a terminal CO group.

Compared with the original phosphine-free system with $[HFe_3(CO)_{11}]^-$ and $[HFe(CO)_4]^-$ as catalytically relevant species, the main advantages of the electron-poor $[Fe_2(CO)_6(\mu\text{-}CO)\{\mu\text{-}P(R)_2\}]^-$ complexes are their greater durability and resistance to poisoning by the decomposition products of the iridium photosensitizer. Consequently, the stability of the iridium photosensitizer limits the yield of the system. The exact mechanism and catalytic cycle of the proton reduction by $[Fe_2(CO)_6(\mu\text{-}CO)\{\mu\text{-}P(R)_2\}]^-$ is not known yet and has to be elucidated in future work.

We classify $[Fe_2(CO)_6(\mu\text{-}CO)\{\mu\text{-}P(R)_2\}]^-$ as a sulfur-free [FeFe]-H_2ase mimic. Due to its self-assembly (even in the absence of the photosensitizer), a time-consuming synthesis is not necessary. This allows for easy regeneration of the catalyst, which is important for the longevity of modern solar fuel devices.[1b]

The system is improved by the direct application of the molecularly defined $[NEt_4][Fe_2(CO)_6(\mu\text{-}CO)\{\mu\text{-}P(R)_2\}]$ instead of the in situ system, increasing the rate and yield of proton reduction, with the highest initial TOF_{cat} of 306 h^{-1} and TON_{cat} of 1111 at 20 h for $R = C_6H_4\text{-}3,5\text{-}(CF_3)_2$.

In contrast to neutral diphosphido-bridged diiron compounds like $[Fe_2(CO)_6\{\mu\text{-}P(Ph)_2\}_2]$ investigated by Best and coworkers,[24b,42] $[Fe_2(CO)_6(\mu\text{-}CO)\{\mu\text{-}P(C_6H_4\text{-}4\text{-}CF_3)_2\}]^-$ did not show a good performance in electrocatalytic proton reduction in an acidic electrolyte with tosylic acid as the proton source. We have attributed the differing performances in the electrochemical and photochemical catalytic reactions to the distinct solvent environment, because the photocatalytic system works in a mixture of THF, triethylamine, and water at pH 12.

There are several further possibilities for the future improvement or application of the photocatalytic system, for example, the use of quantum dots as photosensitizer or the application of water-soluble phosphines like $P(C_6H_4SO_3Na)_3$, which allows the water content in the solvent mixture to be increased. Immobilization of the catalyst on polymer supports or electrode surfaces would allow for its integration into dye-sensitized photoelectrochemical cells.[56] Such devices dispense with the use of sacrificial reagents. The immobilization could be realized in situ, for example, by application of diarylphosphine-functionalized polystyrenes instead of molecular $P(R)_3$.[28a] In addition, derivates that have not yet been accessible by the self-assembly reaction could be applied as catalysts in molecular systems, for example, complexes of the type $[Fe_2(CO)_6(\mu\text{-}CO)\{\mu\text{-}P(O\text{^}O)\}]^-$ or $[Fe_2(CO)_6(\mu\text{-}CO)\{\mu\text{-}P(R)_2\}MY_x]$.[24a,57] As regards the latter, with $MY_x = Cu(Bathocuproine)$, even light-harvesting dyads are conceivable. These ideas illustrate the potential of $[Fe_2(CO)_6(\mu\text{-}CO)\{\mu\text{-}P(R)_2\}]^-$ as catalysts and their relevance in future applications.

Experimental Section

General: All experiments and synthetic procedures were carried out in an argon atmosphere and under the exclusion of air by using Schlenk techniques.

Chemicals: Solvents were purified and degassed according to standard procedures prior to use. The compounds **3**CO, P(**a**–**i**)$_3$, $[NBu_4][PF_6]$, and $[NBu_4][ClO_4]$ were purchased from a commercial supplier (Sigma–Aldrich, Alfa Aesar, Acros). The complexes $[Ir(bpy)(p\text{-}py)_2]PF_6$,[58] $[HNEt_3][HFe_3(CO)_{11}]$,[59] and $[NEt_4][HFe(CO)_4]$[60] were synthesized according to literature procedures.

Synthesis of the complexes [NEt$_4$][2COP(c–f)$_2$]: $[NEt_4][$**2**$COP(\mathbf{e})_2]$ was synthesized by the procedure reported by Walther et al.[24a] The other diferrates $[NEt_4][$**2**$COP(\mathbf{c})_2]$, $[NEt_4][$**2**$COP(\mathbf{d})_2]$, and $[NEt_4][$**2**$COP(\mathbf{f})_2]$ were synthesized starting with the preparation of $[NEt_4]_2[Fe_2(CO)_8]$.[61] The subsequent reaction with $PClR_2$ was carried

out according to a procedure similar to those described by Osterloh and Reina et al.[25,62] $[NEt_4]_2[Fe_2(CO)_8]$ (0.6 mmol) was dispersed in THF (18 mL) at 50 °C. After the addition of $PClR_2$ (0.6 mmol), the deep-red slurry was stirred for 30 min. Subsequently, further $PClR_2$ (0.15 mmol) was added and stirring was maintained for another 10 min. The solution was then irradiated by UV light (320–500 nm) for 2 h at room temperature. During this time, the color turned from deep red to deep brown. After filtration, the solution was concentrated to dryness and the solid was suspended in pentane (5 mL), filtered, and washed with additional pentane (5 mL). The resulting brown residue was dissolved in a mixture of CH_2Cl_2 (1.3 mL) and diethyl ether (1 mL). Pentane was added until the product precipitated as brownish yellow crystals. The latter were filtered, washed with pentane, and dried under vacuum. Yields: 35–67%.

Data for $[NEt_4][\mathbf{2}COP(\mathbf{c})_2]$: ^{1}H NMR (300 MHz, $[D_8]$THF): $\delta = 8.15$ (d, $J = 10.3$ Hz, 4H), 7.93 (s, 2H), 3.23 (m, 8H), 1.21 ppm (m, 12H); ^{19}F NMR (282 MHz, $[D_8]$THF): $\delta = -63.2$ ppm (s); ^{31}P NMR (121.5 MHz, $[D_8]$THF): $\delta = 122.3$ ppm (s); IR (THF): $\tilde{\nu} = 2025$ (m), 1977 (s), 1947 (m), 1928 (m), 1747 cm^{-1} (w).

Data for $[NEt_4][\mathbf{2}COP(\mathbf{d})_2]$: ^{1}H NMR (300 MHz, $[D_8]$THF): $\delta = 7.79$ (t, $J = 9.0$ Hz, 4H), 7.53 (d, $J = 7.7$ Hz, 4H), 3.27 (q, $J = 7.2$ Hz, 8H), 1.27 ppm (t, $J = 7.2$ Hz, 12H); ^{19}F NMR (282 MHz, $[D_8]$THF): $\delta = -62.8$ ppm (s); ^{31}P NMR (121.5 MHz, $[D_8]$THF): $\delta = 122.8$ ppm (s); IR (THF): $\tilde{\nu} = 2021$ (m), 1971 (s), 1941 (m), 1921 (m), 1741 cm^{-1} (w).

Data for $[NEt_4][\mathbf{2}COP(\mathbf{e})_2]$: ^{1}H NMR (300 MHz, $[D_8]$THF): $\delta = 7.61$ (m, 4H), 7.17 (m, 6H), 3.26 (q, $J = 7.3$ Hz, 8H), 1.26 ppm (t, $J = 7.3$ Hz, 12H); ^{31}P NMR (121.5 MHz, $[D_8]$THF): $\delta = 125.9$ ppm (s); IR (THF): $\tilde{\nu} = 2016$ (m), 1965 (s), 1934 (m), 1916 (m), 1736 cm^{-1} (w).

Data for $[NEt_4][\mathbf{2}COP(\mathbf{f})_2]$: ^{1}H NMR (300 MHz, $[D_8]$THF): $\delta = 7.50$ (dd, $J = 10.4$, 8.8 Hz, 4H), 6.73 (dd, $J = 8.8$, 1.5 Hz, 4H), 3.72 (s, 6H), 2.79 (m, 8H), 0.82 ppm (m, 12H); ^{31}P NMR (121.5 MHz, $[D_8]$THF): $\delta = 123.2$ ppm (s); IR (THF): $\tilde{\nu} = 2014$ (m), 1963 (s), 1932 (m), 1913 (m), 1736 cm^{-1} (w).

Experimental setup, procedure, and data analysis: The experimental setup (see Scheme SI1 in the Supporting Information) for time-resolved operando continuous-flow FTIR experiments under light irradiation consists of a reaction vessel connected to an FTIR spectrometer and an automatic gas burette. Hence, this setup allows monitoring of gas evolution and the simultaneous acquisition of IR spectra. A mercury vapor lamp (LUMATEC) was attached to the double-walled thermostatically controlled reaction vessel at a fixed position by means of a fiber optic cable. This lamp emits visible light between 380 and 700 nm. The reaction solution was stirred with a magnetic stirrer at a constant and reproducible speed and was continuously circulated through the thermostatted measuring cell of the IR spectrometer by using a microannular gear pump (HNP). The cell had CaF_2 windows and an optical path length of 100 μm. The FTIR measurements made with a Bruker Tensor 27 spectrometer equipped with a mercury-cadmium-telluride (MCT) detector. The gas evolution was monitored by using an automatic gas burette (MESSEN NORD) at a constant pressure of 1020 mbar and its temperature was kept constant at 25 °C. A condenser was installed in between the reaction vessel and the gas burette and maintained at 5 °C to retain volatile solvent.[63]

A typical experiment was carried out as follows: The whole apparatus was evacuated and purged with argon five times to provide oxygen-free conditions. The reaction vessel was then filled with solvent (20 mL). After temperature adjustment an IR spectrum was recorded and used as a background spectrum. The solid catalysts were added to the system. After reaching thermal equilibrium between gas and condensed phase (10 min), the reaction was initiated by irradiation of the solution (1500 mW). An IR spectrum consisting of 64 scans was recorded every 2 min. The obtained hydrogen evolution curve was corrected by the system's blind value, which was obtained in an experiment without catalysts. Turnover numbers were calculated according to the expression $TON = V_{H2}/V_m/n_{catalyst}$ in which V_{H2} is the volume of hydrogen gas, $n_{catalyst}$ is the amount of catalyst and $V_m = 24.3035$ L mol^{-1} (molar volume of an ideal gas at 1020 mbar and 298.15 K).

Extraction of the IR concentration profiles and determination of the IR extinction coefficients were carried out by alignment of the pure component spectra onto the in situ IR spectra. The pure component spectra were obtained from solutions of synthesized compounds ($H\mathbf{3}^-$, $H\mathbf{1}^-$ and $\mathbf{2}COP(\mathbf{c}–\mathbf{f})_2^-$) or by subtraction of these from the in situ spectra ($\mathbf{1}P(R)_3$ and $\mathbf{2}P(\mathbf{d})_3P(\mathbf{d})_2^-$). The spectrum and concentration curve of $[Fe(CO)_3(bpy)]$ was extracted by an algorithm based on factor analysis.[64] The extinction coefficient of $[Fe(CO)_3(bpy)]$ was presumed to be equal to that of $H\mathbf{1}^-$. In Figure 9, the absorption curves were recorded at the maximum absorption of each species as a function of time.

Hydrogen evolution experiments under optimized conditions (Figure 7, Table 3) were performed in a similar experimental setup to that already described elsewhere by Beller and co-workers.[13,14] It differs from the setup described in the previous paragraphs by the absence of the microannular gear pump and the IR unit. A 300 W Xe lamp (Lot-Oriel-300-W-Xe-lamp, LSB530) was used as the light source. At the end of these experiments, the collected gas was analyzed by GC (gas chromatograph HP6890N, carboxen 1000, TCD or TCD + methanizer/FID, external calibration). Apart from argon, traces of solvent vapor, and CO dissociated from the catalyst, only hydrogen was found in the gas mixture. Turnover numbers were calculated according to the expression $TON = V_{H2}/V_m/n_{catalyst}$ with $V_m = 24.465$ L mol^{-1} (molar volume of an ideal gas at 1 atmosphere and 298.15 K).

NMR spectra were recorded with a Bruker Avance AV-300 (^{1}H: 300 MHz, ^{31}P: 121 MHz, ^{19}F: 282 MHz) or a Bruker Avance AV-400 (^{1}H: 400 MHz, ^{31}P: 162 MHz) instrument. ^{1}H shifts are reported in parts per million downfield from tetramethylsilane. ^{31}P NMR shifts are proton-decoupled and reported in parts per million downfield from $H_3PO_4^-$. ^{19}F NMR spectra were recorded with **Ir-PS** as the internal standard ($\delta = -71.80$ and -74.31 ppm). The chemical shifts are reported in ppm downfield from $CFCl_3$.

The X-ray absorption measurements were carried out at the ANKA synchrotron facility. The synchrotron beam current was in the range 80–140 mA at 2.5 GeV storage ring energy. A Si(111) double-crystal monochromator was used for measurements at the Fe K-edge (7.112 keV). The second monochromator crystal was tilted for optimal harmonic rejection. To perform operando studies, the spectra were recorded in fluorescence mode by using a hyperpure germanium detector. Energy calibration was performed with an iron metal foil prior to the measurements. Samples in solution were measured in a specially designed fluorescence cell, which allowed evacuation, flushing with inert gas and filling under inert gas flow.[65] An argon atmosphere was applied to the cell in the course of the measurements to allow evolving gas to escape the cell. Details of the analysis are described elsewhere.[66] EXAFS data analysis was performed according to the curved wave formalism of the EXCURV98 program with the XALPHA phase and amplitude functions.[67] The amplitude reduction factor (AFAC) was allowed to float in the fit. Fourier-filtered back-transformed spectra were analyzed in k-space. Fourier filtering was applied in the range 1.0–3.2 Å.

Cyclic voltammetry experiments were carried out with a Metrohm Autolab PGSTAT302N or PalmSens EmStat3+ Blue potentiostat. Electrodes from the company ALS were used: 2 mm^2 glassy carbon

disc working electrode, platinum wire counter electrode, and Ag/$AgNO_3$ reference electrode (silver wire in 0.01 M $AgNO_3$/0.1 M $TBAClO_4$/acetonitrile). The reference electrode was separated from the experimental solution with a vycor frit. Ferrocene as internal standard was added at the end of each experiment.

Acknowledgements

This work has been partly supported by the Bundesministerium für Bildung und Forschung (BMBF) within the project "Light2Hydrogen" (Spitzenforschung und Innovation in den Neuen Ländern) by the European Union (European Social Funds, ESF) within the project "PS4H" and by the Ministry for Education, Science and Culture of Mecklenburg-Vorpommern. We thank Wolfgang Baumann for supporting the NMR measurements, Robert Francke, Felix Gärtner, Michael Karnahl, Nils Rockstroh, and Petra Bartels for providing chemicals and expertise, Peter Kumm and Martin Riedel for technical support, as well as Anika Wilhelms and Elisabeth Oberem for experimental support. M.B. thanks the BMBF for support within the project "SusChEmX" and "TrExHigh" and the ANKA synchrotron facility for provision of beamtime.

Conflict of interest

The authors declare no conflict of interest.

Keywords: enzyme mimics · EXAFS spectroscopy · hydrogen · IR spectroscopy · photocatalysis · proton reduction

[1] a) N. Armaroli, V. Balzani, *Angew. Chem. Int. Ed.* **2007**, *46*, 52 – 66; *Angew. Chem.* **2007**, *119*, 52 – 67; b) L. Hammarström, *Chem* **2016**, *1*, 515 – 518; c) N. Armaroli, V. Balzani, *Chem. Eur. J.* **2016**, *22*, 32 – 57.

[2] a) R. Eisenberg, *Science* **2009**, *324*, 44 – 45; b) H. Junge, N. Rockstroh, S. Fischer, A. Brückner, R. Ludwig, S. Lochbrunner, O. Kühn, M. Beller, *Inorganics* **2017**, *5*, 14.

[3] Z. Han, R. Eisenberg, *Acc. Chem. Res.* **2014**, *47*, 2537 – 2544.

[4] a) P. Du, R. Eisenberg, *Energy Environmental Science* **2012**, *5*, 6012 – 6021; b) A. C. Brooks, K. Basore, S. Bernhard, *Chem. Commun.* **2014**, *50*, 5196 – 5199; c) H. Junge, Z. Codolà, A. Kammer, N. Rockstroh, M. Karnahl, S.-P. Luo, M.-M. Pohl, J. Radnik, S. Gatla, S. Wohlrab, J. Lloret, M. Costas, M. Beller, *J. Mol. Catal. A* **2014**, *395*, 449 – 456; d) W. T. Eckenhoff, *Coord. Chem. Rev.* **2018**, *373*, 295 – 316.

[5] a) J. W. Peters, W. N. Lanzilotta, B. J. Lemon, L. C. Seefeldt, *Science* **1998**, *282*, 1853 – 1858; b) Y. Nicolet, C. Piras, P. Legrand, C. E. Hatchikian, J. C. Fontecilla-Camps, *Structure* **1999**, *7*, 13 – 23; c) Y. Nicolet, A. L. de Lacey, X. Vernède, V. M. Fernandez, E. C. Hatchikian, J. C. Fontecilla-Camps, *J. Am. Chem. Soc.* **2001**, *123*, 1596 – 1601; d) A. Silakov, B. Wenk, E. Reijerse, W. Lubitz, *Phys. Chem. Chem. Phys.* **2009**, *11*, 6592 – 6599; e) G. Berggren, A. Adamska, C. Lambertz, T. R. Simmons, J. Esselborn, M. Atta, S. Gambarelli, J. M. Mouesca, E. Reijerse, W. Lubitz, T. Happe, V. Artero, M. Fontecave, *Nature* **2013**, *499*, 66.

[6] a) J.-F. Capon, F. Gloaguen, P. Schollhammer, J. Talarmin, *Coord. Chem. Rev.* **2005**, *249*, 1664 – 1676; b) S. Tschierlei, S. Ott, R. Lomoth, *Energy Environmental Science* **2011**, *4*, 2340 – 2352; c) N. Wang, M. Wang, L. Chen, L. Sun, *Dalton Trans.* **2013**, *42*, 12059 – 12071; d) W. Lubitz, H. Ogata, O. Rüdiger, E. Reijerse, *Chem. Rev.* **2014**, *114*, 4081 – 4148; e) D. Schilter, J. M. Camara, M. T. Huynh, S. Hammes-Schiffer, T. B. Rauchfuss, *Chem. Rev.* **2016**, *116*, 8693 – 8749; f) M. Watanabe, Y. Honda, H. Hagiwara, T. Ishihara, *J. Photochem. Photobiol. C* **2017**, *33*, 1 – 26.

[7] P. Zhang, M. Wang, Y. Na, X. Li, Y. Jiang, L. Sun, *Dalton Trans.* **2010**, *39*, 1204 – 1206.

[8] T. Yu, Y. Zeng, J. Chen, Y.-Y. Li, G. Yang, Y. Li, *Angew. Chem. Int. Ed.* **2013**, *52*, 5631 – 5635; *Angew. Chem.* **2013**, *125*, 5741 – 5745.

[9] J.-X. Jian, Q. Liu, Z.-J. Li, F. Wang, X.-B. Li, C.-B. Li, B. Liu, Q.-Y. Meng, B. Chen, K. Feng, C.-H. Tung, L.-Z. Wu, *Nat. Commun.* **2013**, *4*, 2695.

[10] J.-X. Jian, C. Ye, X.-Z. Wang, M. Wen, Z.-J. Li, X.-B. Li, B. Chen, C.-H. Tung, L.-Z. Wu, *Energy Environmental Science* **2016**, *9*, 2083 – 2089.

[11] J. I. Goldsmith, W. R. Hudson, M. S. Lowry, T. H. Anderson, S. Bernhard, *J. Am. Chem. Soc.* **2005**, *127*, 7502 – 7510.

[12] Both **Ru-PS** and **Ir-PS** belong to the same class. Nevertheless, the former has a lower activity than the latter by a factor of eight.[11] Multiplying this factor by the TON for $[Fe_2\{\mu\text{-}S(CH_2)_2SO_3Na\}_2(CO)_6]$ still results in a TON lower than those observed in the phosphine containing system of Beller and co-workers.[14a, 15]

[13] F. Gärtner, B. Sundararaju, A.-E. Surkus, A. Boddien, B. Loges, H. Junge, P. H. Dixneuf, M. Beller, *Angew. Chem. Int. Ed.* **2009**, *48*, 9962 – 9965; *Angew. Chem.* **2009**, *121*, 10147 – 10150.

[14] a) F. Gärtner, A. Boddien, E. Barsch, K. Fumino, S. Losse, H. Junge, D. Hollmann, A. Brückner, R. Ludwig, M. Beller, *Chem. Eur. J.* **2011**, *17*, 6425 – 6436; b) D. Hollmann, F. Gärtner, R. Ludwig, E. Barsch, H. Junge, M. Blug, S. Hoch, M. Beller, A. Brückner, *Angew. Chem. Int. Ed.* **2011**, *50*, 10246 – 10250; *Angew. Chem.* **2011**, *123*, 10429 – 10433; c) A. Neubauer, G. Grell, A. Friedrich, S. I. Bokarev, P. Schwarzbach, F. Gärtner, A.-E. Surkus, H. Junge, M. Beller, O. Kühn, S. Lochbrunner, *J. Phys. Chem. Lett.* **2014**, *5*, 1355 – 1360; d) S. Fischer, O. S. Bokareva, E. Barsch, S. I. Bokarev, O. Kühn, R. Ludwig, *ChemCatChem* **2016**, *8*, 404 – 411.

[15] F. Gärtner, D. Cozzula, S. Losse, A. Boddien, G. Anilkumar, H. Junge, T. Schulz, N. Marquet, A. Spannenberg, S. Gladiali, M. Beller, *Chem. Eur. J.* **2011**, *17*, 6998 – 7006.

[16] J. A. S. Howell, N. Fey, J. D. Lovatt, P. C. Yates, P. McArdle, D. Cunningham, E. Sadeh, H. E. Gottlieb, Z. Goldschmidt, M. B. Hursthouse, M. E. Light, *J. Chem. Soc. Dalton Trans.* **1999**, 3015 – 3028.

[17] In a previous article,[14a] a sample of $\mathbf{3}CO + P(\mathbf{c})_3$ dissolved in THF/TEA/H_2O was also studied by ^{31}P NMR spectroscopy. The spectrum shows a signal at $\delta = 84.7$ ppm, which most probably belongs to $\mathbf{1}P(\mathbf{c})_3$ rather than $[Fe_3(CO)_{12}P(\mathbf{c})_3]$ as assumed in the previous article (see Table SI1 in the Supporting Information).

[18] a) A. F. Clifford, A. K. Mukherjee, *Inorg. Chem.* **1963**, *2*, 151 – 153; b) S. M. Grant, A. R. Manning, *Inorg. Chim. Acta* **1978**, *31*, 41 – 48; c) A. Shojaie, J. D. Atwood, *Organometallics* **1985**, *4*, 187 – 190.

[19] S. B. Butts, D. F. Shriver, *J. Organomet. Chem.* **1979**, *169*, 191 – 197.

[20] In the operando IR experiments of this work, an optical filter was installed in front of the mercury light source and the reaction solution was irradiated with visible light of wavelengths in the range of 380–700 nm.

[21] a) G. Bor, *Inorg. Chim. Acta* **1967**, *1*, 81 – 92; b) M. Y. Darensbourg, H. L. Conder, D. J. Darensbourg, C. Hasday, *J. Am. Chem. Soc.* **1973**, *95*, 5919 – 5924; c) D. J. Darensbourg, H. H. Nelson, C. L. Hyde, *Inorg. Chem.* **1974**, *13*, 2135 – 2145.

[22] a) H. L. Conder, M. Y. Darensbourg, *Inorg. Chem.* **1974**, *13*, 506 – 511; b) M. O. Albers, N. J. Coville, T. V. Ashworth, E. Singleton, *J. Organomet. Chem.* **1981**, *217*, 385 – 390; c) L. R. Martin, F. W. B. Einstein, R. K. Pomeroy, *Inorg. Chem.* **1985**, *24*, 2777 – 2785; d) J. E. Ellis, Y. S. Chen, *Organometallics* **1989**, *8*, 1350 – 1361; e) J. A. S. Howell, J. D. Lovatt, P. McArdle, D. Cunningham, E. Maimone, H. E. Gottlieb, Z. Goldschmidt, *Inorg. Chem. Commun.* **1998**, *1*, 118 – 120; f) N. J. Farrer, R. McDonald, J. S. McIndoe, *Dalton Trans.* **2006**, 4570 – 4579.

[23] C. A. Tolman, *Chem. Rev.* **1977**, *77*, 313 – 348.

[24] a) B. Walther, H. Hartung, H.-C. Böttcher, U. Baumeister, U. Böhland, J. Reinhold, J. Sieler, J. Ladriere, H.-M. Schiebel, *Polyhedron* **1991**, *10*, 2423 – 2435; b) M. H. Cheah, S. J. Borg, M. I. Bondin, S. P. Best, *Inorg. Chem.* **2004**, *43*, 5635 – 5644.

[25] W. T. Osterloh, Ph.D. thesis, The University of Texas (Austin), **1982**.

[26] a) E. P. Kyba, R. E. Davis, C. N. Clubb, S.-T. Liu, H. O. A. Palacios, J. S. McKennis, *Organometallics* **1986**, *5*, 869 – 877; b) R. T. Baker, J. C. Calabrese, P. J. Krusic, M. J. Therien, W. C. Trogler, *J. Am. Chem. Soc.* **1988**, *110*, 8392 – 8412.

[27] A. Rahaman, F. R. Alam, S. Ghosh, M. Haukka, S. E. Kabir, E. Nordlander, G. Hogarth, *J. Organomet. Chem.* **2013**, *730*, 123 – 131.

[28] a) P. E. Garrou, *Chem. Rev.* **1985**, *85*, 171 – 185; b) P. W. N. M. van Leeuwen, *Appl. Catal. A* **2001**, *212*, 61 – 81; c) A. W. Parkins, *Coord. Chem. Rev.* **2006**, *250*, 449 – 467; d) S. A. Macgregor, *Chem. Soc. Rev.* **2007**, *36*, 67 – 76.

[29] a) L. W. Gosser, *Inorg. Chem.* **1977**, *16*, 430 – 434; b) M. A. Alvarez, C. Alvarez, M. E. García, V. Riera, M. A. Ruiz, C. Bois, *Organometallics* **1997**, *16*, 2581 – 2589.
[30] a) F. H. Westheimer, S. Huang, F. Covitz, *J. Am. Chem. Soc.* **1988**, *110*, 181 – 185; b) S. K. McIntyre, T. M. Alam, *Magn. Reson. Chem.* **2007**, *45*, 1022 – 1026.
[31] A. G. Abatjoglou, E. Billig, D. R. Bryant, *Organometallics* **1984**, *3*, 923 – 926.
[32] N. M. Doherty, G. Hogarth, S. A. R. Knox, K. A. Macpherson, F. Melchior, D. A. V. Morton, A. G. Orpen, *Inorg. Chim. Acta* **1992**, *198 – 200*, 257 – 270.
[33] K. Kiyotomi, S. Kotaro, T. Shiichiro, *Chem. Lett.* **1979**, *8*, 821 – 822.
[34] W. A. Herrmann, C. Broßmer, K. Öfele, M. Beller, H. Fischer, *J. Mol. Catal. A* **1995**, *103*, 133 – 146.
[35] a) M. Bauer, H. Bertagnolli, in *Methods in Physical Chemistry*, Wiley-VCH, Weinheim, **2012**, pp. 231 – 269; b) M. G. Pfeffer, B. Schäfer, G. Smolentsev, J. Uhlig, E. Nazarenko, J. Guthmuller, C. Kuhnt, M. Wächtler, B. Dietzek, V. Sundström, S. Rau, *Angew. Chem. Int. Ed.* **2015**, *54*, 5044 – 5048; *Angew. Chem.* **2015**, *127*, 5132 – 5136.
[36] a) N. Binsted, S. L. Cook, J. Evans, G. N. Greaves, R. J. Price, *J. Am. Chem. Soc.* **1987**, *109*, 3669 – 3676; b) N. Binsted, J. Evans, G. N. Greaves, R. J. Price, *J. Chem. Soc, Chem. Commun.* **1987**, 1330 – 1333; c) T. E. Westre, A. Di Cicco, A. Filipponi, C. R. Natoli, B. Hedman, E. I. Solomon, K. O. Hodgson, *J. Am. Chem. Soc.* **1995**, *117*, 1566 – 1583.
[37] A particular shell denotes an ensemble of back-scattering atoms of the same type at a particular distance from the iron atom.
[38] R. Jennerjahn, R. Jackstell, I. Piras, R. Franke, H. Jiao, M. Bauer, M. Beller, *ChemSusChem* **2012**, *5*, 734 – 739.
[39] D. Braga, L. Farrugia, F. Grepioni, B. F. G. Johnson, *J. Organomet. Chem.* **1994**, *464*, C39 – C41.
[40] a) M. Bauer, H. Bertagnolli, *J. Phys. Chem. B* **2007**, *111*, 13756 – 13764; b) M. Bauer, C. Gastl, C. Köppl, G. Kickelbick, H. Bertagnolli, *Monatsh. Chem.* **2006**, *137*, 567 – 581; c) E. Hunstock, C. Mealli, M. J. Calhorda, J. Reinhold, *Inorg. Chem.* **1999**, *38*, 5053 – 5060.
[41] To compare this TON with the previously published TONs for the precursor system **3**CO + $P(R)_3$ by Beller et al.,[14a,15] one has to re-calculate the latter, because they were calculated as $n(H_2)/n(\mathbf{3}CO)$ rather than $n(H_2)/n(\mathbf{2}COP(R)_2^-)$, n = amount of substance. In the system **3**CO + $P(R)_3$, the trinuclear precursor was converted into the dinuclear species **2**$COP(R)_2^-$. In this way, the amount of catalyst increases and the TON decreases by a factor of 1.5.
[42] M. H. Cheah, S. J. Borg, S. P. Best, *Inorg. Chem.* **2007**, *46*, 1741 – 1750.
[43] a) S.-P. Luo, E. Mejía, A. Friedrich, A. Pazidis, H. Junge, A.-E. Surkus, R. Jackstell, S. Denurra, S. Gladiali, S. Lochbrunner, M. Beller, *Angew. Chem. Int. Ed.* **2013**, *52*, 419 – 423; *Angew. Chem.* **2013**, *125*, 437 – 441; b) E. Mejía, S.-P. Luo, M. Karnahl, A. Friedrich, S. Tschierlei, A.-E. Surkus, H. Junge, S. Gladiali, S. Lochbrunner, M. Beller, *Chem. Eur. J.* **2013**, *19*, 15972 – 15978; c) S. Fischer, D. Hollmann, S. Tschierlei, M. Karnahl, N. Rockstroh, E. Barsch, P. Schwarzbach, S.-P. Luo, H. Junge, M. Beller, S. Lochbrunner, R. Ludwig, A. Brückner, *ACS Catal.* **2014**, *4*, 1845 – 1849; d) A. J. J. Lennox, S. Fischer, M. Jurrat, S.-P. Luo, N. Rockstroh, H. Junge, R. Ludwig, M. Beller, *Chem. Eur. J.* **2016**, *22*, 1233 – 1238.
[44] L. L. Tinker, N. D. McDaniel, P. N. Curtin, C. K. Smith, M. J. Ireland, S. Bernhard, *Chem. Eur. J.* **2007**, *13*, 8726 – 8732.
[45] B. T. Cooper, J. A. Johnson, S. W. Buckner, *Inorg. Chem.* **1995**, *34*, 5375 – 5377.
[46] In both solvent environments (THF or THF/TEA/H_2O) in the absence of **Ir-PS** and under light irradiation, weak IR contributions of transient species originating from the decomposition of **2**$COP(\mathbf{d})_2^-$ were detected at 2000, 1933, 1920, and 1895 cm^{-1}.
[47] Under catalytic conditions in THF/TEA/H_2O in the presence of **Ir-PS** and under light irradiation, weak IR contributions of transient species originating from the decomposition of **2**$COP(\mathbf{d})_2^-$ were detected at 2043, 1988, 1956, 1890, and 1871 cm^{-1}.
[48] Y.-F. Yu, J. Gallucci, A. Wojcicki, *J. Chem. Soc. Chem. Commun.* **1984**, 653 – 655.
[49] Y. F. Yu, J. Gallucci, A. Wojcicki, *J. Am. Chem. Soc.* **1983**, *105*, 4826 – 4828.
[50] a) L. E. Orgel, *Inorg. Chem.* **1962**, *1*, 25 – 29; b) P. S. Braterman, *Metal Carbonyl Spectra*, Academic Press, London, New York, **1975**.
[51] B. D. McCarthy, D. J. Martin, E. S. Rountree, A. C. Ullman, J. L. Dempsey, *Inorg. Chem.* **2014**, *53*, 8350 – 8361.
[52] F. Gloaguen, *Inorg. Chem.* **2016**, *55*, 390 – 398.
[53] G. A. N. Felton, R. S. Glass, D. L. Lichtenberger, D. H. Evans, *Inorg. Chem.* **2006**, *45*, 9181 – 9184.
[54] M. Zeng, Y. Li, *J. Mater. Chem. A* **2015**, *3*, 14942 – 14962.
[55] L. Bertini, P. Fantucci, L. De Gioia, G. Zampella, *Inorg. Chem.* **2013**, *52*, 9826 – 9841.
[56] Z. Yu, F. Li, L. Sun, *Energy Environmental Sci.* **2015**, *8*, 760 – 775.
[57] a) M. Ferrer, A. Julià, R. Reina, O. Rossell, M. Seco, D. de Montauzon, *J. Organomet. Chem.* **1998**, *560*, 147 – 153; b) M. Ferrer, O. Rossell, M. Seco, M. Soler, M. Font-Bardía, X. Solans, D. de Montauzon, *J. Organomet. Chem.* **2000**, *598*, 215 – 221; c) M. Friederici, I. Angurell, M. Seco, O. Rossell, J. Llorca, *Dalton Trans.* **2011**, *40*, 7934 – 7940.
[58] E. D. Cline, S. E. Adamson, S. Bernhard, *Inorg. Chem.* **2008**, *47*, 10378 – 10388.
[59] W. McFarlane, G. Wilkinson, W. Hübel, in *Inorganic Syntheses, Vol. 8* (Ed.: H. F. Holtzclaw), Wiley, **2007**, pp. 181 – 183.
[60] I. Y. Guzman-Jimenez, J. W. van Hal, K. H. Whitmire, *Organometallics* **2003**, *22*, 1914 – 1922.
[61] a) J. P. Collman, R. G. Finke, P. L. Matlock, R. Wahren, R. G. Komoto, J. I. Brauman, *J. Am. Chem. Soc.* **1978**, *100*, 1119 – 1140; b) T. M. Bockman, H. C. Cho, J. K. Kochi, *Organometallics* **1995**, *14*, 5221 – 5231.
[62] a) R. Reina, O. Rossell, M. Seco, *J. Organomet. Chem.* **1990**, *398*, 285 – 291; b) D. Seyferth, K. S. Brewer, T. G. Wood, M. Cowie, R. W. Hilts, *Organometallics* **1992**, *11*, 2570 – 2579.
[63] a) B. Loges, H. Junge, B. Spilker, C. Fischer, M. Beller, *Chemie Ingenieur Technik* **2007**, *79*, 741 – 753; b) A. Boddien, B. Loges, H. Junge, M. Beller, *ChemSusChem* **2008**, *1*, 751 – 758.
[64] K. Neymeyr, M. Sawall, D. Hess, *J. Chemometrics* **2010**, *24*, 67 – 74.
[65] M. Bauer, C. Gastl, *Phys. Chem. Chem. Phys.* **2010**, *12*, 5575 – 5584.
[66] D. Mellmann, E. Barsch, M. Bauer, K. Grabow, A. Boddien, A. Kammer, P. Sponholz, U. Bentrup, R. Jackstell, H. Junge, G. Laurenczy, R. Ludwig, M. Beller, *Chem. Eur. J.* **2014**, *20*, 13589 – 13602.
[67] N. Binsted, S. S. Hasnain, *J. Synchrotron Radiat.* **1996**, *3*, 185 – 196.

Manuscript received: May 28, 2018
Accepted manuscript online: August 23, 2018
Version of record online: October 19, 2018

6.3 Death and Rebirth: Photocatalytic Hydrogen Production by a Self-Organizing Copper-Iron System

Steffen Fischer, Dirk Hollmann, Stefanie Tschierlei, Michael Karnahl, Nils Rockstroh, Enrico Barsch, Patrick Schwarzbach, Shu-Ping Luo, Henrik Junge, Matthias Beller, Stefan Lochbrunner, Ralf Ludwig, and Angelika Brückner

Communication: *ACS Catal.*, **2014**, *4* (6), 1845-1849
DOI: 10.1021/cs500387e

Shortened Abstract

This study provides detailed mechanistic insights into light-driven hydrogen production using an abundant copper–iron system. It focuses on the role of the heteroleptic copper photosensitizer [Cu(P^P)(N^N)]$^+$, which can be oxidized or reduced after photoexcitation. By means of IR, EPR, and UV/vis spectroscopy as well as computational studies and spectroelectrochemistry, the possibility of both mechanisms was confirmed. UV/vis spectroscopy revealed the reorganization of the original heteroleptic photosensitizer during catalysis toward a homoleptic [Cu(N^N)$_2$]$^+$ species. Operando FTIR spectroscopy showed the formation of a catalytic diiron intermediate, which resembles well-known hydrogenase active site models.

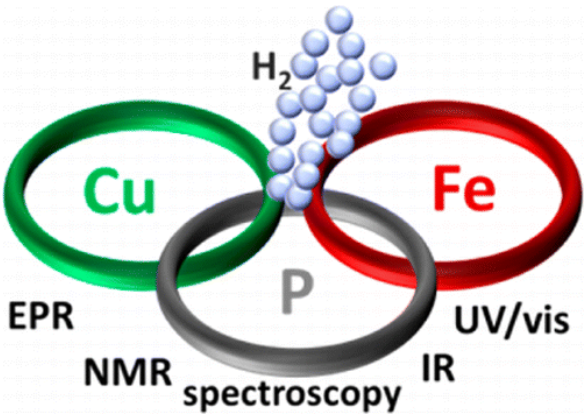

Contribution to this work (25%)

Steffen Fischer designed and performed the operando continuous flow FTIR and NMR experiments. He analyzed the spectroscopic data thereby collected and identified the formation of the complex [Fe$_2$(CO)$_6$(μ-CO)(μ-P(Ph)$_2$)]$^-$. Steffen Fischer participated significantly in the evaluation and discussion of the results and was involved in the preparation of the manuscript. The overall contribution is about 25%.

ACS Catalysis

Letter

pubs.acs.org/acscatalysis

Death and Rebirth: Photocatalytic Hydrogen Production by a Self-Organizing Copper−Iron System

Steffen Fischer,[†,‡] Dirk Hollmann,[‡] Stefanie Tschierlei,[§] Michael Karnahl,[‡] Nils Rockstroh,[‡] Enrico Barsch,[†,‡] Patrick Schwarzbach,[§] Shu-Ping Luo,[‡,∥] Henrik Junge,[‡] Matthias Beller,[‡] Stefan Lochbrunner,[§] Ralf Ludwig,[†,‡,*] and Angelika Brückner*[,‡]

[†]Institute of Chemistry, Department Physical Chemistry, University of Rostock, Dr. Lorenz-Weg 1, 18059 Rostock, Germany

[‡]Leibniz Institute for Catalysis at the University of Rostock, Albert Einstein-Straße 29a, 18059 Rostock, Germany

[§]Institute of Physics, University of Rostock, Universitätsplatz 3, 18055 Rostock, Germany

[∥]State Key Laboratory Breeding Base of Green Chemistry-Synthesis Technology, Zhejiang University of Technology, 310014 Hangzhou, China

Supporting Information

ABSTRACT: This study provides detailed mechanistic insights into light-driven hydrogen production using an abundant copper−iron system. It focuses on the role of the heteroleptic copper photosensitizer $[Cu(P\text{^}P)(N\text{^}N)]^+$, which can be oxidized or reduced after photoexcitation. By means of IR, EPR, and UV/vis spectroscopy as well as computational studies and spectroelectrochemistry, the possibility of both mechanisms was confirmed. UV/vis spectroscopy revealed the reorganization of the original heteroleptic photosensitizer during catalysis toward a homoleptic $[Cu(N\text{^}N)_2]^+$ species. Operando FTIR spectroscopy showed the formation of a catalytic diiron intermediate, which resembles well-known hydrogenase active site models.

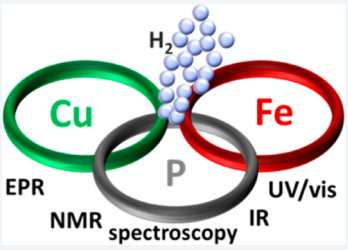

KEYWORDS: *proton reduction, iron catalysts, copper photosensitizer, operando spectroscopy, catalytic intermediates*

The global rising population and energy demand are leading to a faster depletion of fossil resources and boost the search for sustainable alternatives.[1,2] These options ideally utilize natural energy sources such as water, wind or solar power that produce no waste and emissions such as carbon dioxide.[3,4] A second major requirement is the constant availability of energy, which calls for efficient energy storage materials and capacities.[5] Currently, several approaches are controversially discussed in the literature, ranging from electricity storage in batteries and supercapacitors to chemical energy storage mainly in hydrogen or hydrogen-releasing molecules (liquid organic hydrogen carriers).[6] In particular, hydrogen is very attractive because of its high energy content and clean combustion.[7] However, sustainable hydrogen production from water using sunlight is still demanding and needs further improvement in several aspects, such as the replacement of noble metals, increased efficiency, use of pure visible light and a thorough understanding of the underlying processes.[8,9] Recent progress on the replacement of noble metals showing high hydrogen production rates for a system composed of a nonprecious iron water reduction catalyst (WRC), a heteroleptic copper photosensitizer (CuPS **1**), and triethylamine acting as sacrificial reductant (SR) was made in our groups.[10−12]

Systematic variation of the CuPS and its ligand structure resulted in the most efficient fully noble-metal-free hydrogen generating system so far, with a maximum turnover number (TON_H) of 1330.[12,15] However, the lifetime of the overall catalytic system varied from 5 to 60 h, depending on the applied conditions and copper complexes. Preliminary experiments suggested the predominance of an oxidative reaction pathway in which the CuPS is first oxidized after photoexcitation (Scheme 1).

Interestingly, negligible activity was observed with the homoleptic sensitizer $[Cu(N\text{^}N)_2]^{2+}$ (CuPS **2**) with two phenanthroline ligands, although it also absorbs UV−vis light and should thus be able to act as a photosensitizer, as well. The missing activity may be due to two possible reasons: The redox potentials required for the electron transfer are not sufficient[13] or the lifetime of the excited triplet state of complex **2** is too short.[14]

Information about the different activation and deactivation pathways of the iron WRC and the CuPS as well as their catalytic intermediates is still rare. Thus, a detailed understanding of the catalytic cycle may contribute to the development of more efficient systems. Therefore, it was the aim of this study to investigate the mechanism of the light-driven production of hydrogen by a heteroleptic CuPS and an iron WRC using several methods, such as operando FTIR spectroscopy, UV/vis and in situ EPR spectroscopy, as well as their combinations with spectroelectrochemical[16,17] techniques.

Received: March 24, 2014
Revised: April 29, 2014
Published: May 1, 2014

   dx.doi.org/10.1021/cs500387e | *ACS Catal.* 2014, 4, 1845−1849

Scheme 1. Reductive (red) and Oxidative (blue) Reaction Pathway and the Initial Structures of the Applied Copper Photosensitizer (CuPS, e.g., 1) and Water Reduction Catalyst (WRC)

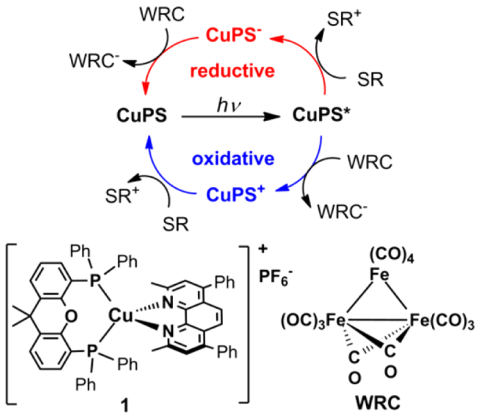

The experimental results are supported by computational studies as well as by catalytic measurements.

The heteroleptic copper complex **1** $[Cu(P^P)(N^N)]^+$, which contains bidentate P^P (Xantphos) and N^N (2,9-dimethyl-4,7-diphenyl-1,10-phenanthroline) chelate ligands, exhibits a distorted tetrahedral structure of the Cu^+ center in the ground state (Scheme 1).[18−20] Upon photoexcitation, a metal-to-ligand charge transfer (MLCT) to the phenanthroline ligand occurs, followed by a structural transformation to a triplet excited state; with a more square planar geometry in terms of the ligand orientation around the formal Cu^{2+} center; and finally, an intersystem crossing.[21] This long-lived excited state can now be reduced or oxidized, depending on the reaction partners in the catalytic system, resulting in $\mathbf{1}^-$ or $\mathbf{1}^+$, respectively.[14] Both pathways could be considered to be responsible for photocatalytic activity. At the beginning, the reductive pathway was investigated by means of EPR spectroscopy. In this context, a reduced CuPS was detected under UV/vis irradiation in the presence of triethylamine (TEA), which acts as a sacrificial reductant (Figure 1a).

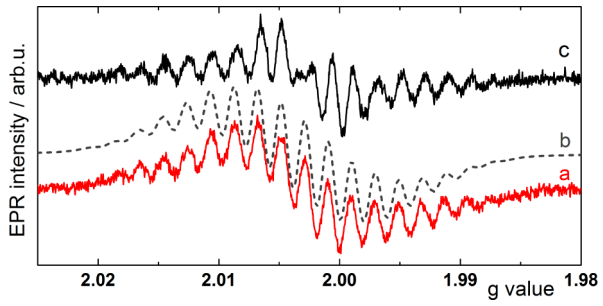

Figure 1. EPR spectra of (a) CuPS **1** in THF/TEA (4/1) under UV/vis irradiation, (b) the respective EPR simulation (g = 2.0034, line width ΔB = 2.5G, 2 × A_H = 10.0G, 2 × A_H = 7.0G, 2 × A_N = 3.4G, 1 × A_{Cu} = 3.4G), and (c) $\mathbf{1}^-$ obtained at −1.5 V vs Ag/Ag^+.

Analysis of the superhyperfine structure (shfs) revealed the coupling of the free electron to all hydrogen and nitrogen nuclei of the aromatic system in the phenanthroline ligand (4 × H (I = 1/2), 2 × N (I = 1)) as well as to the copper nucleus (I = 3/2) (Figure 1b). In combination with the g value of 2.0034, which is close to that of the free electron, the shfs coupling constants suggest a complete electron delocalization within the N^N ligand,[22] in contrast to a partial ligand-metal delocalization observed in an analogous iridium photosensitizer (IrPS).[23] This finding was further supported by EPR spectroelectrochemistry, providing the same EPR spectrum (Figure 1c). Moreover, the full reversibility of the reductive cycle along with the high stability of complex **1** under reductive conditions was proven by UV/vis absorption spectroscopy (Supporting Information (SI) Figures S1, S2). Here, the electrochemical as well as the photochemical reduction did not lead to any changes in the absorption behavior.

In contrast to the reductive pathway, the formation of $\mathbf{1}^+$ within an oxidative pathway can occur with $[Fe_3(CO)_{12}]$ as an electron acceptor (Scheme 1). Applying EPR spectroscopy, characteristic decomposition products $[Fe_3(CO)_{12}]^{\bullet-}$, $[Fe_3(CO)_{11}]^{\bullet-}$, and $[Fe_2(CO)_8]^{\bullet-}$, which were detected for the analogous IrPS system, as well,[24] were monitored. Neither $Cu^{II}PS$[25] nor $Cu^{I}PS^+$ species have been detected in the present study. Even with EPR spectroelectrochemistry (+1.5 V vs Ag/Ag^+), no oxidized copper complex was observed, indicating an unexpected reaction pathway under oxidative conditions.

This oxidation pathway was examined by UV/vis spectroscopy, which can distinguish among various redox states of the copper species by their different MLCT transitions. For instance, in complex **1** only the phenanthroline moiety contributes to the MLCT transition around 390 nm. This band decreases after several redox cycles, each composed of an oxidation step, followed by a rereduction process (Figure 2),

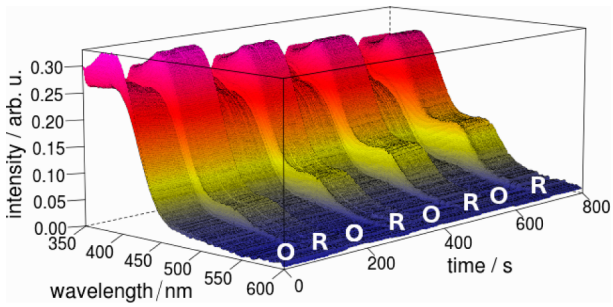

Figure 2. Oxidation (O, +1.5 V) and rereduction (R, at −0.5 V vs Ag/Ag^+) cycles (duration of each step: 100 s) of **1** in acetonitrile solution monitored by UV/vis spectroelectrochemistry.

indicating that the concentration of **1** in the solution becomes lower. Furthermore, a new band at 475 nm rises during each rereduction step, which corresponds to the well-known homoleptic CuPS $[Cu(N^N)_2]^+$ (**2**), showing an absorption band exactly in this range (see SI). Thus, the concentration of the new generated complex **2** increases during the redox cycles. Consequently, the concentration of the oxidized species $\mathbf{2}^+$, formed within these oxidation steps, also rises. However, the absorption spectra of the oxidized species $\mathbf{1}^+$ (still present) and $\mathbf{2}^+$ (gradually formed) during the several oxidation processes are almost identical, which is caused by the exclusive contribution of the phenanthroline ligand to the MLCT transition in the respective complexes (O in Figure 2).

In addition, the absorption spectra were measured under photochemically induced oxidative conditions with methylviologen (MV, 1,1′-dimethyl-4,4′-bipyridinium dichloride) as chemical oxidant and light irradiation at 350 nm.[26,27] Again, the MCLT band of **1** decreases, and the band of complex **2** appears in the visible region over time (SI Figure S2).

dx.doi.org/10.1021/cs500387e | ACS Catal. 2014, 4, 1845−1849

As mentioned above, the absorption behavior suggests that the original heteroleptic complex **1** is decomposed exclusively under the oxidative conditions by a dissociation of the sterically demanding diphosphine ligand. Indeed, DFT calculations of the oxidized species of **1** point to an elongation of the Cu−P bond from 0.233 nm (**1**) to 0.239 nm ($\mathbf{1}^{+}$) and 0.240 nm in ($\mathbf{1}^{2+}$) and to a decreasing P−Cu−P bite angle in the order 116.8° (**1**) > 109.2 ($\mathbf{1}^{+}$) > 103.2 ($\mathbf{1}^{2+}$), which provides further evidence for the proposed dissociation reaction (SI Table S1). However, this dissociation does not lead to a complete destruction of the structure of **1**. Instead, a second phenanthroline ligand coordinates to resaturate the copper center, forming the homoleptic complex $[Cu(N\text{^}N)_2]^+$ **2**. This dynamic ligand exchange between hetero- and homoleptic copper complexes was also recently reported for related CuPS.[18]

Following the aforementioned results, the crucial role of the diphosphine ligand became obvious. Caused by an electrochemical oxidation of **1**, without $[Fe_3(CO)_{12}]$ as electron acceptor, the P^P ligand is converted to Xantphosdioxide, as proven by ^{31}P NMR spectroscopy (SI Figure S4).[28] In contrast, the irradiation of **1** in the presence of the electron acceptor MV does not lead to Xantphosdioxide, revealing a different mechanism under photooxidative conditions (SI Figure S4). Thus, especially the role of the electron acceptor seems to determine the respective reaction.

Consequently, the reaction of the diphosphine ligand with the iron precursor $[Fe_3(CO)_{12}]$ has been studied by operando FTIR spectroscopy. Starting with **1** and $[Fe_3(CO)_{12}]$ in a solution of THF/TEA/H_2O, the conversion of the iron precursor to $[HFe_3(CO)_{11}]^-$ is observed within the first minute of irradiation, giving rise to characteristic bands at 2064(w), 1999(s), 1993(s), 1975(m), and 1748(m) cm^{-1} (Figure 3, red).[24,29] This complex is already known as active WRC in related iridium-based photocatalytic systems.[24,29] As the reaction proceeds, $[HFe_3(CO)_{11}]^-$ is transformed into $[Fe_2(\mu\text{-}PPh_2)(\mu\text{-}CO)(CO)_6]^-$ (**3**) with four intense bands at 2015(m), 1965(vs), 1934(m), 1916(s) cm^{-1} (Figure 3, blue). This transformation is accompanied by an enhanced hydrogen evolution (Figure 3, black curve). Temporarily appearing intermediate complexes are not identified yet (SI Figure S5). After 35 h, **3** is the only carbonyl compound present in solution. In the further course, its concentration drops after 120 h, which is consistent with the end of hydrogen evolution, showing the catalytic relevance of this species (SI Figure S6).

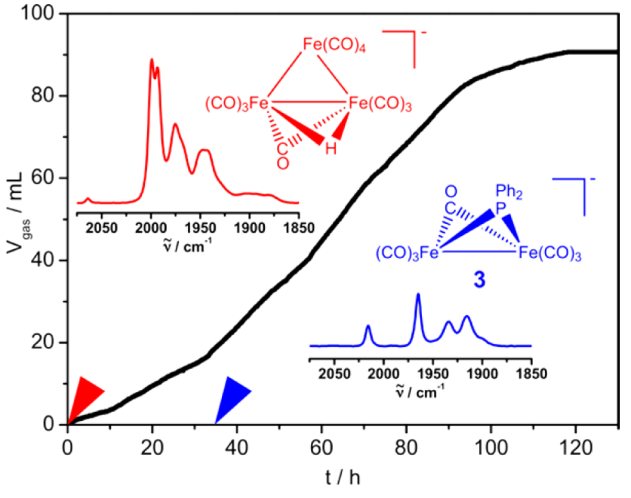

Figure 3. Results of the operando FTIR measurements: gas evolution curve (black) and IR spectrum of the solution at t = 1 min (red) and t = 35 h (blue). Conditions: 7.0 μmol of **1**, 10.0 μmol of $[Fe_3(CO)_{12}]$, 20 mL of THF/TEA/H_2O (4/1/1), visible light irradiation (1.5 W), 25 °C.

The assignment of **3** is supported by spectral data specified in works of Ellis, Walther, or Best et al.[30−32] (SI Table S2) and by DFT calculations (SI Figure S7). Its structure is analogous to monoreduced diiron hydrogenase mimics, which possess similar IR patterns.[33−36] The present PPh_2 ligand most probably originates from the decomposition of free Xantphos,[37] which is closely related to observations made with PPh_3 in the presence of hydrogen or heat.[38,39]

After complete conversion of $[Fe_3(CO)_{12}]$ to **3**, assured by operando FTIR spectroscopy, a sample of the reaction mixture was analyzed by means of NMR spectroscopy. The respective ^{31}P NMR spectrum (Figure 4, blue) displays a singlet peak at δ = 126.9 ppm, which is in good agreement with the chemical shift of **3**.[31,32]

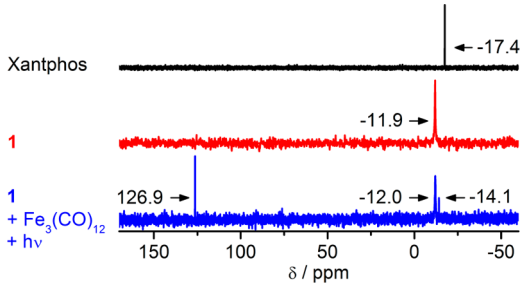

Figure 4. ^{31}P NMR investigations: black, free Xantphos ligand; red, **1**; blue, 21.3 μmol of **1** and 22.6 μmol of $[Fe_3(CO)_{12}]$ in 20 mL of solvent mixture after 5.5 h of visible light irradiation (6 W). All compounds were dissolved in THF/TEA/H_2O (4/1/1).

The additional signal at δ = −12.0 ppm can be assigned to complex **1**, showing that even after long reaction times, some **1** is still left, whereas the small signal at δ = −14.1 ppm does not match to the uncoordinated Xantphos and remains unassigned. The corresponding ^{1}H NMR spectrum of the reaction mixture reveals no hydride signal, which supports the structural assignment of the catalytically active species **3**.

Indeed, application of the homoleptic complex **2** along with the Xantphos ligand and $[Fe_3(CO)_{12}]$ yielded the same photocatalytic activity as determined for **1** and $[Fe_3(CO)_{12}]$ (Figure 5 and SI Table S4). The respective turnover numbers ($TON_{H,Cu}$) and frequencies (TOF) are nearly the same within the error of the catalytic experiments (SI Table S4). Note that under these conditions, CuPS **1** has been detected by ^{31}P NMR. This indicates a ligand exchange that leads to a "rebirth" of the active photosensitizer **1**.

It can be concluded that in both cases, the catalytic activity originates from the same dinuclear iron-diphenylphosphido species **3**, arising from a self-organization process. The nature of this essential species was further proven by an experiment without the diphosphine ligand, in which no activity could be observed (Figure 5, gray curve). Hence, the diphenylphosphido fragment is a crucial part of the active species, and only its existence enables an efficient hydrogen production within this fully noble-metal-free system.

In the present work, the mechanism and catalytic intermediates of the photoinduced iron-catalyzed hydrogen

dx.doi.org/10.1021/cs500387e | ACS Catal. 2014, 4, 1845−1849

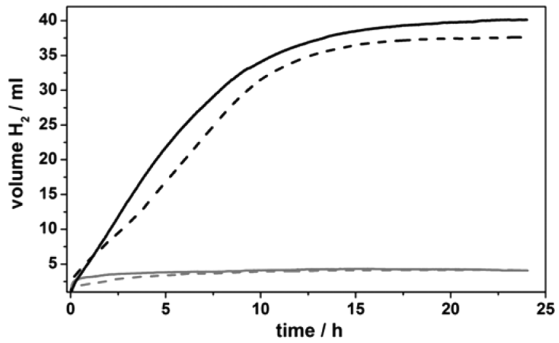

Figure 5. Hydrogen evolution curves using CuPS (5 μmol) in the presence of $[Fe_3(CO)_{12}]$ (5 μmol) as WRC in a mixture of THF/TEA/H_2O (4/3/1, 10 mL). Black dashed, **1**; black solid, **2** with Xantphos (5 μmol); gray solid, **2** without Xantphos; gray dashed, only Xantphos and $[Fe_3(CO)_{12}]$. See SI Table S4.

production in the presence of a heteroleptic CuPS were investigated. First, the attention was focused on the photosensitizer, which could be oxidized or reduced after photoexcitation. UV/vis and in situ EPR spectroscopy and their combination with electrochemistry revealed the existence of both an oxidative and a reductive pathway. The latter one is reversible with respect to the CuPS. Instead, the obtained results for the oxidative pathway, supported by DFT calculations, evidenced a photoinduced reassembling of the copper-bound ligands forming partly a homoleptic phenanthroline complex. After liberation from copper, the uncoordinated phosphine ligand releases a (PPh_2) fragment, which reacts with $[Fe_3(CO)_{12}]$ to $[Fe_2(\mu\text{-}PPh_2)(\mu\text{-}CO)(CO)_6]^-$ (**3**). The structural assignment of this catalytic intermediate was confirmed by operando FTIR and NMR spectroscopy as well as DFT.

This unique self-organizing process provides a comfortable access to an efficient and fully noble-metal-free system for the photocatalytic reduction of protons without demanding synthesis. Furthermore, the detailed understanding of the mechanism supports rational catalyst design.

■ ASSOCIATED CONTENT

Ⓢ Supporting Information

Experimental and catalytic details, UV/vis spectroelectrochemical data, IR spectra, and DFT calculations. This material is available free of charge via the Internet at http://pubs.acs.org.

■ AUTHOR INFORMATION

Corresponding Authors

*Fax: (+49) 381 498 6524. E-mail: ralf.ludwig@uni-rostock.de.
*Fax: (+49) 381 1281 51244. E-mail: angelika.brueckner@catalysis.de.

Notes

The authors declare no competing financial interest.

■ ACKNOWLEDGMENTS

Financial support from the Federal Ministry of Education and Research of Germany (BMBF) within the project "Light2-Hydrogen" is gratefully acknowledged.

■ REFERENCES

(1) Lewis, N. S.; Nocera, D. G. *Proc. Natl. Acad. Sci. U.S.A.* **2006**, *103*, 15729−15735.
(2) Armaroli, N.; Balzani, V. *Angew. Chem., Int. Ed.* **2007**, *46*, 52−66.
(3) Schiermeier, Q.; Tollefson, J.; Scully, T.; Witze, A.; Morton, O. *Nature* **2008**, *454*, 816−823.
(4) Armaroli, N.; Balzani, V. *Energy for a Sustainable World − From the Oil Age to a Sun-Powered Future*; Wiley-VCH: Weinheim, 2010.
(5) Jacobson, M. Z. *Energy Environ. Sci.* **2009**, *2*, 148−173.
(6) Styring, S. *Faraday Discuss.* **2012**, *155*, 357−376.
(7) Amouyal, E. *Sol. Energy Mater. Sol. Cells* **1995**, *38*, 249−276.
(8) Du, P.; Eisenberg, R. *Energy Environ. Sci.* **2012**, *5*, 6012−6021.
(9) Khnayzer, R. S.; McCusker, C. E.; Olaiya, B. S.; Castellano, F. N. *J. Am. Chem. Soc.* **2013**, *135*, 14068−14070.
(10) Luo, S.-P.; Mejía, E.; Friedrich, A.; Pazidis, A.; Junge, H.; Surkus, A.-E.; Jackstell, R.; Denurra, S.; Gladiali, S.; Lochbrunner, S.; Beller, M. *Angew. Chem., Int. Ed.* **2013**, *52*, 419−423.
(11) Karnahl, M.; Mejía, E.; Rockstroh, N.; Tschierlei, S.; Luo, S.-P.; Grabow, K.; Kruth, A.; Brüser, V.; Junge, H.; Lochbrunner, S.; Beller, M. *ChemCatChem.* **2014**, *6*, 82−86.
(12) Mejía, E.; Luo, S.-P.; Karnahl, M.; Friedrich, A.; Tschierlei, S.; Surkus, A.-E.; Junge, H.; Gladiali, S.; Lochbrunner, S.; Beller, M. *Chem.—Eur. J.* **2013**, *19*, 15972−15978.
(13) Neubauer, A.; Grell, G.; Friedrich, A.; Bokarev, S. I.; Schwarzbach, P.; Gärtner, F.; Surkus, A.-E.; Junge, H.; Beller, M.; Kühn, O.; Lochbrunner, S. *J. Phys. Chem. Lett.* **2014**, *5*, 1355−1360.
(14) Armaroli, N. *Chem. Soc. Rev.* **2001**, *30*, 113−124.
(15) van den Bosch, B.; Chen, H.-C.; van der Vlugt, J. I.; Brouwer, A. M.; Reek, J. N. H. *ChemSusChem* **2013**, *6*, 790−793.
(16) Dunsch, L. *J. Solid State Electrochem.* **2011**, *15*, 1631−1646.
(17) Kaim, W.; Fiedler, J. *Chem. Soc. Rev.* **2009**, *38*, 3373−3382.
(18) Kaeser, A.; Mohankumar, M.; Mohanraj, J.; Monti, F.; Holler, M.; Cid, J.-J.; Moudam, O.; Nierengarten, I.; Karmazin-Brelot, L.; Duhayon, C.; Delavaux-Nicot, B.; Armaroli, N.; Nierengarten, J.-F. *Inorg. Chem.* **2013**, *52*, 12140−12151.
(19) Penfold, T. J.; Karlsson, S.; Capano, G.; Lima, F. A.; Rittmann, J.; Reinhard, M.; Rittmann-Frank, M. H.; Braem, O.; Baranoff, E.; Abela, R.; Tavernelli, I.; Rothlisberger, U.; Milne, C. J.; Chergui, M. *J. Phys. Chem. A* **2013**, *117*, 4591−4601.
(20) McCusker, C. E.; Castellano, F. N. *Inorg. Chem.* **2013**, *52*, 8114−8120.
(21) Iwamura, M.; Watanabe, H.; Ishii, K.; Takeuchi, S.; Tahara, T. *J. Am. Chem. Soc.* **2011**, *133*, 7728−7736.
(22) Kaim, W.; Ernst, S. *J. Phys. Chem.* **1986**, *90*, 5010−5014.
(23) Bokarev, S. I.; Hollmann, D.; Pazidis, A.; Neubauer, A.; Radnik, J.; Kühn, O.; Lochbrunner, S.; Junge, H.; Beller, M.; Brückner, A. *Phys. Chem. Chem. Phys.* **2014**, *16*, 4789−4796.
(24) Hollmann, D.; Gärtner, F.; Ludwig, R.; Barsch, E.; Junge, H.; Blug, M.; Hoch, S.; Beller, M.; Brückner, A. *Angew. Chem., Int. Ed.* **2011**, *50*, 10246−10250.
(25) Tromp, M.; van Strijdonck, G. P. F.; van Berkel, S. S.; van den Hoogenband, A.; Feiters, M. C.; de Bruin, B.; Fiddy, S. G.; van der Eerden, A. M. J.; van Bokhoven, J. A.; van Leeuwen, P. W. N. M.; Koningsberger, D. C. *Organometallics* **2010**, *29*, 3085−3097.
(26) Streich, D.; Astuti, Y.; Orlandi, M.; Schwartz, L.; Lomoth, R.; Hammarström, L.; Ott, S. *Chem.—Eur. J.* **2010**, *16*, 60−63.
(27) Lomoth, R.; Häupl, T.; Johansson, O.; Hammarström, L. *Chem.—Eur. J.* **2002**, *8*, 102−110.
(28) Deb, B.; Dutta, D. K. *Polyhedron* **2009**, *28*, 2258−2262.
(29) Gärtner, F.; Boddien, A.; Barsch, E.; Fumino, K.; Losse, S.; Junge, H.; Hollmann, D.; Brückner, A.; Ludwig, R.; Beller, M. *Chem.—Eur. J.* **2011**, *17*, 6425−6436.
(30) Ellis, J. E.; Chen, Y. S. *Organometallics* **1989**, *8*, 1350−1361.
(31) Walther, B.; Hartung, H.; Böttcher, H.-C.; Baumeister, U.; Böhland, U.; Reinhold, J.; Sieler, J.; Ladriere, J.; Schiebel, H.-M. *Polyhedron* **1991**, *10*, 2423−2435.
(32) Cheah, M. H.; Borg, S. J.; Bondin, M. I.; Best, S. P. *Inorg. Chem.* **2004**, *43*, 5635−5644.
(33) Gimbert-Suriñach, C.; Bhadbhade, M.; Colbran, S. B. *Organometallics* **2012**, *31*, 3480−3491.
(34) Cheah, M. H.; Borg, S. J.; Best, S. P. *Inorg. Chem.* **2007**, *46*, 1741−1750.

(35) Tschierlei, S.; Ott, S.; Lomoth, R. *Energy Environ. Sci.* **2011**, *4*, 2340−2352.
(36) Tard, C.; Pickett, C. J. *Chem. Rev.* **2009**, *109*, 2245−2274.
(37) Garrou, P. E. *Chem. Rev.* **1985**, *85*, 171−185.
(38) Almeida Lenero, K. Q.; Guari, Y.; Kamer, P. C. J.; van Leeuwen, P. W. N. M.; Donnadieu, B.; Sabo-Etienne, S.; Chaudret, B.; Lutz, M.; Spek, A. L. *Dalton Trans.* **2013**, *42*, 6495−6512.
(39) Bradford, C. W.; Nyholm, R. S. *J. Chem. Soc., Dalton Trans.* **1973**, 529−533.

6.4 Copper-Based Photosensitizers in Water Reduction: A More Efficient In Situ Formed System and Improved Mechanistic Understanding

Alastair J. J. Lennox, Steffen Fischer, Mark Jurrat, Shu-Ping Luo, Nils Rockstroh, Henrik Junge, Ralf Ludwig, and Matthias Beller

Communication: *Chem. Eur. J.*, **2016**, *22* (4), 1233-1238
DOI: 10.1002/chem.201503812

Shortened Abstract

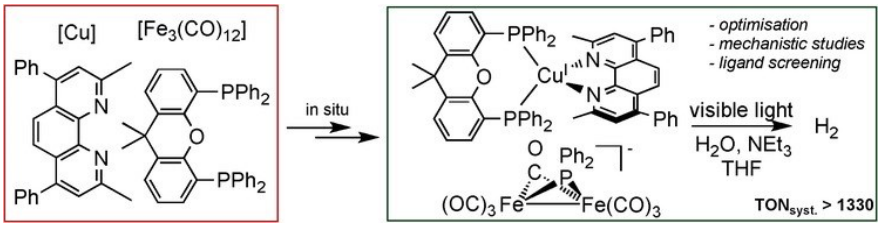

Cheap ′n′ easy H_2: The reduction of water was achieved through a non-noble-metal-based homogeneous catalyst system that is formed in situ. Mechanistic studies confirm a heteroleptic Cu complex as the active photosensitiser (PS) and an in situ formed Fe–phosphido dimer complex as the water reduction catalyst (see scheme). The in situ method was used to screen a range of ligands for the active PS, which led to the identification of a number of structural features important to longevity and performance.

Contribution to this work (30%)

Steffen Fischer was involved in synthesis and characterization of the iron catalyst $[NEt_4][Fe_2(CO)_6(\mu\text{-}CO)(\mu\text{-}P(Ph)_2)]$ as well as experiments for assessing the performance of this complex. He carried out the operando FTIR ESI-MS gas volumetric experiments and analyzed the IR spectroscopic data. Furthermore, he performed FTIR experiments investigating the conditions for the P-C cleavage reaction. Steffen Fischer participated in the evaluation and discussion of the results and in the preparation of the manuscript. The overall contribution is about 30%.

ChemPubSoc Europe

DOI: 10.1002/chem.201503812

CHEMISTRY A European Journal Communication

Homogeneous Catalysis

Copper-Based Photosensitisers in Water Reduction: A More Efficient In Situ Formed System and Improved Mechanistic Understanding

Alastair J. J. Lennox,[a] Steffen Fischer,[b] Mark Jurrat,[a] Shu-Ping Luo,[c] Nils Rockstroh,[a] Henrik Junge,[a] Ralf Ludwig,[b] and Matthias Beller*[a]

Abstract: The reduction of water has been achieved through a non-noble-metal-based homogeneous catalyst system that is formed in situ. Optimisation of the ligand quantities increased catalyst turnover numbers compared to preformed complexes. Mechanistic studies confirm a heteroleptic Cu complex as the active photosensitiser (PS) and an in situ formed Fe–phosphido dimer complex as the water reduction catalyst. The in situ method has been used to screen a range of ligands for the active PS, which has led to the identification a number of structural features important to longevity and performance.

Transfer to a "hydrogen economy"[1] is considered a viable solution to prevent the well-documented negative effects associated with the rate of our fossil fuel consumption. Presently, H_2 is generated by steam reformation of fossil fuels themselves, thereby rendering the whole process ineffectual in its original objectives. Sustainable generation of this energy-dense and clean-burning gas, using renewable energy and materials, must therefore be realised.[2,3] To this end, solar-promoted water-splitting has become a hugely popular research endeavour,[4–8] from which the exploitation of homogeneous photocatalysis has experienced particular success,[9–11] especially in the utilisation of visible light, in contrast to the vast volume of literature on UV-absorbing semiconductor-based heterogeneous systems.[12–14]

There is a class of molecular systems that are composed of three-components and linked through a cascade.[15] They were originally inspired by nature, where reduction equivalents are generated by light in combination with coupled redox cycles in photosystems II and I.[16,17] An organometallic photosensitiser (PS) complex can be excited with visible light by a metal-to-ligand-charge-transfer ($d\rightarrow\pi^*$), which undergoes electron transfer to a water reduction catalyst (WRC) and from a sacrificial reductant (SR). The reduced WRC can then reduce aqueous protons to liberate hydrogen gas (Figure 1). Due to their high redox potentials and activity under visible light irradiation, PSs based on Ru[18–20] and Ir[21–24] have become popular choices. However, despite numerous advances, there remain very significant, fundamental limitations that restrict the utility of this technology. One such limitation is the cost and complexity of the catalysts employed, which has prompted the birth of cheap non-noble-metal systems.[25–28] In 2013, we demonstrated that, in the presence of an iron-based WRC, heteroleptic Cu complexes, containing a bidentate phosphine and a phenanthroline ligand, behave as suitable photosensitisers for proton reduction reactions.[29,30] These Cu-based complexes exhibit long excited-state lifetimes and a wide, ligand-dependent, range of reduction potentials.[30] We previously found evidence for both oxidative and reductive quenching pathways of the excited state (Figure 1).[31]

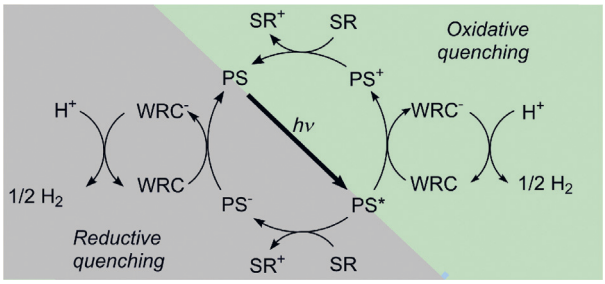

Figure 1. The two possible pathways in the generalised homogeneous photocatalytic cascade mechanism for the reduction of protons to H_2 gas. PS = photosensitiser, WRC = water reduction catalyst, SR = sacrificial reductant.

The Cu PS complexes are prepared by a two-step synthesis involving an overnight reflux, followed by a second reflux and recrystallisation. In order to improve the system, bypassing the synthesis of the organometallic complex is necessary to render the process operationally simpler and therefore time and cost effective. In addition, it would provide a facile method by which a broad range of ligands could be tested in order to es-

[a] Dr. A. J. J. Lennox, M. Jurrat, Dr. N. Rockstroh, Dr. H. Junge, Prof. Dr. M. Beller
Leibniz Institute for Catalysis at the University of Rostock
Albert Einstein-Straße 29a, 18059 Rostock (Germany)
E-mail: Matthias.beller@catalysis.de

[b] S. Fischer, Prof. Dr. R. Ludwig
Institute of Chemistry, Department Physical Chemistry
University of Rostock, Dr. Lorenz-Weg 1, 18059 Rostock (Germany)

[c] Dr. S.-P. Luo
State Key Laboratory Breeding Base of
Green Chemistry-Synthesis Technology, Zhejiang University of Technology
310014 Hangzhou (P.R. China)

Supporting information and ORCID(s) from the author(s) for this article are available on the WWW under http://dx.doi.org/10.1002/chem.201503812.

tablish a more stable and active system, whilst rapidly learning about the important structural features. To this end, a model system was identified, composed of a simple copper salt ($[Cu(MeCN)_4]PF_6$, (**1**)), a bidentate phosphine ligand (xantphos (**2a**)), a phenanthroline derivative previously known to be effective in harvesting light (bathocuproine (**3a**)) and a WRC precursor ($[Fe_3(CO)_{12}]$ (**4**)); see Figure 2, right. Employing equimolar amounts of each component, it was established that upon their dissolution in THF and water, with the addition of a sacrificial reductant (NEt_3) and subsequent visible light irradiation, H_2 could be generated in comparable volumes to the use of a molecularly defined, preformed, PS (Figure 2). This confirmed that rapid and selective formation of the active PS complex occurs in situ. Analysis of the generated gas mixture showed the presence of $>98\%$ H_2 with small ($<0.4\%$) quantities of CO dissociating from the WRC.

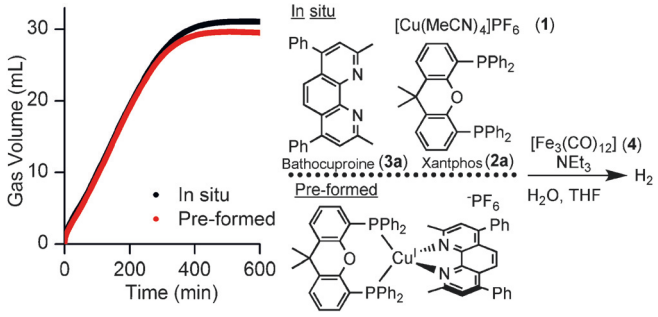

Figure 2. Gas evolution curves from the use of pre-formed (red) and in situ formed (black) catalyst systems.

When the catalyst components were added as solids to the flask, followed by the solvent mixture, the system was found to be very sensitive and reproducibility was poor. The use of stock solutions for each reacting component allowed for a more controlled and accurate addition of each species and the reproducibility could be improved. However, the catalyst activity, longevity and decay rates were found to be dependent on the order of their addition. This interesting observation was initial evidence of the multiple processes occurring in solution and their relative rates. The most dramatic effect occurred when bathocuproine (**3a**) was added at the very end, as no H_2 was formed, possibly indicating a competitive complexation of the SR to Cu. In addition, it was observed that higher volumes of gas were produced when the phosphine was mixed with copper before addition of bathocuproine (**3a**).[32] The most reliable and active system arose from the addition of bathocuproine (**3a**) after allowing xantphos (**2a**) and copper (**1**) to premix, followed by NEt_3, water and finally the addition of the $[Fe_3(CO)_{12}]$ (**4**) complex.

Previous mechanistic studies spectroscopically detected (operando FT-IR) a new iron dimer (**5**) under the reaction conditions (Figure 3).[31] With a bridging diphenylphosphido moiety, it closely resembles the efficient iron-based hydrogenase water reduction catalysts.[16,27,33,34] Proposed to be a resting state in the catalytic cycle of water reduction, the formation of this species was assumed to arise from oxidative decomposition of the phosphine-containing heteroleptic PS, by a derivative of the iron trimer pre-catalyst. Taking into account this phosphine consumption, and the possibility of further ligand degradation, the in situ system should allow for higher activities and longer catalyst lifetimes, as the equivalents of each reacting component can be varied. Keeping the concentration of **1** constant, the quantities of **2a**, **3a** and **4**, were all systematically varied, and the quantity and rate of H_2 generation was assessed. Due to the interconnection of the two catalysts and no clear single expensive component to optimise the system towards, it is most logical to judge the efficiency through the system turnover number, that is, the combination of catalyst turnover numbers ($TON_{syst.} = TON_{Cu}^{H} + TON_{Fe}^{H2}$).[35] Indeed, optimisation of ligand equivalents (Figure 3) provided almost an additional 30% of activity ($TON_{syst.} = 1050$ (unoptimised) vs. 1330 (optimised)). The highest activity was observed using equimolar amounts of **1** and **2a** in combination with an excess of **3a** (1.5 equiv) and sub-stoichiometric quantities of **4** (0.7 equiv; Figure 3).

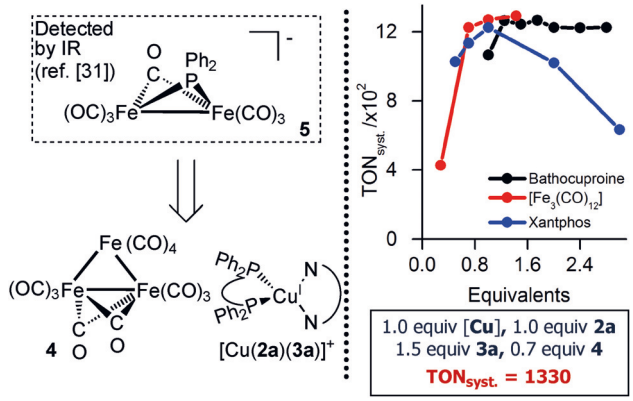

Figure 3. Left: the previously proposed resting state detected by operando FT-IR spectroscopy, which is assumed to be formed from reaction between the iron pre-catalyst **4**, or derivative thereof, and the heteroleptic [Cu(**2a**)(**3a**)]. Right: variation of the quantities of the catalyst components in the reduction of protons to H_2 gas. General conditions: $[Cu(MeCN)_4]PF_6$ (**1**) (3.5 μmol, 1.3 mg, 1 equiv), THF (5 mL), NEt_3 (3.75 mL) and water (1.25 mL), Xe lamp (input 300 W, output 1.5 W). Xantphos (**2a**) variation: **3a** (2 equiv) and **4** (0.7 equiv); bathocuproine (**3a**) variation: **2a** (1 equiv) and **4** (0.7 equiv); Fe-trimer (**4**) variation: **3a** (2 equiv), **2a** (1 equiv).

An increase in the relative amount of phosphine ligand induces a negative effect on the catalyst activity (Figure 3), a fact that is surprising considering its apparent extra necessity in formation of the proposed active WRC and its role in forming the assumed active heteroleptic copper PS ($[Cu(2a)(3a)]^+$) complex. Additionally, the highest TON_{syst} comes from employing an excess of bathocuproine. It is well known there exists an equilibrium between copper heteroleptic, for example, $[Cu(2a)(3a)]^+$ and homoleptic, for example, $[Cu(3a)_2]^+$, complexes,[36] and thus it seems entirely plausible from the evidence presented thus far that the excess of **3a** serves to favour the equilibrium in the direction of a homoleptic complex ($[Cu(3a)_2]^+$) that is active, as observed in other applica-

tions.[37,38] Thus, the role of **2a** would be to provide a phosphido fragment to form the active Fe dimer (**5**) WRC. In order to rationalise the optimised conditions and to aid further optimisations, mechanistic investigations were conducted with the first aim of elucidating the identity of the active PS and WRC species.

In order to establish the dominant species in solution, the equilibrium (K_{eq}) between the homoleptic ($[Cu(\mathbf{3a})_2]^+$) and heteroleptic ($[Cu(\mathbf{2a})(\mathbf{3a})]^+$) complexes (Figure 4) was studied. The K_{eq} was measured (^{1}H NMR spectroscopy) in a range of solvents. In DCM, CH_3CN, acetone and in THF there was no, or very little, evidence of $[Cu(\mathbf{3a})_2]^+$ formation. There was evidence for $[Cu(\mathbf{3a})_2]^+$ in MeOH, but, surprisingly, in $CDCl_3$ the equilibrium lies almost entirely towards it. In the reaction solvent ($THF/NEt_3/H_2O$ 4:3:1) the equilibrium constant was measured (ESI-MS) as 0.29, meaning that over 65% of Cu exists as $([Cu(\mathbf{2a})(\mathbf{3a})]^+$. By changing the addition order of the ligands to copper, the rate of equilibration was found to be relatively slow. When **3a** was pre-mixed with **1** before addition of **2a**, the equilibrium favoured $[Cu(\mathbf{3a})_2]^+$ by a further 6%, which readjusted over a period of 24 h in the dark, or 2 h of light irradiation. When this addition order was followed under catalytic conditions, the activity of the system dropped. This evidence provides the first hint that the homoleptic complex, which is formed in a greater proportion when bathocuproine (**3a**) is added before copper, is *not* the active PS species. The influence of visible light on K_{eq} was also tested (^{1}H NMR spectroscopy) in $[D_8]$THF and found to effect a shift towards $[Cu(\mathbf{3a})_2]^+$. This is consistent with previous electrochemical studies that show a progressive build-up of homoleptic complex upon redox cycling,[31] and thus light-induced excitation is shown here to effect the same process.

Having established that $[Cu(\mathbf{2a})(\mathbf{3a})]^+$ is the species in highest concentration, it was important to establish their relative reactivity, due to the possibility of a small proportion of highly reactive PS responsible for the observed activity. To do this, it was first necessary to confirm that the observed Fe phosphido-bridged dimer (**5**) is an active species. Thus **5** was independently synthesised,[39] and tested in combination with pre-formed $[Cu(\mathbf{2a})(\mathbf{3a})]^+$ and compared to the use of pre-catalyst trimer **4**. When ensuring the same number of Fe atoms are present, the same volume of H_2 was observed (Figure 5), thereby confirming the role of **5** as an active WRC. This is consistent with previous studies that have shown improved activities with the addition of monodentate tris[3,5-bis(trifluoromethyl)-phenyl] phosphine to $[Fe_3(CO)_{12}]$ (**4**) in combination with a pre-formed stable Ir-based PS.[40] Addition of the same phosphine to this Cu-based system resulted in no significant increase in activity.

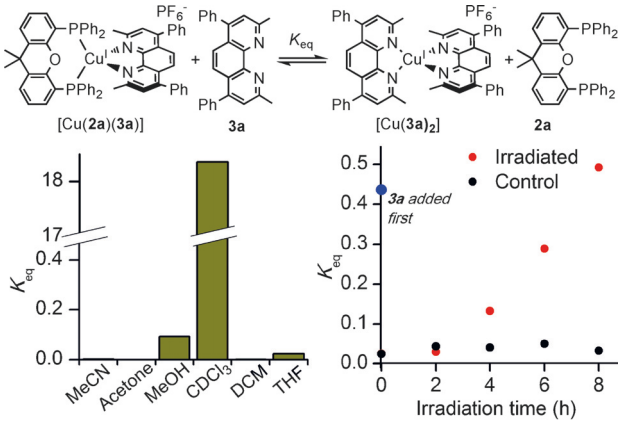

Figure 4. Equilibrium between $[Cu(\mathbf{2a})(\mathbf{3a})]^+$ and $[Cu(\mathbf{3a})_2]^+$, showing the equilibrium constant (K_{eq}), left, in different solvents and, right, changing under the effect of light irradiation (Xe-lamp, output: 1.5 W) in a THF solution.

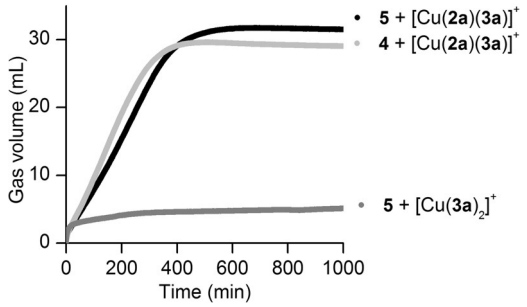

Figure 5. Gas evolution curves for synthesised Fe-dimer **5** with heteroleptic $[Cu(\mathbf{2a})(\mathbf{3a})]^+$, Fe-trimer **4** with heteroleptic $[Cu(\mathbf{2a})(\mathbf{3a})]^+$ and Fe-dimer **5** with homoleptic $[Cu(\mathbf{3a})_2]^+$.

Despite this evidence strongly suggesting that $[Cu(\mathbf{2a})(\mathbf{3a})]^+$ is the active PS, the possibility of its disproportionation to form homoleptic $[Cu(\mathbf{3a})_2]^+$ means this cannot be directly confirmed. However, when **5** was used in combination with $[Cu(\mathbf{3a})_2]^+$, in a system with no available bidentate phosphine ligand, no gas was evolved, thereby confirming $[Cu(\mathbf{2a})(\mathbf{3a})]^+$ as the active PS. This is consistent with the excited-state lifetime of the homoleptic complex being orders of magnitude shorter than the heteroleptic complex,[30,42] which renders the kinetic requirement of electron transfer much more demanding.

A drawback of the homogeneous systems is their limited activity, as H_2 gas production levels out as catalyst degradation proceeds. A progressive build-up of black precipitate and the detection of CO by GC provide evidence for dissociation of the Fe-stabilising CO ligand and subsequent agglomeration of Fe atoms. Attempts to prolong activity through the addition of slow-releasing CO agents, such as $Mo(CO)_6$ and PhCHO, unfortunately failed. Concurrent quantitative monitoring of the WRC by operando IR analysis of the C≡O stretching vibration and H_2 evolution showed the presence of **5** after gas evolution had ceased.[32] This evidence implies that WRC **5** outlives the PS co-catalyst. Indeed, $TON_{syst.}$ is higher employing sub-stoichiometric quantities of **4**, because then it cannot quantitatively destroy all $[Cu(\mathbf{2a})(\mathbf{3a})]^+$, when converting its phosphine to **5**.

In order to gain a handle on all system components, it was necessary to combine the operando IR with a technique suitable for simultaneously monitoring the PS concentration. Due to the positively charged copper complex, ESI-MS (positive

ion-mode) was ideal, as it has proven useful in detecting sensitive reaction intermediates.[43,44] Thus, with periodic sampling for ESI analysis and quantification through external calibration before and after every sample, the developed operando IR/ex situ ESI technique provided all the information necessary (Figure 6). An initial rise in the concentration of $[Cu(\mathbf{3a})_2]^+$ was observed due to light irradiation, as explained by Figure 4. However, it gradually decays whilst $[Cu(\mathbf{2a})(\mathbf{3a})]^+$ remains relatively stable. Upon consumption of $[Cu(\mathbf{3a})_2]^+$, rapid degradation of $[Cu(\mathbf{2a})(\mathbf{3a})]^+$ then ensues. This indicates that **3a** dissociation is a major PS degradation pathway and that $[Cu(\mathbf{3a})_2]^+$ serves as a reservoir of **3a** to regenerate $[Cu(\mathbf{2a})(\mathbf{3a})]^+$ through adjustment of its equilibrium. This may explain why using an increased proportion of **3a** provides higher TON_{syst}. Plotting the rate of gas evolution versus both the concentration of $[Cu(\mathbf{2a})(\mathbf{3a})]^+$ and **5** allowed for a quantitative assessment of the catalyst degradation pathways.[32] In both cases, linear relationships were recorded, but the *y*-intercept only crossed 0 with $[Cu(\mathbf{2a})(\mathbf{3a})]^+$, that is, **5** was still present despite the activity having already ceased. In combination with analysis of the gas evolution curves, these data suggest the degradation of the catalysts are linked to each other but led by the PS through decoordinative loss of **3a**. A clear first order decay of **5** ensues *after* initiation of the rapid degradation of $[Cu(\mathbf{2a})(\mathbf{3a})]^+$. Dimer **5** is stabilised by catalytic turn-over, but when this starts to attenuate due to PS degradation, CO loss and Fe agglomeration follows.

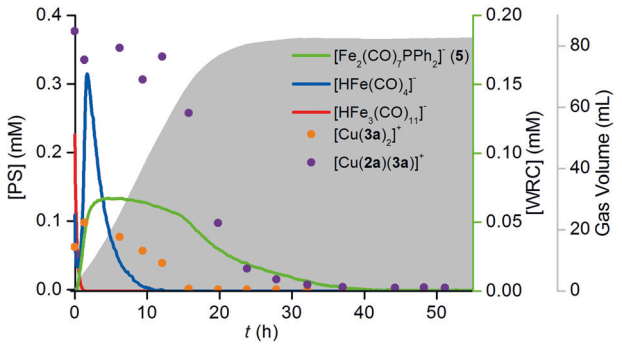

Figure 6. Operando IR/ex-situ ESI measurements showing concentrations of Fe species (coloured lines) and Cu complexes (blue dots: heteroleptic ($[Cu(\mathbf{2a})(\mathbf{3a})]^+$) and orange dots homoleptic ($[Cu(\mathbf{3a})_2]^+$)). Shaded area indicates gas volume evolved. Conditions: $[Cu(MeCN)_4]PF_6$ (7 μmol), xantphos (7 μmol), bathocuproine (10.5 μmol), $[Fe_3(CO)_{12}]$ (5 μmol), THF/NEt_3/H_2O (4:3:1, 20 mL).

A series of control reactions were undertaken to further understand the mechanism for the formation of **5**. C–P bond cleavage in aryl phosphines has been well studied[41a–e] and used.[41f–h] As it has been shown to readily occur under reductive conditions (e.g., with alkali metals[41d,e]) we suspected the formation of PPh_2^- to be highly influenced by reduction equivalents produced by the combination of a PS and the TEA electron source. Indeed, after 5 h of light irradiation on solutions deficient in either CuPS or TEA, no evidence (IR) of **5** formation was provided. An extremely attenuated build-up of **5** was in fact observed in the absence of CuPS, but the time scale was far extended beyond that observed under the optimised conditions. In the absence of TEA, all Fe complexes had been consumed after 4 h, but none of which was **5**.[32] Thus, reductive C–P cleavage in xantphos provides the anionic PPh_2^- fragment, which coordinates to a dimeric Fe carbonyl complex to yield dimer **5**.

With an optimised model system in hand and mechanistic understanding enhanced, the in situ method was exploited to explore variation of the bidentate phosphine (**2**), to establish the important features pertinent to this parameter. The HOMO of the heteroleptic complex ($[Cu(\mathbf{2})(\mathbf{3a})]^+$) is not purely localised on Cu, but contains a substantial portion of phosphine character.[42a] Thus, the phosphine moiety can modify the electronic structure and stabilise the excited state. Thirty two different ligands were tested under the optimised conditions, the majority of which are bidentate phosphines (**2a–w**),[32] but also a small number of BIANs (**6**), phosphites (**7**) and NHCs (**8**) were tested. A sample was removed at the start for ESI-MS analysis to determine the $[Cu(\mathbf{2})(\mathbf{3a})]^+/[Cu(\mathbf{3a})_2]^+$ ratio. From the gas evolution curves, it was immediately obvious that the rate of H_2 production, $TON_{syst.}$ and lifetime of the system are all dependent on the phosphine ligand.[32] The rate differs dramatically, which could be evidence for a change in the dominant quenching mechanism (Figure 1). In addition, the proportion of heteroleptic compared to homoleptic PS is very sensitive to the nature of the phosphine (^{1}H NMR spectroscopy), as previously observed by Armaroli and co-workers.[36] Plotting this percentage against $TON_{syst.}$ reveals the important influence of $[Cu(\mathbf{2})(\mathbf{3a})]^+$, and is directly consistent with our mechanistic studies. With a greater proportion of the active complex, and thus a lower K_{eq}, higher turn-over numbers are achieved (Figure 7).

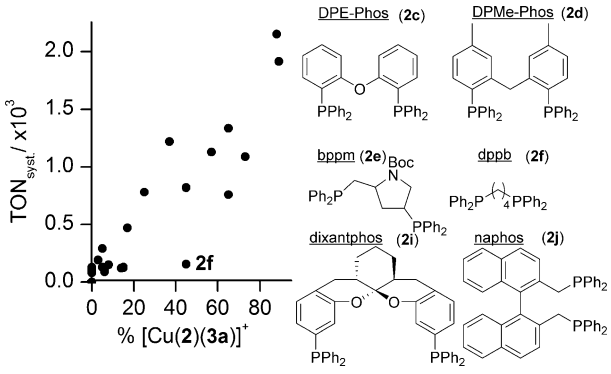

Figure 7. Left: TON_{syst} versus % $[Cu(\mathbf{2})(\mathbf{3})]^+$, where the remaining copper is all homoleptic complex $[Cu(\mathbf{3})_2]^+$, and right: structures of some diphosphines tested.

Many of the efficient phosphines contain a bridging O-atom, which may play a role in stabilising the excited state through a hemi-labile coordination. Comparison of the percentage of $[Cu(\mathbf{2})(\mathbf{3a})]^+$ for DPE-Phos (**2c**) and DPMe-Phos (**2d**) suggests that the bridging-O aids in increasing the proportion of heteroleptic complex and thus the TON_{syst}. Changing the electronics

Table 1. A selection of ligands tested in the developed in-situ system.[32]

Ligand[a]	Vol. H_2 [mL][b]	$TON_{syst.}$[c]	% Heteroleptic[d]
xantphos (**2a**)	32.4	1335	65
BISBI (**2b**)	19.5	760	65
DPE-Phos (**2c**)	27.3	1090	73
DPMe-Phos (**2d**)	20.4	780	25
bppm (**2e**)	13.7	470	17
dppb (**2f**)	5.0	155	45
xantphos-*t*Bu (**2g**)	5.2	120	14
thixantphos (**2h**)	27.9	1130	57
dixantphos (**2i**)	11.1	190	3
naphos (**2j**)	30.0	1220	37
naphos-CF_3 (**2k**)	9.1	290	5

[a] See the Supporting Information for the reaction conditions and a full list of ligands and their structures (**2a**–**w**). [b] Volume of H_2 calculated by removing the blank volume (measured as 2.40 mL) and taking into account the $\%H_2$ detected by GC (generally $<98\%$). [c] $TON_{syst.} = TON_{Cu}^{H} + TON_{Fe}^{H2}$. TON rounded to nearest 5. [d] Remaining Cu is all homoleptic complex, $[Cu(\mathbf{3a})_2]^+$.

and/or the bulk at phosphorous will also have an effect on the proportion of PS_{hetero} present. Switching phenyl for *any* substituent in the xantphos or naphos range resulted in lower or no heteroleptic complex formation, which is reflected in lower catalytic activities (Figure 7 and Table 1). This implies that a balanced electron demand is ideal for high activity.

However, the vertical spread of activity between the points of similar percent $[Cu(\mathbf{2})(\mathbf{3a})]^+$ proves it is not the only important parameter. This was further demonstrated by subjecting a pure preformed heteroleptic complex, with dppp (**2q**) and **3a** ligated to Cu, $[Cu(\mathbf{2q})(\mathbf{3a})]^+$,[45] to the reaction conditions and observing no gas evolution. Knör and Monkowius provided a model that showed increasing bite-angles stabilise the HOMO by reducing the orbital overlap between ligand and metal. This effect will widen the redox potential and increase the thermodynamic driving force, which may provide a rationale for the ineffectual alkyl phosphines with a small bite-angle. However, comparison between bppm (**2e**) and dppb (**2f**), which share the same bite-angle and similar electronic properties at phosphorus also reveal the importance of a rigid backbone. The flexible dppb (**2f**) is the major outlier in Figure 7, as it forms good proportions of heteroleptic complex but shows much lower activity than bppm (**2e**), which is restricted by a cyclised backbone. This may also be the reason for a lower activity observed in the case of dixantphos (**2i**), which is a more flexible variant of xantphos (**2a**). In addition to the increased orbital overlap aided by increased flexibility in the diphosphine, it is likely that a greater degree of flattening to a square planar complex occurs upon excitation. This process leads to shorter lifetimes through solvent-induced exciplex quenching.[30,46] Thus, like sterics, rigidity can restrict the distortion away from a pseudo-tetrahedron and stabilise the excited state.

Replacing the methyl groups at the 2,9-positions of bathocuproine (**3a**) with increasing bulk provides increasingly more active systems and correlates nicely to Taft's steric parameter.[32] This is consistent with the use of preformed complexes, the excited-state lifetimes of which were measured and found to rise with increasing bulk.[30] Using the in situ system, it was found that the ratio of $[Cu(\mathbf{2})(\mathbf{3})]^+$ to $[Cu(\mathbf{3})_2]^+$ (ESI-MS) also rises with increasing bulk in the 2,9-positions. Thus, the increased life-time and concentration of active PS both contribute to the larger observed rates. The use of stabilising NHC or phosphite (**7**) ligands in combination with the light harvesting bathocuproine showed no ability to generate H_2 gas. Monodentate NHC leads to a trigonal planar complex, which is particularly vulnerable to non-radiative decay pathways.[47] Additionally, replacing the bathocuproine completely with a BIAN (**6**) ligand in combination with phosphine predictably showed no activity.

In summary we have demonstrated a viable solution to the problem of the organometallic complex synthesis in non-noble metal water reduction systems. Optimisation of the quantity of ligands led to improvements in the system efficiency. Synthesis of the dimeric iron WRC **5** established it to be the active species. In combination with studies on the homoleptic/heteroleptic equilibrium, the heteroleptic $[Cu(\mathbf{2a})(\mathbf{3a})]^+$ was also confirmed to be the active PS. The dominant degradation pathway was elucidated through monitoring the reaction by operando IR/in situ ESI and involves destruction of the active $[Cu(\mathbf{2a})(\mathbf{3a})]^+$, which is likely caused through loss of the **3a** unit. The ease of catalyst preparation by the in situ system allowed for further rapid exploration of the system. A large range of alternative ligands for Cu were screened and the proportion of $[Cu(\mathbf{2})(\mathbf{3})]^+$, that is, K_{eq}, was found to be integral for high activities. Additionally, a rigid backbone, wide bite-angle and balanced electronic properties at phosphorus were all found to be important. These data provide a rationale for future optimisations in the PS and the WRC.

Acknowledgements

A.J.J.L. would like to thank the Alexander von Humboldt Foundation for generous funding. This work was also supported by the Ministry for Education, Science and Culture of Mecklenburg Vorpommern and the European Union (Investing in our Future, European Regional Development) within the project PS4H and a joint DFG/NFSC project. We would like to thank Andreas Koch for assistance with the quantitative ESI measurements, E. Oberem and A. Rösel for preparation of compound **5** (see ref. [39]) and Dr. A. Spannenberg for X-ray crystallography.

Keywords: copper · homogeneous catalysis · photocatalysis · reaction mechanisms · reduction

[1] J. O. Bockris, *Science* **1972**, *176*, 1323.
[2] J. A. Turner, *Science* **2004**, *305*, 972–974.
[3] T. R. Cook, D. K. Dogutan, S. Y. Reece, Y. Surendranath, T. S. Teets, D. G. Nocera, *Chem. Rev.* **2010**, *110*, 6474–6502.
[4] T. Hisatomi, J. Kubota, K. Domen, *Chem. Soc. Rev.* **2014**, *43*, 7520–7535.
[5] K. Maeda, *J. Photochem. Photobiol. C* **2011**, *12*, 237–268.
[6] K. S. Joya, Y. F. Joya, K. Ocakoglu, R. van de Krol, *Angew. Chem. Int. Ed.* **2013**, *52*, 10426–10437; *Angew. Chem.* **2013**, *125*, 10618–10630.
[7] M. Ashokkumar, *Int. J. Hydrogen Energy* **1998**, *23*, 427–438.
[8] V. Balzani, A. Credi, M. Venturi, *ChemSusChem* **2008**, *1*, 26–58.

[9] A. J. Esswein, D. G. Nocera, *Chem. Rev.* **2007**, *107*, 4022 – 4047.
[10] M. A. Gross, A. Reynal, J. R. Durrant, E. Reisner, *J. Am. Chem. Soc.* **2014**, *136*, 356 – 366.
[11] J. J. Concepcion, R. L. House, J. M. Papanikolas, T. J. Meyer, *Proc. Natl. Acad. Sci. USA* **2012**, *109*, 15560 – 15564.
[12] X. Chen, S. Shen, L. Guo, S. S. Mao, *Chem. Rev.* **2010**, *110*, 6503 – 6570.
[13] Y. Ma, X. Wang, Y. Jia, X. Chen, H. Han, C. Li, *Chem. Rev.* **2014**, *114*, 9987 – 10043.
[14] A. L. Linsebigler, G. Lu, J. T. Yates, *Chem. Rev.* **1995**, *95*, 735 – 758.
[15] W. T. Eckenhoff, R. Eisenberg, *Dalton Trans.* **2012**, *41*, 13004 – 13021.
[16] A. Magnuson, M. Anderlund, O. Johansson, P. Lindblad, R. Lomoth, T. Polivka, S. Ott, K. Stensjö, S. Styring, V. Sundström, L. Hammarström, *Acc. Chem. Res.* **2009**, *42*, 1899 – 1909.
[17] S. Styring, *Faraday Discuss.* **2012**, *155*, 357 – 376.
[18] K. Kalyanasundaram, J. Kiwi, M. Grätzel, *Helv. Chim. Acta* **1978**, *61*, 2720 – 2730.
[19] G. C. Vougioukalakis, A. I. Philippopoulos, T. Stergiopoulos, P. Falaras, *Coord. Chem. Rev.* **2011**, *255*, 2602 – 2621.
[20] A. Abbotto, N. Manfredi, *Dalton Trans.* **2011**, *40*, 12421 – 12438.
[21] J. I. Goldsmith, W. R. Hudson, M. S. Lowry, T. H. Anderson, S. Bernhard, *J. Am. Chem. Soc.* **2005**, *127*, 7502 – 7510.
[22] B. F. DiSalle, S. Bernhard, *J. Am. Chem. Soc.* **2011**, *133*, 11819 – 21.
[23] F. Gärtner, D. Cozzula, S. Losse, A. Boddien, G. Anilkumar, H. Junge, T. Schulz, N. Marquet, A. Spannenberg, S. Gladiali, M. Beller, *Chem. Eur. J.* **2011**, *17*, 6998 – 7006.
[24] F. Gärtner, S. Denurra, S. Losse, A. Neubauer, A. Boddien, A. Gopinathan, A. Spannenberg, H. Junge, S. Lochbrunner, M. Blug, S. Hoch, J. Busse, S. Gladiali, M. Beller, *Chem. Eur. J.* **2012**, *18*, 3220 – 3225.
[25] P. Du, R. Eisenberg, *Energy Environ. Sci.* **2012**, *5*, 6012 – 6021.
[26] Y. Amao, T. Hirakawa, N. Himeshima, *Catal. Commun.* **2008**, *9*, 131 – 134.
[27] S. Tschierlei, S. Ott, R. Lomoth, *Energy Environ. Sci.* **2011**, *4*, 2340 – 2352.
[28] P. Poddutoori, D. T. Co, A. P. S. Samuel, C. H. Kim, M. T. Vagnini, M. R. Wasielewski, *Energy Environ. Sci.* **2011**, *4*, 2441 – 2450.
[29] S.-P. Luo, E. Mejía, A. Friedrich, A. Pazidis, H. Junge, A.-E. Surkus, R. Jackstell, S. Denurra, S. Gladiali, S. Lochbrunner, M. Beller, *Angew. Chem. Int. Ed.* **2013**, *52*, 419 – 423; *Angew. Chem.* **2013**, *125*, 437 – 441.
[30] E. Mejía, S.-P. Luo, M. Karnahl, A. Friedrich, S. Tschierlei, A.-E. Surkus, H. Junge, S. Gladiali, S. Lochbrunner, M. Beller, *Chem. Eur. J.* **2013**, *19*, 15972 – 15978.
[31] S. Fischer, D. Hollmann, S. Tschierlei, M. Karnahl, N. Rockstroh, E. Barsch, P. Schwarzbach, S.-P. Luo, H. Junge, M. Beller, S. Lochbrunner, R. Ludwig, A. Brückner, *ACS Catal.* **2014**, *4*, 1845 – 1849.
[32] See the Supporting Information for more details.
[33] D. Streich, Y. Astuti, M. Orlandi, L. Schwartz, R. Lomoth, L. Hammarström, S. Ott, *Chem. Eur. J.* **2010**, *16*, 60 – 63.
[34] W. Lubitz, E. J. Reijerse, J. Messinger, *Energy Environ. Sci.* **2008**, *1*, 15 – 31.
[35] As the photosensitiser undergoes two turnovers per H_2 formed, the TON is calculated for H rather than H_2, that is, $TON_H = n\,H/n\,Cu$. Whereas, Fe undergoes one turnover per H_2 formed, and is thus calculated for H_2, that is, $TON_{H2} = n\,H_2/n\,Fe$.
[36] A. Kaeser, M. Mohankumar, J. Mohanraj, F. Monti, M. Holler, J.-J. Cid, O. Moudam, I. Nierengarten, L. Karmazin-Brelot, C. Duhayon, B. Delavaux-Nicot, N. Armaroli, J.-F. Nierengarten, *Inorg. Chem.* **2013**, *52*, 12140 – 12151.
[37] D. R. McMillin, K. M. McNett, *Chem. Rev.* **1998**, *98*, 1201 – 1220.
[38] D. V. Scaltrito, D. W. Thompson, J. A. O'Callaghan, G. J. Meyer, *Coord. Chem. Rev.* **2000**, *208*, 243 – 266.
[39] B. Walther, H. Hartung, H.-C. Böttcher, U. Baumeister, U. Böhland, J. Reinhold, J. Sieler, J. Ladriere, H.-M. Schiebel, *Polyhedron* **1991**, *10*, 2423 – 2435.
[40] F. Gärtner, A. Boddien, E. Barsch, K. Fumino, S. Losse, H. Junge, D. Hollmann, A. Brückner, R. Ludwig, M. Beller, *Chem. Eur. J.* **2011**, *17*, 6425 – 6436.
[41] a) P. E. Garrou, *Chem. Rev.* **1985**, *85*, 171 – 185; b) K. Q. Almeida Leñero, Y. Guari, P. C. J. Kamer, P. W. N. M. van Leeuwen, B. Donnadieu, S. Sabo-Etienne, B. Chaudret, M. Lutz, A. L. Spek, *Dalton Trans.* **2013**, *42*, 6495 – 6512; c) C. W. Bradford, R. S. Nyholm, *J. Chem. Soc. Dalton Trans.* **1973**, 529 – 533; d) A. M. Aguiar, J. Beisler, A. Mills, *J. Org. Chem.* **1961**, *26*, 1001 – 1005; e) I. Toth, B. E. Hanson, M. E. Davis, *Organometallics* **1990**, *9*, 675 – 680; f) K. F. Crespo Andrada, L. E. Peisino, M. Güney, A. Daştan, A. B. Pierini, *Org. Biomol. Chem.* **2013**, *11*, 955 – 965; g) M. W. Bezpalko, B. M. Foxman, C. M. Thomas, *Inorg. Chem.* **2013**, *52*, 12329 – 12331; h) V. A. Stepanova, V. V. Dunina, I. P. Smoliakova, *Organometallics* **2009**, *28*, 6546 – 6558.
[42] a) A. K. Ichinaga, J. R. Kirchhoff, D. R. McMillin, C. O. Dietrich-Buchecker, P. A. Marnot, J. P. Sauvage, *Inorg. Chem.* **1987**, *26*, 4290 – 4292; b) A. Kaeser, O. Moudam, G. Accorsi, I. Séguy, J. Navarro, A. Belbakra, C. Duhayon, N. Armaroli, B. Delavaux-Nicot, J.-F. Nierengarten, *Eur. J. Inorg. Chem.* **2014**, 1345 – 1355.
[43] L. S. Santos, C. H. Pavam, W. P. Almeida, F. Coelho, M. N. Eberlin, *Angew. Chem. Int. Ed.* **2004**, *43*, 4330 – 4333; *Angew. Chem.* **2004**, *116*, 4430 – 4433.
[44] G. W. Amarante, H. M. S. Milagre, B. G. Vaz, B. R. Vilachã Ferreira, M. N. Eberlin, F. Coelho, *J. Org. Chem.* **2009**, *74*, 3031 – 3037.
[45] T. Tsubomura, K. Kimura, M. Nishikawa, T. Tsukuda, *Dalton Trans.* **2015**, *44*, 7554 – 7562.
[46] S. Tschierlei, M. Karnahl, N. Rockstroh, H. Junge, M. Beller, S. Lochbrunner, *ChemPhysChem* **2014**, *15*, 3709 – 3713.
[47] V. A. Krylova, P. I. Djurovich, M. T. Whited, M. E. Thompson, *Chem. Commun.* **2010**, *46*, 6696 – 6698.

Received: September 23, 2015
Published online on December 22, 2015

6.5 Light to Hydrogen: Photocatalytic Hydrogen Generation from Water with Molecularly-Defined Iron Complexes

Henrik Junge, Nils Rockstroh, Steffen Fischer, Angelika Brückner, Ralf Ludwig, Stefan Lochbrunner, Oliver Kühn and Matthias Beller

Review: *Inorganics,* **2017**, *5* (1), 14
DOI: 10.3390/inorganics5010014

Abstract

Photocatalytic hydrogen generation is considered to be attractive due to its combination of solar energy conversion and storage. Currently used systems are either based on homogeneous or on heterogeneous materials, which possess a light harvesting and a catalytic subunit. The subject of this review is a brief summary of homogeneous proton reduction systems using sacrificial agents with special emphasis on non-noble metal systems applying convenient iron(0) sources. Iridium photosensitizers, which were proven to have high quantum yields of up to 48% (415 nm), have been employed, as well as copper photosensitizers. In both cases, the addition or presence of a phosphine led to the transformation of the iron precursor with subsequently increased activities. Reaction pathways were investigated by photoluminescence, electron paramagnetic resonance (EPR), Raman, FTIR and mass spectroscopy, as well as time-dependent DFT-calculations. In the future, this knowledge will set the basis to design photo(electro)chemical devices with tailored electron transfer cascades and without the need for sacrificial agents

Contribution to this work (15%)

Steffen Fischer provided mechanistic information about the phosphine containing photocatalytic proton reduction system, which had been unpublished until the preparation of this review. This implies the elemental description of the formation of $[Fe_2(CO)_6(\mu\text{-}CO)(\mu\text{-}P(R)_2)]^-$. Further, he was involved in the discussion and preparation of the manuscript. The overall contribution is about 15%

inorganics

MDPI

Review

Light to Hydrogen: Photocatalytic Hydrogen Generation from Water with Molecularly-Defined Iron Complexes

Henrik Junge [1], Nils Rockstroh [1], Steffen Fischer [2], Angelika Brückner [1], Ralf Ludwig [1,2], Stefan Lochbrunner [3], Oliver Kühn [3] and Matthias Beller [1,*]

1 Leibniz Institute for Catalysis, University of Rostock (LIKAT), Albert-Einstein-Straße 29a, 18059 Rostock, Germany; Henrik.Junge@catalysis.de (H.J.); Nils.Rockstroh@catalysis.de (N.R.); Angelika.Brueckner@catalysis.de (A.B.)

2 Institute of Chemistry, Department Physical Chemistry, University of Rostock, Dr.-Lorenz-Weg 1, 18059 Rostock, Germany; Steffen.Fischer@uni-rostock.de (S.F.); Ralf.Ludwig@uni-rostock.de (R.L.)

3 Institute of Physics, University of Rostock, Albert-Einstein-Straße 23-24, 18059 Rostock, Germany; Stefen.Lochbrunner@uni-rostock.de (S.L.); Oliver.Kuehn@uni-rostock.de (O.K.)

* Correspondence: Matthias.Beller@catalysis.de; Tel.: +49-381-1281-113

Academic Editor: Matthias Bauer
Received: 27 January 2017; Accepted: 27 February 2017; Published: 9 March 2017

Abstract: Photocatalytic hydrogen generation is considered to be attractive due to its combination of solar energy conversion and storage. Currently-used systems are either based on homogeneous or on heterogeneous materials, which possess a light harvesting and a catalytic subunit. The subject of this review is a brief summary of homogeneous proton reduction systems using sacrificial agents with special emphasis on non-noble metal systems applying convenient iron(0) sources. Iridium photosensitizers, which were proven to have high quantum yields of up to 48% (415 nm), have been employed, as well as copper photosensitizers. In both cases, the addition or presence of a phosphine led to the transformation of the iron precursor with subsequently increased activities. Reaction pathways were investigated by photoluminescence, electron paramagnetic resonance (EPR), Raman, FTIR and mass spectroscopy, as well as time-dependent DFT-calculations. In the future, this knowledge will set the basis to design photo(electro)chemical devices with tailored electron transfer cascades and without the need for sacrificial agents.

Keywords: hydrogen; iron; copper; hydrogenases; photosensitizer; photocatalysis; water splitting; spectroscopy

1. Introduction

An increasing number of pilot plants combining wind mills or photovoltaic devices with classical water electrolysis is installed all over the world. This reflects the progressive contribution of the renewable energies wind and sunlight to a sufficient and sustainable energy supply [1–4] and thereby raises the necessity to store the harvested electric energy due to its fluctuating occurrence. In this respect, hydrogen is of particular interest as the primary product of the interconversion of electric and chemical energy, as well as a secondary energy carrier [1–4]. Besides the hydrogen generation from water, also its storage and back conversion to electrical energy are current topics of intensive research [1–7]. A more efficient way for the conversion of the Sun's energy to hydrogen compared to the combination of photovoltaic devices with water electrolysis [8–17], which possesses an overall efficiency between 10% and 14% [18,19], may constitute the direct photocatalytic water splitting into hydrogen and oxygen. So far, the two half reactions water oxidation and water reduction are mainly studied separately. Disadvantageously, this requires the application of sacrificial reagents (SR) as

electron donors or electron acceptors (Scheme 1) [11–17,20–29]. On the other hand, it allows for a simplification of the complex system of overall water splitting and hence a more detailed understanding of the basic processes as a prerequisite for improvements. Within the development of more efficient and stable catalyst systems for photocatalytic hydrogen generation from water, an additional trend towards the usage of 3d metals is obvious. This is motivated by several advantages of such catalysts due to lower costs and higher abundance compared to noble metals. Exemplarily, significant efforts have been reported applying cobalt and nickel complexes as proton reduction catalysts (WRC) (Although the term "water reduction catalyst" as well as the related abbreviation WRC is commonly used in relevant literature it should be named proton reduction catalyst in the strict sense) [30–40]. For example, various groups investigated cobaloxime-based catalysts [25,31]. Recently, these systems have been outperformed by pentapyridyl cobalt complexes achieving a turnover number (TON) with respect to Co of up to 11,000 with a Re-photosensitizer (PS) and ascorbic acid (SR) [36]. Prominent examples of nickel catalysts constitute the DuBois catalyst [37], as well as tris(2-pyridylthiolate) [38], 2-aminobenzenethiolate, 2-mercaptophenolate and 2-mercaptopyridyl-*N*-oxide [39] nickel complexes by Eisenberg. The DuBois system showed excellent activity with a TOF up to 100,000 s^{-1} in the electrocatalytic hydrogen evolution reaction (HER) [41,42]. However, in photocatalytic hydrogen generation, this system achieved only a TON_{Ni} of 2700 over 150 h with Ru photosensitizer **A** and ascorbic acid (SR) [37], while applying thiolate nickel complexes improved the TON_{Ni} up to 7300 after 30 h with fluorescein, a xanthene-type organic dye, as the photosensitizer and TEA as SR [40]. A stability of more than 100 h was obtained using this system with TEOA as the electron donor [39]. More than 280,000 turnovers were obtained by replacing the PS and SR by water-soluble CdSe quantum dots and ascorbic acid, respectively [39]. Very recently, also stabilized nickel [43], iron [44], zinc [45] and copper nanoparticles [46] were reported to constitute active WRC in the photocatalytic hydrogen generation from water.

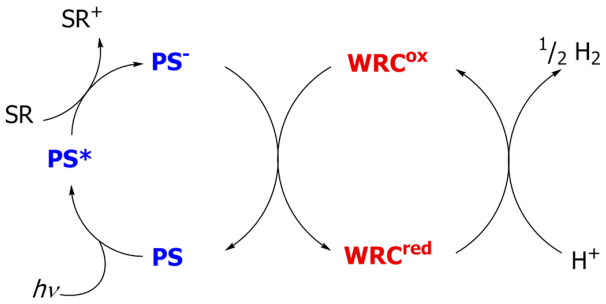

Scheme 1. The basic concept of hydrogen generation from water (hydrogen half reaction) via a reductive quenching pathway applying a photosensitizer (PS) and a proton reduction catalyst (WRC) in the presence of the sacrificial reductant (SR).

In this review, we present a brief overview about iron-based WRC, including noble metal-free PS systems. Exemplarily, mechanistic investigations and the working mode of a selected system by employing a tool of combined analytical methods are summarized.

2. Overview of Molecularly-Defined Iron WRCs and the Respective Photosensitizers

Iron is a very important and abundant base metal constituting, e.g., the active centers in hydrogenases [47–49] and showing impressive activities for hydrogen generation and cleavage with up to 9000 molecules H_2 per second and site [50]. Because of this outstanding activity, especially [FeFe] hydrogenases have attracted much attention for more than a decade, although the real structure regarding the central atom of the dithiolate bridge was identified to be nitrogen only in 2009 [51,52]. Thus, besides CO and CN ligands, the dinuclear iron complex contains an internal base, which is of fundamental importance since it allows for the heterolytic splitting/formation of H_2 by metal ligand

cooperative catalysis. This principle has also been adopted for other (de)hydrogenation reactions applying non-innocent ligand iron complexes [53–60].

Inspired by the above-mentioned lead structure several groups, e.g., Wang and Sun [61,62], as well as Hammarström [23], Ott [63] and Reek [64] successfully developed a variety of Fe-based WRC, which resulted in catalyst turnover numbers of up to 466 regarding Fe (Scheme 2). An overview of the applied PS is provided in Scheme 3; selected conditions and TONs are listed in Table 1. It should be noted here that a direct comparison of turnover numbers is sometimes intricate as it depends on the concentration of the involved components, i.e., WRC, PS and SR.

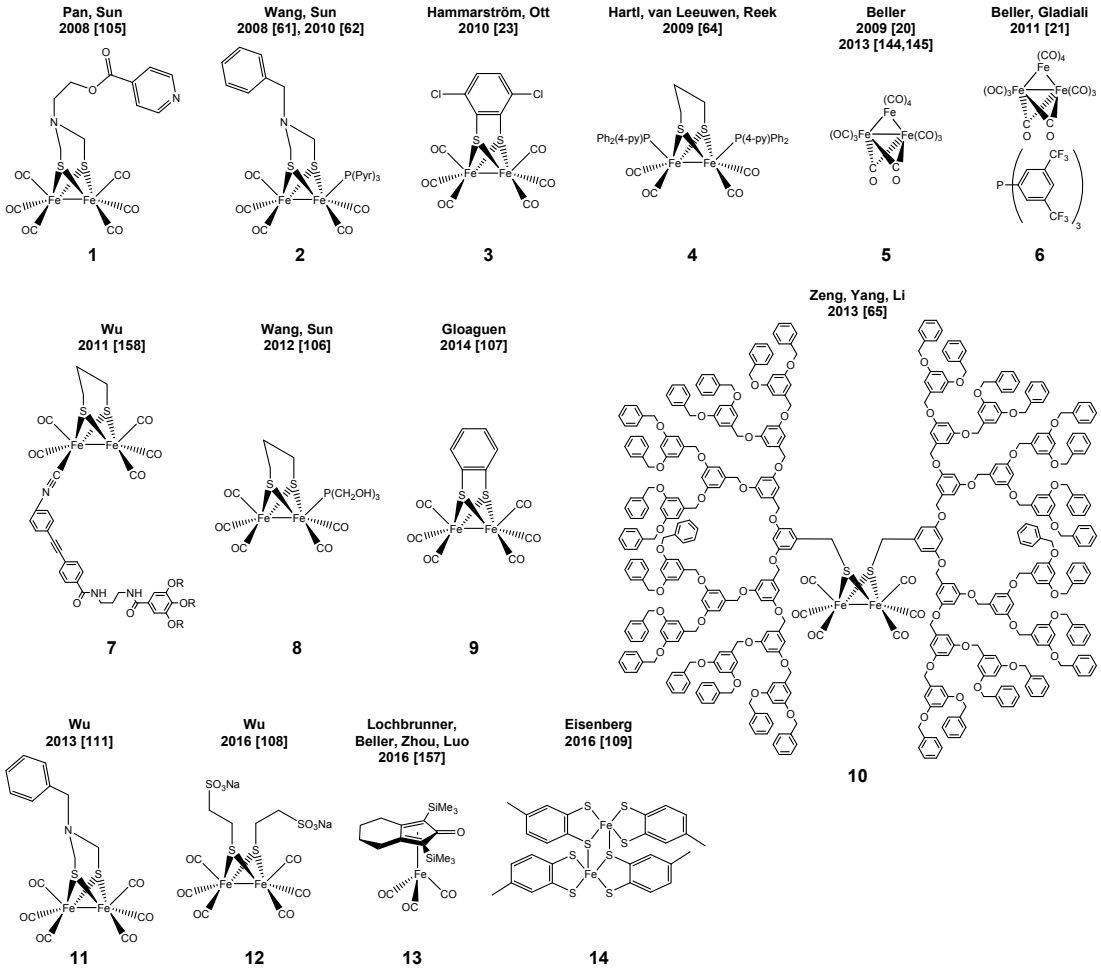

Scheme 2. Iron-based WRCs inspired by hydrogenases. Turnover numbers (TONs) with respect to the WRC are reported in Table 1. The used photosensitizers (PS) are shown in Scheme 3.

In 2013, Yu et al. reported a TON of 22,200 with a dendrimer-based diiron hydrogenase mimic applying only 10 nmol of the catalyst [65]. The same year, other mimics were applied for visible light-driven hydrogen production embedded in a MOF [66] or later in a protein matrix [67]. However, in these cases, productivities (TON) of only ca. 5 and 130, respectively, were achieved in the presence of Ru-PS **B** (Scheme 3).

Besides the WRC, the photosensitizer (PS) is a second important component in water reduction. For this purpose, especially ruthenium complexes have played a key role since the 1970s [68–74], later followed by various iridium [75,76], platinum [77–79] and rhenium [80–85] complexes. In contrast, more abundant metals or even metal-free photocatalytic systems were reported: examples include, e.g., iron [86], zinc [24,25,87–89] and magnesium-based [24,90–94] photosensitizers, CdTe [95], CdSe [39] or carbon [96] quantum dots or organic dyes [38–40,97–104] together with either cobalt or nickel catalysts.

Mostly, the reported activities and stabilities were still low. However, Eisenberg recently reported a TON for a nickel WRC as high as 280,000 together with water-soluble CdSe quantum dots with tripodal S-donor capping agents as PS and ascorbic acid as the sacrificial electron donor at pH 4.5 [39].

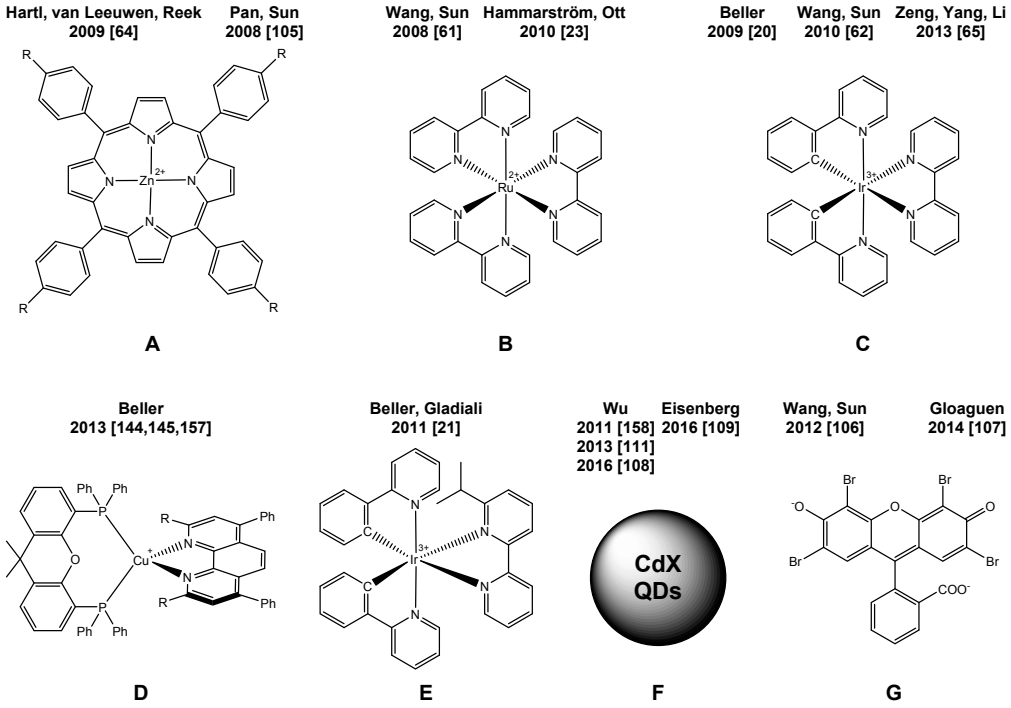

Scheme 3. Photosensitizers (PS) applied in iron-based water reduction systems with the WRCs depicted in Scheme 2. TONs with respect to the photosensitizer are reported in Table 1.

A few of the above-mentioned iron-based WRC were also used as a part of fully noble metal-free water reduction systems applying either Zn porphyrins [64,105] or organic dyes [106,107] instead of Ru-PS [23,61] and Ir-PS [62]. Applying the latter (i.e., EY^{2-}) in a micellar solution resulted in a TON of 117 (Scheme 2: **9**, Scheme 3: **G**) [107].

Very recently, CdSe quantum dots were independently successfully applied as light-harvesting units by Wu [108] and Eisenberg [109] in a system containing different [FeFe]-Hydrogenase mimics (Scheme 2, **12** and **14**). In both cases, outstanding TONs of 26,500 and 29,400, respectively, were obtained. Applying $[Ru(bpy)_3]^{2+}$ as PS resulted in a comparably low TON of only 178 [108]. In addition, co-embedded CdSe quantum dots and the [FeFe]-hydrogenase mimic in lipid membranes were used, however resulting in a much lower TON of 651 [110]. As an alternative, also CdTe quantum dots were applied resulting in the hitherto highest observed TON_{Fe} as high as 52,800 [111] for **11** (Scheme 2).

All of these results might be compared, e.g., with the use of an isolated [NiFe] hydrogenase in visible light-driven hydrogen production on C_3N_4/TiO_2 with an excellent productivity (TON) of 580,000 [112].

Surprisingly, the promising application of copper (I) complexes with polypyridine ligands as photosensitizers has been neglected for a long time with only one early communication from the group of Sauvage [113]. As their photo- and electro-chemical properties have been known for decades, they are already applied as active components in organic light-emitting diodes (OLEDs), light-emitting electrochemical cells (LECs) or luminescence-based sensors and dye-sensitized solar cells (DSSCs) [114–125]. Besides, molecularly-defined copper compounds showed a significant ability to act as catalysts for electrochemical water reduction [126] and oxidation [127–130] and CO_2 reduction [131]. In addition, heterogeneous cupric and cuprous oxides have been used as co-catalysts, mainly supported on titania [132–136], or as light-harvesting semiconductors [137–139] for water reduction. Although a

variety of homo- and hetero-leptic Cu complexes have been developed [121,125,140–146], only recently, two different examples of its successful application as photosensitizers in efficient noble metal-free photocatalytic systems for proton reduction have been reported (Scheme 3) [144,145,147].

3. Light to Hydrogen: Development and Improvement of an Iron Carbonyl-Based Catalytic System

Within the frame of our project "Light to Hydrogen", an initial focus laid on the development of efficient catalysts and photosensitizers based on abundant metals in order to substitute rare and expensive noble metals. The realization of a noble metal-free system for photocatalytic hydrogen generation from water was achieved in several steps. In the first step, Beller and coworkers identified simple, inexpensive, readily-available and abundant iron(0) carbonyl complexes to be appropriate WRC applying $[(ppy)_2Ir(bpy)]PF_6$ as PS and triethylamine as SR in 10 mL of a solution of THF/TEA/H_2O (4/1/1) at 25 °C under Xe-light irradiation for 3 h. In these experiments, turnover numbers with respect to Fe of 114, 141 and 132, respectively, were achieved with either $Fe(CO)_5$, $Fe_2(CO)_9$ or $Fe_3(CO)_{12}$ as WRC precursors (Scheme 2 and Table 1, Entry 6). Applying the latter under optimized conditions (exclusion of UV light by 420 nm cut-off filter, ratio Ir-PS:WRC = 1.61:1) resulted in a maximum TON_{Fe} of 400 and deactivation after three hours (Scheme 2) [20]. A significant improvement of the WRC was achieved by the addition of 1.5 equivalents of tris(4-trifluoromethylphenyl)phosphine $P(C_6H_4(CF_3))_3$ or tris[3,5-bis(trifluoromethyl)phenyl]phosphine $(P(C_6H_3(CF_3)_2)_3$. Applying the latter together with $Fe_3(CO)_{12}$, the *in situ*-generated WRC achieved a TON of up to 1610 after 24 h under slightly changed conditions (THF/TEA/H_2O = 3/2/1, without filter) [76]. Thus, besides the productivity, also the stability of the catalyst system could be increased. Noteworthy, the incident photon to hydrogen efficiency reached 13.4% at 440 nm. Further improvement was achieved by application of novel monocationic Iridium(III)-photosensitizers with the general formula $[Ir^{III}(C\hat{}N)_2(N\hat{}N)]^+$ (C^N: mono deprotonated cyclometallating phenyl pyridine, N^N: neutral bidentate ligand) and $[Ir(phenyloxazole)_2(bpy)]PF_6$ (bpy: 2,2′-bipyridine) [21,22]. In this series, $[(2\text{-phenylbenz-oxazole})_2Ir(bpy)]PF_6$ and $[(ppy)_2Ir(6\text{-}^{i}Pr\text{-}bpy)]PF_6$ (Scheme 3, Table 1, Entry 9) turned out to be the most efficient photosensitizer with $[HNEt_3][HFe_3(CO)_{11}]$/tris[3,5-bis(trifluoromethyl)phenyl]-phosphine as the water reduction catalyst and triethylamine as the sacrificial reductant. Accordingly, TONs were improved up to 2770 for the Fe-WRC and 4550 for the Ir-PS applying 15 µmol and 0.5 µmol of the photosensitizer $[(ppy)_2Ir(6\text{-}^{i}Pr\text{-}bpy)]PF_6$, respectively. These experiments have been performed under 440-nm irradiation by a Lumatec mercury lamp (Figure 1).

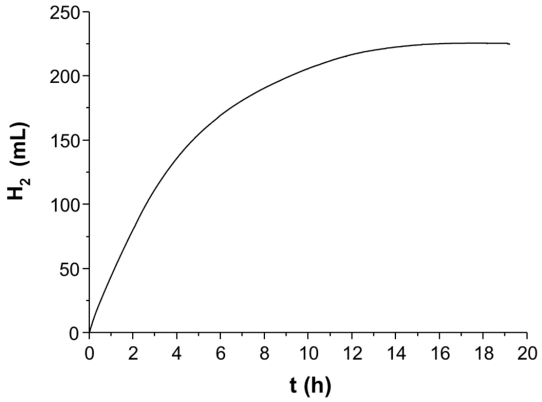

Figure 1. Typical hydrogen evolution curve. Reaction conditions: 3.3 µmol $[HNEt_3][HFe_3(CO)_{11}]$, 15.0 µmol Ir-PS, 5.0 µmol $P(C_6H_3\text{-}3,5\text{-}(CF_3)_2)_3$, 440-nm irradiation 1.5 W, 20 mL THF/TEA/H_2O (3/2/1), 25 °C.

The incident photon to hydrogen yield was also increased to 16.4% applying this system [21]. In order to render light the limiting factor, the lamp performance was decreased to a value of 0.09 W·cm^{-2}. The number of photons was then determined by chemical actinometer experiments [148]. Obviously, only 46%–65% of the provided photons were available inside the reactor depending on the wavelength and the power. Taking this into consideration, significantly improved quantum yields of up to 48% at a wavelength of 415 nm and 41% at 440 nm, respectively, were achieved (Figure 2).

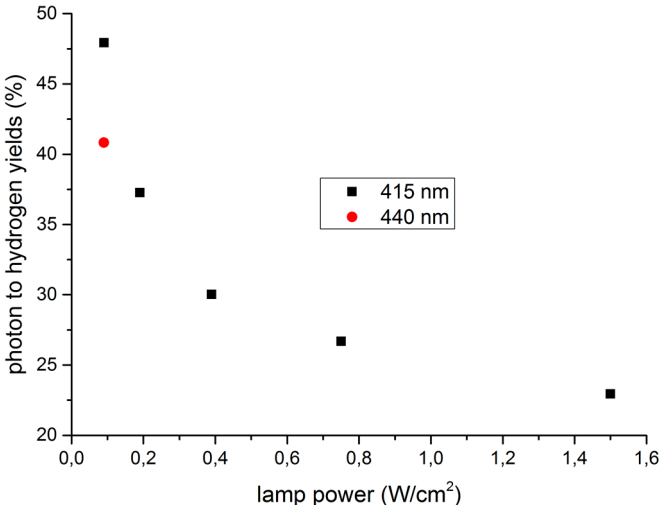

Figure 2. Photon to hydrogen yield determination with dependence on lamp performance and wavelength. Reaction conditions: 3.3 μmol $Fe_3(CO)_{12}$; 15.0 μmol $[(ppy)_2Ir(bpy)]PF_6$; 5.0 μmol ligand (tris[3,5-bis(trifluoromethyl)phenyl]-phosphine); ($Fe_3(CO)_{12}$/PR_3 = 1:1.5); 10 mL THF/TEA/H_20 (3:2:1); 25 °C, 20 h.

Noteworthy, a noble metal-free water reduction system could be realized applying a copper-based PS instead of the Ir complex. In this respect, we focused on heteroleptic copper complexes with the general formula $[Cu(N^{\wedge}N)(P^{\wedge}P)]^+$ (**D** in Scheme 3, Table 1, Entries 7, 8 and 16). While the absorption and fluorescence spectra of these complexes are similar to those of ruthenium [73,74,149–153] or iridium [21] complexes with polypyridine ligands, the excited state lifetime reaches up to 54 μs and, thus, demonstrates that the non-radiative decay is indeed slow and does not interfere with photocatalytic electron transfer processes. A key issue is the improvement of steric and electronic factors in order to get long-lived metal to ligand charge transfer (MLCT) exited states. This was achieved in heteroleptic complexes, especially those bearing the bathocuproine ligand. The methyl groups located at the 2- and 9-position are important to avoid the expansion of the coordination sphere of the metal center [154] and at the same time favor the tetrahedral (T_d) geometry. Thus, in the MLCT exited state, the flattening to the preferred square planar geometry is significantly reduced [155,156]. A number of molecularly-defined Cu-PS has been synthesized based on various combinations of bidentate phosphines and amines. Subsequent tests as PS in the photocatalytic proton reduction in the presence of $[Fe_3(CO)_{12}]$ as WRC and TEA as SR (THF:TEA:H_2O = 4:3:1) revealed a TON of up to 1330 for the Cu-PS (Scheme 3) [144,145]. Thus, these noble metal-free systems already achieved productivities in the same order of magnitude as those containing Ru- or Ir-PS.

Finally, the activity of the catalytic proton reduction was improved applying Knölker's iron complexes instead of iron carbonyl complexes. In combination with the mentioned Cu-PS, the activity was increased up to 15 times (Scheme 2 and Table 1, Entry 16) [157]. Noteworthy, this class of complexes allows for a metal ligand cooperative catalysis, as the oxygen atom at the cyclopentadienyl ring provides a basic center, which can be protonated like the azadithiolate moiety in the [FeFe] hydrogenase, enabling facile heterolytic hydrogen generation [157].

Table 1. Selected reported iron-based WRCs (Scheme 2) in photocatalytic hydrogen generation in the presence of photosensitizers (Scheme 3) and sacrificial agents.

Entry	WRC	PS	Conditions [1]	Light (t_{irr}/h)	TON_{WRC}	TON_{PS}	Ref.
1	**1**	**A** R = H	10 mL DCM, 25 μM **1**; 50 μM **A**; 5 mM thiosalicylic acid, 1 mM TFA	Xe, λ ≥ 400 nm (2.5 h)	0.16	- [2]	[105]
2	**2**	**B**	5 mL ACN, 5 mL H_2O, 10 μmol **2**, 1 μmol **B**, 1 mmol ascorbic acid	Xe, λ ≥ 400 nm (3 h)	4.3	86	[61]
3	**2**	**C**	acetone/water (9:1 *v*/*v*), 0.05 M **2**, 0.05 M **C**, 0.14 M TEA	Xe, λ ≥ 400 nm (8 h)	466	- [2]	[62]
4	**3**	**B**	1.5 mL DMF/H_2O (1:1), 14 μM **3**, 140 μM **B**, 100 mM ascorbic acid (adjusted to pH 5.5 with 1 M NaOH)	455–850 nm (2.5 h)	200	20	[23]
5	**4**	**A** R = H + OMe	5 mL toluene, 5 μmol **4**, 20 μmol **A**, 50 μmol [N^iPr_2EtH] [OAc]	Xe, λ ≥ 390 nm (80 min)	5	4	[64]
6	**5**	**C**	10 mL THF/TEA/H_2O (4:1:1 *v*/*v*/*v*), 18.5 μmol **5**, 7.5 μmol **C**	Xe, λ ≥ 420 nm (output 1.5 W) (6 h)	400	3035	[20]
7	**5**	**D** R = Me	10 mL THF/TEA/H_2O (4:1:1 *v*/*v*/*v*), 5 μmol **5**, 3.5 μmol **D**	Xe, λ ≥ 200 nm (output 1.5 W) (27 h)	547	781	[144]
8	**5**	**D** R = ^{s}Bu	10 mL THF/TEA/H_2O (4:1:1 *v*/*v*/*v*), 5 μmol **5**, 3.5 μmol **D**	Xe, λ ≥ 200 nm (output 1.5 W) (60 h)	931	1330	[145]
9	**6**	**E**	20 mL THF/TEA/H_2O (3:2:1, *v*/*v*/*v*), **6**: 3.3 μmol [Fe] + 5.0 μmol L, 0.5 or 15.0 μmol **E**	Hg, λ = 440 nm (output 1.5 W) (20 h)	2770	4550	[21]
10	**7**	**F** X = Te	10 mL H_2O, 156 μM **7**, 50 μM **F**, 85.2 mM ascorbic acid	Hg, λ ≥ 400 nm (18 h)	505	79	[158]
11	**8**	**G**	10 mL EtOH/H_2O (1:1, *v*/*v*), 0.1 mM **8**, 1.0 mM **G**, 10% TEA	Xe, λ > 450 nm (15 h)	226	59	[106]
12	**9**	**G**	10 mL H_2O, 0.1 mM **9**, 20 mM sodium dodecyl sulfate, 0.2 mM **G**, 10 vol % TEA	LED, λ = 455 nm (output 0.3 W) (4.5 h)	117	58	[107]
13	**10**	**C**	10 mL acetone/H_2O (9:1, *v*/*v*), 0.25–1.0 μM **10**, 0.5 mM **C**, 0.6 M TEA	Xe, 400 < λ < 800 nm (8 h)	22,200	44	[65]
14	**11**	**F** X = Te	10 mL H_2O/MeOH (3:1, *v*/*v*), 1.0 μM **11**, 0.684 μM **F** + 10 mg chitosan, 0.2 M ascorbic acid	LED, λ = 410 nm (60 h)	52,800	- [2]	[111]
15	**12**	**F** X = Se	10 mL H_2O, 1.0 μM **12**, 5.2 μM **F**, 0.2 M ascorbic acid	LED, λ = 520 nm (12 h)	26,500	- [2]	[108]
16	**13**	**D** R = Me	10 mL THF/TEA/H_2O (4:3:1 *v*/*v*/*v*), 12 μmol **13**, 12 μmol Et_4NOH, 3.5 μmol **D**	Xe, λ ≥ 200 nm (output 1.5 W) (7 h)	131	449	[157]
17	**14**	**F** X = Se	5 mL EtOH/H_2O (1:1, *v*/*v*), 0.5 μM **14**, 0.2 μM **F** (with 80 μM capping agent), 0.2 M ascorbic acid	LED, λ = 520 nm (output 0.15 W) (80 h)	29,400	- [2]	[109]

[1] Abbreviations: irr, irradiation; ref., reference; DCM, dichloromethane; TFA, trifluoroacetic acid; ACN, acetonitrile; TEA, triethylamine; DMF, dimethylformamide; THF, tetrahydrofuran. [2] Not provided.

4. Improving Mechanistic Understanding by an Approach of Combined Analytical Methods

The project "Light to Hydrogen" brought together research groups with catalytic, analytical, opto-physical, as well as theoretical expertise, which provided an excellent opportunity to gain deeper mechanistic insights. As a consequence, the Ir–Fe water (proton) reduction system belongs to the most investigated and best understood ones reported so far. Therefore, it will be demonstrated in the following section how a combination of various analytical and theoretical methods clarifies the intricate work mode of the different components including the detection of intermediates. These comprehensive mechanistic studies included Raman, NMR, EPR, *in situ*, as well as operando FTIR spectroscopy and DFT calculations [159]. In particular, the trimeric complex $[HFe_3(CO)_{11}]^-$ was identified as a key intermediate during water reduction by NMR, Raman and *in situ* FTIR spectroscopy. Comparison with a synthesized $[HNEt_3][HFe_3(CO)_{11}]$ proved the assignment of the Raman bands at 223 and 165 cm^{-1} to this intermediate, as well as the characteristic band pattern in the IR spectrum (bands at 2064, 1999,

1993, 1975, 1941 and 1748 cm^{-1}). In addition, the monomeric $[HFe(CO)_4]^-$ species was detected via *in situ* IR spectroscopy (bands at 1998, 1908 and 1878 cm^{-1}), while EPR spectroscopy enabled the identification of the dimeric $[H_2Fe_2(CO)_7]^-$ (g = 2.0432) and $[Fe_2(CO)_8]^{\bullet -}$ (g = 2.0385) intermediates. The latter two dimeric species are products of a side reaction and constitute intermediates toward $[HFe(CO)_4]^-$ (M11), which acts as a resting state [160,161]. Deactivation pathways during catalysis are both CO release from the WRC mediated by light irradiation and the decomposition of the Ir-PS especially at high PS/WRC ratios. Then, the released ligand is transferred towards the iron center of the WRC to form $[Fe(CO)_3(bpy)]$, which was detected by *in situ* IR spectroscopy. Further, these assumptions are supported by DFT calculations [161,162]. Based on the obtained data, a proposal for the mechanism has been developed (Scheme 4).

In the left cycle, electrons of $[(ppy)_2Ir(bpy)]^+$ (M1) are promoted via light irradiation to form the excited $[(ppy)_2Ir(bpy)]^{+*}$ (M2). Time-resolved photoluminescence experiments showed reductive quenching of M2 by TEA, which is the rate-determining step of the overall system. The resulting $[(ppy)_2Ir(bpy)]$ (M3) possesses a reduction potential sufficiently high to reduce $[Fe_3(CO)_{11}]^{\bullet -}$ (M6), as well as $[HFe_3(CO)_{11}]^-$ (M7) in the right cycle [163]. The sacrificial reductant TEA is converted to oxidized TEA radicals and finally to acetaldehyde after hydrolysis.

The precursor $Fe_3(CO)_{12}$ (M5) is quickly reduced already in the dark by electron transfer from TEA forming the electron-rich 19-electron complex $[Fe_3(CO)_{12}]^{\bullet -}$. This unstable complex undergoes decarbonylation to the electron-deficient 17-electron complex $[Fe_3(CO)_{11}]^{\bullet -}$, as well as $[Fe_2(CO)_8]^{\bullet -}$ and $Fe(CO)_5$ (M6). Under light irradiation, reduction of M6 by $Ir\text{-}PS^-$ and subsequent proton transfer result in the formation of the active catalyst $[HFe_3(CO)_{11}]^-$ (M7). Subsequently, a second electron transfer is supposed to form $[HFe_3(CO)_{11}]^{2-}$ (M8) followed by a proton transfer to form $[H_2Fe_3(CO)_{11}]^-$ (M9). H_2 is released from M9, and $[Fe_3(CO)_{11}]^{2-}$ (M10) is restored after further reduction by the $Ir\text{-}PS^-$ in order to restart the cycle. In parallel, M7 can also be converted into $[Fe_2(CO)_8]^{\bullet -}$ and the resting state $[HFe(CO)_4]^-$ (M11) by incorporation of CO and reduction (vide supra). The reverse reaction from M11 to M7 and reactivation of the WRC are mediated by irradiation [76,160,161,163].

It should be noted that this broad range of methods is unparalleled for a single proton reduction system. The rich chemistry of $Fe_3(CO)_{12}$ in reaction solution in the dark is extended to several more species under illumination in the presence of an Ir-PS with sufficiently high reduction potential in its excited state.

Further, the exact role of added phosphine ligand and its enhancing effect on the TON was of special interest. Recent *in situ* FTIR experiments reveal the formation of $[Fe_2(CO)_7P(C_6H_4(CF_3))_2]^-$ (bands at 2021,1971,1941 and 1922 cm^{-1}), when $P(C_6H_4(CF_3))_3$ was added to the reaction mixture (Figure 3, top). This phosphidodiferrate is more stable than the phosphorus-deficient compounds $[HFe_3(CO)_{11}]^-$ (M7) and $[HFe(CO)_4]^-$ (M11), and thus, it constitutes the only iron carbonyl complex present in solution after 15 h of light irradiation (Figure 3, right). At his time, hydrogen generation still continues (Figure 3, left, violet curve), while it stops in the absence of a phosphine ligand (Figure 3, left, grey curve). The spectral assignment of $[Fe_2(CO)_7P(C_6H_4(CF_3))_2]^-$ is confirmed by DFT calculations and comparison with $[Fe_2(CO)_7PPh_2]^-$ [164–166]. The latter shows the same IR contributions shifted by 5 cm^{-1} to lower wavenumbers due to the less electron withdrawing effect of the phenyl group compared to $C_6H_4(CF_3)$.

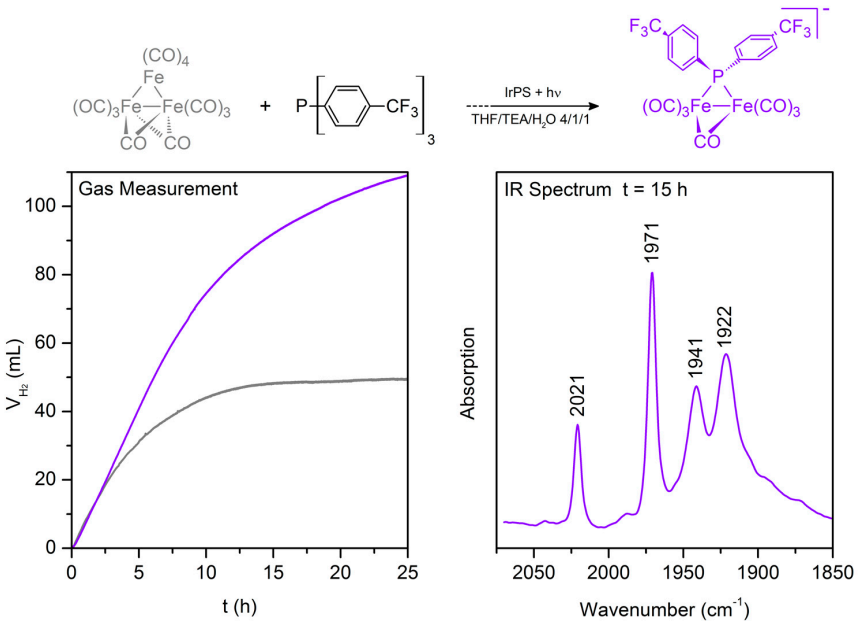

Figure 3. Formation scheme of the phosphidodiferrate $[Fe_2(CO)_7P(C_6H_4(CF_3))_2]^-$ and gas evolution curves with (left, violet curve) and without (left, grey curve) application of $P(C_6H_4(CF_3))_3$. After 15 h of light irradiation, the phosphidodiferrate is the only WRC present in solution (right, violet spectrum). Reaction conditions: 6.1 µmol $Fe_3(CO)_{12}$; 10.0 µmol $[(ppy)_2Ir(bpy)]PF_6$; 6.1 µmol (violet) or 0 µmol (grey) $P(–C_6H_4(CF_3))_3$; 20 mL THF/TEA/$H_2$0 (4:1:1); 25 °C; 1.5 W visible light. For experimental details, see [161,165,166].

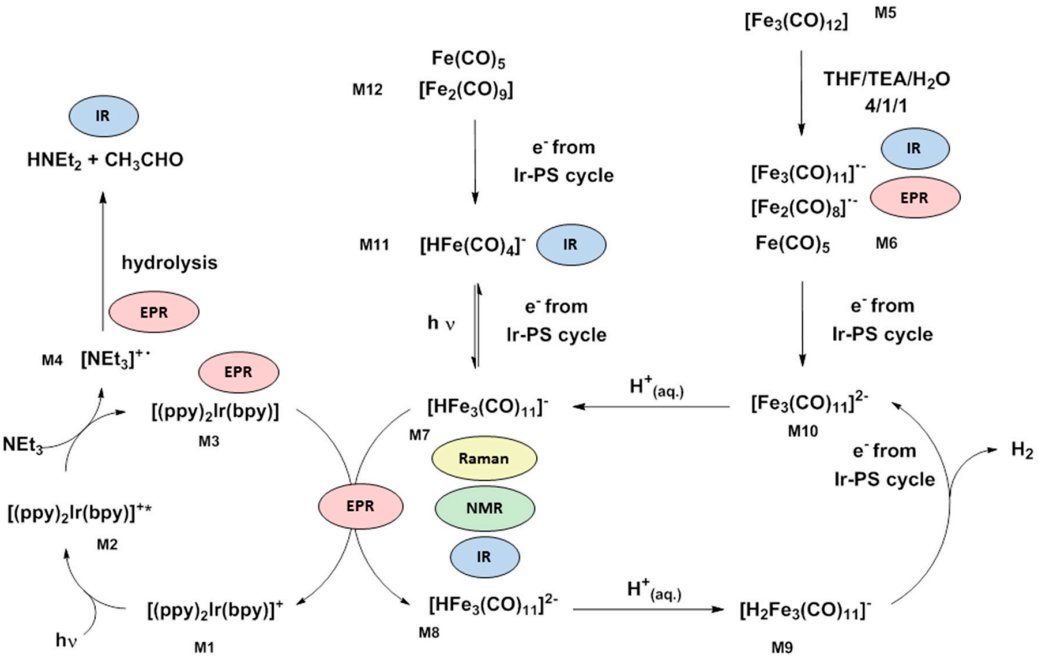

Scheme 4. Proposed catalytic mechanism for light-driven hydrogen generation with $[(ppy)_2Ir(bpy)]PF_6$ and iron(0) carbonyl precursors. The respective methods of identification are highlighted next to the involved species [76,160–163,165,166].

Interestingly, an analogue phosphidodiferrate constitutes the active WRC in the photocatalytic proton reduction applying also Cu-PS and $Fe_3(CO)_{12}$. Mechanistic investigations revealed the existence of an equilibrium between the homo- and hetero-leptic Cu complexes in solution according to

Figure 4 [141,165]. Thus, a part of the released xantphos is available as the precursor for the PR_2 unit. Besides, the heteroleptic [Cu(bathocuproine)(xantphos)]PF_6 was established to present the active PS [166].

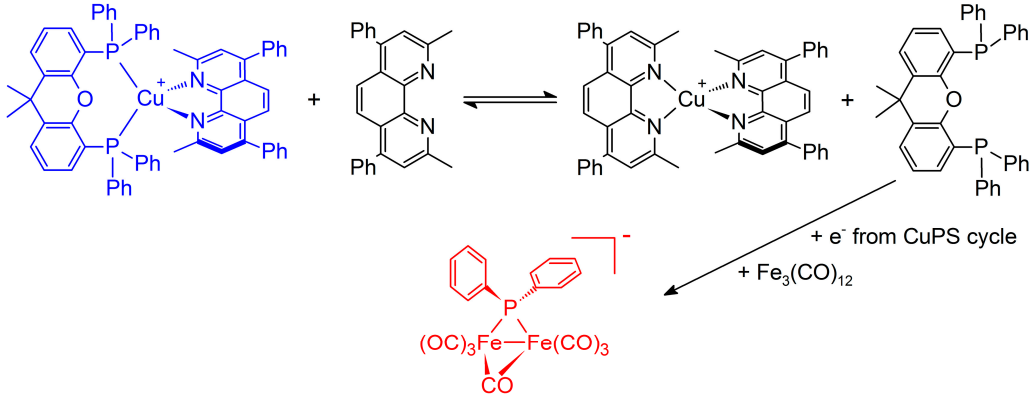

Figure 4. Equilibrium between hetero- and homoleptic Cu-PS and the formation of the phosphidodiferrate initiated by reductively-induced xantphos fragmentation. The active Cu-PS and WRC are highlighted in blue and red, respectively.

Taking the equilibrium in Figure 4 into consideration, we successfully developed an *in situ* method for the synthesis of the organometallic copper complex. Instead of the time-consuming pre-synthesis of molecularly-defined complexes, the application of this method allowed for further optimization of the quantity of ligands leading to improved system efficiency [166].

To investigate the primary steps initiated by the absorption of light for both systems, the Ir-PS/Fe-WRC, as well as the Cu-PS/Fe-WRC, time-resolved UV/Vis absorption and photoluminescence measurements applying a femtosecond pump-probe setup and a streak camera were performed. The UV/Vis absorption spectrum of the Ir-PS $[(ppy)_2Ir(bpy)]^+$ **C** results from electronic transitions to ligand centered states and to metal to ligand charge transfer (MLCT) states involving the ppy- and the bpy-ligands at longer wavelengths. After optical excitation ultrafast intersystem crossing (ISC) takes place within the time resolution of the pump-probe experiment of 150 fs [167]. Then, vibrational redistribution and relaxation within the triplet manifold results in the population of the lowest triplet MLCT state on the picosecond timescale. In this state, the excited electron is located on the bpy-ligand, and if the ppy-ligand is originally excited, an ultrafast interligand charge transfer is observed [167].

In the case of the Cu-PS **D**, ISC takes 7 ps and is preceded by a flattening of the complex structure within the first picosecond [156]. As in the case of the Ir-PS **C**, the long lifetime of the resulting ^{3}MLCT is a crucial factor for the performance as a sensitizer in photocatalysis.

The electron transfer steps between the photosensitizer and the SR and the WRC were studied by quenching of the photoluminescence from the ^{3}MLCT state (Figure 5). In pure THF, the Ir-PS $[(ppy)_2Ir(bpy)]^+$ **C** exhibited a lifetime of 0.37 µs, which reduces drastically to 15 ns in the presence of 17 vol % TEA (Figure 5, left). This is caused by reductive quenching, i.e., an electron transfer from the SR to the metal center of the Ir-PS. The quenching rate can be compared with the calculated diffusion rate. It turns out that the transfer happens only for a small fraction of collisions between TEA and Ir-PS molecules since a specific collision geometry is required for this process [163]. However, the high TEA concentration compensates for the low collision yield and guarantees an effective transfer. At the applied WRC concentrations, the WRC does not significantly contribute to the quenching. Rather, it accepts the electron from the already reduced Ir-PS, and the transfer chain follows a reductive pathway. In the case of the Cu-PS, the situation is different (Figure 5, right). The lifetime of the ^{3}MLCT in THF is 2.9 µs at a Cu-PS concentration of 0.35 mM. This concentration is also applied in the photocatalytic experiments, but results already in some self-quenching of the PS. If it is reduced to

0.02 mM, the lifetime doubles to 6.4 µs [145]. Adding TEA (17 vol %) causes a moderate reduction of the luminescence lifetime to 1 µs, while it strongly decreases down to 50 ns if the TEA solution also contains 0.5 mM of the WRC. Obviously, the first electron transfer step is here from the Cu-PS to the WRC and is hence associated with an oxidation of the Cu-PS. The reduction of the sensitizer by the SR back to its original configuration occurs as the second step on longer time scales. Accordingly, the electron transfer sequence proceeds via an oxidative route. However, the dominant pathway depends on the specific photocatalytic system, as was shown by the application of Knölker's iron complexes **13** with Cu-PS **D**, where the reductive pathway is dominant again [157].

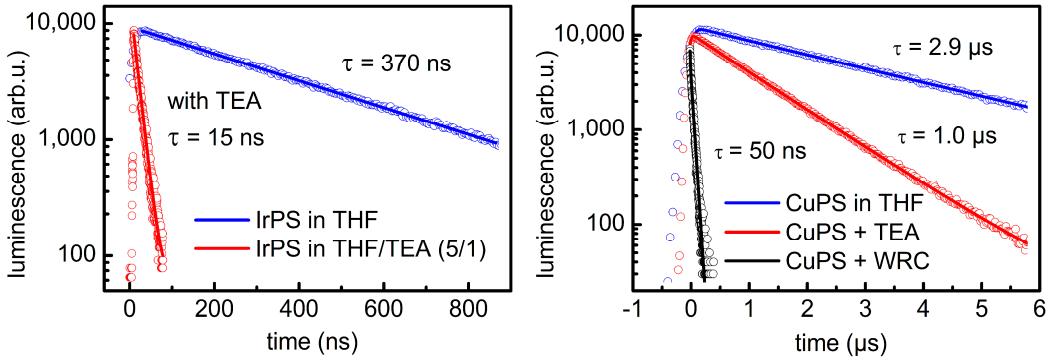

Figure 5. Time resolved photoluminescence and fitted exponential decays of the Ir-PS $[(ppy)_2Ir(bpy)]^+$ **C** (**left**) and the Cu-PS **D** (**right**) in THF. Adding 17 volume percent of TEA (red) results in quenching of the luminescence with respect to pure solvent (blue). This effect is particular strong for the Ir-PS, while in the case of the Cu-PS, the addition of 0.5 mM WRC $[HFe_3(CO)_{11}]^-$ (black) leads to a much faster luminescence decay.

5. Summary and Outlook

The productivities of non-noble metal-based WRCs were significantly increased during the last 6–8 years: Thus, the TONs for Ni and Co were improved by four and three orders of magnitude, respectively. The same trend is obvious for iron. While the first successful experiments containing an iron-based WRC gave a TON of 90 in 2006, already five years later, a TON of 2770 was achieved. This trend is continuing, as is demonstrated by the latest records of >58,000 turnovers in 2013. Thus, these WRCs already show a comparable or even better performance compared to previously applied Pt, Rh- or Ru-based WRCs. An additional trend focuses on the development of fully noble metal-free photocatalytic systems in order to substitute expensive Ir and Ru photosensitizers by semiconductors, quantum dots or organic dyes.

In this article, we present the development of a water reduction system containing only base metals. In the first step, a readily-available, simple and inexpensive iron carbonyl compound has been shown to catalyze the proton reduction together with an iridium photosensitizer as the light-harvesting component. The performance of this Fe-WRC was stepwise improved up to a TON of 2770 by the addition of an appropriate phosphine and the development of the more efficient PS $[(ppy)_2Ir(6\text{-}^i Pr\text{-}bpy)]PF_6$. The active Fe-WRC was identified to be a phosphidodiferrate $[Fe_2(CO)_7P(C_6H_4(CF_3))_2]^-$. Quantum efficiencies of up to 48% were achieved with these systems applying blue light (415 nm). Finally, we successfully substituted the Ir-PS by molecularly-defined heteroleptic copper photosensitizers of the general formula $[Cu(N^\wedge N)(P^\wedge P)]PF_6$. A combination of $Fe_3(CO)_{12}$ and Cu-PS in the light-driven water reduction using TEA as the sacrificial reagent resulted in turnover numbers of up to 1330 and a stability of more than two days. Noteworthy, the Cu-PS can even be generated in an *in situ* method from the precursors during light irradiation, thus avoiding time-consuming synthesis procedures. Besides the catalytic tests, a careful investigation of the reaction mechanism allowed for a deep insight into the reaction mode, including loss channels.

Spectroscopic studies showed that after optical excitation of the photosensitizer, intramolecular processes result in a fast population of the lowest ^{3}MLCT state, which itself has an intrinsic lifetime of some tenth to several ten microseconds depending on the sensitizer. This long lifetime allows for efficient electron transfer processes from the SR and to the WRC. Whether the reductive or the oxidative pathway prevails depends again on the specific photocatalytic system.

So far, homogeneous catalyst materials have been tested mainly in the water reduction half reaction applying sacrificial reagents as electron donors. This allows for a simplification of the complex system of the overall water splitting and, hence, a more detailed understanding of the basic processes as a prerequisite for improvements. However, a challenge for the next time has to be the application of the developed catalyst systems in photocatalytic or photoelectrocatalytic overall water splitting. This will help avoid the undesired influences of sacrificial reagents onto the catalytic systems, like side reactions, deactivation and changing driving forces.

Acknowledgments: The work has been funded by the Federal Ministry of Education and Research of Germany within the interdisciplinary project "Light to Hydrogen" (L2H), which was a part of the program "Spitzenforschung und Innovation in den Neuen Ländern", the Ministry for Education, Science and Culture of Mecklenburg Western Pomerania and the European Union (Investing in our Future, European Regional Development) within the project PS4H and a joint DFG/NFSC project. We thank all thirteen partners from universities and scientific institutions for fruitful cooperation and their contributions to several aspects of the direct photocatalytic water cleavage. Especially, we thank Felix Gärtner, Esteban Mejía, Shu-Ping Luo, Michael Karnahl, Annette-Enrica Surkus, Daniela Cozzula, Sebastian Losse, Anilkumar Gopinathan, Alastair J. J. Lennox, Mark Jurrat, Dirk Hollmann, Enrico Barsch, Arend Rösel, Elisabeth Oberem, Antje Neubauer, Stefanie Tschierlei, Alexandra Pazidis, Aleksej Friedrich, Sergey I. Bokarev, Olga S. Bokareva and Gilbert Grell. In addition, we acknowledge Anja Kammer, Petra Bartels, Christine Fischer, Wolfgang Baumann and Andreas Koch for their technical and analytical support, as well as Anke Spannenberg for X-ray crystallography.

Author Contributions: Henrik Junge, Nils Rockstroh, Steffen Fischer, Stefan Lochbrunner and Matthias Beller wrote the article. Henrik Junge, Nils Rockstroh and Matthias Beller developed the concept for catalyst development and photocatalytic experiments and supervised these experiments. Nils Rockstroh also partly performed catalyst synthesis and photocatalytic experiments. Steffen Fischer was engaged in the operando FTIR measurements which were supervised by Ralf Ludwig. Stefan Lochbrunner developed the concept and supervised the time resolved photoluminescence spectroscopy experiments. Angelika Brückner developed the concept and supervised the EPR and Raman investigation. Oliver Kühn supervised the theoretical calculations and discussions.

Conflicts of Interest: The authors declare no conflict of interest.

References

1. Armaroli, N.; Balzani, V. The Future of Energy Supply: Challenges and Opportunities. *Angew. Chem. Int. Ed.* **2007**, *46*, 52–66. [CrossRef] [PubMed]
2. Schiermeier, Q.; Tollefson, J.; Scully, T.; Witze, A.; Morton, O. Electricity without Carbon. *Nature* **2008**, *454*, 816–823. [CrossRef] [PubMed]
3. Jacobson, M.Z. Review of solutions to global warming, air pollution, and energy security. *Energy Environ. Sci.* **2009**, *2*, 148–173. [CrossRef]
4. Armaroli, N.; Balzani, V. *Energy for a Sustainable World*, 1st ed.; Wiley-VCH: Weinheim, Germany, 2011.
5. Arakawa, H.; Aresta, M.; Armor, J.N.; Barteau, M.A.; Beckman, E.J.; Bell, A.T.; Bercaw, J.E.; Creutz, C.; Dinjus, E.; Dixon, D.A.; et al. Catalysis Research of Relevance to Carbon Management: Progress, Challenges, and Opportunities. *Chem. Rev.* **2001**, *101*, 953–996. [CrossRef] [PubMed]
6. Lewis, N.S.; Nocera, D.G. Powering the planet: Chemical challenges in solar energy utilization. *Proc. Natl. Acad. Sci. USA* **2006**, *103*, 15729–15735. [CrossRef] [PubMed]
7. Centi, G.; Perathoner, S. Towards Solar Fuels from Water and CO_2. *ChemSusChem* **2010**, *3*, 195–208. [CrossRef] [PubMed]
8. Balzani, V.; Credi, A.; Venturi, M. Photochemical Conversion of Solar Energy. *ChemSusChem* **2008**, *1*, 26–58. [CrossRef] [PubMed]
9. Lubitz, W.; Reijerse, E.J.; Messinger, J. Solar water-splitting into H_2 and O_2: Design principles of photosystem II and hydrogenases. *Energy Environ. Sci.* **2008**, *1*, 15–31. [CrossRef]
10. Armaroli, N.; Balzani, V. The Hydrogen Issue. *ChemSusChem* **2011**, *4*, 21–36. [CrossRef] [PubMed]

11. Esswein, A.J.; Nocera, D.G. Hydrogen Production by Molecular Photocatalysis. *Chem. Rev.* **2007**, *107*, 4022–4047. [CrossRef] [PubMed]
12. Osterloh, F.E. Inorganic Materials as Catalysts for Photochemical Splitting of Water. *Chem. Mater.* **2008**, *20*, 35–54. [CrossRef]
13. Nocera, D.G. Personalized Energy: The Home as a Solar Power Station and Solar Gas Station. *ChemSusChem* **2009**, *2*, 387–390. [CrossRef] [PubMed]
14. Kudo, A.; Miseki, Y. Heterogeneous photocatalyst materials for water splitting. *Chem. Soc. Rev.* **2009**, *38*, 253–278. [CrossRef] [PubMed]
15. Yerga, R.M.N.; Galván, M.C.Á.; del Valle, F.; de la Mano, J.A.V.; Fierro, J.L.G. Water Splitting on Semiconductor Catalysts under Visible-Light Irradiation. *ChemSusChem* **2009**, *2*, 471–485. [CrossRef] [PubMed]
16. Chen, X.; Shen, S.; Guo, L.; Mao, S.S. Semiconductor-based Photocatalytic Hydrogen Generation. *Chem. Rev.* **2010**, *110*, 6503–6570. [CrossRef] [PubMed]
17. Schulz, M.; Karnahl, M.; Schwalbe, M.; Vos, J.G. The role of the bridging ligand in photocatalytic supramolecular assemblies for the reduction of protons and carbon dioxide. *Coord. Chem. Rev.* **2012**, *256*, 1682–1705. [CrossRef]
18. Blankenship, R.E.; Tiede, D.M.; Barber, J.; Brudvig, G.W.; Fleming, G.; Ghirardi, M.; Gunner, M.R.; Junge, W.; Kramer, D.M.; Melis, A.; et al. Comparing Photosynthetic and Photovoltaic Efficiencies and Recognizing the Potential for Improvement. *Science* **2011**, *332*, 805–809. [CrossRef] [PubMed]
19. Bensaid, S.; Centi, G.; Garrone, E.; Perathoner, S.; Saracco, G. Towards Artificial Leaves for Solar Hydrogen and Fuels from Carbon Dioxide. *ChemSusChem* **2012**, *5*, 500–521. [CrossRef] [PubMed]
20. Gärtner, F.; Sundararaju, B.; Surkus, A.-E.; Boddien, A.; Loges, B.; Junge, H.; Dixneuf, P.H.; Beller, M. Light-Driven Hydrogen Generation: Efficient Iron-Based Water Reduction Catalysts. *Angew. Chem. Int. Ed.* **2009**, *48*, 9962–9965. [CrossRef] [PubMed]
21. Gärtner, F.; Cozzula, D.; Losse, S.; Boddien, A.; Anilkumar, G.; Junge, H.; Schulz, T.; Marquet, N.; Spannenberg, A.; Gladiali, S.; et al. Synthesis, Characterisation and Application of Iridium(III) Photosensitisers for Catalytic Water Reduction. *Chem. Eur. J.* **2011**, *17*, 6998–7006. [CrossRef] [PubMed]
22. Gärtner, F.; Denurra, S.; Losse, S.; Neubauer, A.; Boddien, A.; Anilkumar, G.; Spannenberg, A.; Junge, H.; Lochbrunner, S.; Blug, M.; et al. Synthesis and Characterization of New Iridium Photosensitizers for Catalytic Hydrogen Generation from Water. *Chem. Eur. J.* **2012**, *18*, 3220–3225. [CrossRef] [PubMed]
23. Streich, D.; Astuti, Y.; Orlandi, M.; Schwartz, L.; Lomoth, R.; Hammarström, L.; Ott, S. High-Turnover Photochemical Hydrogen Production Catalyzed by a Model Complex of the [FeFe]-Hydrogenase Active Site. *Chem. Eur. J.* **2010**, *16*, 60–63. [CrossRef] [PubMed]
24. Zhang, P.; Wang, M.; Li, C.; Li, X.; Dong, J.; Sun, L. Photochemical H_2 production with noble-metal-free molecular devices comprising a porphyrin photosensitizer and a cobaloxime catalyst. *Chem. Commun.* **2010**, *46*, 8806–8808. [CrossRef] [PubMed]
25. Lazarides, T.; Delor, M.; Sazanovich, I.V.; McCormick, T.M.; Georgakaki, I.; Charalambidis, G.; Weinstein, J.A.; Coutsolelos, A.G. Photocatalytic hydrogen production from a noble metal free system based on a water soluble porphyrin derivative and a cobaloxime catalyst. *Chem. Commun.* **2014**, *50*, 521–523. [CrossRef] [PubMed]
26. Luca, O.R.; Blakemore, J.D.; Konezny, S.J.; Praetorius, J.M.; Schmeier, T.J.; Hunsinger, G.B.; Batista, V.S.; Brudvig, G.W.; Hazary, N.; Crabtree, R.H. Organometallic Ni Pincer Complexes for the Electrocatalytic Production of Hydrogen. *Inorg. Chem.* **2012**, *51*, 8704–8709. [CrossRef] [PubMed]
27. Sala, X.; Romero, I.; Rodriguez, M.; Escriche, L.; Llobet, A. Molecular Catalysts that Oxidize Water to Dioxygen. *Angew. Chem. Int. Ed.* **2009**, *48*, 2842–2852. [CrossRef] [PubMed]
28. Limburg, B.; Bouwman, E.; Bonnet, S. Molecular water oxidation catalysts based on transition metals and their decomposition pathways. *Coord. Chem. Rev.* **2012**, *256*, 1451–1467. [CrossRef]
29. Young, K.J.; Martini, L.A.; Milot, R.L.; Snoeberger, R.C., III; Batista, V.S.; Schmuttenmaer, C.A.; Crabtree, R.H.; Brudvig, G.W. Light-driven water oxidation for solar fuels. *Coord. Chem. Rev.* **2012**, *256*, 2503–2520. [CrossRef] [PubMed]
30. Du, P.; Eisenberg, R. Catalysts made of earth-abundant elements (Co, Ni, Fe) for water splitting: Recent progress and future challenges. *Energy Environ. Sci.* **2012**, *5*, 6012–6021. [CrossRef]

31. Eckenhoff, W.T.; Eisenberg, R. Molecular systems for light driven hydrogen production. *Dalton Trans.* **2012**, *41*, 13004–13021. [CrossRef] [PubMed]
32. Wang, M.; Chen, L.; Sun, L. Recent progress in electrochemical hydrogen production with earth-abundant metal complexes as catalysts. *Energy Environ. Sci.* **2012**, *5*, 6763–6778. [CrossRef]
33. Wang, M.; Sun, L. Hydrogen Production by Noble-Metal-Free Molecular Catalysts and Related Nanomaterials. *ChemSusChem* **2010**, *3*, 551–554. [CrossRef] [PubMed]
34. Losse, S.; Vos, J.G.; Rau, S. Catalytic hydrogen production at cobalt centres. *Coord. Chem. Rev.* **2010**, *254*, 2492–2504. [CrossRef]
35. Artero, V.; Chavarot-Kerlidou, M.; Fontecave, M. Splitting Water with Cobalt. *Angew. Chem. Int. Ed.* **2011**, *50*, 7238–7266. [CrossRef] [PubMed]
36. Bachmann, C.; Guttentag, M.; Spingler, B.; Alberto, R. 3d Element Complexes of Pentadentate Bipyridine-Pyridine-Based Ligand Scaffolds: Structures and Photocatalytic Activities. *Inorg. Chem.* **2013**, *52*, 6055–6061. [CrossRef] [PubMed]
37. Mc Laughlin, M.P.; Mc Cormick, T.M.; Eisenberg, R.; Holland, P.L. A stable molecular nickel catalyst for the homogeneous photogeneration of hydrogen in aqueous solution. *Chem. Commun.* **2011**, *47*, 7989–7991. [CrossRef] [PubMed]
38. Han, Z.; McNamara, W.R.; Eum, M.E.; Holland, P.L.; Eisenberg, R. A Nickel Thiolate Catalyst for the Long-Lived Photocatalytic Production of Hydrogen in a Noble-Metal-Free System. *Angew. Chem. Int. Ed.* **2012**, *51*, 1667–1670. [CrossRef] [PubMed]
39. Das, A.; Han, Z.; Brennessel, W.W.; Holland, P.L.; Eisenberg, R. Nickel Complexes for Robust Light-Driven and Electrocatalytic Hydrogen Production from Water. *ACS Catal.* **2015**, *5*, 1397–1406. [CrossRef]
40. Han, Z.; Shen, L.; Brennessel, W.W.; Holland, P.L.; Eisenberg, R. Nickel Pyridinethiolate Complexes as Catalysts for the Light-Driven Production of Hydrogen from Aqueous Solutions in Noble-Metal-Free Systems. *J. Am. Chem. Soc.* **2013**, *135*, 14659–14669. [CrossRef] [PubMed]
41. Wilson, A.D.; Newell, R.H.; McNevin, M.J.; Muckermann, J.T.; DuBois, M.R.; DuBois, D.L. Hydrogen Oxidation and Production Using Nickel-Based Molecular Catalysts with Positioned Proton Relays. *J. Am. Chem. Soc.* **2006**, *128*, 358–366. [CrossRef] [PubMed]
42. Helm, M.L.; Stewart, M.P.; Bullock, R.M.; DuBois, M.R.; DuBois, D.L. A Synthetic Nickel Electrocatalyst with a Turnover Frequency Above 100,000 s^{-1} for H_2 Production. *Science* **2011**, *333*, 863–866. [CrossRef] [PubMed]
43. Wang, C.; Cao, S.; Fu, W.-F. A stable dual-functional system of visible-light-driven Ni(II) reduction to a nickel nanoparticle catalyst and robust *in situ* hydrogen production. *Chem. Commun.* **2013**, *49*, 11251–11253. [CrossRef] [PubMed]
44. Wang, C.J.; Cao, S.; Qin, B.; Zhang, C.; Li, T.-T.; Fu, W.-F. Photoreduction of Iron(III) to Iron(0) Nanoparticles for Simultaneous Hydrogen Evolution in Aqueous Solution. *ChemSusChem* **2014**, *7*, 1924–1933. [CrossRef] [PubMed]
45. Brooks, A.C.; Basore, K.; Bernhard, S. Organocatalytic photoreduction of Zn(II) to zinc metal. *Chem Commun.* **2014**, *50*, 5196–5199. [CrossRef] [PubMed]
46. Junge, H.; Codolà, Z.; Kammer, A.; Rockstroh, N.; Karnahl, M.; Luo, S.-P.; Pohl, M.-M.; Radnik, J.; Gatla, S.; Wohlrab, S.; et al. Copper-based water reduction catalysts for efficient light-drivenhydrogen generation. *J. Mol. Catal. A Chem.* **2014**, *395*, 449–456. [CrossRef]
47. Fontecilla-Camps, J.C.; Volbeda, A.; Cavazza, C.; Nicolet, Y. Structure/Function Relationships of [NiFe]- and [FeFe]-Hydrogenases. *Chem. Rev.* **2007**, *107*, 4273–4303. [CrossRef] [PubMed]
48. Vignais, P.M.; Billoud, B. Occurrence, Classification, and Biological Function of Hydrogenases: An Overview. *Chem. Rev.* **2007**, *107*, 4206–4272. [CrossRef] [PubMed]
49. Lubitz, W.; Ogata, H.; Rüdiger, O.; Reijerse, E. Hydrogenases. *Chem. Rev.* **2014**, *114*, 4081–4148. [CrossRef] [PubMed]
50. Frey, M. Hydrogenases: Hydrogen-Activating Enzymes. *ChemBioChem* **2002**, *3*, 153–160. [CrossRef]
51. Silakov, A.; Wenk, B.; Reijerse, E.; Lubitz, W. ^{14}N HYSCORE investigation of the H-cluster of [FeFe] hydrogenase: Evidence for a nitrogen in the dithiol bridge. *Phys. Chem. Chem. Phys.* **2009**, *11*, 6592–6599. [CrossRef] [PubMed]

52. Erdem, Ö.F.; Schwartz, L.; Stein, M.; Silakov, A.; Kaur-Ghumaan, S.; Huang, P.; Ott, S.; Reijerse, E.J.; Lubitz, W. A Model of the [FeFe] Hydrogenase Active Site with a Biologically Relevant Azadithiolate Bridge: A Spectroscopic and Theoretical Investigation. *Angew. Chem. Int. Ed.* **2011**, *50*, 1439–1443. [CrossRef] [PubMed]
53. Liu, T.; Wang, X.; Hoffmann, C.; DuBois, D.L.; Bullock, R.M. Heterolytic Cleavage of Hydrogen by an Iron Hydrogenase Model: An Fe–H···H–N Dihydrogen Bond Characterized by Neutron Diffraction. *Angew. Chem. Int. Ed.* **2014**, *53*, 5300–5304. [CrossRef] [PubMed]
54. Zell, T.; Ben-David, Y.; Milstein, D. Unprecedented Iron-Catalyzed Ester Hydrogenation. Mild, Selective, and Efficient Hydrogenation of Trifluoroacetic Esters to Alcohols Catalyzed by an Iron Pincer Complex. *Angew. Chem. Int. Ed.* **2014**, *53*, 4685–4689. [CrossRef] [PubMed]
55. Langer, R.; Iron, M.A.; Konstantinovski, L.; Diskin-Posner, Y.; Leitus, G.; Ben-David, Y.; Milstein, D. Iron Borohydride Pincer Complexes for the Efficient Hydrogenation of Ketones under Mild, Base-Free Conditions: Synthesis and Mechanistic Insight. *Chem. Eur. J.* **2012**, *18*, 7196–7209. [CrossRef] [PubMed]
56. Alberico, E.; Sponholz, P.; Cordes, C.; Nielsen, M.; Drexler, H.-D.; Baumann, W.; Junge, H.; Beller, M. Selective Hydrogen Production from Methanol with a Defined Iron Pincer Catalyst under Mild Conditions. *Angew. Chem. Int. Ed.* **2013**, *52*, 14162–14166. [CrossRef] [PubMed]
57. Werkmeister, S.; Junge, K.; Wendt, B.; Alberico, E.; Jiao, H.; Baumann, W.; Junge, H.; Gallou, F.; Beller, M. Hydrogenation of Esters to Alcohols with a Well-Defined Iron Complex. *Angew. Chem. Int. Ed.* **2014**, *53*, 8722–8726. [CrossRef] [PubMed]
58. Bornschein, C.; Werkmeister, S.; Wendt, B.; Jiao, H.; Alberico, E.; Baumann, W.; Junge, H.; Junge, K.; Beller, M. Mild and selective hydrogenation of aromatic and aliphatic (di)nitiles with a well-defined iron pincer complex. *Nat. Commun.* **2014**, *5*, 4111. [CrossRef] [PubMed]
59. Lagaditis, P.O.; Sues, P.E.; Sonnenberg, J.F.; Wan, K.Y.; Lough, A.J.; Morris, R.H. Iron(II) Complexes Containing Unsymmetrical P–N–P′ Pincer Ligands for the Catalytic Asymmetric Hydrogenation of Ketones and Imines. *J. Am. Chem. Soc.* **2014**, *136*, 1367–1380. [CrossRef] [PubMed]
60. Chakraborty, S.; Lagaditis, P.O.; Förster, M.; Bielinsky, B.A.; Hazari, N.; Holthausen, M.C.; Joones, W.D.; Schneider, S. Well-Defined Iron Catalysts for the Acceptorless Reversible Dehydrogenation-Hydrogenation of Alcohols and Ketones. *ACS Catal.* **2014**, *4*, 3994–4003. [CrossRef]
61. Na, Y.; Wang, M.; Pan, J.; Zhang, P.; Åkermark, B.; Sun, L. Visible Light-Driven Electron Transfer and Hydrogen Generation Catalyzed by Bioinspired [2Fe2S] Complexes. *Inorg. Chem.* **2008**, *47*, 2805–2810. [CrossRef] [PubMed]
62. Zhang, P.; Wang, M.; Na, Y.; Li, X.; Jiang, Y.; Sun, L. Homogeneous photocatalytic production of hydrogen from water by a bioinspired [Fe2S2] catalyst with high turnover numbers. *Dalton Trans.* **2010**, *39*, 1204–1206. [CrossRef] [PubMed]
63. Lomoth, R.; Ott, S. Introducing a dark reaction to photochemistry: Photocatalytic hydrogen from [FeFe] hydrogenase active site model complexes. *Dalton Trans.* **2009**, 9952–9959. [CrossRef] [PubMed]
64. Kluwer, A.M.; Kapre, R.; Hartl, F.; Lutz, M.; Spek, A.L.; Brouwer, A.M.; van Leeuwen, P.W.N.M.; Reek, J.N.H. Self-assembled biomimetic [2Fe2S]-hydrogenase-based photocatalyst for molecular hydrogen evolution. *Proc. Natl. Acad. Sci. USA* **2009**, *106*, 10460–10465. [CrossRef] [PubMed]
65. Yu, T.; Zeng, Y.; Chen, J.; Li, Y.-Y.; Yang, G.; Li, Y. Exceptional Dendrimer-Based Mimics of Diiron Hydrogenase for the Photochemical Production of Hydrogen. *Angew. Chem. Int. Ed.* **2013**, *52*, 5631–5635. [CrossRef] [PubMed]
66. Pullen, S.; Fei, H.; Orthaber, A.; Cohen, S.M.; Ott, S. Enhanced Photochemical Hydrogen Production by a Molecular Diiron Catalyst Incorporated into a Metal−Organic Framework. *J. Am. Chem. Soc.* **2013**, *135*, 16997–17003. [CrossRef] [PubMed]
67. Onoda, A.; Kihara, Y.; Fukumoto, K.; Sano, Y.; Hayashi, T. Photoinduced Hydrogen Evolution Catalyzed by a Synthetic Diiron Dithiolate Complex Embedded within a Protein Matrix. *ACS Catal.* **2014**, *4*, 2645–2648. [CrossRef]
68. Lehn, J.-M.; Sauvage, J.-P. Chemical storage of light energy. Catalytic generation of hydrogen by visible light or sunlight. Irradiation of neutral aqueous solutions. *Nouv. J. Chim.* **1977**, *1*, 449–451.
69. Kalyanasundaram, K.; Kiwi, J.; Grätzel, M. Hydrogen Evolution from Water by Visible Light, a Homogeneous Three Component Test System for Redox Catalysis. *Helv. Chim. Acta* **1978**, *61*, 2720–2730. [CrossRef]

70. Kiwi, J.; Grätzel, M. Dynamics of Light-Induced Redox Processes in Microemulsion Systems. *J. Am. Chem. Soc.* **1978**, *100*, 6314–6320. [CrossRef]
71. Moradpour, A.; Amouyal, E.; Keller, P.; Kagan, H. Hydrogen production by visible light irradiation of aqueous solutions of tris(2,2′-bipyridine)ruthenium(2+). *Nouv. J. Chim.* **1978**, *2*, 547–549.
72. Kirch, M.; Lehn, J.-M.; Sauvage, J.-P. Hydrogen Generation by Visible Light Irradiation of Aqueous Solutions of Metal Complexes. An Approach to the Photochemical Conversion and Storage of Solar Energy. *Helv. Chim. Acta* **1979**, *62*, 1345–1384. [CrossRef]
73. Abbotto, A.; Manfredi, N. Electron-rich heteroaromatic conjugated polypyridine ruthenium sensitizers for dye-sensitized solar cells. *Dalton Trans.* **2011**, *40*, 12421–12438. [CrossRef] [PubMed]
74. Vougioukalakis, G.C.; Philippopoulos, A.I.; Stergiopoulos, T.; Falaras, P. Contributions to the development of ruthenium-based sensitizers for dye-sensitized solar cells. *Coord. Chem. Rev.* **2011**, *255*, 2602–2621. [CrossRef]
75. DiSalle, B.F.; Bernhard, S. Orchestrated Photocatalytic Water Reduction Using Surface-Adsorbing Iridium Photosensitizers. *J. Am. Chem. Soc.* **2011**, *133*, 11819–11821. [CrossRef] [PubMed]
76. Gärtner, F.; Boddien, A.; Barsch, E.; Fumino, K.; Losse, S.; Junge, H.; Hollmann, D.; Brückner, A.; Ludwig, R.; Beller, M. Photocatalytic Hydrogen Generation from Water with Iron Carbonyl Phosphine Complexes: Improved Water Reduction Catalysts and Mechanistic Insights. *Chem. Eur. J.* **2011**, *17*, 6425–6436. [CrossRef] [PubMed]
77. Du, P.W.; Knowles, K.; Eisenberg, R. A Homogeneous System for the Photogeneration of Hydrogen from Water Based on a Platinum(II) Terpyridyl Acetylide Chromophore and a Molecular Cobalt Catalyst. *J. Am. Chem. Soc.* **2008**, *130*, 12576–12577. [CrossRef] [PubMed]
78. Okazaki, R.; Masaoka, S.; Sakai, K. Photo-hydrogen-evolving activity of chloro(terpyridine)platinum(II): A single-component molecular photocatalyst. *Dalton Trans.* **2009**, 6127–6133. [CrossRef] [PubMed]
79. Wang, W.-G.; Wang, F.; Wang, H.-Y.; Tung, C.-H.; Wu, L.-Z. Electron transfer and hydrogen generation from a molecular dyad: Platinum(II) alkynyl complex anchored to [FeFe] hydrogenase subsite mimic. *Dalton Trans.* **2012**, *41*, 2420–2426. [CrossRef] [PubMed]
80. Jiang, W.N.; Liu, J.H.; Li, C. Photochemical hydrogen evolution catalyzed by trimetallic [Re–Fe] complexes. *Inorg. Chem. Commun.* **2012**, *16*, 81–85. [CrossRef]
81. Probst, B.; Kolano, C.; Hamm, P.; Alberto, R. An Efficient Homogeneous Intermolecular Rhenium-Based Photocatalytic System for the Production of H_2. *Inorg. Chem.* **2009**, *48*, 1836–1843. [CrossRef] [PubMed]
82. Takeda, H.; Koike, K.; Morimoto, T.; Inumaru, H.; Ishitani, O. Photochemistry and photocatalysis of rhenium(I) diimine complexes. *Adv. Inorg. Chem.* **2011**, *63*, 137–186.
83. Wang, H.-Y.; Wang, W.-G.; Si, G.; Wang, F.; Tung, C.-H.; Wu, L.-Z. Photocatalytic Hydrogen Evolution from Rhenium(I) Complexes to [FeFe] Hydrogenase Mimics in Aqueous SDS Micellar Systems: A Biomimetic Pathway. *Langmuir* **2010**, *26*, 9766–9771. [CrossRef] [PubMed]
84. Probst, B.; Guttentag, M.; Rodenberg, A.; Hamm, P.; Alberto, R. Photocatalytic H_2 Production from Water with Rhenium and Cobalt Complexes. *Inorg. Chem.* **2011**, *50*, 3404–3412. [CrossRef] [PubMed]
85. Probst, B.; Rodenberg, A.; Guttentag, M.; Hamm, P.; Alberto, R. A Highly Stable Rhenium-Cobalt System for Photocatalytic H_2 Production: Unraveling the Performance-Limiting Steps. *Inorg. Chem.* **2010**, *49*, 6453–6460. [CrossRef] [PubMed]
86. Harlang, T.C.B.; Liu, Y.; Gordivska, O.; Fredin, L.A.; Ponseca, C.S., Jr.; Huang, P.; Chabera, P.; Kjaer, K.S.; Mateos, H.; Uhlig, J.; et al. Iron sensitizer converts light to electrons with 92% yield. *Nat. Chem.* **2015**, *7*, 883–889. [CrossRef] [PubMed]
87. Poddutoori, P.; Co, D.T.; Samuel, A.P.S.; Kim, C.H.; Vagnini, M.T.; Wasielewski, M.R. Photoinitiated multistep charge separation in ferrocene–zinc porphyrin–diiron hydrogenase model complex triads. *Energy Environ. Sci.* **2011**, *4*, 2441–2450. [CrossRef]
88. Yamaguchi, H.; Onji, T.; Ohara, H.; Ikeda, N.; Harada, A. Photoinduced Hydrogen-Evolution System with an Antibody-Porphyrin Complex as a Photosensitizer. *Bull. Chem. Soc. Jpn.* **2009**, *82*, 1341–1346. [CrossRef]
89. Zorlu, Y.; Dumoulin, F.; Durmus, M.; Ahsen, V. Comparative studies of photophysical and photochemical properties of solketal substituted platinum(II) and zinc(II) phthalocyanine sets. *Tetrahedron* **2010**, *66*, 3248–3258. [CrossRef]

90. Amao, Y.; Aoki, K. Artificial Photosynthesis System Using Mg Chlorophyll-*a* Conjugated Nanocrystalline TiO_2 Film Electrode via the Axial Imidazole-4-Acetic Acid Ligand. *J. Biobased Mater. Bioenergy* **2008**, *2*, 51–56. [CrossRef]
91. Amao, Y.; Hirakawa, T. Hydrolysis of a mixture of saccharides by cellulase from *Aspergillus niger* and its application for visible-light-induced hydrogen gas production system using Mg chlorophyll-*a* and platinum nanoparticles. *Int. J. Hydrogen Energy* **2010**, *35*, 6624–6628. [CrossRef]
92. Amao, Y.; Hirakawa, T.; Himeshima, N. Photoinduced biohydrogen production from saccharide mixture with the photosensitization of Mg chlorophyll *a* from green plant. *Catal. Commun.* **2008**, *9*, 131–134. [CrossRef]
93. Amao, Y.; Maki, Y.; Fuchino, Y. Photoinduced Hydrogen Production with Artificial Photosynthesis System Based on Carotenoid-Chlorophyll Conjugated Micelles. *J. Phys. Chem. C* **2009**, *113*, 16811–16815. [CrossRef]
94. Tomonou, Y.; Amao, Y. Visible and near-IR light induced biohydrogen production using the system containing Mg chlorophyll-*a* from *Spirulina* and colloidal platinum. *Biometals* **2003**, *16*, 419–424. [CrossRef] [PubMed]
95. Gimbert-Suriñach, C.; Albero, J.; Stoll, T.; Fortage, J.; Collomb, M.-N.; Deronzier, A.; Palomares, E.; Llobet, A. Efficient and Limiting Reactions in Aqueous Light-Induced Hydrogen Evolution Systems using Molecular Catalysts and Quantum Dots. *J. Am. Chem. Soc.* **2014**, *136*, 7655–7661. [CrossRef] [PubMed]
96. Martindale, B.C.M.; Hutton, G.A.M.; Caputo, C.A.; Reisner, E. Solar Hydrogen Production Using Carbon Quantum Dots and a Molecular Nickel Catalyst. *J. Am. Chem. Soc.* **2015**, *137*, 6018–6025. [CrossRef] [PubMed]
97. McCormick, T.M.; Calitree, B.D.; Orchard, A.; Kraut, N.D.; Bright, F.V.; Detty, M.R.; Eisenberg, R. Reductive Side of Water Splitting in Artificial Photosynthesis: New Homogeneous Photosystems of Great Activity and Mechanistic Insight. *J. Am. Chem. Soc.* **2010**, *132*, 15480–15483. [CrossRef] [PubMed]
98. Dong, J.; Wang, M.; Zhang, P.; Yang, S.; Liu, J.; Li, X.; Sun, L. Promoting Effect of Electrostatic Interaction between a Cobalt Catalyst and a Xanthene Dye on Visible-Light-Driven Electron Transfer and Hydrogen Production. *J. Phys Chem. C* **2011**, *115*, 15089–15096. [CrossRef]
99. Mori, K.; Kakudo, H.; Yamashita, H. Creation of Nickel-Based Active Species within a Macroreticular Acidic Resin: A Noble-Metal-Free Heterogeneous Catalyst for Visible-Light-Driven H_2 Evolution from Water. *ACS Catal.* **2014**, *4*, 4129–4135. [CrossRef]
100. Yong, Y.; Wang, M.; Xue, L.; Zhang, F.; Chen, L.; Ahlquist, M.S.G.; Sun, L. Nickel Complex with Internal Bases as Efficient Molecular Catalyst for Photochemical H_2 Production. *ChemSusChem* **2014**, *7*, 2889–2897. [CrossRef] [PubMed]
101. Cui, H.-H.; Wang, J.-Y.; Hu, M.-Q.; Ma, C.-B.; Wen, H.-M.; Song, X.-W.; Chen, C.-N. Efficient photo-driven hydrogen evolution by binuclear nickel catalysts of different coordination in noble-metal-free systems. *Dalton Trans.* **2013**, *42*, 8684–8691. [CrossRef] [PubMed]
102. Lazarides, T.; McCormick, T.; Du, P.; Luo, G.; Lindley, B.; Eisenberg, R. Making Hydrogen from Water Using a Homogeneous System Without Noble Metals. *J. Am. Chem. Soc.* **2009**, *131*, 9192–9194. [CrossRef] [PubMed]
103. Zhang, P.; Wang, M.; Dong, J.; Li, X.; Wang, F.; Wu, L.; Sun, L. Photocatalytic Hydrogen Production from Water by Noble-Metal-Free Molecular Catalyst Systems Containing Rose Bengal and the Cobaloximes of BF_x-Bridged Oxime Ligands. *J. Phys Chem. C* **2010**, *114*, 15868–15874. [CrossRef]
104. Zhang, W.; Hong, J.; Zheng, J.; Huang, Z.; Zhou, J.; Xu, R. Nickel−Thiolate Complex Catalyst Assembled in One Step in Water for Solar H_2 Production. *J. Am. Chem. Soc.* **2011**, *133*, 20680–20683. [CrossRef] [PubMed]
105. Li, X.; Wang, M.; Zhang, S.; Pan, J.; Na, Y.; Liu, J.; Åkermark, B.; Sun, L. Noncovalent Assembly of a Metalloporphyrin and an Iron Hydrogenase Active-Site Model: Photo-Induced Electron Transfer and Hydrogen Generation. *J. Phys. Chem. B* **2008**, *112*, 8198–8202. [CrossRef] [PubMed]
106. Li, X.; Wang, M.; Chen, L.; Wang, X.; Dong, J.; Sun, L. Photocatalytic Water Reduction and Study of the Formation of $Fe^{I}Fe^{0}$ Species in Diiron Catalyst Sytems. *ChemSusChem* **2012**, *5*, 913–919. [CrossRef] [PubMed]
107. Orain, C.; Quentel, F.; Gloaguen, F. Photocatalytic Hydrogen Production Using Models of the Iron–Iron Hydrogenase Active Site Dispersed in Micellar Solution. *ChemSusChem* **2014**, *7*, 638–643. [CrossRef] [PubMed]
108. Jian, J.-X.; Ye, C.; Wang, X.-Z.; Wen, M.; Li, Z.-J.; Li, X.-B.; Chen, B.; Tung, C.-H.; Wu, L.-Z. Comparison of H_2 photogeneration by [FeFe]-hydrogenase mimics with CdSe QDs and $Ru(bpy)_3Cl_2$ in aqueous solution. *Energy Environ. Sci.* **2016**, *9*, 2083–2089. [CrossRef]

109. Lv, H.; Ruberu, P.A.; Fleischauer, V.E.; Brennessel, W.W.; Neidig, M.L.; Eisenberg, R. Catalytic Light-Driven Generation of Hydrogen from Water by Iron Dithiolene Complexes. *J. Am. Chem. Soc.* **2016**, *138*, 11654–11663. [CrossRef] [PubMed]
110. Tropmann, S.; König, B. Functionalized Vesicles with Co-Embedded CdSe Quantum Dots and [FeFe]-Hydrogenase Mimic for Light-Driven Hydrogen Production. *ChemistrySelect* **2016**, *1*, 1405–1409. [CrossRef]
111. Jian, J.-X.; Liu, Q.; Li, Z.-J.; Wang, F.; Li, X.-B.; Li, C.-B.; Liu, B.; Meng, Q.-Y.; Chen, B.; Feng, K.; et al. Chitosan confinement enhances hydrogen photogeneration from a mimic of the diiron subsite of [FeFe]-hydrogenase. *Nat. Commun.* **2013**, *4*, 2695. [CrossRef] [PubMed]
112. Caputo, C.A.; Wang, L.; Beranek, R.; Reisner, E. Carbon nitride–TiO_2 hybrid modified with hydrogenase for visible light driven hydrogen production. *Chem. Sci.* **2015**, *6*, 5690–5694. [CrossRef]
113. Edel, A.; Marnot, P.A.; Sauvage, J.P. Photochemical reduction of water via energy transfer from a copper(I) complex. *Nouv. J. Chim.* **1984**, *8*, 495–498.
114. Armaroli, N.; Accorsi, G.; Holler, M.; Moudam, O.; Nierengarten, J.-F.; Zhou, Z.; Wegh, R.T.; Welter, R. Highly Luminescent Cu^I Complexes for Light-Emitting Electrochemical Cells. *Adv. Mater.* **2006**, *18*, 1313–1316. [CrossRef]
115. Cuttell, D.G.; Kuang, S.M.; Fanwick, P.E.; McMillin, D.R.; Walton, R.A. Simple Cu(I) Complexes with Unprecedented Excited-State Lifetimes. *J. Am. Chem. Soc.* **2002**, *124*, 6–7. [CrossRef] [PubMed]
116. Harkins, S.B.; Peters, J.C. A Highly Emissive Cu_2N_2 Diamond Core Complex Supported by a $[PNP]^-$ Ligand. *J. Am. Chem. Soc.* **2005**, *127*, 2030–2031. [CrossRef] [PubMed]
117. Smith, C.S.; Branham, C.W.; Marquardt, B.J.; Mann, K.R. Oxygen Gas Sensing by Luminescence Quenching in Crystals of Cu(xantphos)(phen)$^+$ Complexes. *J. Am. Chem. Soc.* **2010**, *132*, 14079–14085. [CrossRef] [PubMed]
118. Kuang, S.-M.; Cuttell, D.G.; McMillin, D.R.; Fanwick, P.E.; Walton, R.A. Synthesis and Structural Characterization of Cu(I) and Ni(II) Complexes that Contain the Bis[2-(diphenylphosphino)phenyl]ether Ligand. Novel Emission Properties for the Cu(I) Species. *Inorg. Chem.* **2002**, *41*, 3313–3322. [CrossRef] [PubMed]
119. Alonso-Vante, N.; Nierengarten, J.-F.; Sauvage, J.-P. Spectral Sensitization of Large-band-gap Semiconductors (Thin Films and Ceramics) by a Carboxylated Bis(1,10-Phenanthroline)copper(I) Complex. *J. Chem. Soc. Dalton Trans.* **1994**, 1649–1654. [CrossRef]
120. Bessho, T.; Constable, E.C.; Graetzel, M.; Hernandez Redondo, A.; Housecroft, C.E.; Kylberg, W.; Nazeeruddin, M.K.; Neuburger, M.; Schaffner, S. An element of surprise—Efficient copper-functionalized dye-sensitized solar cells. *Chem. Commun.* **2008**, 3717–3719. [CrossRef] [PubMed]
121. Bergmann, L.; Friedrichs, J.; Mydlack, M.; Baumann, T.; Nieger, M.; Bräse, S. Outstanding luminescence from neutral copper(I) complexes with pyridyl-tetrazolate and phosphine ligands. *Chem. Commun.* **2013**, *49*, 6501–6503. [CrossRef] [PubMed]
122. Costa, R.D.; Ortí, E.; Bolink, H.J.; Monti, F.; Accorsi, G.; Armaroli, N. Luminescent Ionic Transition-Metal Complexes for Light-Emitting Electrochemical Cells. *Angew. Chem. Int. Ed.* **2012**, *51*, 8178–8211. [CrossRef] [PubMed]
123. Sandroni, M.; Kayanuma, M.; Planchat, A.; Szuwarski, N.; Blart, E.; Pellegrin, Y.; Daniel, C.; Boujtita, M.; Odobel, F. First application of the HETPHEN concept to new heteroleptic bis(diimine) copper(I) complexes as sensitizers in dye sensitized solar cells. *Dalton Trans.* **2013**, *42*, 10818–10827. [CrossRef] [PubMed]
124. Yuasa, J.; Dan, M.; Kawai, T. Phosphorescent properties of metal-free diphosphine ligands and effects of copper binding. *Dalton Trans.* **2013**, *42*, 16096–16101. [CrossRef] [PubMed]
125. Czerwieniec, R.; Kowalski, K.; Yersin, H. Highly efficient thermally activated fluorescence of a new rigid Cu(I) complex [Cu(dmp)(phanephos)]$^+$. *Dalton Trans.* **2013**, *42*, 9826–9830. [CrossRef] [PubMed]
126. Zhang, P.; Wang, M.; Yang, Y.; Yao, T.; Sun, L. A Molecular Copper Catalyst for Electrochemical Water Reduction with a Large Hydrogen-Generation Rate Constant in Aqueous Solution. *Angew. Chem. Int. Ed.* **2014**, *53*, 13803–13807. [CrossRef] [PubMed]
127. Chen, Z.; Meyer, T.J. Copper(II) Catalysis of Water Oxidation. *Angew. Chem. Int. Ed.* **2013**, *52*, 700–703. [CrossRef] [PubMed]

128. Barnett, S.M.; Goldberg, K.I.; Mayer, J.M. A soluble copper–bipyridine water-oxidation electrocatalyst. *Nat. Chem.* **2012**, *4*, 498–502. [CrossRef] [PubMed]
129. Zhang, T.; Wang, C.; Liu, S.; Wang, J.-L.; Lin, W. A Biomimetic Copper Water Oxidation Catalyst with Low Overpotential. *J. Am. Chem. Soc.* **2014**, *136*, 273–281. [CrossRef] [PubMed]
130. Coggins, M.K.; Zhang, M.-T.; Chen, Z.; Song, N.; Meyer, T.J. Single-Site Copper(II) Water Oxidation Electrocatalysis: Rate Enhancements with HPO_4^{2-} as a Proton Acceptor at pH 8. *Angew. Chem. Int. Ed.* **2014**, *53*, 12226–12230. [CrossRef] [PubMed]
131. Chen, Z.; Kang, P.; Zhang, M.-T.; Stoner, B.R.; Meyer, T.J. Cu(II)/Cu(0) electrocatalyzed CO_2 and H_2O splitting. *Energy Environ. Sci.* **2013**, *6*, 813–817. [CrossRef]
132. Choi, H.-J.; Kang, M. Hydrogen production from methanol/water decomposition in a liquid photosystem using the anatase structure of Cu loaded TiO_2. *Int. J. Hydrogen Energy* **2007**, *32*, 3841–3848. [CrossRef]
133. Yoong, L.S.; Chong, F.K.; Dutta, B.K. Development of copper-doped TiO_2 photocatalyst for hydrogen production under visible light. *Energy* **2009**, *34*, 1652–1661. [CrossRef]
134. Xu, S.; Sun, D.D. Significant improvement of photocatalytic hydrogen generation rate over TiO_2 with deposited CuO. *Int. J. Hydrogen Energy* **2009**, *34*, 6096–6104. [CrossRef]
135. Sakata, Y.; Yamamoto, T.; Okazaki, T.; Imamura, H.; Tsuchiya, S. Generation of Visible Light Response on the Photocatalyst of a Copper Ion Containing TiO_2. *Chem. Lett.* **1998**, *27*, 1253–1254. [CrossRef]
136. Kumar, D.P.; Shankar, M.V.; Kumari, M.M.; Sadanandam, G.; Srinivas, B.; Durgakumari, V. Nano-size effects on CuO/TiO_2 catalysts for highly efficient H_2 production under solar light irradiation. *Chem. Commun.* **2013**, *49*, 9443–9445. [CrossRef] [PubMed]
137. Paracchino, A.; Laporte, V.; Sivula, K.; Grätzel, M.; Thimsen, E. Highly active oxide photocathode for photoelectrochemical water reduction. *Nat. Mater.* **2011**, *10*, 456–461. [CrossRef] [PubMed]
138. Barreca, D.; Fornasiero, P.; Gasparotto, A.; Gombac, V.; Maccato, C.; Montini, T.; Tondello, E. The Potential of Supported Cu_2O and CuO Nanosystems in Photocatalytic H_2 Production. *ChemSusChem* **2009**, *2*, 230–233. [CrossRef] [PubMed]
139. Somasundaram, S.; Chenthamarakshan, C.R.N.; de Tacconi, N.R.; Rajeshwar, K. Photocatalytic production of hydrogen from electrodeposited p-Cu_2O film and sacrificial electron donors. *Int. J. Hydrogen Energy* **2007**, *32*, 4661–4669. [CrossRef]
140. McCusker, C.E.; Castellano, F.N. Design of a Long-Lifetime, Earth-Abundant, Aqueous Compatible Cu(I) Photosensitizer Using Cooperative Steric Effects. *Inorg. Chem.* **2013**, *52*, 8114–8120. [CrossRef] [PubMed]
141. Kaeser, A.; Mohankumar, M.; Mohanraj, J.; Monti, F.; Holler, M.; Cid, J.-J.; Moudam, O.; Nierengarten, I.; Karmazin-Brelot, L.; Duhayon, C.; et al. Heteroleptic Copper(I) Complexes Prepared from Phenanthroline and Bis-Phosphine Ligands. *Inorg. Chem.* **2013**, *52*, 12140–12151. [CrossRef] [PubMed]
142. Chen, J.-L.; Cao, X.-F.; Wang, J.-Y.; He, L.-H.; Liu, Z.-Y.; Wen, H.-R.; Chen, Z.-N. Synthesis, Characterization, and Photophysical Properties of Heteroleptic Copper(I) Complexes with Functionalized 3-(2′-Pyridyl)-1,2,4-triazole Chelating Ligands. *Inorg. Chem.* **2013**, *52*, 9727–9740. [CrossRef] [PubMed]
143. Huang, J.; Buyukcakir, O.; Mara, M.W.; Coskun, A.; Dimitrijevic, N.M.; Barin, G.; Kokhan, O.; Stickrath, A.B.; Ruppert, R.; Tiede, D.M.; et al. Highly Efficient Ultrafast Electron Injection from the Singlet MLCT Excited State of Copper(I) Diimine Complexes to TiO_2 Nanoparticles. *Angew. Chem. Int. Ed.* **2012**, *51*, 12711–12715. [CrossRef] [PubMed]
144. Luo, S.-P.; Mejía, E.; Friedrich, A.; Pazidis, A.; Junge, H.; Surkus, A.-E.; Jackstell, R.; Denurra, S.; Gladiali, S.; Lochbrunner, S.; et al. Photocatalytic Water Reduction with Copper-Based Photosensitizers: A Noble-Metal-Free System. *Angew. Chem. Int. Ed.* **2013**, *52*, 419–423. [CrossRef] [PubMed]
145. Mejía, E.; Luo, S.-P.; Karnahl, M.; Friedrich, A.; Tschierlei, S.; Surkus, A.-E.; Junge, H.; Gladiali, S.; Lochbrunner, S.; Beller, M. A Noble-Metal-Free System for Photocatalytic Hydrogen Production from Water. *Chem. Eur. J.* **2013**, *19*, 15972–15978. [CrossRef] [PubMed]
146. Karnahl, M.; Mejía, E.; Rockstroh, N.; Tschierlei, S.; Luo, S.-P.; Grabow, K.; Kruth, A.; Brüser, V.; Junge, H.; Lochbrunner, S.; et al. Photocatalytic Hydrogen Production with Copper Photosensitizer–Titanium Dioxide Composites. *ChemCatChem* **2014**, *6*, 82–86. [CrossRef]
147. Khnayzer, R.S.; McCusker, C.E.; Olaiya, B.S.; Castellano, F.N. Robust Cuprous Phenanthroline Sensitizer for Solar Hydrogen Photocatalysis. *J. Am. Chem. Soc.* **2013**, *52*, 14068–14070. [CrossRef] [PubMed]
148. Montalti, M.; Credi, A.; Prodi, L.; Gandolfi, T. Chemical Actinometry. In *Handbook of Photochemistry*, 3rd ed.; CRC: Boca Raton, FL, USA, 2011; pp. 601–616.

149. Carneiro, Z.A.; de Moraes, J.C.B.; Rodrigues, F.P.; de Lima, R.G.; Curti, C.; da Rocha, Z.N.; Paulo, M.; Bendhack, L.M.; Tedesco, A.C.; Formiga, A.L.B.; et al. Photocytotoxic activity of a nitrosyl phthalocyanine ruthenium complex—A system capable of producing nitric oxide and singlet oxygen. *J. Inorg. Biochem.* **2011**, *105*, 1035–1043. [CrossRef] [PubMed]
150. Heussner, K.; Peuntinger, K.; Rockstroh, N.; Nye, L.C.; Ivanovic-Burmazovic, I.; Rau, S.; Streb, C. Solution and solid-state interactions in a supramolecular ruthenium photosensitizer–polyoxometalate aggregate. *Chem. Commun.* **2011**, *47*, 6852–6854. [CrossRef] [PubMed]
151. La Ganga, G.; Puntoriero, F.; Campagna, S.; Bazzan, I.; Berardi, S.; Bonchio, M.; Sartorel, A.; Natali, M.; Scandola, F. Light-driven water oxidation with a molecular tetra-cobalt(III) cubane cluster. *Faraday Discuss.* **2012**, *155*, 177–190. [CrossRef] [PubMed]
152. Pan, Q.J.; Guo, Y.R.; Li, L.; Odoh, S.O.; Fu, H.G.; Zhang, H.X. Structures, spectroscopic properties and redox potentials of quaterpyridyl Ru(II) photosensitizer and its derivatives for solar energy cell: A density functional study. *Phys. Chem. Chem. Phys.* **2011**, *13*, 14481–14489. [CrossRef] [PubMed]
153. Shimakoshi, H.; Nishi, M.; Tanaka, A.; Chikama, K.; Hisaeda, Y. Photocatalytic function of a polymer-supported B_{12} complex with a ruthenium trisbipyridine photosensitizer. *Chem. Commun.* **2011**, *47*, 6548–6550. [CrossRef] [PubMed]
154. McMillin, D.R.; Kirchhoff, J.R.; Goodwin, K.V. Exciplex quenching of photo-excited copper complexes. *Coord. Chem. Rev.* **1985**, *64*, 83–92. [CrossRef]
155. Riesgo, E.C.; Hu, Y.-Z.; Bouvier, F.; Thummel, R.P.; Scaltrito, D.V.; Meyer, G.J. Crowded Cu(I) Complexes Involving Benzo[*h*]quinoline: π-Stacking Effects and Long-Lived Excited States. *Inorg. Chem.* **2001**, *40*, 3413–3422. [CrossRef] [PubMed]
156. Tschierlei, S.; Karnahl, M.; Rockstroh, N.; Junge, H.; Beller, M.; Lochbrunner, S. Substitution-Controlled Excited State Processes in Heteroleptic Copper(I) Photosensitizers Used in Hydrogen Evolving Systems. *ChemPhysChem* **2014**, *17*, 3709–3713. [CrossRef] [PubMed]
157. Sun, Y.-Y.; Wang, H.; Chen, N.-Y.; Lennox, A.J.J.; Friedrich, A.; Xia, L.-M.; Lochbrunner, S.; Junge, H.; Beller, M.; Zhou, S.; et al. Efficient Photocatalytic Water Reduction Using *In Situ* Generated Knölker's Iron Complexes. *ChemCatChem* **2016**, *8*, 2340–2344. [CrossRef]
158. Weng, F.; Wang, W.-G.; Wang, X.-J.; Wang, H.-Y.; Tung, C.-H.; Wu, L.-Z. A Highly Efficient Photocatalytic System for Hydrogen Production by a Robust Hydrogenase Mimic in an Aqueous Solution. *Angew. Chem. Int. Ed.* **2011**, *50*, 3193–3197. [CrossRef] [PubMed]
159. Bokarev, S.I.; Bokareva, O.S.; Kühn, O. A theoretical perspective on charge transfer in photocatalysis. The example of Ir-based systems. *Coord. Chem. Rev.* **2015**, *304–305*, 133–145. [CrossRef]
160. Hollmann, D.; Gärtner, F.; Ludwig, R.; Barsch, E.; Junge, H.; Blug, M.; Hoch, S.; Beller, M.; Brückner, A. Insights into the Mechanism of Photocatalytic Water Reduction by DFT-Supported *In Situ* EPR/Raman Spectroscopy. *Angew. Chem. Int. Ed.* **2011**, *50*, 10246–10250. [CrossRef] [PubMed]
161. Fischer, S.; Bokareva, O.S.; Barsch, E.; Bokarev, S.I.; Kühn, O.; Ludwig, R. Mechanistic Study of Photocatalytic Hydrogen Generation with Simple Iron Carbonyls as Water Reduction Catalysts. *ChemCatChem* **2016**, *8*, 404–411. [CrossRef]
162. Bokarev, S.I.; Hollmann, D.; Pazidis, A.; Neubauer, A.; Radnik, J.; Kühn, O.; Lochbrunner, S.; Junge, H.; Beller, M.; Brückner, A. Spin density distribution after electron transfer from triethylamine to an $[Ir(ppy)_2(bpy)]^+$ photosensitizer during photocatalytic water reduction. *Phys. Chem. Chem. Phys.* **2014**, *16*, 4789–4796. [CrossRef] [PubMed]
163. Neubauer, A.; Grell, G.; Friedrich, A.; Bokarev, S.I.; Schwarzbach, P.; Gärtner, F.; Surkus, A.-E.; Junge, H.; Beller, M.; Kühn, O.; et al. Electron- and Energy-Transfer Processes in a Photocatalytic System Based on an Ir(III)-Photosensitizer and an Iron Catalyst. *J. Phys. Chem. Lett.* **2014**, *5*, 1355–1360. [CrossRef] [PubMed]
164. Walther, B.; Hartung, H.; Böttcher, H.-C.; Baumeister, U.; Böhland, U.; Reinhold, J.; Sieler, J.; Ladriere, J.; Schiebel, H.M. Unexpected reaction of $[Ni(CO)_{4-n}(R_2PCl)_n]$ (n = 1, 2; R = Bu^t, Cy, Ph) with $Na_2[Fe_2(CO)_8]$. Synthesis and electronic structure of the anions $[Fe_2(\mu\text{-}CO)(CO)_6(\mu\text{-}PR_2)]^-$ and their reactions with H^+ and $[M(PPh_3)]^+$ (M = Cu, Ag, Au). *Polyhedron* **1991**, *10*, 2423–2435. [CrossRef]
165. Fischer, S.; Hollmann, D.; Tschierlei, S.; Karnahl, M.; Rockstroh, N.; Barsch, E.; Schwarzbach, P.; Luo, S.-P.; Junge, H.; Beller, M.; et al. Death and Rebirth: Photocatalytic Hydrogen Production by a Self-Organizing Copper−Iron System. *ACS Catal.* **2014**, *4*, 1845–1849. [CrossRef]

166. Lennox, A.J.J.; Fischer, S.; Jurrat, M.; Luo, S.-P.; Rockstroh, N.; Junge, H.; Ludwig, R.; Beller, M. Copper-Based Photosensitisers in Water Reduction: A More Efficient *In Situ* Formed System and Improved Mechanistic Understanding. *Chem. Eur. J.* **2016**, *22*, 1233–1238. [CrossRef] [PubMed]
167. Tschierlei, S.; Neubauer, A.; Rockstroh, N.; Karnahl, M.; Schwarzbach, P.; Junge, H.; Beller, M.; Lochbrunner, S. Ultrafast excited state dynamics of iridium(III) complexes and their changes upon immobilisation onto titanium dioxide layers. *Phys. Chem. Chem. Phys.* **2016**, *18*, 10682–10687. [CrossRef] [PubMed]

VII. REFERENCES

[1] N. Armaroli, V. Balzani, *Chem. – A Eur. J.* **2016**, *22*, 32–57.

[2] IRENA, *Global Energy Transformation: A Roadmap to 2050 (2019 Edition)*, International Renewable Energy Agency, Abu Dhabi, **2019**.

[3] *BP Statistical Review of World Energy 2020*, **2020**.

[4] N. Armaroli, V. Balzani, *ChemSusChem* **2011**, *4*, 21–36.

[5] A. J. Esswein, D. G. Nocera, *Chem. Rev.* **2007**, *107*, 4022–4047.

[6] S. Niaz, T. Manzoor, A. H. Pandith, *Renew. Sustain. Energy Rev.* **2015**, *50*, 457–469.

[7] E. Riedel, *Anorganische Chemie*, De Gruyter, Berlin, Boston, **2004**.

[8] G. Ankit, S. Agarwal, *Hydrogen Generation Market Size By Delivery Mode, By Process, By Application, Industry Analysis Report, Regional Outlook, Price Trends, Competitive Market Share & Forcast*, **2020**.

[9] L. Sun, L. Hammarström, B. Åkermark, S. Styring, *Chem. Soc. Rev.* **2001**, *30*, 36–49.

[10] L. Hammarström, *Chem* **2016**, *1*, 515–518.

[11] M. C. Hanna, A. J. Nozik, *J. Appl. Phys.* **2006**, *100*, 74510.

[12] R. Eisenberg, *Science* **2009**, *324*, 44–45.

[13] Z. Yu, F. Li, L. Sun, *Energy Environ. Sci.* **2015**, *8*, 760–775.

[14] W. E. I. Sha, X. Ren, L. Chen, W. C. H. Choy, *Appl. Phys. Lett.* **2015**, *106*, 221104.

[15] J. A. S. Roberts, R. M. Bullock, *Inorg. Chem.* **2013**, *52*, 3823–3835.

[16] D. G. Nocera, *Acc. Chem. Res.* **2012**, *45*, 767–776.

[17] S. Y. Reece, J. A. Hamel, K. Sung, T. D. Jarvi, A. J. Esswein, J. J. H. Pijpers, D. G. Nocera, *Science* **2011**, *334*, 645–648.

[18] J. Liu, Y. Liu, N. Liu, Y. Han, X. Zhang, H. Huang, Y. Lifshitz, S.-T. Lee, J. Zhong, Z. Kang, *Science* **2015**, *347*, 970–974.

[19] W.-J. Ong, L.-L. Tan, Y. H. Ng, S.-T. Yong, S.-P. Chai, *Chem. Rev.* **2016**, *116*, 7159–7329.

[20] O. Khaselev, J. A. Turner, *Science* **1998**, *280*, 425–427.

[21] O. Khaselev, A. Bansal, J. A. Turner, *Int. J. Hydrogen Energy* **2001**, *26*, 127–132.

[22] B. Zhang, L. Sun, *Chem. Soc. Rev.* **2019**, *48*, 2216–2264.

[23] Y. Pellegrin, F. Odobel, *Comptes Rendus Chim.* **2017**, *20*, 283–295.

[24] V. V Pavlishchuk, A. W. Addison, *Inorganica Chim. Acta* **2000**, *298*, 97–102.

[25] J.-H. Shon, T. S. Teets, *ACS Energy Lett.* **2019**, *4*, 558–566.

[26] Z. Han, R. Eisenberg, *Acc. Chem. Res.* **2014**, *47*, 2537–2544.

[27] Y.-J. Yuan, Z.-T. Yu, D.-Q. Chen, Z.-G. Zou, *Chem. Soc. Rev.* **2017**, *46*, 603–631.

[28] D. M. Hedstrand, W. H. Kruizinga, R. M. Kellogg, *Tetrahedron Lett.* **1978**, *19*, 1255–1258.

[29] M. Kirch, J.-M. Lehn, J.-P. Sauvage, *Helv. Chim. Acta* **1979**, *62*, 1345–1384.

[30] D. M. Arias-Rotondo, J. K. McCusker, *Chem. Soc. Rev.* **2016**, *45*, 5803–5820.

[31] J. I. Goldsmith, W. R. Hudson, M. S. Lowry, T. H. Anderson, S. Bernhard, *J. Am. Chem. Soc.* **2005**, *127*, 7502–7510.

[32] P. Du, K. Knowles, R. Eisenberg, *J. Am. Chem. Soc.* **2008**, *130*, 12576–12577.

[33] H. Takeda, K. Koike, T. Morimoto, H. Inumaru, O. Ishitani, in *Inorg. Photochem.* (Eds.: R. van Eldik, G.B.T.-A. in I.C. Stochel), Academic Press, **2011**, pp. 137–186.

[34] T. C. B. Harlang, Y. Liu, O. Gordivska, L. A. Fredin, C. S. Ponseca, P. Huang, P. Chábera, K. S. Kjaer, H. Mateos, J. Uhlig, R. Lomoth, R. Wallenberg, S. Styring, P. Persson, V. Sundström, K. Wärnmark, *Nat. Chem.* **2015**, *7*, 883–889.

[35] P. Chábera, Y. Liu, O. Prakash, E. Thyrhaug, A. El Nahhas, A. Honarfar, S. Essén, L. A. Fredin, T. C. B. Harlang, K. S. Kjær, K. Handrup, F. Ericson, H. Tatsuno, K. Morgan, J. Schnadt, L. Häggström, T. Ericsson, A. Sobkowiak, S. Lidin, P. Huang, S. Styring, J. Uhlig, J. Bendix, R. Lomoth, V. Sundström, P. Persson, K. Wärnmark, *Nature* **2017**, *543*, 695–699.

[36] P. Zhang, M. Wang, C. Li, X. Li, J. Dong, L. Sun, *Chem. Commun.* **2010**, *46*, 8806–8808.

[37] T. Lazarides, M. Delor, I. V Sazanovich, T. M. McCormick, I. Georgakaki, G. Charalambidis, J. A. Weinstein, A. G. Coutsolelos, *Chem. Commun.* **2014**, *50*, 521–523.

[38] N. Armaroli, *Chem. Soc. Rev.* **2001**, *30*, 113–124.

[39] S.-P. Luo, E. Mejía, A. Friedrich, A. Pazidis, H. Junge, A.-E. Surkus, R. Jackstell, S. Denurra, S. Gladiali, S. Lochbrunner, M. Beller, *Angew. Chemie Int. Ed.* **2013**, *52*, 419–423.

[40] T. Lazarides, T. McCormick, P. Du, G. Luo, B. Lindley, R. Eisenberg, *J. Am. Chem. Soc.* **2009**, *131*, 9192–9194.

[41] L. Li, L. Duan, F. Wen, C. Li, M. Wang, A. Hagfeldt, L. Sun, *Chem. Commun.* **2012**, *48*, 988–990.

[42] S. Ahmad, E. Guillén, L. Kavan, M. Grätzel, M. K. Nazeeruddin, *Energy Environ. Sci.* **2013**, *6*, 3439–3466.

[43] N. Herron, J. C. Calabrese, W. E. Farneth, Y. Wang, *Science* **1993**, *259*, 1426–1428.

[44] M. L. Steigerwald, L. E. Brus, *Acc. Chem. Res.* **1990**, *23*, 183–188.

[45] H.-L. Wu, X.-B. Li, C.-H. Tung, L.-Z. Wu, *Adv. Sci.* **2018**, *5*, 1870023.

[46] T. Rajh, O. I. Micic, A. J. Nozik, *J. Phys. Chem.* **1993**, *97*, 11999–12003.

[47] F. E. Osterloh, *Chem. Soc. Rev.* **2013**, *42*, 2294–2320.

[48] M. A. Holmes, T. K. Townsend, F. E. Osterloh, *Chem. Commun.* **2012**, *48*, 371–373.

[49] P. Du, R. Eisenberg, *Energy Environ. Sci.* **2012**, *5*, 6012–6021.

[50] W. T. Eckenhoff, *Coord. Chem. Rev.* **2018**, *373*, 295–316.

[51] M. Beller, A. Renken, R. A. van Santen, Eds. , *Catalysis : From Principles to*

Applications, Wiley-VCH Verlag, Germany, **2012**.

[52] J.-M. Lehn, J.-P. Sauvage, *Nouv. J. Chim.* **1977**, *1*, 449–451.

[53] J. Kiwi, M. Grätzel, *Nature* **1979**, *281*, 657–658.

[54] D. S. Miller, A. J. Bard, G. McLendon, J. Ferguson, *J. Am. Chem. Soc.* **1981**, *103*, 5336–5341.

[55] W. R. McNamara, Z. Han, C.-J. (Madeline) Yin, W. W. Brennessel, P. L. Holland, R. Eisenberg, *Proc. Natl. Acad. Sci.* **2012**, *109*, 15594–15599.

[56] A. Das, Z. Han, M. G. Haghighi, R. Eisenberg, *Proc. Natl. Acad. Sci.* **2013**, *110*, 16716–16723.

[57] Z. Han, W. R. McNamara, M.-S. Eum, P. L. Holland, R. Eisenberg, *Angew. Chemie Int. Ed.* **2012**, *51*, 1667–1670.

[58] Z. Han, F. Qiu, R. Eisenberg, P. L. Holland, T. D. Krauss, *Science* **2012**, *338*, 1321–1324.

[59] A. Das, Z. Han, W. W. Brennessel, P. L. Holland, R. Eisenberg, *ACS Catal.* **2015**, *5*, 1397–1406.

[60] W. Lubitz, H. Ogata, O. Rüdiger, E. Reijerse, *Chem. Rev.* **2014**, *114*, 4081–4148.

[61] D. Schilter, J. M. Camara, M. T. Huynh, S. Hammes-Schiffer, T. B. Rauchfuss, *Chem. Rev.* **2016**, *116*, 8693–8749.

[62] J. W. Peters, W. N. Lanzilotta, B. J. Lemon, L. C. Seefeldt, *Science* **1998**, *282*, 1853–1858.

[63] Y. Nicolet, C. Piras, P. Legrand, C. E. Hatchikian, J. C. Fontecilla-Camps, *Structure* **1999**, *7*, 13–23.

[64] Y. Nicolet, A. L. de Lacey, X. Vernède, V. M. Fernandez, E. C. Hatchikian, J. C. Fontecilla-Camps, *J. Am. Chem. Soc.* **2001**, *123*, 1596–1601.

[65] A. Silakov, B. Wenk, E. Reijerse, W. Lubitz, *Phys. Chem. Chem. Phys.* **2009**, *11*, 6592–6599.

[66] G. Berggren, A. Adamska, C. Lambertz, T. R. Simmons, J. Esselborn, M. Atta, S. Gambarelli, J.-M. Mouesca, E. Reijerse, W. Lubitz, T. Happe, V. Artero, M. Fontecave, *Nature* **2013**, *499*, 66–69.

[67] H. Junge, N. Rockstroh, S. Fischer, A. Brückner, R. Ludwig, S. Lochbrunner, O. Kühn, M. Beller, *Inorganics* **2017**, *5*, DOI 10.3390/inorganics5010014.

[68] J.-F. Capon, F. Gloaguen, P. Schollhammer, J. Talarmin, *Coord. Chem. Rev.* **2005**, *249*, 1664–1676.

[69] S. Tschierlei, S. Ott, R. Lomoth, *Energy Environ. Sci.* **2011**, *4*, 2340–2352.

[70] N. Wang, M. Wang, L. Chen, L. Sun, *Dalt. Trans.* **2013**, *42*, 12059–12071.

[71] M. Watanabe, Y. Honda, H. Hagiwara, T. Ishihara, *J. Photochem. Photobiol. C Photochem. Rev.* **2017**, *33*, 1–26.

[72] R. Cammack, *Nature* **1999**, *397*, 214–215.

[73] P. Zhang, M. Wang, Y. Na, X. Li, Y. Jiang, L. Sun, *Dalt. Trans.* **2010**, *39*, 1204–1206.

[74] T. Yu, Y. Zeng, J. Chen, Y.-Y. Li, G. Yang, Y. Li, *Angew. Chemie Int. Ed.* **2013**, *52*, 5631–5635.

[75] J.-X. Jian, Q. Liu, Z.-J. Li, F. Wang, X.-B. Li, C.-B. Li, B. Liu, Q.-Y. Meng, B. Chen, K. Feng, C.-H. Tung, L.-Z. Wu, *Nat. Commun.* **2013**, *4*, 2695.

[76] J.-X. Jian, C. Ye, X.-Z. Wang, M. Wen, Z.-J. Li, X.-B. Li, B. Chen, C.-H. Tung, L.-Z. Wu, *Energy Environ. Sci.* **2016**, *9*, 2083–2089.

[77] F. Gärtner, B. Sundararaju, A.-E. Surkus, A. Boddien, B. Loges, H. Junge, P. H. Dixneuf, M. Beller, *Angew. Chemie Int. Ed.* **2009**, *48*, 9962–9965.

[78] F. Gärtner, A. Boddien, E. Barsch, K. Fumino, S. Losse, H. Junge, D. Hollmann, A. Brückner, R. Ludwig, M. Beller, *Chem. – A Eur. J.* **2011**, *17*, 6425–6436.

[79] T. B. Rauchfuss, *Acc. Chem. Res.* **2015**, *48*, 2107–2116.

[80] D. Hollmann, F. Gärtner, R. Ludwig, E. Barsch, H. Junge, M. Blug, S. Hoch, M. Beller, A. Brückner, *Angew. Chemie Int. Ed.* **2011**, *50*, 10246–10250.

[81] M. Masui, H. Sayo, Y. Tsuda, *J. Chem. Soc. B* **1968**, 973–976.

[82] L. C. Portis, V. V Bhat, C. K. Mann, *J. Org. Chem.* **1970**, *35*, 2175–2178.

[83] F. Kanoufi, Y. Zu, A. J. Bard, *J. Phys. Chem. B* **2001**, *105*, 210–216.

[84] P. J. DeLaive, T. K. Foreman, C. Giannotti, D. G. Whitten, *J. Am. Chem. Soc.* **1980**, *102*, 5627–5631.

[85] J. F. Perez-Benito, C. Arias, *Int. J. Chem. Kinet.* **1991**, *23*, 717–732.

[86] K. Abbas, D. Marji, *Zeitschrift für Naturforsch. A* **n.d.**, *60*, 667–671.

[87] F. Gärtner, D. Cozzula, S. Losse, A. Boddien, G. Anilkumar, H. Junge, T. Schulz, N. Marquet, A. Spannenberg, S. Gladiali, M. Beller, *Chem. – A Eur. J.* **2011**, *17*, 6998–7006.

[88] E. Mejía, S.-P. Luo, M. Karnahl, A. Friedrich, S. Tschierlei, A.-E. Surkus, H. Junge, S. Gladiali, S. Lochbrunner, M. Beller, *Chem. – A Eur. J.* **2013**, *19*, 15972–15978.

[89] A. Juris, V. Balzani, F. Barigelletti, S. Campagna, P. Belser, A. von Zelewsky, *Coord. Chem. Rev.* **1988**, *84*, 85–277.

[90] Y. Umena, K. Kawakami, J.-R. Shen, N. Kamiya, *Nature* **2011**, *473*, 55–60.

[91] M. Suga, F. Akita, M. Sugahara, M. Kubo, Y. Nakajima, T. Nakane, K. Yamashita, Y. Umena, M. Nakabayashi, T. Yamane, T. Nakano, M. Suzuki, T. Masuda, S. Inoue, T. Kimura, T. Nomura, S. Yonekura, L.-J. Yu, T. Sakamoto, T. Motomura, J.-H. Chen, Y. Kato, T. Noguchi, K. Tono, Y. Joti, T. Kameshima, T. Hatsui, E. Nango, R. Tanaka, H. Naitow, Y. Matsuura, A. Yamashita, M. Yamamoto, O. Nureki, M. Yabashi, T. Ishikawa, S. Iwata, J.-R. Shen, *Nature* **2017**, *543*, 131–135.

[92] V. Krewald, M. Retegan, N. Cox, J. Messinger, W. Lubitz, S. DeBeer, F. Neese, D. A.

Pantazis, *Chem. Sci.* **2015**, *6*, 1676–1695.

[93] S. W. Gersten, G. J. Samuels, T. J. Meyer, *J. Am. Chem. Soc.* **1982**, *104*, 4029–4030.

[94] L. Wang, L. Duan, B. Stewart, M. Pu, J. Liu, T. Privalov, L. Sun, *J. Am. Chem. Soc.* **2012**, *134*, 18868–18880.

[95] L. Wang, L. Duan, Y. Wang, M. S. G. Ahlquist, L. Sun, *Chem. Commun.* **2014**, *50*, 12947–12950.

[96] L. Duan, F. Bozoglian, S. Mandal, B. Stewart, T. Privalov, A. Llobet, L. Sun, *Nat. Chem.* **2012**, *4*, 418–423.

[97] Y. Sato, S. Takizawa, S. Murata, *Eur. J. Inorg. Chem.* **2015**, *2015*, 5495–5502.

[98] N. S. McCool, D. M. Robinson, J. E. Sheats, G. C. Dismukes, *J. Am. Chem. Soc.* **2011**, *133*, 11446–11449.

[99] S. Berardi, G. La Ganga, M. Natali, I. Bazzan, F. Puntoriero, A. Sartorel, F. Scandola, S. Campagna, M. Bonchio, *J. Am. Chem. Soc.* **2012**, *134*, 11104–11107.

[100] B. O'Regan, M. Grätzel, *Nature* **1991**, *353*, 737–740.

[101] Z. Ji, M. He, Z. Huang, U. Ozkan, Y. Wu, *J. Am. Chem. Soc.* **2013**, *135*, 11696–11699.

[102] K. A. Click, D. R. Beauchamp, Z. Huang, W. Chen, Y. Wu, *J. Am. Chem. Soc.* **2016**, *138*, 1174–1179.

[103] A. Krawicz, J. Yang, E. Anzenberg, J. Yano, I. D. Sharp, G. F. Moore, *J. Am. Chem. Soc.* **2013**, *135*, 11861–11868.

[104] J. Gu, Y. Yan, J. L. Young, K. X. Steirer, N. R. Neale, J. A. Turner, *Nat. Mater.* **2016**, *15*, 456–460.

[105] K. Fan, F. Li, L. Wang, Q. Daniel, E. Gabrielsson, L. Sun, *Phys. Chem. Chem. Phys.* **2014**, *16*, 25234–25240.

[106] A. Kaeser, M. Mohankumar, J. Mohanraj, F. Monti, M. Holler, J.-J. Cid, O. Moudam, I. Nierengarten, L. Karmazin-Brelot, C. Duhayon, B. Delavaux-Nicot, N. Armaroli, J.-F. Nierengarten, *Inorg. Chem.* **2013**, *52*, 12140–12151.

[107] H. Guenzler, H. U. Gremlich, *IR Spectroscopy An Introduction*, Wiley-VCH, Germany, **2002**.

[108] P. Larkin, *Infrared and Raman Spectroscopy: Principles and Spectral Interpretation*, Elsevier, **2017**.

[109] K. Neymeyr, M. Sawall, D. Hess, *J. Chemom.* **2010**, *24*, 67–74.

[110] B. Loges, H. Junge, B. Spilker, C. Fischer, M. Beller, *Chemie Ing. Tech.* **2007**, *79*, 741–753.

[111] A. Boddien, B. Loges, H. Junge, M. Beller, *ChemSusChem* **2008**, *1*, 751–758.

[112] H. Friebolin, J. K. Becconsall, *Basic One-and Two-Dimensional NMR Spectroscopy*, Wiley-Vch Weinheim:, **2005**.

[113] D. G. Gorenstein, *Prog. Nucl. Magn. Reson. Spectrosc.* **1984**, *16*, 1–98.

[114] P. S. Pregosin, *Coord. Chem. Rev.* **2008**, *252*, 2156–2170.

[115] S. Gross, M. Bauer, *Adv. Funct. Mater.* **2010**, *20*, 4026–4047.

[116] S. Calvin, *XAFS for Everyone*, CRC Press, **2013**.

[117] M. Bauer, H. Bertagnolli, *Methods Phys. Chem.* **2012**, 231–269.

[118] M. G. Pfeffer, B. Schäfer, G. Smolentsev, J. Uhlig, E. Nazarenko, J. Guthmuller, C. Kuhnt, M. Wächtler, B. Dietzek, V. Sundström, S. Rau, *Angew. Chemie Int. Ed.* **2015**, *54*, 5044–5048.

[119] M. Bauer, C. Gastl, *Phys. Chem. Chem. Phys.* **2010**, *12*, 5575–5584.

[120] D. Mellmann, E. Barsch, M. Bauer, K. Grabow, A. Boddien, A. Kammer, P. Sponholz, U. Bentrup, R. Jackstell, H. Junge, G. Laurenczy, R. Ludwig, M. Beller, *Chem. – A Eur. J.* **2014**, *20*, 13589–13602.

[121] N. Binsted, S. S. Hasnain, *J. Synchrotron Radiat.* **1996**, *3*, 185–196.

[122] C. H. Hamann, W. Vielstich, W.-V. Elektrochemie, **2005**.

[123] G. A. N. Felton, R. S. Glass, D. L. Lichtenberger, D. H. Evans, *Inorg. Chem.* **2006**, *45*, 9181–9184.

[124] E. S. Rountree, B. D. McCarthy, T. T. Eisenhart, J. L. Dempsey, *Inorg. Chem.* **2014**, *53*, 9983–10002.

[125] M. J. Frisch, G. W. Trucks, H. B. Schlegel, G. E. Scuseria, M. A. Robb, J. R. Cheeseman, G. Scalmani, V. Barone, G. A. Petersson, H. Nakatsuji, X. Li, M. Caricato, A. V Marenich, J. Bloino, B. G. Janesko, R. Gomperts, B. Mennucci, H. P. Hratchian, J. V Ortiz, A. F. Izmaylov, J. L. Sonnenberg, D. Williams-Young, F. Ding, F. Lipparini, F. Egidi, J. Goings, B. Peng, A. Petrone, T. Henderson, D. Ranasinghe, V. G. Zakrzewski, J. Gao, N. Rega, G. Zheng, W. Liang, M. Hada, M. Ehara, K. Toyota, R. Fukuda, J. Hasegawa, M. Ishida, T. Nakajima, Y. Honda, O. Kitao, H. Nakai, T. Vreven, K. Throssell, J. A. Montgomery Jr., J. E. Peralta, F. Ogliaro, M. J. Bearpark, J. J. Heyd, E. N. Brothers, K. N. Kudin, V. N. Staroverov, T. A. Keith, R. Kobayashi, J. Normand, K. Raghavachari, A. P. Rendell, J. C. Burant, S. S. Iyengar, J. Tomasi, M. Cossi, J. M. Millam, M. Klene, C. Adamo, R. Cammi, J. W. Ochterski, R. L. Martin, K. Morokuma, O. Farkas, J. B. Foresman, D. J. Fox, **2016**.

[126] A. D. Becke, *J. Chem. Phys.* **1993**, *98*, 1372–1377.

[127] C. Lee, W. Yang, R. G. Parr, *Phys. Rev. B* **1988**, *37*, 785–789.

[128] A. D. McLean, G. S. Chandler, *J. Chem. Phys.* **1980**, *72*, 5639–5648.

[129] R. Krishnan, J. S. Binkley, R. Seeger, J. A. Pople, *J. Chem. Phys.* **1980**, *72*, 650–654.

[130] C. Chi, J. Cui, Z. H. Li, X. Xing, G. Wang, M. Zhou, *Chem. Sci.* **2012**, *3*, 1698–1706.

[131] H. Iikura, T. Tsuneda, T. Yanai, K. Hirao, *J. Chem. Phys.* **2001**, *115*, 3540–3544.

[132] A. M. Bond, P. A. Dawson, B. M. Peake, B. H. Robinson, J. Simpson, *Inorg. Chem.* **1977**, *16*, 2199–2206.

[133] L. L. Tinker, S. Bernhard, *Inorg. Chem.* **2009**, *48*, 10507–10511.

[134] D. N. Chirdon, W. J. Transue, H. N. Kagalwala, A. Kaur, A. B. Maurer, T. Pintauer, S. Bernhard, *Inorg. Chem.* **2014**, *53*, 1487–1499.

[135] P. E. Garrou, *Chem. Rev.* **1985**, *85*, 171–185.

[136] R. Giereth, W. Frey, H. Junge, S. Tschierlei, M. Karnahl, *Chem. – A Eur. J.* **2017**, *23*, 17432–17437.

[137] R. Giereth, A. K. Mengele, W. Frey, M. Kloß, A. Steffen, M. Karnahl, S. Tschierlei, *Chem. – A Eur. J.* **2020**, *26*, 2675–2684.

[138] M. Rentschler, S. Iglesias, M.-A. Schmid, C. Liu, S. Tschierlei, W. Frey, X. Zhang, M. Karnahl, D. Moonshiram, *Chem. – A Eur. J.* **2020**, *26*, 9527–9536.

[139] M. Rentschler, M.-A. Schmid, W. Frey, S. Tschierlei, M. Karnahl, *Inorg. Chem.* **2020**, *59*, 14762–14771.

[140] H. Chen, L.-X. Xu, L.-J. Yan, X.-F. Liu, D.-D. Xu, X.-C. Yu, J.-X. Fan, Q.-A. Wu, S.-P. Luo, *Dye. Pigment.* **2020**, *173*, 108000.

[141] T. Brandl, C. Kerzig, L. Le Pleux, A. Prescimone, O. S. Wenger, M. Mayor, *Chem. – A Eur. J.* **2020**, *26*, 3119–3128.

[142] M. Ferrer, O. Rossell, M. Seco, M. Soler, M. Font-Bardía, X. Solans, D. de Montauzon, *J. Organomet. Chem.* **2000**, *598*, 215–221.

VIII. SELBSTSTÄNDIGKEITSERKLÄRUNG

Ich gebe hiermit folgende Erklärung ab:

1. Die Gelegenheit zum vorliegenden Promotionsvorhaben ist mir nicht kommerziell vermittelt worden. Insbesondere habe ich keine Organisation eingeschaltet, die gegen Entgelt Betreuerinnen/Betreuer für die Anfertigung von Dissertationen sucht oder die mir obliegenden Pflichten hinsichtlich der Prüfungsleistungen für mich ganz oder teilweise erledigt.

2. Ich versichere hiermit an Eides statt, dass ich die vorliegende Arbeit selbstständig angefertigt und ohne fremde Hilfe verfasst habe. Dazu habe ich keine außer den von mir angegebenen Hilfsmitteln und Quellen verwendet und die den benutzten Werken inhaltlich und wörtlich entnommenen Stellen habe ich als solche kenntlich gemacht.

3. Ich habe ein Verfahren zur Erlangung des Doktorgrades bisher weder an der Universität Rostock noch an einer anderen wissenschaftlichen Einrichtung beantragt. Die vorliegende Dissertation wurde bisher weder im Ausland noch im Inland in gleicher oder ähnlicher Form einer anderen Prüfungsbehörde vorgelegt.

Rostock _____ _____

(Abgabedatum) (Vollständige Unterschrift)

IX. CURRICULUM VITAE

Steffen Fischer

Feldstraße 38, 18057 Rostock

+49 (0)1575 8054702

steffenfischer-rostock@web.de

Personal Information

Date of birth	June 18th, 1986 in Rostock
Civil status	unmarried, no children

Professional Career

Since June 2021	**Head of Data Analysis** at Centogene GmbH, Rostock
Sep. 2020 – May 2021	**Senior Scientist** at Centogene GmbH, Rostock
June 2019 – Aug 2020	**Scientist** at Centogene GmbH, Rostock
June 2018 – May 2019	**Junior Scientist** at Centogene GmbH, Rostock
Sep. 2017 – June 2018	**Physics teacher** at the adult education center Rostock (Volkshochschule der Hanse- und Universitätsstadt Rostock)
Dec. 2011 – Sep. 2016	**Research fellow** in the Department of Physical and Theoretical Chemistry at the University of Rostock

Qualification

Dec. 2011 – July 2021	**PhD** in the Department of Physical and Theoretical Chemistry at the University of Rostock *PhD thesis*: „ Mechanistic Understanding and Improvement of Photochemical Proton Reduction Catalyzed by Iron Carbonyl Complexes for Sustainable Hydrogen Production" (supervision: Prof. Dr. Ralf Ludwig, grade: *magna cum laude*)
Oct. 2009 – Oct. 2011	**Chemistry graduate studies** at the University of Rostock *Main research field*: catalysis *Diploma thesis*: „Investigation of catalytic species in the photocatalytic water reduction by means of In-situ-FTIR-spectroscopy" (supervision: Prof. Dr. Ralf Ludwig, Dr. Enrico Barsch, grade: 1.0) *Degree*: diploma (grade: 1.4)
Oct. 2008 – July 2009	**Studies abroad** at the Universidade da Coruña, Erasmus program in A Coruña, Spain
Oct. 2005 – Sep. 2008	**Chemistry undergraduate studies** at the University of Rostock *Degree*: preliminary diploma (grade: 1.5)
1996 – 2005	**University-preparatory school**, ISG Rostock *Advanced courses*: math and chemistry *Degree*: Abitur (A-levels, grade: 2.2)

Professional Skills

- leadership of employees
- data analysis
- IT project management and ownership
- profound knowledge of analytical chemistry: IR, Raman and NMR spectroscopy, cyclic voltammetry, Mass spectrometry
- competent knowledge in theoretical chemistry regarding quantum mechanical calculations
- basic knowledge of analytical chemistry: XAS
- versed in use of gloveboxes and Schlenk lines
- expertise in design, construction and optimization of experimental setups
- profound computer literacy:
    - R (RStudio), Python, Bash (Linux), Matlab
    - MS-Office, LaTeX, Endnote, Mendely, Origin, Inkscape, TYPO3, UNIFI, Progenesis, OPUS, MestReNova, Gaussian 09, Molden, Chemdraw,
    - Use of: Sci-Finder, Web of Science, Reaxys
- driver‘s license: Klasse B

Language Skills

- english – business fluent
- spanish – fluent, UNIcert III (European Level C1)

Further Education

Sep. 14th 2016	Vacuum seminar organized by the Leybold Company, Rostock
Sep. 01st – 06th 2014	Summer School 2014 „Methods in Molecular Energy Research: Theory and Spectroscopy", Gelsenkirchen
June 19th 2014	Working safety in the laboratory, Dummerstorf

Rostock, Oct. 16th 2021

Publications

2020 "Treatment Efficiency in Gaucher Patients Can Reliably Be Monitored by Quantification of Lyso-Gb1 Concentrations in Dried Blood Spots"
C. Cozma, P. Cullufi, G. Kramp, M. Hovakimyan, V. Velmishi, A. Gjikopulli, S. Tomori, S. Fischer, S. Oppermann, U. Grittner, P. Bauer, C. Beetz, and A. Rolfs
Int. J. Mol. Sci., 21, 4577, 2020

2018 "Diferrate $[Fe_2(CO)_6(\mu\text{-}CO)\{\mu\text{-}P(aryl)_2\}]^-$ as Self-Assembling Iron/Phosphor-Based Catalyst for the Hydrogen Evolution Reaction in Photocatalytic Proton Reduction — Spectroscopic Insights"
S. Fischer, A. Rösel, M. Bauer, A. Kammer, E. Barsch, R. Schoch, H. Junge, M. Beller and R. Ludwig
Chem. Eur. J., 24, 16052-16065, 2018

"Mechanistic Insights into the Electrochemical Reduction of CO_2 Catalyzed by Iron Cyclopentadienone Complexes"
E. Oberem, A. F. Roesel, A. Rosas-Hernández, T. Kull, S. Fischer, A. Spannenberg, H. Junge, M. Beller, R. Ludwig, M. Roemelt, and R. Francke
Organometallics, 38, 1236-1247, 2018

2017 "Light to Hydrogen: Photocatalytic Hydrogen Generation from Water with Molecularly-Defined Iron Complexes"
H. Junge, N. Rockstroh, S. Fischer, A. Brückner, R. Ludwig, S. Lochbrunner, O. Kühn, M. Beller
Inorganics, 5(1), 14, 2017

"A Stable Manganese Pincer Catalyst for the Selective Dehydrogenation of Methanol"
M. Andérez-Fernández, L. K. Vogt, S. Fischer, W. Zhou, H. Jiao, M. Garbe, S. Elangovan, K. Junge, H. Junge, R. Ludwig, M. Beller
Angew. Chem., 129, 2, 574-577, 2017
Angew. Chem. Int. Ed., 56, 2, 559–562, 2017

2016	“Selective Catalytic Hydrogenations of Nitriles, Ketones, and Aldehydes by Well-Defined Manganese Pincer Complexes” S. Elangovan, C. Topf, S. Fischer, H. Jiao, A. Spannenberg, W. Baumann, R. Ludwig, K. Junge, M. Beller *J. Am. Chem. Soc.*, 138, 8809–8814, 2016
	"Copper-based Photosensitizers in Water Reduction: a more efficient in situ-formed System and improved mechanistic Understanding” A. J. J. Lennox, S. Fischer, M. Jurrat, S.-P. Luo, N. Rockstroh, H. Junge, R. Ludwig, M. Beller *Chem. Eur. J.*, 22, 1233-1238, 2016
	“Mechanistic Study of Photocatalytic Hydrogen Generation with Simple Iron Carbonyls as Water Reduction Catalysts” S. Fischer, O. S. Bokarev, E. Barsch, S. I. Bokarev, O. Kühn, R. Ludwig *ChemCatChem*, 8, 404-411, 2016
2014	„Dead and Rebirth: Photocatalytic Hydrogen Production by a Self-Organizing Copper-Iron System“ S. Fischer, D. Hollmann, S. Tschierlei, M. Karnahl, N. Rockstroh, E. Barsch, P. Schwarzbach, S.-P. Luo, H. Junge, M. Beller, S. Lochbrunner, R. Ludwig, A. Brückner *ACS Catal.,* 4, 1845-1849, **2014**

Conferences

May 05th 2016	115. General Assembly of the German Bunsen Society for Physical Chemistry, Rostock *„Mechanistic Understanding of Photocatalytic Water Reduction with Iron Carbonyl Phosphides by Means of In Situ Spectroscopy and Time Dependent - DFT Calculations" (Vortrag)*
Jan. 22nd 2016	Post graduate program of the interdisciplinary faculty LLM at the University of Rostock, Rostock *„IR-Spectroelectrochemistry - Setup and Application“ (lecture)*
Sep. 10th 2015	EMLG Annual Meeting, Rostock
Jan. 23rd 2015	Post graduate program of the interdisciplinary faculty LLM at the University of Rostock, Rostock

	„Photocatalytic Hydrogen Generation via Ordinary Iron Carbonyl Catalysts – An In-Situ FTIR Study" (lecture)
June 20th 2014	Evaluation LLM, Rostock
May 29th 2014	113. General Assembly of the German Bunsen Society for Physical Chemistry, Hamburg *"Photocatalytic Hydrogen Generation via Ordinary Iron Carbonyl Catalysts - An In-Situ FTIR Study" (lecture)*
May 14th 2014	Symposium "Sustainable Hydrogen and Fuels – Status and Perspectives", Rostock *"Photocatalytic Hydrogen Production by a Self-Organizing Copper-Iron System" (poster)*
Nov. 14th 2013	Project meeting Light 2 Hydrogen, Berlin *"Mechanistic Studies of Photocatalytic Water-Reduction Systems by means of FTIR- and EPR-Spectroscopy" (lecture)*
June 6th 2013	Project meeting Light 2 Hydrogen, Rostock *"Mechanistic Studies of an Iron Carbonyl based Photocatalytic Water-Reduction by means of FTIR-Spectroscopy" (lecture)*
May 9th 2013	112. General Assembly of the German Bunsen Society for Physical Chemistry, Karlsruhe *"Photocatalytic Hydrogen Generation via Iron based Water Reduction Catalysts - An In situ FTIR study" (poster)*
Nov. 29th 2012	Project meeting Light 2 Hydrogen, Berlin *"In situ IR Investigations of a Light Driven Water Reduction System" (poster)*
May 3rd 2012	Evaluation LLM, IOW Warnemünde
May 17th 2012	111. General Assembly of the German Bunsen Society for Physical Chemistry, Leipzig *"Photokatalytische Wasserreduktion - Aufklärung des Katalysezyklus mittels In-situ-FTIR-Spektroskopie"* (poster)
June 2nd 2011	110. General Assembly of the German Bunsen Society for Physical Chemistry. Berlin